Novel Oxynitride Lithium Ion Conductors

Rouzbeh Jarkaneh

Submitted for the degree of Doctor of Philosophy

Thesis Supervisor: Professor Anthony R. West

Department of Materials Science and Engineering

The University of Sheffield

January 2010- March 2015

اسرار ازل را نه تو دانی و نه من

وین حرف معما نه تو خوانی و نه من

هست از پس پرده گفتگوی من و تو

چون پرده برافتد نه تو مانی و نه من

There was the Door to which I found no Key;
There was the Veil through which I might not see:
Some little talk awhile of Me and Thee
There was—and then no more of Thee and Me

Omar khayyam, rendered into English verse by Edward FitzGerald

Declaration

This thesis is submitted in consideration for the award of Doctor of Philosophy.

It is believed to be completely original, except where acknowledgment has been given.

Rouzbeh Jarkaneh

March 2015

Acknowledgments

First and foremost I would like to thank my supervisor Professor Anthony R. West for his continues support, guidance and patience during my studies. I am grateful to acknowledge all my friends in the Electroceramics Research Group and department of Materials Science and Engineering for their immense help and advice and thoughtful discussions and everyone who made my time in Sheffield enjoyable.

This work is dedicated to my family, to my parents, brother, sister and partner. This thesis is simply the result of their support.

Abstract

In the search for solid electrolytes for application in all-solid-state batteries, synthesis of nitrogen-doped, crystalline, Li_3PO_4-based materials by partial substitution of oxygen by nitrogen in order to create interstitial lithium ions and enhance Li-ion conductivity was investigated. Amorphous lithium phosphorus oxynitrides have been previously studied and excellent ionic conductivity and chemical stability was discovered in thin film LiPON; however, the detailed structure and the effect of nitrogen on its properties are not known due to the glassy state. In two previous studies on crystalline forms of this material, lithium vacancy formation in the structure of N-doped Li_3PO_4 and N-doping of $LiPO_3$ was examined. Computational studies on Li-ion conduction of Li_3PO_4 predicted that an interstitial defect mechanism would provide the most efficient Li-ion transport. This thesis reports the first study to investigate nitrogen doping of crystalline, Li_3PO_4-based materials, to create interstitial Li^+ ions. Samples were prepared by solid-state reaction with Li_3N, as nitrogen-containing reactant, by a new modified synthesis technique. Synthesis procedures were designed to reduce any possible nitrogen loss before and/or during the synthesis.

$Li_{(3+X)}(P,V)O_{4-X}N_X$ and $Li_{2+Y}(Zn,Mg)SiO_{4-Y}N_Y$ solid solutions have been successfully synthesised and identified as mainly single phase by X-ray diffraction. Secondary phases were seen only in nitrogen-rich, N-doped compositions of Li_3PO_4 and $Li_2(Zn,Mg)SiO_4$ and also in N-doped Li_2MgSiO_4 close to the 1:1 composition, where lithia loss had been reported previously. N-doping of all compositions yielded a γ-type phase, except in Li_3VO_4 that resulted in a β phase. Orthorhombic with *Pnma* and *Pmn2₁* symmetries were assigned to $Li_{3+x}PO_{4-X}N_X$ and $Li_{3+x}VO_{4-X}N_X$ compositions, respectively, similar to their undoped polymorphs. The unit cell variation is small upon adding nitrogen and the solid solution limit is X≤0.2 in $Li_{(3+X)}(P,V)O_{4-X}N_X$. The unit cell variation is more significant in $Li_{2+Y}(Zn,Mg)SiO_{4-Y}N_Y$. Compositions with low concentration of nitrogen have a γ_0 structure (monoclinic with *P2₁/n* symmetry), similar to undoped polymorphs, with reduced unit cell volumes compared to undoped samples. Nitrogen doping encourages the monoclinicity by distorting the γ_0 phase to lithia-γ_0, similar to Li-rich compositions. Compositions with higher concentrations of nitrogen match with Li-rich compositions in $Li_{2+2X}(Zn,Mg)_{1-X}SiO_4$: lithia-$\gamma_0$ for N-doped Li_2ZnSiO_4 and a mixture of lithia-γ_0 and Li_4SiO_4-type phase in N-doped Li_2MgSiO_4.

Electrical properties were studied by impedance spectroscopy using high-density pellets prepared by one-step, reaction-sintering synthesis. N-doping improved the conductivity significantly by about two orders of magnitude in N-doped $Li_3(P,V)O_4$ and by 4-6 orders of magnitude in N-doped $Li_2(Zn,Mg)SiO_4$. The impedance data indicated that the level of electronic conductivity in N-doped compositions is small or negligible and the principal current carriers are lithium ions seen by a low frequency inclined spike with associated capacitance values of $\approx 10^{-6}$ Fcm^{-1} in the Z^* complex plane plots of N-doped samples. Linear Arrhenius behaviour was observed for undoped samples at all temperatures and for N-doped $Li_3(P,V)O_4$ and $Li_2(Zn,Mg)SiO_4$ below $\approx 350°$ and 200°C, respectively. The activation energy decreased by about 0.3 eV in N-doped $Li_3(P,V)O_4$, between 0.05-0.15 eV in N-doped Li_2ZnSiO_4 with a low concentration of nitrogen and between 0.6-0.7 eV in N-doped Li_2ZnSiO_4 with a high concentration of nitrogen and N-doped Li_2MgSiO_4. Ionic conductivity data of N-doped Li_3PO_4 (2.5×10^{-14} Scm^{-1} at 25°C and activation energy of 0.91 eV) are comparable to experimental and computational studies reported in the literature. N-doped Li_2ZnSiO_4 also showed similar conductivities to Li-rich compositions ($Li_{2+2X}Zn_{1-X}SiO_4$). Higher ionic conductivity and lower activation energy in N-doped samples was attributed to the high number of interstitial lithium ions created as the result of the substitution of nitrogen for oxygen. Above the mentioned temperatures a fully reversible, nonlinear behavior was evidenced, where the curvature in Arrhenius plots leads to near zero activation energies similar to many fast ion conductors and $Li_{2+2X}Zn_{1-X}SiO_4$. TGA/DSC results indicated that N-doped samples might have reacted with atmosphere at high temperatures.

Nitrogen content was determined using combustion analysis, which confirmed nitrogen incorporation into the N-doped samples. It was revealed that a great deal of nitrogen loss had occurred. Nitrogen loss that was also reported in previous studies of crystalline LiPON, was suggested to be due to the high temperature required for the solid-state reaction, early decomposition of Li_3N and/or by decomposition of N-doped products before N-analysis.

Electrochemical testing was performed on $Li_{3.4}VO_{3.6}N_{0.4}$ and compared with Li_3VO_4. $Li_{3.4}VO_{3.6}N_{0.4}$ showed improved electrochemical properties such as higher (dis)charge capacity and improved cycle life attributed to its enhanced ionic conductivity. As a result of its low working voltage (0.8-1.2V), high capacity and reasonable cycling performance it was suggested as a potential candidate for anode material.

Contents

Chapter 1

Introduction and literature review

"Battery is here to stay."

— Metallica

Lithium ion batteries

In the past thirty years, there has been a sharp rise in demand for portable electronic devices such as mobile phones and laptops, creating huge interest in small lightweight batteries, in addition to the need for rechargeable batteries for electric vehicles (EVs) due to environmental issues [1]. Battery electrochemistry is relatively a young science, since the first modern electrochemical storage device was invented 200 years ego by Volta. Chemical storage of electricity has come a long way since the discovery of Volta; however, many of today's battery technologies are based on earlier discoveries, such as the lead-acid battery, which was invented in 1859 as the first rechargeable battery and is still widely in use.

The exponential growth in electronic portable devices has led to enormous interest in compact lightweight batteries with high energy densities. Lithium, therefore, has become dominant in this field because of two unique properties, having the highest electrochemical reduction potential and being light. These two unique properties together with high voltage, high energy density, low self discharge rate and wide temperature range of operation has made it superior to all other battery technologies [2]. The first primary lithium battery was introduced commercially in the 1970s, based on the use of metallic lithium as the anode. Attempts to develop rechargeable lithium metal batteries failed due to safety concerns as a result of non-uniform metal deposition and dendrite formation on the lithium metal [3]. Goodenough [4] showed that lithium could be electrochemically inserted and removed from the structure of Li_XMO_2 (M=Co, Mn and Ni) without a major change in the structure. Subsequently, in the 1990s the first

rechargeable lithium battery was commercialised based on the use of insertion compounds as electrodes [5].

Batteries are a collection of electrochemical cells that convert chemical energy into electrical energy and vice versa. Each cell consists of two electrodes, cathode (+) and anode (−), separated by an electrolyte. In a lithium ion battery, lithium ions move from the anode via the electrolyte to the cathode, forcing reduction-oxidation (redox) reactions to take place during discharge: the transition metal cation is reduced (from M^{4+} to M^{3+} for example), enabling the cathode to intercalate Li^+. The electrons generated from the reaction, $Li=Li^+ + e^-$ in the anode, flow as current through the external circuit. In a reverse reaction, chemical energy can be stored in the anode by an external electrical force (Figure 1.1). Thus, the electrodes must allow for the passage of both electrons and ions, unlike electrolytes that must be a good ionic conductor but an electronic insulator to avoid self-discharge. The amount of electrical energy, which is presented either per unit weight or volume (Wh/kg and Wh/l respectively), is a function of cell potential (V) and capacity (Ah/kg), both related to the intrinsic property of the materials that form the positive and negative electrodes [6]. The cycle-life, lifetime and safety are dependent on the nature of the interfaces between the electrodes and electrolyte and the stability of the electrode materials in contact with them [6].
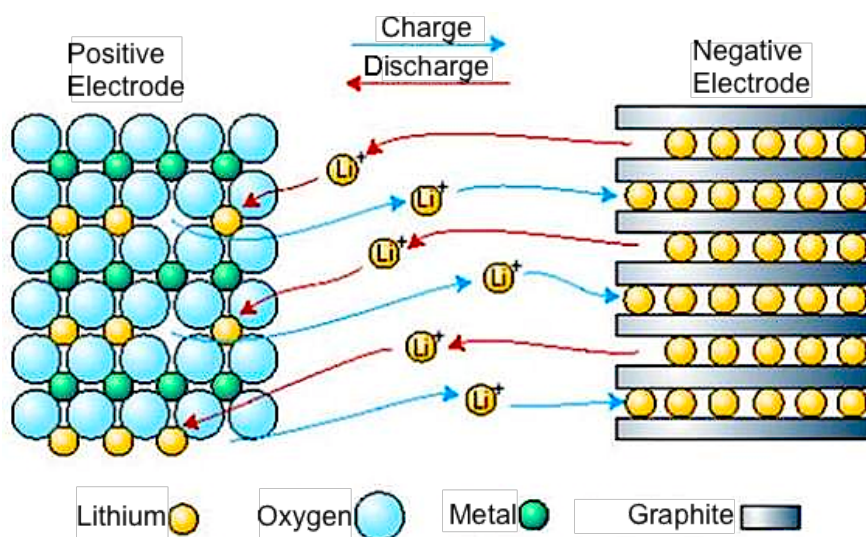
Figure 1.1. Schematic illustration of a lithium ion battery (graphite/electrolyte/lithium metal oxide) [7].

Almost all of the cathodes in the lithium ion battery market are based on three classes of materials [8]. First, layer structure materials, such as $LiCoO_2$ [4], $LiNi_{1-Y}Co_YO_2$ [9] and $LiNi_YMn_YCo_{1-2Y}O_2$ [10] (where either alternate layers are occupied by redox-active transition metals and lithium), metal dichalcogenides, such as TiS_2 [11] and high valent oxides, such as V_2O_5 [12]. Second, spinels, such as $LiMn_2O_4$ [13], with 3D framework structure and third, transition metal phosphates, such as olivine $LiFePO_4$ [14].

Carbons are used as the dominant anode material in commercial lithium ion batteries, mostly in graphitic (layer structure) type; however, they have the disadvantage of low energy density (theoretically 375 mAh/g) and safety issues related to lithium deposition (graphite intercalates Li at low potentials close to Li-plating) [15]. The proposed alternative anodes are mainly based on three categories [16]: first, alloy anodes, mainly based on Si and Sn-based composites with ultra high capacities but large volume change that restricts their use [17]. Second, conversion reaction materials, such as transition metal oxides/sulphides that despite high capacities suffer from capacity fading after the first cycles due to structural instability [18] and third, intercalation/deintercalation materials, typically titanium oxides, based on reversible insertion of mobile Li^+ into the empty lattice sites of the crystalline host while the structural layout of the host material is conserved, which offers a high reversibility but suffers from limited capacity and high operation voltage [19].

Good ionic conductivity ($\geq 10^{-4}$ Scm^{-1} at room temperature) and minimal electronic conductivity ($\leq 10^{-12}$ Scm^{-1}) are essential properties required by an electrolyte, in addition to being unreactive towards other cell components and being environmentally friendly. Furthermore, electrolytes should have a wide electrochemical window and must go through no chemical changes during operation. Electrochemical stability against electrodes is increasingly challenged by the development of new battery systems with higher energy densities, hence usage of more redox-active materials as cathodes and anodes. This has brought some safety concerns due to the flammable nature of organic electrolytes that are widely used in today's batteries. Most compositions of lithium electrolytes are based on solutions of lithium salts (like $LiBF_4$ and $LiPF_6$) in carbonate based solvents (like propylene and ethylene carbonates) [20]. Much research has been directed to reduce the potential hazard of organic electrolytes by application of additives [21] or development of new organic electrolytes like solid polymer electrolytes (SPEs) [22] and gel polymer electrolytes (GPE) [23]; however, such efforts have been met

with difficulty, since more often the improvement in the inflammability property is achieved at the expense of other vital properties [24].

Solid electrolytes

One of the other such alternatives to enhance safety is to substitute the flammable organic electrolyte with a solid inorganic material. Much attention, therefore, has been paid to solid electrolytes in order to improve lithium battery reliability. Solid-state batteries demonstrate an excellent long cycling performance, are free from leakage and fire hazards and have a wide range of operating temperature [25]. Moreover, solid electrolytes are generally single ion conductors, in other words, only Li^+ ions can move while anions and other cations form a rigid framework [26]. Solid state batteries however, have not been broadly used to date, due to the low ionic conductivity of solid electrolytes and high impedances at solid-solid interfaces; hence, their applications have been limited to stand-alone microelectronic devices, medical implants and high temperature applications [27]. On the other hand, an all-solid-state configuration can facilitate miniaturisation, using thin film technologies, where even rather resistive solid electrolytes may compete favourably with thicker, more conductive, organic electrolytes [28]. Apart from their flexible design, thin film batteries are one of the most competitive power sources due to their high volumetric energy density (Wh/l) and gravimetric energy density (Wh/kg) [29]. Figure 1.2 shows the energy density of thin film batteries and compares it with that of other batteries. Furthermore, tremendous effort in developing new solid electrolytes can be witnessed, leading to discovery of new solid electrolytes. The ionic conductivity of some of these new solid electrolytes can match that of organic liquid electrolytes at room temperatures. Figure 1.3 shows the temperature dependence of the ionic conductivity of some of these solid electrolytes compared with other electrolytes used in practical Li-batteries. Inorganic solid lithium electrolytes can be crystalline, amorphous or partly crystalline. Glassy electrolytes have the advantage of isotropic conductivity, ease of fabrication as thin films and lack of grain boundaries, in contrast to crystalline electrolytes, which are more stable, especially at high temperatures [26]. A short survey of the most important inorganic solid electrolytes is given below.
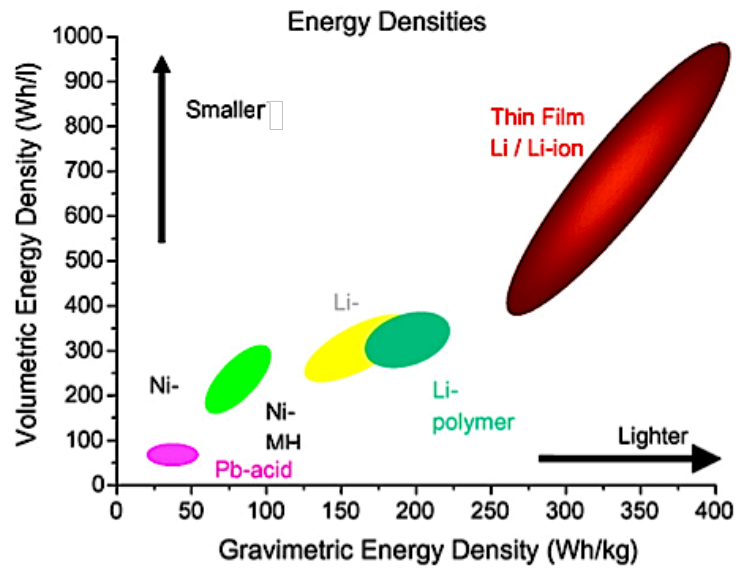
Figure 1.2. Comparison of energy densities of batteries [29].
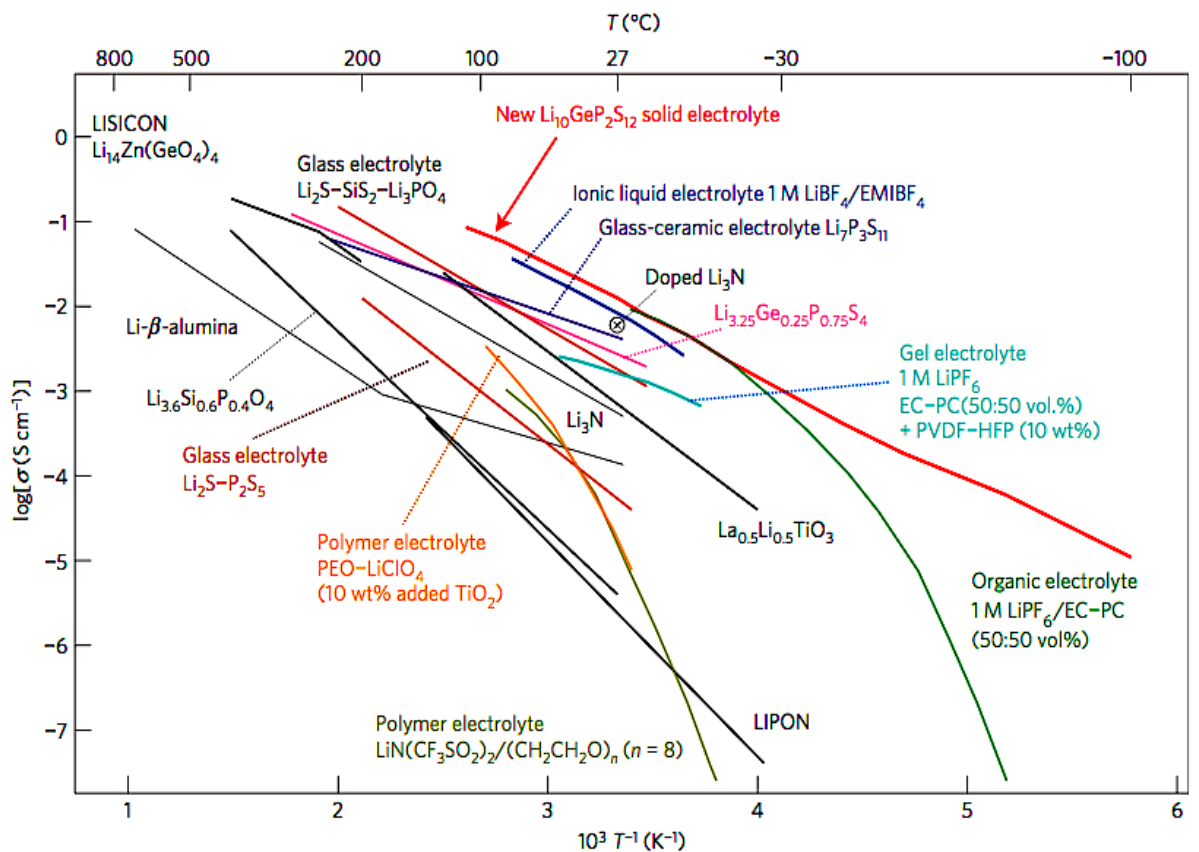
Figure 1.3. Arrhenius plots of the ionic conductivity of some solid electrolytes compared with some practical organic based electrolytes [30].

Lithium halides and nitrides

LiI was the first practical solid electrolyte ($\sigma \approx 5 \times 10^{-7}$ Scm^{-1} at RT), which was introduced in the 1970s and used in the Li/I$_2$ cell for applications in cardiac pacemakers. Aliovalent doping of LiI increases its conductivity [31]. One of the most conductive electrolytes reported to date is a LiI-doped sulphide glass ($\sigma \approx 2 \times 10^{-3}$ Scm^{-1} at RT) [32, 33]. Other lithium halides are almost insulators; however, lithium metal halides such as Li$_9$Bi$_2$Cl$_3$ [34] and Li$_3$InBr$_6$ [35] are reported to have modest ionic conductivity at room temperature.

Li$_3$N has one of the highest Li$^+$ conductivities at room temperature. Li$_3$N has a layer structure and a highly anisotropic conductivity ($\sigma \approx 1 \times 10^{-3}$ Scm^{-1} at RT along the sheets but about two orders of magnitude lower perpendicular to the sheets) [36]. H-doped lithium nitride shows even higher ionic conductivity [37]; however lithium nitrides suffer from low decomposition potential, which limits their usefulness in practical batteries.

Lithium rare earth titanate perovskites

Perovskites (general formula ABX$_3$) have an incredible tolerance for aliovalent and isovalent doping on both A and B sites leading to a large vacancy concentration on the A sublattice and creating open lattice structures. The highest Li$^+$ conductivity was found in Li$_{0.5-3X}$La$_{0.5+3X}$TiO$_3$ [38] with the bulk ionic conductivity as high as 1×10^{-3} Scm^{-1} at RT; however, the total conductivity is much lower due to grain boundary resistances and attempts to eliminate the grain boundary effect lead to substantial Li$_2$O loss due to the high sintering temperature required [39]. At temperatures below 400K, ionic conductivity of this material follows the Arrhenius law, with activation energy as low as 0.34 eV, but above 400K is no longer linear and can be fitted to a Vogel–Tammann–Fulcher relationship [40]. One problem facing these high lithium ion conducting materials is their enhanced electronic conductivity in contact with metallic Li due to Ti^{4+} reduction at the interface; therefore a less reducing, negative electrode must be used [41].

NASICON-type Li-ion conductors

Solid solutions based on aliovalent doping of NaZr$_2$(PO$_4$)$_3$, were discovered to have very high ionic conductivity and were named Na$^+$ super ionic conductors (NASICON) [42]. The lithium-containing analogues, LiM$_2$(PO$_4$)$_3$ (M^{4+}=Zr, Ti, Ge and Hf) also have NASICON-type structures, with corner-sharing MO$_6$ and PO$_4$ polyhehra, forming 3D

pathways for Li^+ movement [43]. Two types of solid solutions are possible to form Li vacancies and interstitials. The highest Li-ion conductivity was evidenced in $Li_{1.3}Al_{0.3}Ti_{1.7}(PO_4)_3$ ($\sigma \approx 3 \times 10^{-3}$ Scm^{-1} at RT for bulk) [44]; however Ti^{4+} reduction against lithium metal is an issue. It is also extremely difficult to eliminate grain boundary resistances in these ceramics and therefore the total conductivity is one to two orders of magnitudes lower than the bulk conductivity [45]. Activation energies are as low as 0.35 eV at low temperatures and Arrhenius plots are often curved at high temperatures [44].

LISICON and Thio-LISICON-type Li-ion conductors

The first material to be named a Li^+ super ionic conductor (LISICON) $Li_{3.5}Zn_{0.25}GeO_4$, showed considerable Li^+ conductivity at high temperatures but low conductivity at room temperature [46, 47]. Shortly afterwards, it led to the discovery of a wide range of crystalline lithium-ion conducting materials based on the general formula $Li_{8-c}A_aB_bO_4$ (c=ma + nb and m, n are the valences of A and B cations) [48]. They are related to a so-called γ structure, where cations are tetrahedrally coordinated. Solid solutions that led to Li-ion vacancies showed lower conductivity compared to those with interstitial Li-ions [49]. Interstitial lithiums hop between various empty tetrahedral and octahedral sites, enhancing the Li-ion conductivity. LISICONs tend to show non-linear Arrhenius behaviour at high temperatures and an ageing effect at low temperatures [50-52], limiting their usefulness in conventional Li-ion batteries but making them good candidates for thermal batteries.

Replacement of oxide ions with larger and more polarisable sulphide ions improved the ionic conductivity [53]. This family of materials was called Thio-LISICON. The improved ionic conductivity, compared to that of oxide systems, was previously seen in Li_2S-SiS_2-LiI [33] and $Li_2S-SiS_2-Li_3PO_4$ [54] glassy sulphides. The best conductivities were found in $Li_{3.4}Si_{0.4}P_{0.6}S_4$ ($\sigma \approx 6.4 \times 10^{-4}$ Scm^{-1} at RT) [55] and $Li_{3.25}Ge_{0.25}P_{0.75}S_4$ ($\sigma \approx 1 \times 10^{-3}$ Scm^{-1} at RT) [56]. A new material from this family, with the formula $Li_{10}GeP_2S_{12}$, has recently shown promising conductivities in the range of organic liquid electrolyte conductivities ($\sigma \approx 1 \times 10^{-2}$ Scm^{-1} at RT) [30].

LiPON

Lithium phosphorus oxynitride thin film was pioneered at the Oak Ridge National Laboratory (ORNL) [57]. It was shown that deposition of 1μm-thick films by RF magnetron sputtering from a high purity Li_3PO_4 ceramic target in nitrogen plasma

enhanced the ionic conductivity by 40 times ($\sigma \approx 2 \times 10^{-6}$ Scm^{-1} at 25°C and activation energy of 0.55 eV) compared to Li$_3$PO$_4$ films, also prepared by sputtering. Improved ionic conductivity in amorphous Li$_3$PO$_4$ by the addition of SiO$_2$, using the RF magnetron sputtering technique, was shown previously [58, 59]. Unfortunately, Li$_{3.6}$Si$_{0.6}$P$_{0.4}$O$_4$ is not stable in contact with lithium metal. In contrast, LiPON is rather stable in comparison with other lithium sulphide or oxide glasses (voltage window 0-5.5 V) [60] and despite its moderate conductivity, has been recognised as a standard solid electrolyte for thin film lithium batteries [29]. Some examples of typical lithium ion thin film batteries are given in table 1.1. Apart from thin films, lithium phosphate oxynitrides have been also made in bulk glass and crystalline forms and will be discussed briefly here.

Table 1.1. Some typical lithium ion, thin film batteries.

Electrolyte	Cathode	Anode	Voltage(V)	Capacity
Li$_{3.6}$Si$_{0.6}$P$_{0.4}$O$_4$ [58]	TiS$_2$	Li	2.5	45-150 μAh/cm^2
Li$_{6.1}$V$_{0.61}$Si$_{0.39}$O$_{5.36}$ [61]	LiMn$_2$O$_4$	Li	3.5-5	33.3 μAh/cm^2
Li$_2$S-SiS$_2$-P$_2$S$_5$ [62]	V$_2$O$_5$-TeO$_2$	Li	2.8-3.1	-
LiI-Li$_2$S-P$_2$S$_5$-P$_2$O$_5$ [63]	TiS$_2$	Li/LiI	1.8-2.8	70 mAh/cm^3
Li$_2$S-SiS$_2$-Li$_3$PO$_4$ [64]	LiCoO$_2$	Li	0-4.5	-
LiPON [65]	LiCoO$_2$	Li	2-4.2	35 μAh/cm^2
LiPON [66]	LiMn$_2$O$_4$	V$_2$O$_5$	1-3.5	18 μAh/cm^2

Phosphate glasses have been of interest mainly due to their high thermal expansion coefficients and low melting temperatures, which make them ideal for sealing applications; however, their poor chemical stability has been a drawback [67, 68]. Marchand showed that nitridation of these glasses under an ammonia atmosphere is a suitable way to improve their chemical resistance [69]. Bates et al was the first to show improved electrical properties in nitrided, lithium phosphate glasses [70]. The composition of these glasses is usually close to lithium metaphosphate (LiPO$_3$) and therefore their structure consists of phosphate chains. During nitridation, either di-coordinated −N= (N$_d$) or tri-coordinated −N< (N$_t$) nitrogen atoms substitute for both bridging and non-

bridging oxygens (BO/NBO) to form PO_3N and PO_2N_2 tetrahedra [71] (figure 1.4). Nitridation proceeds according to $2N_t$=3BO and $2N_d$=2NBO + 1BO equivalences, leading to a decrease in the BO/NBO ratio [72]. It is believed that the rise in the amount of non-bridging oxygens and cross-linking network, as a result of nitridation, could increase the number of available sites for lithium ions and therefore, increase the ionic conductivity as well as enhancing the chemical durability [73].

a)

b)
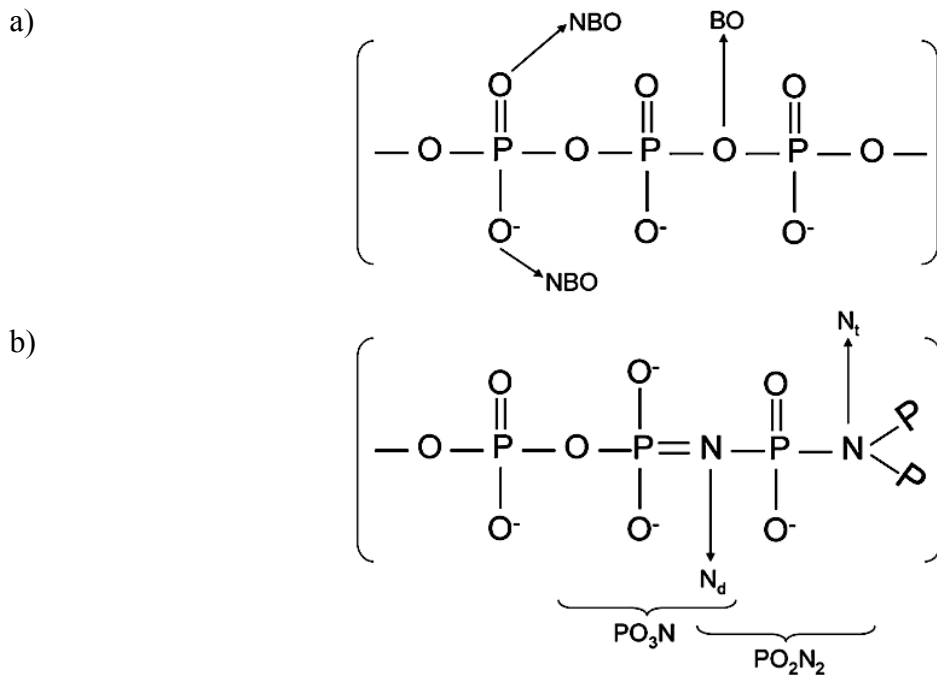
Figure 1.4. Schematic representation of structural features in a) a phosphate glass and b) a nitrided phosphate glass [74].

Thin film $Li_xPO_yN_z$, where x=2y + 3z − 5, is the most widely used solid electrolyte for thin film batteries. Despite its desirable properties, details of the structure, local stoichiometries and most importantly the effect of nitrogen on the ionic conductivity and chemical/mechanical stability are not known. The starting materials and the processing route for obtaining LiPON thin films and bulk glasses are different; however, many authors have compared the structure of deposited LiPON films with that of bulk glasses and therefore offered similar explanations for improved properties in them [74]. The structure of a Li_3PO_4 target in the thin film deposition technique is based on isolated phosphate tetrahedra (PO_4), consequently, no bridging oxygens should be present. An alternative interpretation, therefore, has to be proposed to explain the improved properties of thin film LiPON.

9

Lack of information on the structure, conduction mechanism and basis of conductivity and durability improvements is mainly due to the disordered nature of the LiPON materials; however much can be learned from the related crystalline form. The first successful attempt to synthesise crystalline LiPON was made by Wang et al [75]. During their investigation on bulk glasses they were able to synthesise a doped crystalline material, with $Li_{2.88}PO_{3.73}N_{0.14}$ stiochiometry by reaction between $LiPO_3$ and Li_3N, which has a γ-Li_3PO_4 structure. The ionic conductivity of this material was reported as $\approx 1 \times 10^{-13}$ Scm^{-1} at room temperature with an activation energy of 0.97 eV, significantly better than in pure Li_3PO_4 ($\approx 1 \times 10^{-18}$ Scm^{-1} at RT and activation energy of 1.24 eV). With the help of chemical and spectral analysis they identified P−N−P as well as PO_3N defect groups. As Li_3PO_4 is based on isolated PO_4 tetrahedra, the formation of P−N−P units was proposed to be due to some Li/P disorder by the following mechanism. $Li_{2.88}PO_{3.73}N_{0.14}$ has 4% lithium vacancies per formula unit. It was proposed that mobile Li^+ vacancies could be stabilised, following substitution of oxygen by nitrogen, by removing an oxygen from the lattice to give the general formula $Li_{(3-X)}PO_{(4-2X)}N_X$ [76]. This can lead to the bonding of the neighbouring phosphate groups (O_3P−O−PO_3), in the presence of Li/P disorder, which can be further stabilised by replacing BO with N to form P−N−P units [77]. A neutron diffraction study could not clarify the substitution of oxygen by nitrogen; however, it indicated that the incorporation of nitrogen into the structure did affect P−O and Li−O bond lengths and angles and consequently distorted P and Li tetrahedra. Despite that, the volume of N-doped Li_3PO_4 is nearly identical to that of the undoped composition. The improvement in ionic conductivity of the oxynitride compound is due to its lower activation energy, attributed to Li and O vacancy formation and slightly larger *a* and *b* cell dimensions.

A new crystalline phase with formula Li_2PO_2N was recently reported by Holzwarth and co-workers [78]. Previously, a computational study on lithium phosphate oxynitrides by the same group revealed that it is energetically favourable for N to substitute for an O in a bridging site between two phosphate groups [79]. $LiPO_3$ is known to be made of infinite phosphate chains. Consequently, a new crystalline structure was predicted by replacing each oxygen in the bridging site in $LiPO_3$ with nitrogen and adding one lithium to maintain electroneutrality, to form Li_2PO_2N. Li_2PO_2N has a Li_2SiO_3 structure and is made by reaction between Li_2O, P_2O_5 and P_3N_5. The ionic conductivity of this compound (8.8×10^{-7} Scm^{-1} at 80°C and activation energy of 0.57 eV) was found to be considerably higher than that of the previously-reported crystalline material based on

the Li_3PO_4 structure [75]. The low activation energy of conduction suggests that a significant number of lithium defects must be present in the structure [78].

The results of a simulation study found that it is possible to stabilise extrinsic Li-ion interstitials by doping Li_3PO_4, either by substituting N for O or Si for P to form PO_3N or SiO_4 defects [76]. It also indicated that an interstitial Li-ion diffusion is energetically favourable compared to vacancy diffusion by direct hopping in Li_3PO_4-based materials and predicted the migration energy of N-doped and Si-doped Li_3PO_4 with PO_3N and SiO_4 defects to be 0.9 and 0.8 eV respectively [76, 80, 81]. In the case of introduction of interstitial Li by doping crystalline Li_3PO_4 with Si, there has been a considerable amount of experimental study [82], which showed the highest conductivity in $Li_{3.4}P_{0.6}Si_{0.4}O_4$ with an activation energy as low as 0.51 eV. Similar effects have been observed in LISICONs and many other gamma (γ) structure materials [49, 83, 84]. However, there have not been any reports or experiments to introduce interstitial Li by doping Li_3PO_4 with N. The first aim of this project was to investigate the possible formation of crystalline lithium phosphorous oxynitride, based on an interstitial defect mechanism.

Nitridation

Cation substitution is the most common way of altering the physical and chemical properties of oxide materials. Anion doping has been much less investigated due to the high stability of the metal-oxygen bond, which makes the synthesis of anion doped compounds less straightforward [85]. To maintain the structure, the suitable candidates for oxygen substitution should possess similar features such as polarizability, electronegativity, coordination numbers and ionic radii. Among the elements in the periodic table, fluorine and nitrogen are the best candidates to substitute for oxygen [86]. Nitrogen, in particular, shows similar features to oxygen and therefore O and N frequently substitute for each other in the same sites to form oxynitride solid solutions. Nitrogen can be combined with most elements (provided they are less electronegative than nitrogen) to make stable compounds. Nitrogen is between carbon and oxygen in the periodic table and can form compounds with metallic, covalent or ionic bonds with similar structure and properties to both carbides and oxides [87].

To obtain oxynitrides from oxides a nitriding agent is required. Molecular nitrogen is the most naturally available nominee. N_2 is quite stable compared to more reactive O_2, therefore, nitriding reactions with N_2 generally require high temperature; however, even

under these conditions, direct reaction with nitrogen is quite difficult (due to the strong N_2 triple bonds) and only certain kinds of nitrides can be synthesised by direct heating in flowing nitrogen. A more efficient route to obtain nitrides (oxynitrides) by a "gas + solid" reaction is to use a more reactive nitrogen-containing gas such as ammonia (NH_3). The free energies of reactions between binary oxides and NH_3 are generally negative for the transition metals except for group IV, and positive for alkaline, alkaline earth and rare earth metals [88]. Ammonia is both a reducing and nitriding agent and ammonolysis has been widely used in the synthesis of many oxide and oxynitride glasses, oxynitride perovskites and refractory materials (such as Si_3N_4 and AlN). An important drawback of ammonolysis is that the reducing nature of ammonia may lead to (in)complete reaction or decomposition of nitrides [89] and controlled doping may not be possible. Nitridation of crystals, using "gas + solid" reaction, often occurs at very high temperatures and commonly, post-reaction annealing is required to yield a crystalline product [90].

Another method that has been widely used, consists of carbothermal reduction and nitridation; for instance AlN can be synthesised as follows:

$$Al_2O_3 + N_2 + 3C \rightarrow 2AlN + 3CO,$$

or alternatively, by reaction between Al_2O_3 and C_3N_4 [91]. Nitrogen-containing precursors have been broadly used in nitridation (for example, reaction of Si_3N_4 and Al_2O_3 to obtain sialons); however, these sources are normally expensive themselves and difficult to make. They can also be the source of contamination if the precursor acts as both reducing and nitriding agent (like C_3N_4 in making AlN).

High pressure-high temperature synthesis is another possible route for making oxynitrides. $RZrO_2N$ perovskites have been made using this method [92]. A modified procedure, called the solvothermal reaction, has recently gained a lot of attention. It involves reaction between precursors in the presence of a solvent in a closed vessel at a temperature higher than the boiling point of the solvent [93]. With this method, low temperature synthesis of many metal nitrides is possible. High cost of these two processes has limited their widespread usage.

Li_3N is a nitriding agent that has been widely used. Unlike other nitrogen sources it can be easily made by reaction between elemental lithium and nitrogen gas. Lithium is the only alkali element, which forms a stable binary nitride [94]. The main characteristic

of Li_3N is its sensitivity to hydrolysis; hence it can quickly lose nitrogen in contact with the atmosphere to form ammonia. Even if protected from the atmosphere it decomposes at very low temperatures, which is advantageous for a nitriding agent. Parkin et al [95] showed that the combination of lithium nitride with metal halide can produce metal nitrides at low temperature, by a reaction called solid state metathesis (SSM). Chen et al [96] proposed a modified route (MSSM) in which, binary and ternary metal nitrides could be synthesised by reaction between Li_3N and metal oxide. In both cases, the starting mixture was placed in a stainless steel crucible and moved into a sealable silica tube ampoule that was evacuated and filled with nitrogen [97]. The sensitivity of Li_3N to atmospheric moisture means that synthesis procedures have to be carried out under protective conditions.

For years, thin film deposition technologies have been used to make battery component layers [98]. Bates et al [57] first showed nitrogen incorporation into the Li_3PO_4 structure using Radio-Frequency (RF) magnetron deposition. Since then, various deposition approaches have been used such as Pulsed Laser Deposition (PLD) [99], Ion Beam Assisted Deposition (IBAD) [100], E-beam evaporation [101] and plasma assisted direct vapour deposition (PA-DVD) [102]. A schematic illustration of the PA-DVD process is given in figure 1.5. All these techniques are based on the deposition of a thin film by sputtering a Li_3PO_4 target in a nitrogen atmosphere. The differences between them are mainly in deposition rates and structure/morphology of the deposited films. The latter has a direct influence on the conductivity of the film. The composition of the resulting films is difficult to determine due to their amorphous state and therefore a systematic study of the variation of electrical properties with composition is lacking [26]. Moreover, cracks and pores can be formed in the films leading to localised partial discharge when a voltage applied [103] and therefore, a dense and crack free film is desirable.

Nitrogen detection

A number of techniques have been used for nitrogen determination in inorganic materials. The Kjeldahl method is a classic method of determining nitrogen and proceeds by reducing the nitrogen content of the material to ammonium (NH_4^+) and
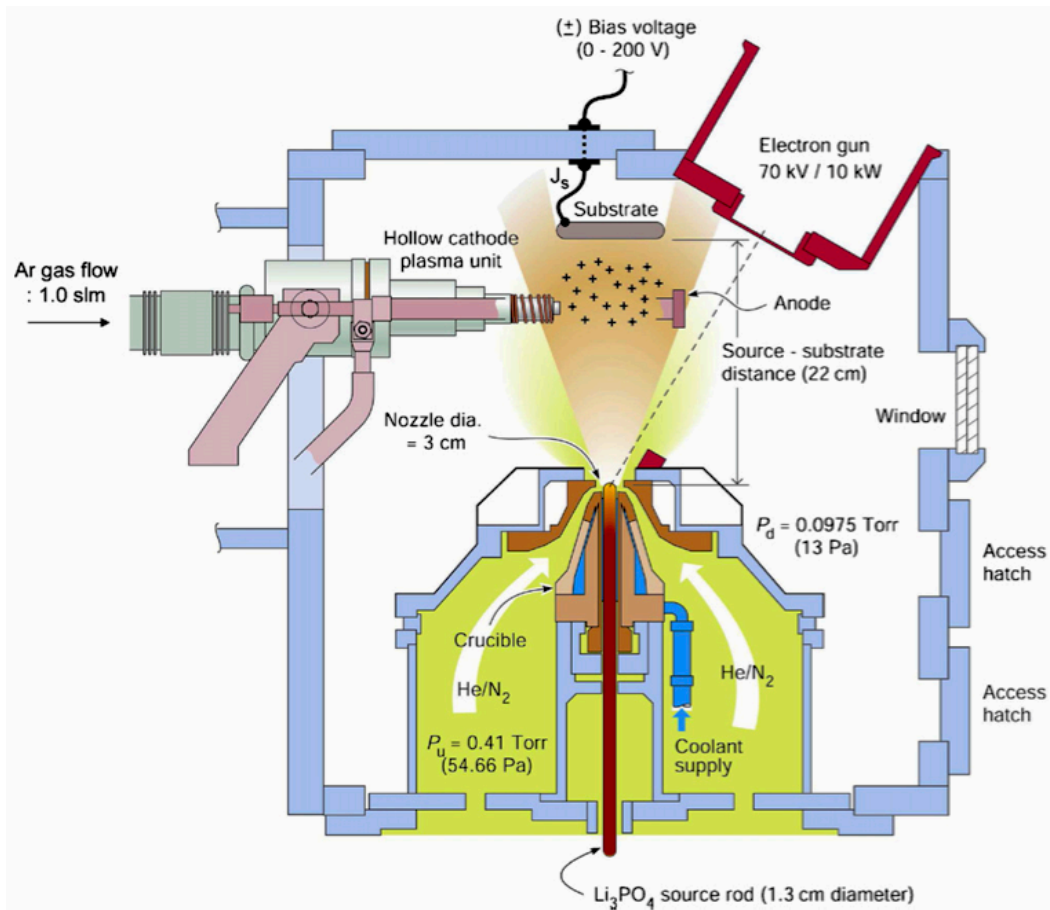
Figure 1.5. Schematic illustration of the plasma-assisted direct vapour deposition (PA-DVD) process [102].

ultimately ammonia (NH_3) by acidic distillation [104]. The amount of ammonia then can be quantified and calculated as nitrogen content. This method is very time consuming and the starting material may not easily dissolve in acid. In another method, the stoichiometry of nitrogen can be calculated from the weight gain during the thermal reoxidation of oxynitride material according to the equation:

$$AO_XN_Y + (3Y/4)O_2 \rightarrow AO_{X+3Y/2} + (Y/2)N_2,$$

using thermogravimetric analysis (TGA) measurements [105]. Additionally, X-ray photoelectron spectroscopy (XPS) has been used for nitrogen detection. Unfortunately XPS is a surface-sensitive quantitative technique and is less reliable for bulk samples. Rutherford backscattering spectrometry (RBS) was employed to study the anionic composition of thin film oxynitrides. In this method, high energy ions are directed onto the sample and the energy distribution and yield of backscattered ions are measured [106].

Combustion analysis is the most commonly-used technique for nitrogen determination. It is also known as the hot gas-extraction and inert gas fusion method. In this method, nitrogen is released as N_2, following fusion under a flowing inert gas and measured by a thermal conductivity cell [107]. A short survey of nitridation techniques that have been used for lithium phosphate oxynitrides and their nitrogen detection methods is given in table 1.2.

Table 1.2. Some lithium phosphate oxynitrides, their synthesis and method of nitrogen determination.

	Form	Synthesis procedure	N-determination
$Li_{2.9}PO_{3.3}N_{0.46}$ [57]	Thin film	RF-magnetron deposition	RBS-XPS
$Li_{0.93}PO_{2.82}N_{0.10}$ [70]	Bulk glass	Thermal ammonolysis of $(LiPO_3)$ base glass	Kjeldahl method
$Li_{1.35}PO_{2.73}N_{0.30}$ [73]	Bulk glass	Thermal ammonolysis of $(LiPO_3)$ base glass	Combustion analysis
$Li_{2.88}PO_{3.73}N_{0.14}$ [75]	Crystalline	$LiPO_3 + Li_3N$ under N_2 in sealed stainless steel furnace liner	TGA
Li_2PO_2N [78]	Crystalline	$Li_2O + P_2O_5 + P_3N_5$ under N_2 in sealed quartz tube	

Conduction mechanisms

Ionic conduction can be treated by "random walk" theory, in which conduction occurs by means of ion hopping or diffusion [108]; therefore, conductivity (σ) is given by:

$$\sigma = \sum_i c_i q_i \mu_i$$

1.1

where c_i is the concentration of the mobile species i, q_i their charge and μ_i their mobility. There are two structural requirements for ion hopping (ionic conductivity): first, there must be available empty sites for ions to hop into and second, the energy barrier to hop should be small. These empty sites are categorised in two broad groups [109].

1. Vacant sites: these are sites that in ideal, defect-free, structures would be occupied, but are empty and therefore, adjacent ions can jump into them, giving rise to so-called vacancy migration (figure 1.6-a)

2. Interstitial sites are those sites that in ideal structures would be empty, but in real structures are occupied by ions that are displaced from their lattice sites. These ions can either jump into their adjacent site, regarded as direct interstitial migration (figure 1.6-b) or push an ion at a regular site into an adjacent empty interstitial site, regarded as indirect interstitial (interstitialcy) migration (figure 1.6-c).
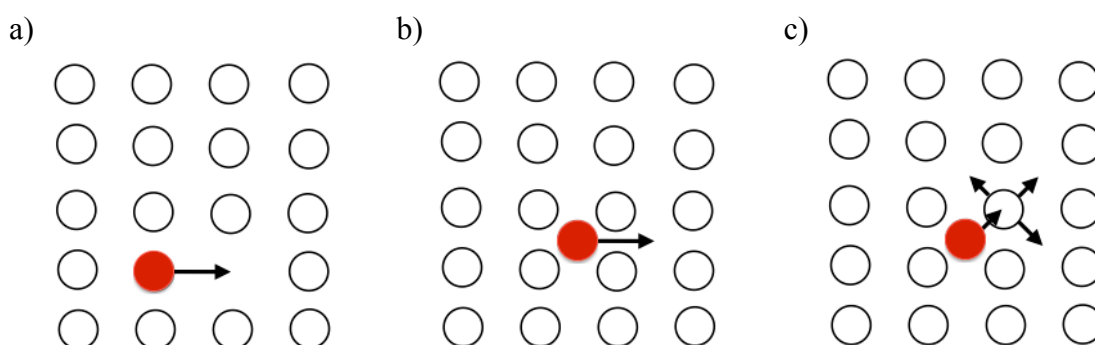
Figure 1.6. Jump mechanisms in ionic crystals: a) vacancy migration, b) direct interstitial migration and c) indirect interstitial (interstitialcy) migration [109]**.**

In most stoichiometric crystals, equivalent lattice sites are completely filled with ions and interstitial sites are empty; therefore, no ionic conduction is possible, except at near-sintering temperatures where there is sufficient thermal energy to excite ions into interstitial sites. In some stoichiometric solids, an order-disorder transition occurs for one of the ionic species at temperatures well below the melting point. AgI for example, undergoes a phase transition at 146°C, which leads to disordering of Ag^+ ions [110]. Above this temperature as a result, all Ag^+ ions are potentially mobile and the ionic conductivity increases dramatically. This material has the advantage of liquid-like conductivity (where only one type of ion moves) combined with mechanical properties of a solid. Very few stoichiometric solids show high ionic conductivity due to an order-disorder transition and therefore, other strategies have to be employed to increase their ionic conductivities.

One way of increasing c_i (interstitial ion or vacancy concentration), in equation 1.1, and therefore σ, is to increase the temperature. At high temperatures not only the defect concentrations are increased but also ions have greater thermal energy and vibrate more. Another way of increasing the value of c_i is by means of doping with aliovalent ions [110]. This means partial replacement of one type of ion by ions with a different charge (i.e. aliovalent ions) and forming a non-stoichiometric solid. In the case of anionic substitution, the difference in oxidation states following the partial substitution of oxygen with nitrogen, for instance, has to be compensated by one of the following charge compensating mechanisms:

1. Replacement of $3O^{2-}$ ions with $2N^{3-}$ ions and oxygen vacancy formation

2. Oxidation of the cationic charge

3. Appropriate cationic replacement

4. Creation of cationic interstitial defects

These charge compensating mechanisms can then be used to control the electrical properties of the oxynitride. For example in mechanism 1, in the presence of H^+ and O^{-2} ions, protonic and oxide ion conduction can be enhanced; in mechanism 2, assuming that the oxidation state of the cation can be easily changed, electronic conductivity can be enhanced.

For the Li_3PO_4 structure, mechanism 4 can be used as a doping strategy to create Li^+ interstitials and consequently enhance the ionic conductivity. Du and Holzwarth studied extensively the migration energies in the Li_3PO_4 structure in the presence of intrinsic and extrinsic defects [76, 80, 81]. It was proposed that one way of stabilising extrinsic Li^+ interstitials is to replace an O with N in the PO_4 group and create a PO_3N defect. In the solid solutions of γ structures, by the help of neutron diffraction, Li-ions were found to occupy various tetrahedral and octahedral interstitial sites to form an essentially three-dimensional conduction pathway [108]. In a recent computational study, the conduction in the γ-Li_3PO_4 crystals was proposed to be anisotropic and the minimum migration barriers were found in a zigzag pathway along *b* and *c* axes with an interstitialcy mechanism [80]. Figure 1.7 shows a ball-and-stick diagram of a γ-Li_3PO_4 supercell with a N ion substituting for O at one site. As a result, interstitial lithium ions can be introduced into c-axis channel sites, the most stable of which are labelled I_0. The energy of migration of $I_0{}^1$ to $I_0{}^2$ (both neighbour the N site) was calculated as E=0.20 eV;

however, the interstitial lithium is "trapped" by the PO_3N defect and therefore, the total migration energy for an interstitial Li^+ ion to escape from I_0^1 position to the bulk region was estimated to be E=0.90 eV [76].
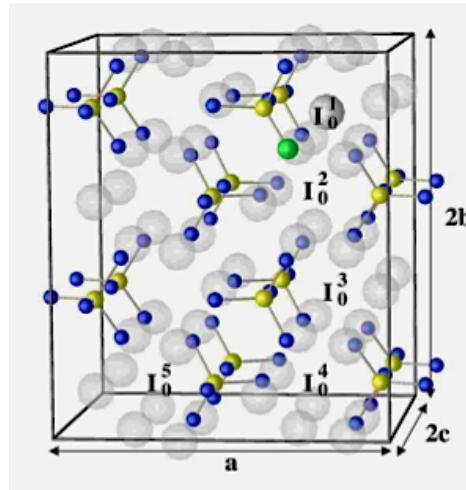
Figure 1.7. Ball-and-stick diagram of a γ-Li$_3$PO$_4$ supercell with N ion substituting for O and addition of a metastable Li-ion to a nearby interstitial site (I_0^1). PO$_4$ groups are shown with bonded yellow and blue spheres, Li ions with gray spheres and N indicated with a green sphere. The site labels I_0^2 , I_0^3 , . . . indicate other (possible) interstitial sites [76].

The replacement mechanism in $Li_{3+X}PO_{4-X}N_X$ is:

$$O^{2-} \rightarrow N^{3-} + Li^+.$$

The substitution of N onto an O site leaves a residual charge of -1 on the site. The lithium interstitial that is introduced carries a +1 charge and therefore the aliovalent impurity and the cation interstitial are likely to attract each other. Consequently, a lithium interstitial must overcome an additional energy barrier in order to move. In such materials, the conductivity values may decline with time at room temperature as the mobile ions gradually become trapped, also called the ageing effect [108, 111].

Ionic conductivity is usually temperature dependent and is given by the Arrhenius equation:

$$\sigma T = A exp(-E/kT) \qquad\qquad 1.2$$

where σ is the conductivity, E the activation energy for migration, k the gas constant (Boltzmann constant), T the absolute temperature and A is the pre-exponential factor, containing several terms such as the number of mobile ions and their vibrational frequency [112]. The activation energy can be determined by plotting *log(σT) vs. 1000/T(K)*. *E* defines the ease of ion hopping and is related to the crystal structure (conduction pathway conditions). In doped materials, the activation energy of migration may be a combination of the energy of migration (ΔH_m) and the trapping energy (ΔH_t) [113].

$$E = \Delta H_m + \tfrac{1}{2}\, \Delta H_t. \qquad\qquad 1.3$$

At higher temperatures, the majority of Li^+ interstitials are freely mobile and the influence of trapping energy is minimised. As a result the Arrhenius conductivity plot is linear at low and non-linear at high temperatures [114].

The conductivity profile in systems with a low concentration of mobile species can be well explained by "random walk" theory and point defect models. In contrast, conductivity in non-stoichiometric compounds with large carrier concentrations can not be easily characterised using this model [111]. Such solid solutions do not consist of isolated defects; on the contrary, defects come together to form clusters and clusters often tend to change with temperature [50]. In general, solid electrolytes are classified as intermediate between normal crystalline solids and liquid electrolytes. A number of theories and models have been offered by different groups; however none of them could fully interpret the conduction mechanism. An alternative model to explain conductivity data therefore is essential.

Tetrahedral structures

Crystal structure can be described as built of polyhedra linked together by sharing corner, edges or faces. In this approach, anions are arranged in close-packed (c.p.) layers, where cations occupy interstitial positions. The advantages of this method are that it illustrates the topology and connectivity of a framework structure and more importantly indicates the location of empty interstitial sites [115]. In this approach coordination number of cations is emphasised. A range of polyhedra occurs in inorganic structures, however, tetrahedra and octahedra are the most common. Tetrahedral

structures are structures in which the coordination of all the atoms is tetrahedral [116]. Any particular atom in tetrahedral structure is surrounded by four next neighbour atoms, located at the vertices of the tetrahedron and the particular atom is the centre of tetrahedron. Three anions that form the base of the tetrahedron belong to one layer of c.p., with the tip of the tetrahedron belong to the other layer. This arrangement provides two types of tetrahedral sites: T_+ and T_-, in which the tip of tetrahedron is up and down respectively.

Zincblende (ZnS) and Wurtzite (ZnS) structure types are two geometrically related structures belong to the tetrahedral structure. The wurtzite derivatives have hexagonal close-packed (hcp) anions with the cations occupying one set of tetrahedral sites (T_+ or T_-) between the anion layers. The zincblende derivatives have similar cation arrangements with cubic closed-packed (ccp) anions. The large-scale model of these two structures is very similar and both can be regarded as network of tetrahedra, where in zincblends layers of tetrahedra form an ABC stacking sequence and in wurtzite the layers form an AB stacking sequence. The wurtzite structure has a parallel oxide structure (ZnO), which the structure of Li_3PO_4 is related to it.

Most of the tetrahedral oxides exhibit polymorphism and essentially fall into two groups: γ and β. Some examples of β structure are illustrated in figure 1.8. For each example, a layer of close-packed oxide ions is shown together with a layer of cations immediately above the oxide layer. Therefore, each cation is coordinated to three oxygens in the layer shown and to the forth oxygen in the next oxide layer above the cation to form a tetrahedron. The structure of ZnO differs from the other β structures shown, by different cation ordering sequences and therefore their unit cell parameters vary accordingly. Other layers of oxygen and cations need to be added in order to build -ABABA- hcp sequences. The difference between A and B layers is that the tetrahedron edges of alternate layers are rotated by 180° about the *c* axis relative to each other. The linkage of the tetrahedra is such that each tetrahedron shares each of its corners with three other tetrahedra. There is no sharing of tetrahedron edges or faces. The unit cell parameters are also shown in figure 1.8. The *c* unit cell dimension consists of two oxygen and two cation layers. The second layer of cations and oxygens to complete the unit cell in β-Li_3PO_4 is shown in a bracket.
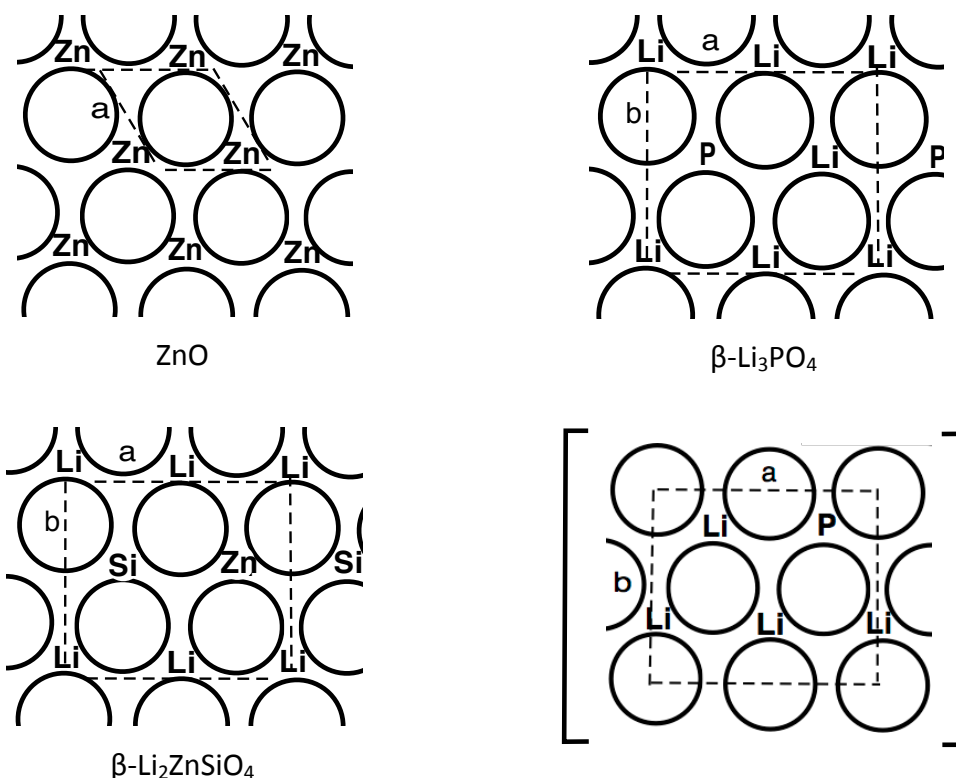
Figure 1.8. Derivation of the β structures from the ZnO structure. For each structure one oxide layer is shown together with a layer of cations in the adjacent set of occupied tetrahedral sites. The next oxygen and cation layers in β-Li₃PO₄ is shown in a bracket. Unit cell parameters are shown by dashed lines [117].

In β structures, the same set of cation sites is occupied. In γ structures however, the cations are distributed equally between both sets of tetrahedral sites. Two of these γ structures are illustrated in figure 1.9 and their cation distribution is compared. For each one, a layer of oxide ions is shown together with a layer of cations. There are two sets of tetrahedral sites available (T$_+$ or T$_-$) between the set of oxide layer shown and the next layer above, half of each is occupied by cations. Cations on the T$_+$ sites are coordinated to three oxygens from the oxide layer shown and one oxygen from the layer above and the tetrahedra formed point upwards. Cations on the T$_-$ sites are coordinated to one oxygen from the oxide layer shown and three oxygens from the oxide layer above. In γ-Li₃PO₄, each PO₄ tetrahedron only shares corners with neighbouring tetrahedra. LiO₄ tetrahedra however, can share edges with each other [117].
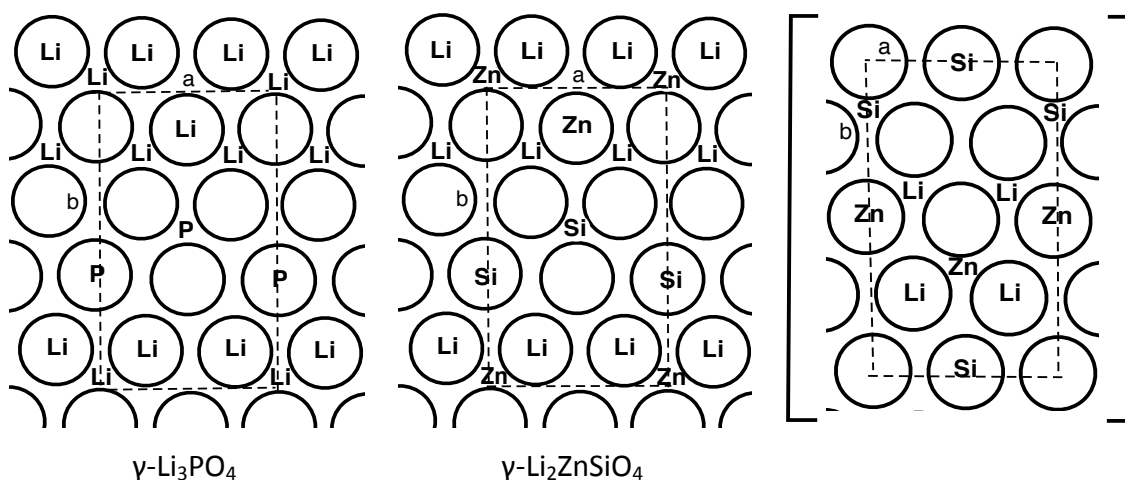
Figure 1.9. γ-Li₃PO₄ and γ-Li₂ZnSiO₄ structures. Details are the same as in figure 1.8. The next oxygen and cation layers in γ-Li₂ZnSiO₄ is shown in a bracket [117].

The β-γ transition in Li_3PO_4 is topotactic [118], where the orientations of the product crystals are determined by the orientation of the initial crystal. Although the oxide packing is more buckled in γ form (presumably due to edge sharing of tetrahedra), a similar close-packing arrangement exists in both structures. Therefore, the β-γ transition is accomplished by cation migration, where the oxide positions remain unchanged. Idealised projections of β and γ Li_3PO_4 are shown in figure 1.10. Half of the Li and P atoms are in similar positions in both β and γ polymorph; however, the remaining Li and P atoms are in different positions. β can be transformed to γ by inversion of certain tetrahedra through their bases; for example by cation exchange between tetrahedral sites that are linked by a common face [117].

The wurtzite superstructures (β structures) can only vary in their cation ordering sequences and therefore only a small number of wurtzite derivative structures are possible. In γ structures however, there are twice as many tetrahedral sites as cations and therefore the empty/full site sequence can vary as well as cation ordering sequences, hence, a fairly large number of γ structure materials are known. A list of tetrahedraly coordinated oxides with γ and/or β structures are given in table 1.3.
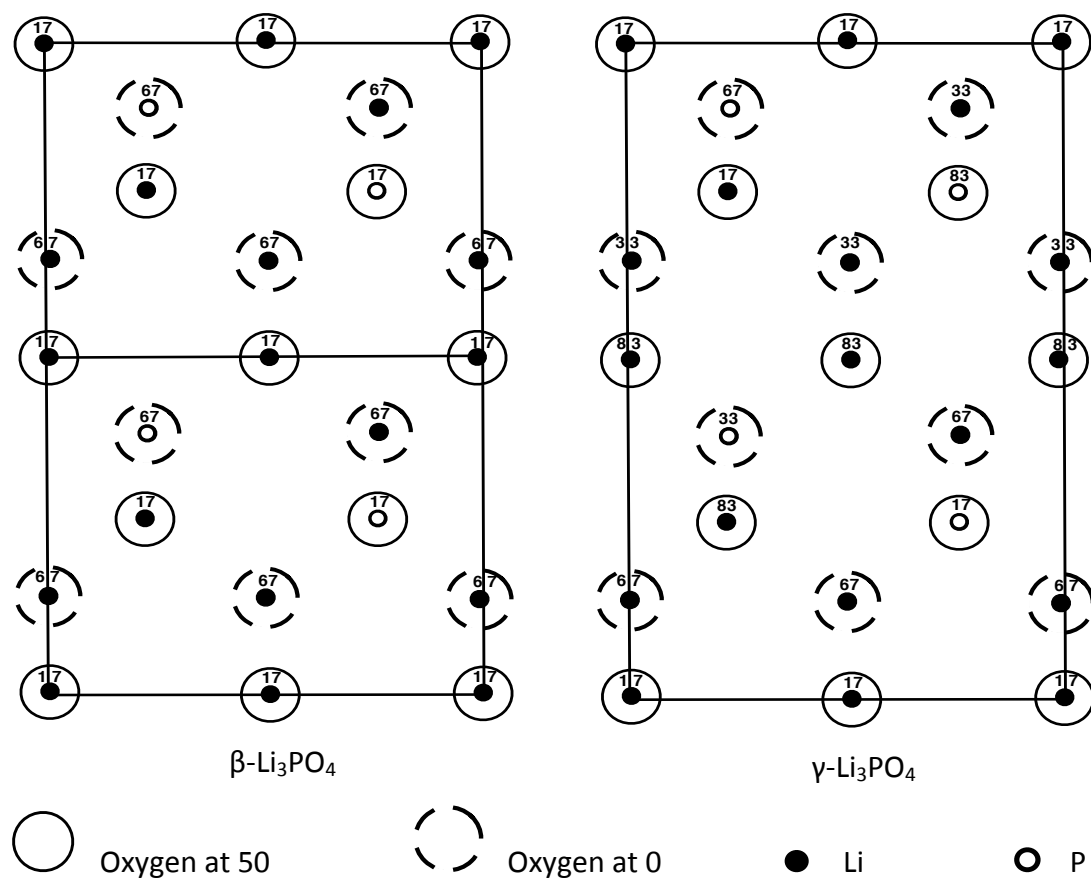
Figure 1.10. Idealised (001) projections of β and γ Li₃PO₄ (two unit cells of β Li₃PO₄ are shown [117].

Table 1.3. Some tetrahedral oxides with γ and/or β structures.

Material	Polymorph
$Li_3(P,V,As)O_4$	γ/β
$Li_2(Zn,Co,Be,Fe,Mn)SiO_4$	γ/β
Li_2MgSiO_4	γ
$Li_2(Zn,Co)GeO_4$	β
Li_2MgGeO_4	γ/β
$NaFeO_2$	γ/β
$(Li,Na)AlO_2$	γ/β

Scope of the project and methodology for materials synthesis

The overall aim of this project is to develop and characterise new solid electrolytes for possible all-solid-state lithium battery applications. This project explores the synthesis of nitrogen-doped, crystalline, Li₃PO₄-based materials, involving an

interstitial defect mechanism, using conventional solid-state synthesis. There is extensive research on amorphous lithium phosphorus oxynitrides, both in thin film and bulk glass form; however, there are very few reports in the literature on crystalline forms of this material.

The development of new synthesis techniques has led to the preparation of many novel oxynitride materials; however, it is often quite difficult to control the composition (N/O ratio in particular), using these synthesis approaches. The use of solid state reactions in N_2 atmosphere, using nitrogen-containing reactants has been broadly examined before [86]. This approach, not only lowers the synthesis temperature (compared to solid state reaction under nitrogen, without using N-containing reagents), but also facilitates control of the composition (compared to ammonolysis for instance). In this study Li_3N was used as the nitrogen-containing source and various compositions of oxynitride compounds were prepared by using different molar ratios of Li_3N to the other precursors. Due to severe reactivity of Li_3N, synthesis procedures had to be designed in a way to minimise sample contact with atmosphere. Chen et al [96] showed synthesis of ternary metal nitrides by Li_3N, using a sealable silica tube ampoule and stainless steel crucible (as was explained in nitridation). We have employed a modified version of this technique and adopted it based on material specifications and equipment available. Experimental procedures and preparation methods are discussed in detail in chapter 2. Following synthesis of N-doped Li_3PO_4, possible formation of $Li_{(3+X)}VO_{4-X}N_X$ and $Li_{2+Y}(Zn,Mg)SiO_{4-Y}N_Y$ solid solutions has been studied.

The second part of the present work is dedicated to the characterisation of the synthesised phases. In chapters 3, 4 and 5 $Li_{3+X}PO_{4-X}N_X$, $Li_{3+X}VO_{4-X}N_X$ and $Li_{2+Y}(Zn,Mg)SiO_{4-Y}N_Y$ new phases are reported, respectively. In each chapter, a systematic investigation of the structure, composition and electrical properties of oxynitride solid solutions is presented and compared to that of the oxide parents.

Lithium vanadium oxides have been investigated elsewhere as electrode materials for batteries due to their enhanced electrochemical properties [119, 120]. Li_3VO_4, in particular, showed promising properties (large specific capacity and low discharge voltage) [16]. The ionic/electronic conductivity of Li_3VO_4, however, is low. Therefore, by improving its conductivity, it can be considered as a potential insertion anode material for lithium ion batteries. Electrochemical properties of Li_3VO_4 and $Li_{3.4}VO_{3.6}N_{0.4}$ are discussed in chapter 4. A general discussion and overview is given in chapter 6.

Chapter 2

Experimental techniques

"The important thing in science is not so much to obtain new facts as to discover new ways of thinking about them."

— ***Sir Lawrence Bragg,*** *the youngest winner of Nobel prize in physics for his service in the analysis of crystal structure by x-ray.*

Synthesis

Samples were prepared by solid-state reaction, using high purity reagents (table 2.1). Reagents were dried at required temperatures before weighing (table 2.1) and stored in either an argon-filled glove box or in a vacuum desiccator. No drying was used for $(NH_4)_2HPO_4$ and Li_3N as they react with the atmosphere even at low temperatures; instead, they were purchased in air-sensitive packages from source, opened and stored inside a glove box.

Table 2.1. Reagents used with their purity and drying temperature, all from Sigma Aldrich (Gillingham, UK).

Reagent	Purity	Drying temperature
$(NH_4)_2HPO_4$	≥99.0%	-
Li_2CO_3	≥99.5%	180°C
Li_3N	≥99.5%	-
MgO	≥99.0%	180°C
SiO_2	≥99.5%	180°C
V_2O_5	≥99.6%	180°C
ZnO	≥99.5%	180°C

Preparation was carried out by two different methods. In samples with no nitrogen, powders were weighed in stoichiometric amounts and wet-mixed using an agate mortar and pestle. Acetone was added to form a slurry and mixed until dry to give a homogeneous powder. The resulting powders were placed in a gold foil boat and moved to a muffle furnace. Heat treatment began by decarbonation of Li_2CO_3; therefore, samples were heated from room temperature to 650°C with a 5°C/min heating rate and calcined for 10 hours. For synthesis of Li_3PO_4, an additional low temperature decomposition was needed for $(NH_4)_2HPO_4$. Therefore, samples were heated at 140°C, 160°C, 180°C, 200°C and 250°C for 15 minutes at each step before decarbonation at 650°C. Final product was made in the form of pellets and in order to achieve higher density pellets, reaction and sintering was carried out in one stage, 'reaction-sintering'. Consequently, after initial decarbonation, samples were reground, pressed into pellets (8-10 mm in diameter and 1-3 mm in height), initially using an uniaxial hand press followed by a cold isostatic press (CIP) and were then sintered at required temperatures (table 2.2) overnight. Prior to sintering, pellets were placed in a gold foil boat (when sintering at <1000°C) or a platinum foil boat (when sintering at >1000°C). In the latter case, a pellet from the same composition was placed between the sample and the foil to avoid possible reaction with platinum.

Table 2.2. Reaction-sintering temperatures of different samples.

Sample	Reaction-sintering temperature
LiZnSiO(N)	1000°C-1100°C
LiMgSiO(N)	1000°C-1100°C
LiPO(N)	750°C-850°C
LiVO(N)	750°C-850°C

For oxynitride samples, due to the severe atmospheric sensitivity of Li_3N even at room temperature, the various dried reagents were stored in an argon-filled glove box at all times. Samples were weighed in stoichiometric amounts, ground and dry-mixed using an agate mortar and pestle, placed in a molybdenum foil boat and then moved to a silica glass tube. Au was replaced by Mo foil at this stage, since reaction between Au and Li_3N was seen on a few occasions. The entire process was conducted in the glove

box under a dry argon atmosphere, to prevent water and oxygen contamination. The silica tube was then sealed with tape at both ends to prevent reaction with atmosphere outside the glove box (figure 2.1). The attached tape is assumed to burn off in the early stages of heating. Sealed silica tubes were moved out of the glove box to a horizontal tube furnace, through which a controlled atmosphere could be passed. Nitrogen gas was used as an inert atmosphere. Prior to each heat treatment, the tube furnace containing samples was purged for one hour by injecting nitrogen at ≥ 2 bar, and then reduced to ≤ 1 bar during heat treatment to ensure an oxygen-free atmosphere. The same heating regime that was described before for undoped samples, was applied to samples mixed with Li_3N; consequently, heating was carried out initially at 650°C for 10 hours for decomposition of Li_2CO_3 and reaction of Li_3N (for N-doped Li_3PO_4 an additional low temperature decomposition of $(NH_4)_2HPO_4$ was needed). Reacted samples were reground following initial reaction, pressed into pellets and reaction-sintered at required temperatures (table 2.2) overnight.

Apart from fabrication of higher density pellets by one-step reaction-sintering, avoiding a second sintering procedure reduced the chance of nitrogen evolution from the sample. After cooling to room temperature, samples were stored in a vacuum desiccator prior to characterisation. Sintered pellets (all appeared as white colour ceramics) were ground and checked for phase purity using X-ray diffraction.
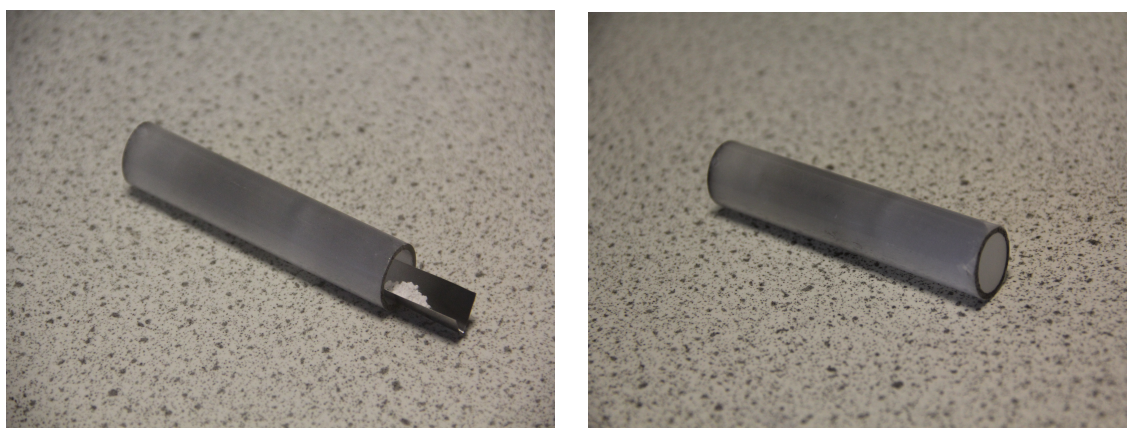
Figure 2.1. Silica tube and tape used to prevent contact between sample and atmosphere outside the glove box.

X-ray diffraction

X-ray diffraction is widely used as a primary technique to determine crystal structure and detect secondary (impurity) phases. It is based on the fact that X-rays have a wavelength similar to the interplanar spacings in a crystalline material ($\approx$1 Å) and hence can be diffracted by the atoms or ions. Moreover, crystals can be considered as made up from layers of semi-transparent mirrors (called lattice planes) with atoms and ions residing within these planes; consequently, diffracted X-rays can provide valuable information about the lattice planes and atomic positions within the structure [121]. First, the X-rays are generated, directed at the sample and subsequently scattered in all directions. In certain directions, the summed amplitude of the scattered waves is maximised if they are in-phase. According to Bragg's law this occurs when the path difference, δ, is an integral number of wavelengths [122]. As shown in figure 2.2, scattering of the X-rays by parallel planes of atoms in a crystal results in differences in path length, i.e. wave 2 has to travel the extra distance δ=CBD compared to wave 1. In-phase diffraction occurs if:

$$\delta = CBD = 2CB = n\,\lambda \qquad\qquad\qquad 2.1$$

by geometry:

$$CB = d\,\sin\theta \qquad\qquad\qquad 2.2$$

substituting equation 2.1 and 2.2 gives Bragg's law:

$$2d\sin\theta = n\lambda \qquad\qquad\qquad 2.3$$

where: d = d-spacing,

θ = reflection or Bragg angle,

n = order of reflection, and

λ = wavelength of incident radiation.

Every crystalline solid has a specific diffraction pattern in terms of position (2θ) and intensity of reflection [110]; therefore, diffraction is commonly used to determine crystal structures, identify phases and detect impurity phases. The position reflections or d-spacing offers information about the size and shape of the unit cell, and the intensities provide information about atomic positions [121].
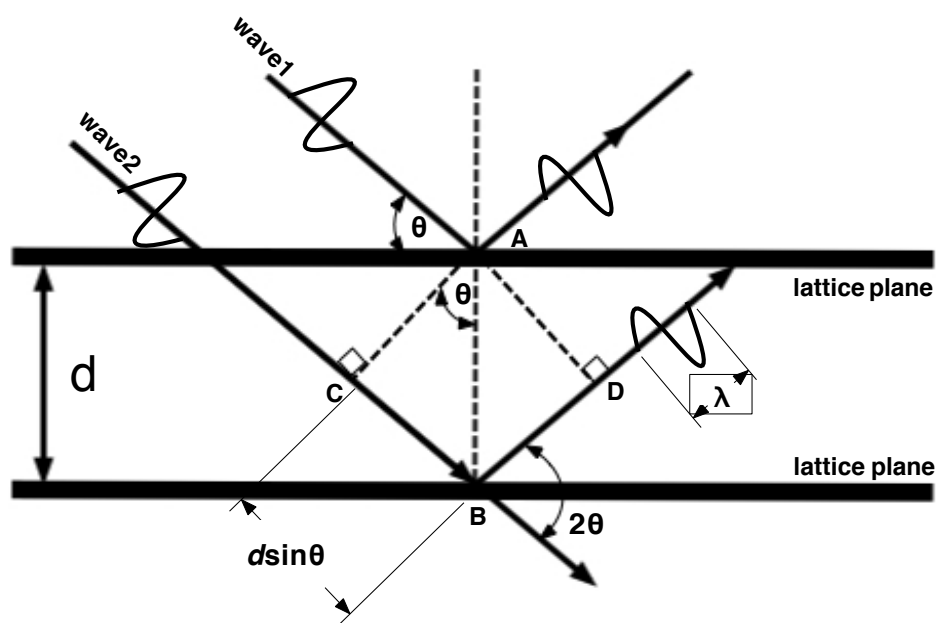
Figure 2.2. Illustration of geometry applied to derive Bragg's law.

Two pieces of equipment were used for the X-ray diffraction experiments reported in this work: A Siemens D5000 Bragg-Brentano diffractometer (Co $K\alpha_1$ radiation, in reflection geometry), for phase analysis and a STOE STADI P diffractometer (Mo $K\alpha_1$ and Cu $K\alpha_1$ radiation, in transmission geometry), with position sensitive detector (PSD), for high quality data and lattice parameter measurements. In the latter case, an angular correction was performed using a silicon standard to achieve accurate 2θ values.

The analysis of diffraction data was performed using $WinX^{POW}$ and PDF-4$^+$ XRD software packages; peaks in the diffraction pattern were matched with cards from the International Centre for Diffraction Data (ICDD) database. The ICDD database provides theoretical and experimental patterns based on information from patterns of known materials. This method is capable of the identification of the phase(s) present in the diffraction pattern.

Differential Scanning Calorimetry (DSC)

Thermal events (exothermic and endothermic reactions) cause a sample to emit or absorb heat from its surroundings. Therefore, comparing the energy changes in a sample with that of an inert reference material can assist to determine these events. DSC measures the energy changes in a sample by heating (cooling) a sample and a reference

at a controlled rate and measures the compensating heat-flux required to maintain both the sample and the reference at the same temperature. The heat-flux can then be plotted against temperature, as shown in Figure 2.3.
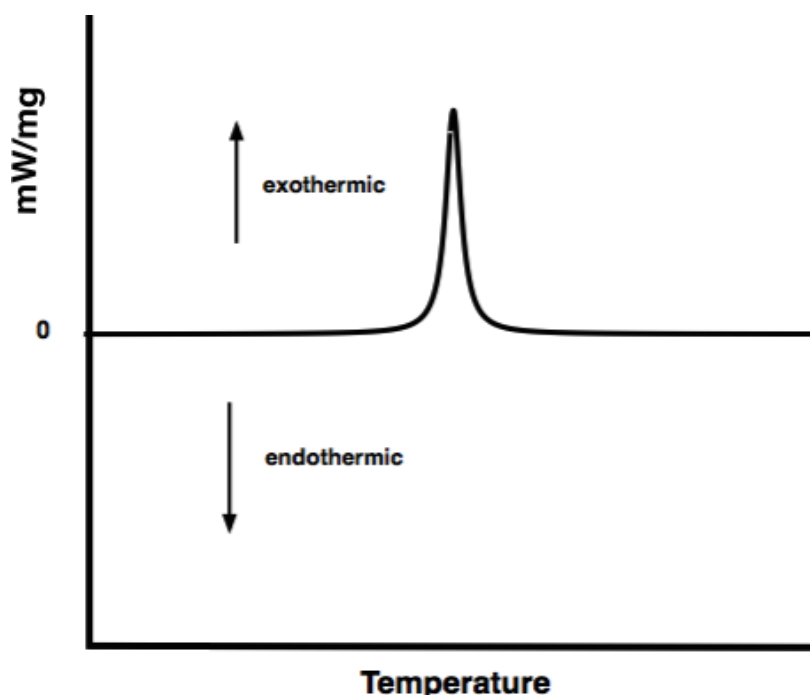
Figure 2.3. Schematic of a typical exothermic DSC peak.

The equipment used was a Netzsch DSC 404C. Argon was passed through the instrument before and during the experiment to protect the instrument from reaction products and humidity. Samples were weighed (30-40 mg) and placed into alumina pans. Heating and cooling rates were set to 10°C/min and samples were purged with nitrogen gas to maintain inert conditions. Data analysis was performed using Proteus Analysis software.

Thermogravimetric Analysis (TGA)

Thermogravimetric analysis (TGA) is employed to determine the change of the sample weight in relation to the change in temperature. The analysis was carried out using a Perkin Elmer Pyris 1 TGA in nitrogen atmosphere to determine weight losses or gains. Small amounts of powder were placed in a platinum crucible and heated to the desired temperature with a temperature ramp of 10°C/min to measure changes in the mass as a function of temperature.

Impedance Spectroscopy (IS)

Impedance spectroscopy is a powerful method for characterising many of the electrical properties of materials such as: ionic, semiconducting, mixed electronic-ionic and dielectric properties [123]. The ac impedance technique measures the electrical response of a material at a specific temperature on application of an alternating potential difference across a sample over a range of frequencies. To describe this technique it is best to go back to basics and to start with Ohm's law, equation 2.4. The applied potential difference and current through a conductor between two points are related by the constant of proportionality, the resistance:

$$V = IR. \hspace{6cm} 2.4$$

The electrical response of resistors is independent of frequency, unlike capacitors and inductors, which are frequency-dependent and their response is known as reactance, X. The combination of resistance and reactance (Ohms (Ω)) is called impedance. The reactance of a capacitor (X_C) is proportional to inverse frequency and capacitance (C), whereas the reactance of an inductor (X_L) is directly related to frequency and inductance (L), equations 2.5 and 2.6:

$$X_C = \frac{1}{\omega C} \hspace{6cm} 2.5$$

and

$$X_L = \omega L \hspace{6cm} 2.6$$

where ω is the radial frequency:

$$\omega = 2\pi f \hspace{6cm} 2.7$$

and f is the applied ac frequency.

For most ceramic materials, IS measurements are dominated by resistive (R) and capacitive effects (X_C), and usually the inductive effects are ignored when trying to model such systems. The combination of resistance and reactance can be shown by using a complex number form, $Z^{\star}$, where there are real (resistive), Z', and imaginary (reactive), Z'', parts:

$$Z^\star = Z' - jZ'' \qquad\qquad 2.8$$

where $j = \sqrt{-1}$.

Data can be analysed using either the impedance ($Z^\star$) or three other complex formalisms [124]: admittance ($Y^\star$), permittivity ($\varepsilon^\star$) and electrical modulus ($M^\star$):

$$M^* = 1/\varepsilon^* = j\omega C_0 Z^* = j\omega C_0 (1/Y^*) \qquad\qquad 2.9$$

where C_0 is the vacuum capacitance of the cell.

For an ideal solid electrolyte, a parallel RC element (Figure 2.4) is used to model and describe the electrical characteristics of the solid.
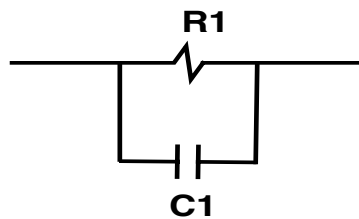
Figure 2.4. Parallel RC element.

For an equivalent circuit based on a single parallel RC element, the electrical response can be modelled. The impedance for each element is:

$$Z^*_R = R \qquad\qquad 2.10$$

and

$$Z^*_C = -j\frac{1}{\omega C} \qquad\qquad 2.11$$

For a parallel RC element, the total admittance is:

$$Y^* = Y_R + Y_C \qquad\qquad 2.12$$

and therefore, the total impedance is:

$$Z^* = (Y^*)^{-1} = [1/R + j\omega C]^{-1} \qquad\qquad 2.13$$

The equation can be expanded as:

$$[1/R + j\omega C]^{-1} = \frac{R}{1 + j\omega RC} \times \frac{(1 - j\omega RC)}{(1 - j\omega RC)} = \frac{R - j\omega R^2 C}{1 + [\omega RC]^2}$$ 2.14

Therefore, the impedance of a parallel RC element is given by:

$$Z^* = \frac{R}{1 + [\omega RC]^2} - \frac{j\omega R^2 C}{1 + [\omega RC]^2}$$ 2.15

Since $Z^\star = Z' - jZ''$:

$$Z' = \frac{R}{1 + [\omega RC]^2}$$ 2.16

$$Z'' = R\left[\frac{\omega RC}{1 + [\omega RC]^2}\right]$$ 2.17

Every element with a characteristic resistance and capacitance has a relaxation or time constant, τ (second). According to ac theory:

$$\tau = RC$$ 2.18

τ is the time it takes for the voltage of a charging (discharging) capacitor to reach (drop to) a certain fraction of its original voltage [125]. By replacing time with frequency:

$$\omega_{max}RC = 1$$ 2.19

where ω_{max} is the frequency where the imaginary part of the impedance reaches a maximum. Therefore, capacitance can be calculated from the maximum value of the arc.

The electric modulus formalism can also be used:

$$M^* = j\omega C_0 Z^* = j\omega C_0 Z' - j^2 \omega C_0 Z''$$ 2.20

From equation 2.16:

$$M'' = \omega C_0 Z' = C_0 / C \left[(\omega RC) / (1 + [\omega RC]^2) \right]$$ 2.21

where *M"* is corrected for both the permittivity of free space and the geometry of the pellet. *(ωRC)/(1+[ωRC]^2)* in *Z"* and *M"* indicates a mathematical representation of a Debye function. *Z"* and *M"* can be combined in one spectroscopic plot, as two Debye peaks, which, if there are deviations, can be used to determine the electrical (in)homogeneity of the sample. The difference in f_{max} (frequency at the peak maximum) between the two peaks can be used to determine how electrically homogenous the sample is: i.e. f_{max} should be the same for both peaks if the sample is electrically homogenous. It is also possible to obtain values of *R* and *C* from these plots:

C = 1/2M"$_{max}$ and R = 2Z"$_{max}$ 2.22

There are various possible ways of plotting the data. In a complex plane plot, the real and imaginary parts are plotted against each other. In spectroscopic plots, either the real or imaginary part is plotted against frequency. In the first case, an impedance complex plane plot (*Z" vs. Z'*), gives a semi-circle for a parallel RC element (also known as Nyquist plot). At very low frequencies (very long times), the impedance is completely resistive and therefore the resistance values can be worked out from the intercept on the *Z'* axis (ideally equals the diameter of the Nyquist plot semi-circle).

A typical electrical microstructure of a polycrystalline material can be explained via the "brickwork model" [126]. The model corresponds to a ceramic with cube-shaped grains (bulk), grain boundaries and sample-electrode interface (figure 2.5), which can be presented as an equivalent circuit with two parallel RC elements (representing bulk and grain boundary responses) connected in series.
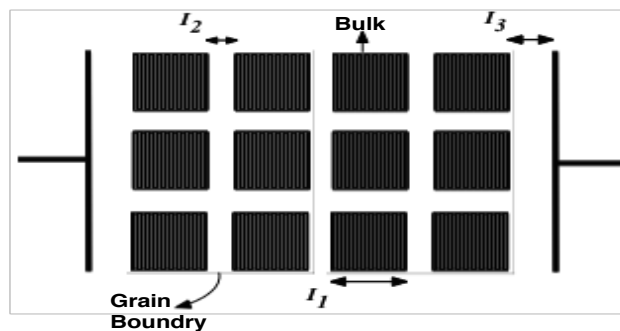
Figure 2.5. Schematic of "brickwork model" of a ceramic containing cube-shaped grain (bulk) of dimension *I$_1$*, grain boundary of thickness *I$_2$* and sample-electrode interface of thickness *I$_3$*.

The sample-electrode interface can store charge, depending on the electrode used. Two types of electrode metals can be employed: blocking or non-blocking. Gold, platinum and silver metals are usually blocking electrodes. In a Li-ion conductor, in the case of a blocking electrode, the metal electrode with an electronically charged surface is in direct contact with oppositely charged Li^+ ions and therefore an electrical double layer is formed that performs as a capacitor (figure 2.6).
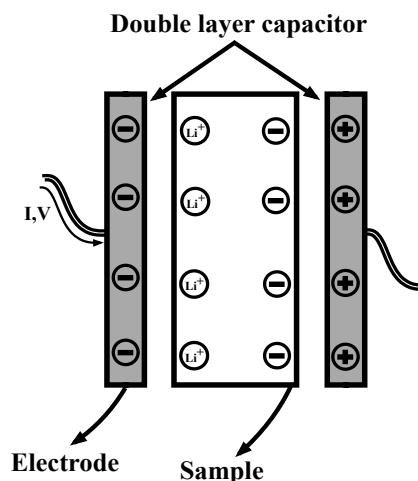
Figure 2.6. Schematic of a double layer capacitor.

Double layer capacitors (C_{dl}) are combined in series with other components in the equivalent circuit. In the case of a polycrystalline solid electrolyte with a blocking electrode, the bulk and grain boundary resistances (R_b and R_{gb}) can be determined from the intercepts on the Z' axis. The bulk and grain boundary capacitances (C_b and C_{gb}) are determined from the Z'' maximum of each semicircle where $\omega_{max}RC=1$. Ideally blocked flat electrodes, in the absence of a charge-transfer reaction at the electrode-sample interface, behave as a capacitor and according to equation 2.11 ($-Z''=1/\omega C$) are illustrated by a vertical spike in low frequency regions of Z^* plots, where $-Z''$ decreases with increasing ω [127]. It indicates that the electronic conduction within the solid electrolyte is negligible compared to the scale of ionic conduction [49, 128]. In reality however, the electrode may be partially blocking due to a rough electrode surface and therefore, the interface impedance is partly resistive and partly capacitive. In this case, the angle of the low frequency spike is less than 90° (also described as an inclined spike). An inclined spike of angle 45°, where $Z'=Z''$, indicates diffusion of mobile species into/away from the electrode material and is referred to Warburg behaviour.

Non-blocking electrodes allow movement of both electrons and ions and $C_{dl}=0$; therefore, the Z* plot does not contain a low frequency spike [127]. Figure 2.7 illustrates some of the effects that are discussed here in a schematic Z* complex plane plot.
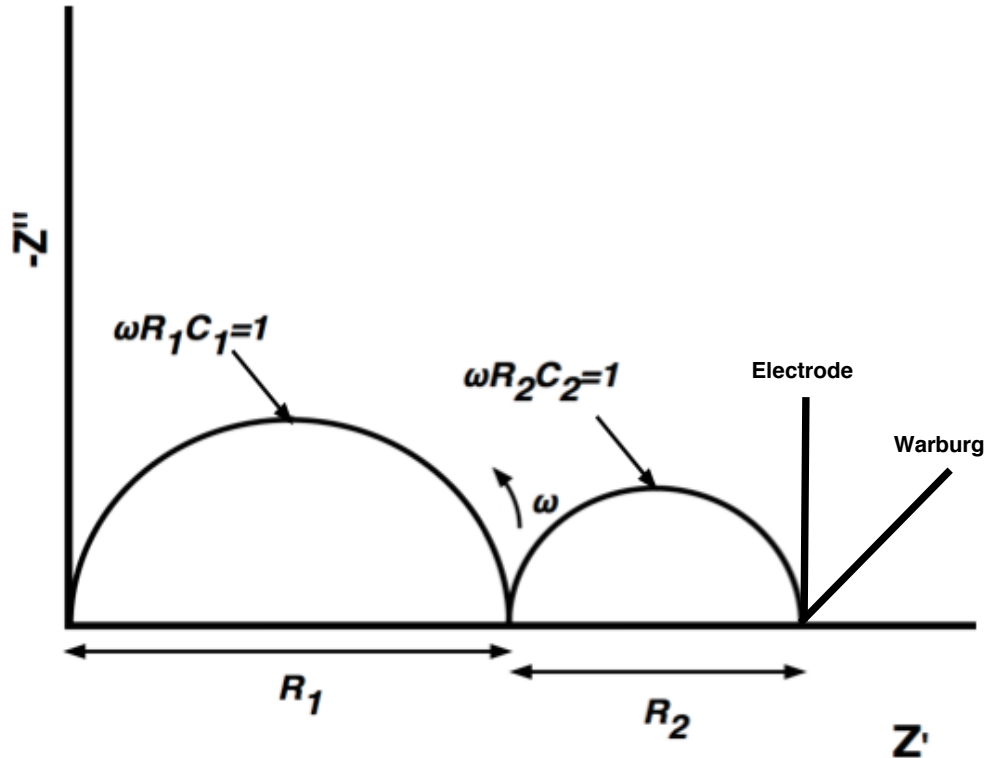
Figure 2.7. A complex plane Z* plot illustrating bulk and grain boundary responses (two semicircles) together with ideal blocking electrode effect and Warburg-type ionic diffusion.

In a sample that can be represented by the "brickwork model", the values of capacitance of each region can be determined by knowing the size of the electrode plates, the thickness of each region (l_1, l_2 and l_3 for instance) and the dielectric properties of each region based on the equation:

$$C = \varepsilon' e_0 (A/l) \qquad\qquad 2.23$$

where: C = capacitance of the region

ε' = sample permittivity

e_0 = permittivity of free space

A = area of the parallel plate

l = plate separation.

Each structural element has a characteristic thickness and therefore a characteristic capacitance, which allows the identification of different electrical regions of the ceramic [126]. For instance, capacitance values of $\approx 10^{-12}$ Fcm^{-1} are attributed to the bulk region for materials with a typical permittivity of ≈ 10 and unit cell constant of $l/A=1$cm^{-1}; capacitance values of $\approx 10^{-6}$ Fcm^{-1} are attributed to double layer capacitance. Examples of capacitance values for different structural regions are presented in Table 2.3:

Table 2.3. Capacitance values and their possible interpretation [126].

Element	C (Fcm^{-1})
Bulk	10^{-12}
Minor, second phase	10^{-11}
Grain boundary	10^{-11}-10^{-8}
Surface layer	10^{-9}-10^{-7}
Sample-electrode interface	10^{-7}-10^{-5}
Electrochemical reactions	10^{-4}

Assuming that only one conduction process is dominant in the sample, conductivity data plotted against temperature usually fits the Arrhenius equation. An activation energy for the conductivity can then be calculated:

$$\sigma T = A exp(-E/kT) \hspace{4cm} 2.24$$

where: E = activation energy

σ = conductivity

A = pre-exponential factor

T = temperature

k = Boltzmann constant.

The activation energy (in electron volts) can be determined by plotting $log(\sigma T)$ vs. $1000/T(K)$ using gradient (m) of the plot:

$$E(eV) = 0.198633 \times m \hspace{4cm} 2.25$$

Impedance measurements were recorded using a Solartron SI 1260 impedance analyser, in the frequency range 10^{-2}-10^7 Hz. Data analysis was performed using the ZView software. As sample dimensions can vary in size, a geometric correction (l/A) is applied to the data, where l = sample thickness and A = electrode area. However, the geometric correction is at best an approximation as it does not take into account the presence of pores and grain boundaries; therefore, it is very useful to have dense pellets with negligible porosities. Density measurements were made directly from the dimensions and mass of the pellet, and compared with the theoretical density:

$$D_{theoretical} = (N_C \times A)/(V_C \times N_A) \qquad\qquad 2.26$$

$$D_{Sample} = mass/volume \qquad\qquad 2.27$$

where: N_C = formula units per unit cell,

A = formula weight (g),

V_C = volume of the unit cell ($Å^3$), and

N_A = Avogadro number.

The volume of the unit cell was obtained from the least squares fit of the XRD traces. The sample density can be described as a percentage of the theoretical density. The density of sintered pellets in this project was generally between 80 to 90% of their theoretical density.

For impedance measurements, it was necessary to apply metal electrodes to the pellet. Therefore an ohmic silver paste was painted on both faces of the pellet. In most of the experiments, no high temperature drying was needed as silver paste can be dried at room temperature; however, in some cases pellets were dried at 600°C for two hours under nitrogen atmosphere to ensure a strong contact between the electrode and the sample. All the impedance measurements were taken by a conductivity atmosphere jig in a tube furnace under nitrogen gas.

Electrochemical measurements

Battery testing was conducted on a Bio-Logic VMP (Variable Multichannel Potentiostat) distributed by Perkin-Elmer connected to a computer with the EC-Lab software to analyse electrochemical data. This instrument used the Galvanostatic Cycling with Potential Limitation (GCPL) technique that applies a constant current

across the cell and monitors the variation in the potential [129]. With this instrument, testing of up to 16 cells simultaneously was possible.

In this study, a ratio of 75:20:5 wt% mix of active cathode material, carbon black (to improve conductivity) and PVDF binder (polyvinylidene difluoride) were pressed into a 10mm diameter pellet. Pellets were moved to a vacuum furnace and dried at 120°C overnight to remove any moisture. The pellets were then moved to a dry, argon-filled glove box and weighed. It is necessary to know the mass of active material to calculate the performance.

The electrolyte solution was a 1:1 wt% mixture of 1M $LiPF_6$ and propylene carbonate (PC). Preparation was carried out in an argon-filled glove box. The electrolyte was stirred using a magnetic stirrer to keep the lithium salt dissolved in the propylene carbonate.

Coin cells (supplied by National Research of Canada) were assembled under dry argon in the glove box using standard C2324. A schematic diagram showing the order of construction of the coin cells is presented in Figure 2.8. Coin cells were pressed together using a pneumatic sealing tool operated by argon gas.
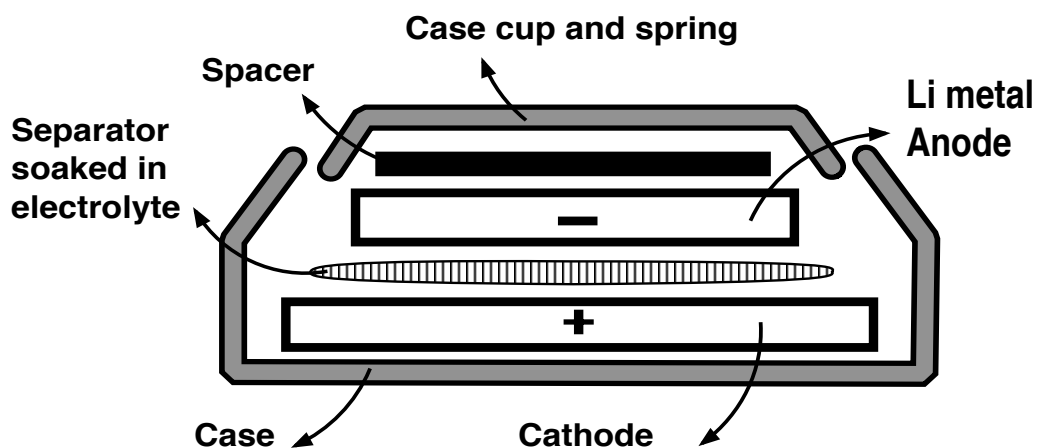
Figure 2.8. Coin cell construction.

To have a better understanding of reactions in a battery, the system was tested using commercially-supplied $LiCoO_2$ (99.8% Sigma-Aldrich). Typical reactions in a lithium/electrolyte/$LiCoO_2$ cell on discharge are presented in figure 2.9.

In this technique it is necessary to know the current rate at which the cell needs to be (dis)charged and the potential window in which electrochemical reactions take place. To know what current rate a cell is being (dis)charged at, it is essential to calculate the theoretical capacity (mAh/g) of the cell:

$$Q_{To} = (e \times F)/(3.6 \times M)$$ 2.28

where: e = number of electrons involved in the reaction,

F = Faraday's constant, 9.469×10^4 C/mol (3.6 Coulomb = 1 mAh),

M = molar mass of active material (g/mol).

Overall reaction: $xLi + Li_{1-x}CoO_2 \rightarrow LiCoO_2$
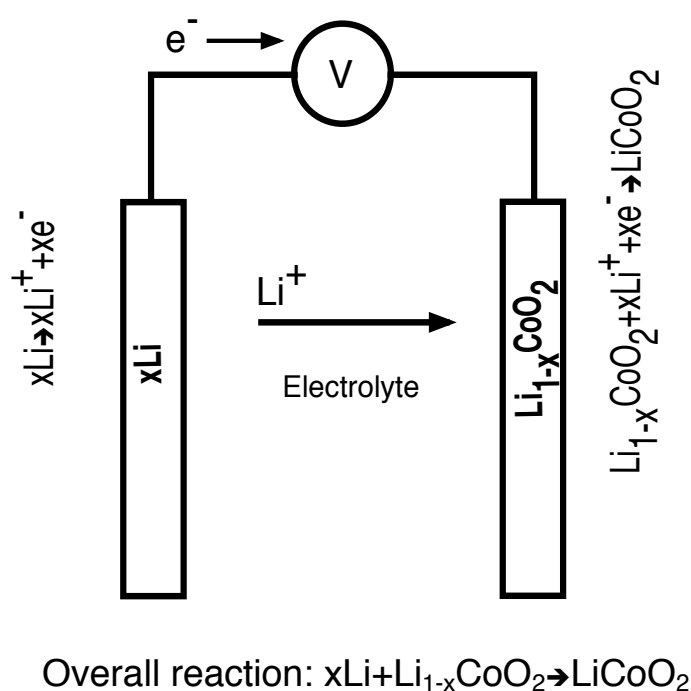
Figure 2.9. Electrochemical reactions on discharging a battery with lithium metal and LiCoO₂ as negative and positive electrodes, respectively.

The measured (dis)charge is represented by different multiples of C, where 1C indicates the rate required to intercalate or deintercalate one lithium ion in one hour. This rate is very fast and a more typical rate for studies is C/20. By knowing the C-rate and the theoretical capacity, the required constant current can be calculated:

$$Q_{To} = I \times t$$ 2.29

where: I = current (mA),

t = time (hours).

In a discharge process, about half of the Li$^+$ ions are electrochemically extracted from the LiCoO$_2$ structure [130, 131]. A $Q \approx 5.9$ mAh is therefore calculated, assuming that 49mg of active material was used (I $\approx$ 0.29mA for C/20 rate).

This constant current is then passed over a chosen potential window to run the experiment. This range is typically somewhere between 0 and 5.5 V and can be chosen after identifying regions of electrochemical activity by performing cyclic voltammetry.

The output data can be presented in the form of graphs of potential and number of lithiums against time. The results can also be plotted for the cycles performed to study the cyclability of the electrode materials. This can be displayed in plots of capacity against cycle number.
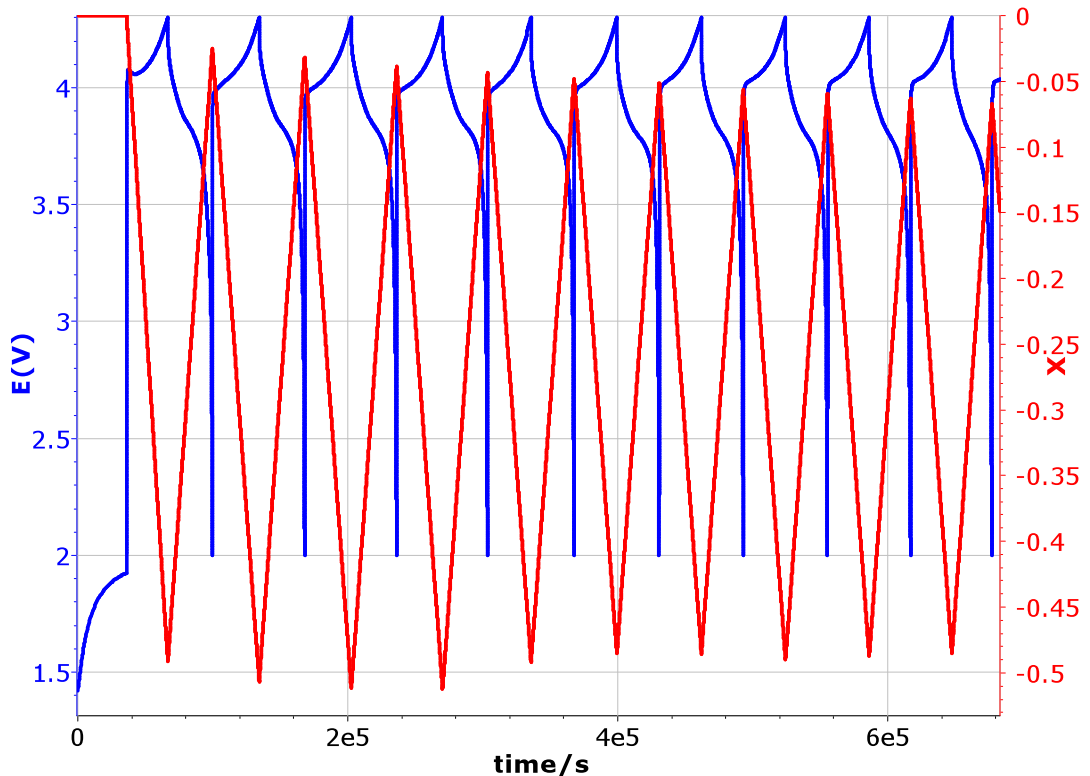
Figure 2.10. Variation of voltage and number of lithiums inserted/extracted vs. time for LiCoO$_2$ cell.

The cycling profile for LiCoO$_2$ in the test cell is presented in figure 2.10. The LiCoO$_2$ cell was cycled at C/20 rate in a 2.0-4.3V potential window. This window was considered from results reported by Yoshio et al [132] . After an initial Open Circuit Voltage (OCV) measurement, to determine whether or not the cell was capable of

holding a registered voltage, about half of the Li^+ ions were extracted by electrochemical oxidation from the cathode (red line). Simultaneously, the charge potential (blue line) leads to a plateau corresponding to a voltage of around 4V (first half cycle). This high operating voltage is associated with the highly oxidised $Co^{3+/4+}$ couple [133]. The process is continued with the insertion of about half the Li^+ ions during discharge by electrochemical reduction and a potential associated with that (second half cycle). The charge/discharge potentials are not coincident due to internal resistance of the cell (also called overpotential), which is responsible for a decrease of potential on discharge and increase of potential on charge [20]. Although the number of lithiums inserted and extracted drops slightly after a few cycles, the reversibility over a number of cycles is reasonably good and the cell is cycling well in its potential window. Capacity data can be extracted for charge/discharge and capacity changes on cycling can be monitored (figure 2.11). According to the graph, the charge/discharge capacity efficiency is almost 100% except for the first cycle and average capacity loss after first drop is not significant, in agreement with the literature.
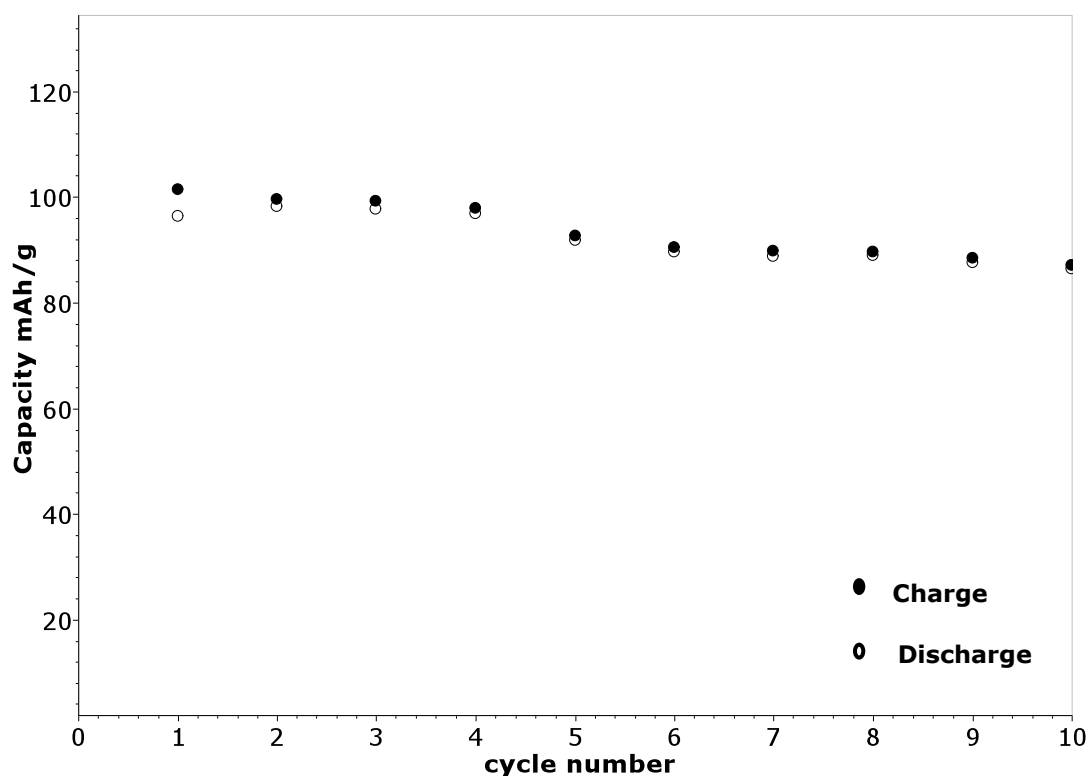
Figure 2.11. Capacity retention on charge and discharge for LiCoO₂ cell.

Combustion analysis

Combustion, combined with thermal-conductivity analysis has been in use for many years to determine total nitrogen in metals and refractory materials [107]. To detect nitrogen, the sample is heated in a furnace in a graphite crucible under a flowing inert gas (helium). Following the fusion process, nitrogen is released as N_2 and measured by a thermal conductivity cell. The measured signal from the thermal conductivity detector for the sample can then be converted into total nitrogen content. Calculations are based on atomic/molecular formula and the results are reported in weight% [134].

Experiments were performed on a Leco TC-500 instrument at the AMG Analytical Services at Rotherham. The instrument is calibrated at least once every ten samples with a blank test and an appropriate Quality Control (QC) sample and the results should fall inside the allowed tolerances. Samples are analysed in duplicates and if the values are within the tolerance, the average value is reported [134].

The nitrogen content can be calculated using the following equation. For $Li_{3+X}VO_{4-X}N_X$ for instance:

X=(N weight/14)/(sample weight/sample molar weight)   2.30

assuming that the sample molar weight is independent of X.

Chapter 3

Preparation and characterisation of crystalline lithium phosphorus oxynitride solid solutions

"Science never solves a problem without creating ten more."

— George Bernard Shaw

Introduction

Li_3PO_4 can be described as having a wurtzite (ZnS) superstructure [135]. Li_3PO_4 is dimorphic (γ and β), and both polymorphs belong to a family of materials called tetrahedral structures, where all cations are tetrahedrally coordinated [136]. The structure of γ-Li_3PO_4 (high temperature form) was determined by Zemann [137]. Prior to that, Li_3PO_4 was classified, incorrectly, as an olivine [138]. The structure of the low temperature (β form) was determined by Tarte [139] and Keffer [140]. The low form of Li_3PO_4 occurs in nature as the lithiophosphate mineral [79]. The crystal structure of β-Li_3PO_4 is orthorhombic space group *Pmn2$_1$*, with *Z=2* and *a=6.1150, b=5.2394, c=4.8554 Å* [140]. The crystal structure of γ-Li_3PO_4 was assigned to the orthorhombic space group *Pnma*, with *Z=4* and *a=10.490, b=6.120, c=4.9266 Å* [141]. In the γ form, the unit cell is doubled along the *a*-axis (along *b* or *c*-axis for *Pmnb* and *Pcmn* space groups) [142].

In both polymorphs, oxide ions are packed into a distorted hexagonal close packed (hcp) array, with cations occupying tetrahedral interstices, to form a framework of tetrahedra. The β and γ crystal structures differ mainly in the orientation of these tetrahedra, in a way that all phosphate tetrahedra are oriented in the same way relative to the *c* axis in the β polymorph, whereas half of the phosphate tetrahedra in the γ polymorph have the opposite orientation [143]. In the low temperature form, one set of tetrahedral sites (T$^+$ or T$^-$) is fully occupied, while in the γ structure the cations are distributed over both sets of T$^+$ and T$^-$ sites [142], leading to some edge-sharing of LiO_4 tetrahedra in γ-Li_3PO_4, whereas in the β polymorph only corner-linked tetrahedra exist

[77, 80] (figure 3.1). There are six sets of atomic positions in the asymmetric unit of both polymorphs that are summarised in table 3.1.

a)
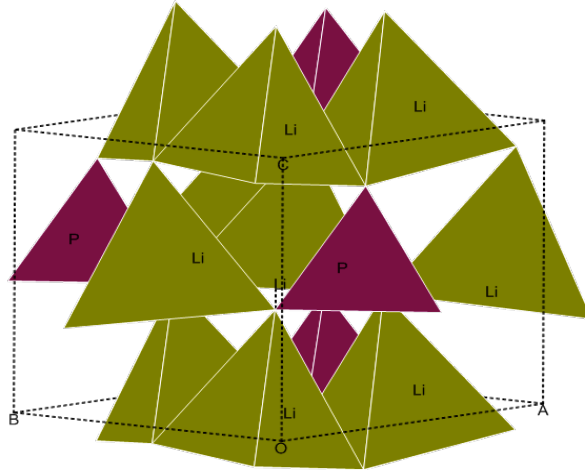
b)
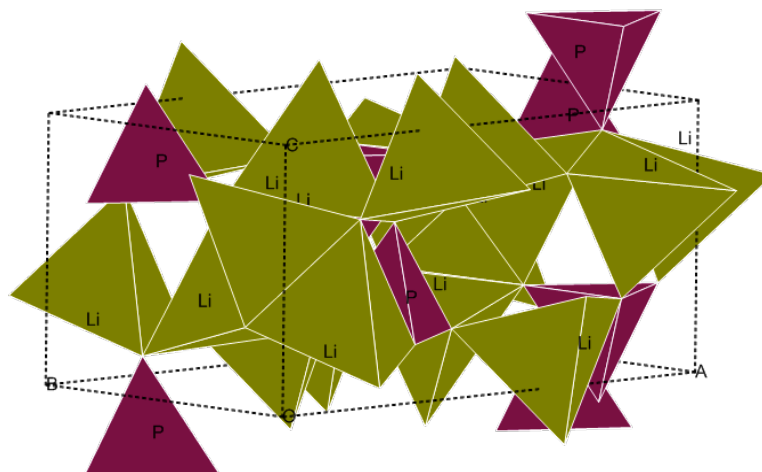
Figure 3.1. Schematic projection of a) β-Li$_3$PO$_4$ and b) γ-Li$_3$PO$_4$.

The transformation of β-Li$_3$PO$_4$ to the γ phase occurs at any temperature higher than 340°C. In the range 340°C- 410°C the transformation shows characteristics of a martensitic transformation [80, 135, 143, 144]. The reverse γ➔β transformation however, does not happen unless under hydrothermal conditions.

Li$_3$PO$_4$ is a member of a large family of tetrahedrally coordinated oxides based on Li$_3$XO$_4$ (X=P, V, As, Cr). The other Li$_3$PO$_4$-related phases are the so-called LISICON structure materials, formed by aliovalent doping of Li$_4$GeO$_4$ or Li$_4$TiO$_4$, solid solutions

between Li_3XO_4 (X=P, V, As, Cr) and Li_4YO_4 (Y=Si, Ge, Ti) and compounds with the general formula: $Li_2M^{2+}Y^{4+}O_4$ (M=Zn, Mg, Mn^{2+}, Co^{2+}), (Y=Si, Ge^{4+}) [145].

Table 3.1. Atomic parameters in the refined structures of γ and β-Li₃PO₄.

Atom	x	y	z	Site
γ-Li₃PO₄ [141]				
Li(1)	0.1639	0.5013	0.3013	8d
Li(2)	0.4237	0.75	0.2056	4c
P	0.41151	0.25	0.30878	4c
O(1)	0.34167	0.04289	0.2057	8d
O(2)	0.05042	0.25	0.2937	4c
O(3)	0.08964	0.75	0.1223	4c
β-Li₃PO₄ [140]				
Li(1)	0.248	0.328	0.986	4b
Li(2)	0.5	0.843	0.989	2a
P	0	0.824	0	2a
O(1)	0.208	0.687	0.896	4b
O(2)	0	0.105	0.900	2a
O(3)	0.5	0.181	0.817	2a

In crystalline Li_3PO_4, all Li-ion sites are fully occupied in the structure, such that there is hardly any lithium ion movement [47]; therefore, the lithium ion conductivity is very low ($\sigma \approx 10^{-18}$ Scm^{-1} at 25°C) [75]. It has been shown that the addition of nitrogen into the structure of amorphous lithium phosphate thin films (LiPON), deposited by sputtering Li_3PO_4 in N_2, increased the lithium ion conductivity by several orders of magnitude ($\sigma \approx 2 \times 10^{-6}$ Scm^{-1} at 25°C) compared to Li_3PO_4 films, also prepared by sputtering [59]. Another feature of this novel material, apart from a reasonable ionic conductivity is its hardness and chemical durability and more importantly its excellent stability in contact with lithium metal [57, 60]. The reason for the increased conductivity and stability of oxynitride thin films has been the subject of many discussions and so far there has been no decisive conclusion on the effect of nitrogen on the improved ionic conductivity of LiPON [74]. However, the effect of nitrogen on the conductivity of lithium phosphate bulk glasses has been extensively investigated. In an oxynitride glass structure, either di-coordinated nitrogen atoms (−N=) or tri-coordinated ones (−N<), substitute for oxygens in PO_4 groups, leading to a decrease in the bridging oxygen/non-

bridging oxygen ratio [146]. In this case, the number of tri-coordinated nitrogens (N_t) is much more effective in terms of increasing structural cross-linking which appears to increase the lithium mobility similar to the "mixed anion effect" [147]. The mixed anion effect implies that the mobility of cations in glasses with mixed anions is modified [148]. In the case of lithium phosphate glasses, the rise in electrical conductivity is believed to be due to the increase in number of non-bridging oxygens and increased cross-linking density in glass network, which create conduction paths for Li-ions with lower activation energy [73]. It was also proposed that decreased electrostatic energy in the more covalent P-N bond instead of the P-O bond, can increase ionic mobility [70].

The actual composition and structure of these oxynitrides (both bulk and thin film) are unclear due to their glassy state. The first crystalline form of this material with the measured stoichiometry of $Li_{2.88}PO_{3.73}N_{0.14}$ was prepared by reaction between Li_3N and $LiPO_3$ in nitrogen atmosphere [75]. The ionic conductivity of this material was reported as $\approx 1 \times 10^{-13}$ Scm^{-1} at room temperature, which is significantly higher than that of pure Li_3PO_4 but lower than thin film LiPON. $Li_{2.88}PO_{3.73}N_{0.14}$ has a Li_3PO_4 structure and is formed by systematically removing one O, removing one Li, and substituting one O with N for each formula unit of Li_3PO_4 to give the general formula $Li_{(3-X)}PO_{(4-2X)}N_X$. High-performance liquid chromatography (HPLC) and X-ray photoelectron spectroscopy (XPS) of $Li_{2.88}PO_{3.73}N_{0.14}$ indicates that most of the nitrogen substitutes for oxygen to form PO_3N structural units with small concentrations of P-N=P [75]. As Li_3PO_4 is based on isolated PO_4 tetrahedra, each share corners with LiO_4 tetrahedra, it was proposed that formation of P-N-P units would require some Li/P disorder [76, 77]. The increased ionic conductivity and lower activation energy was attributed to Li and O vacancy formation and slightly larger cell volume [149].

Recently, a new crystalline phase (Li_2PO_2N) was reported by Holzwarth and co-workers [78], which is synthesised by solid-state reaction between Li_2O, P_2O_5 and P_3N_5 and was reported to have the Li_2SiO_3 structure [78]. The ionic conductivity of this compound was considerably higher (8.8×10^{-7} Scm^{-1} at 80°C and activation energy of 0.57 eV) than that for the previously-reported crystalline structure. Li_2PO_2N is derived from the known crystal structure of $LiPO_3$ by replacing each oxygen in a bridging site between two phosphorus atoms with nitrogen and adding one lithium to maintain electroneutrality [79]. Prior to that, simulation studies on Li-ion conduction in phosphate materials indicated that the activation energy for Li-ion conduction in Li_2PO_2N is slightly larger than Li_3PO_4, mainly due to the large energy cost of defect

47

(vacancy/interstitial) creation [81, 150]. The high ionic conductivity and low activation energy that is found in Li_2PO_2N suggests that a significant number of Li defects must be present in the structure. It was reported that a slight excess of P_3N_5 precursor is needed in order to achieve a single phase compound [78]. It is therefore possible that the extra P_3N_5 that is used has led to some Li defect formation.

Simulation studies on Li-ion conduction of Li_3PO_4 indicates that an interstitial defect mechanism would provide the most efficient Li-ion transport [80]. Li-interstitials can be formed by aliovalent doping of both cations and anions in Li_3PO_4. Li-interstitial formation by the cation doping mechanism has been broadly investigated in LISICONs and many other Li-containing, gamma (γ) structure, materials [47, 83, 145]. However, there has not been any study on the introduction of interstitial lithium by anionic doping of Li_3PO_4 crystals. The first aim of this project is to investigate the possible formation of crystalline lithium phosphorous oxynitride, based on an interstitial defect mechanism.

In N-doping of Li_3PO_4, the replacement of O^{2-} ions with N^{3-} results in a concentration of partially coordinated lithium ions (interstitial Li^+) and a decrease in the activation energy for lithium ion conduction and consequently a significant increase in the mobility [76]. Moreover, substitution of smaller O^{2-} (1.24 Å) ions with bigger N^{3-} (1.32 Å) ions would affect the size of the bottleneck through which Li-ions must pass and accordingly would increase the mobility of Li-ions [75]. In other words, improvement in Li^+ mobility is related to the creation of defects and distortion of the tetrahedral structure [77]. Computational studies indicated that Li-interstitial defects can be stabilised by replacing O with N to form PO_3N defects and predicted the migration energy of these defects, to be 0.9 eV [76].

In this chapter synthesis, structure, composition and electrical properties of solid solutions based on $Li_{3+X}PO_{4-X}N_X$ (0≤X≤0.8) formula is investigated.

Results and discussion

X-ray diffraction

The X-ray diffraction pattern of Li_3PO_4 is shown in figure 3.2. Li_3PO_4 was prepared by mixing and grinding appropriate amounts of Li_2CO_3 and $(NH_4)_2HPO_4$. The mixture was heated initially at 140°C, 160°C, 180°C, 200°C and 250°C for 15 minutes at each step before decarbonation at 650°C for 10 hours and a final heating at 850°C overnight.

All peaks in the XRD pattern correspond well to ICDD card [84-64], match with γ-Li_3PO_4 and can be indexed as orthorhombic with *Pnma* symmetry (♯62) within errors (table 3.2). Our first attempt to make pure nitrogen-doped samples was carried out by mixing appropriate amounts of Li_3PO_4 and Li_3N followed by reaction at 800°C, which led to the presence of Li_2CO_3 and Li_2O secondary phases (red traces in figure 3.2). Elimination of the secondary phases with further grinding and heating at higher temperatures was unsuccessful and a phase mixture remained. A pure phase $Li_{3.4}PO_{3.6}N_{0.4}$ was, however, made by reaction between Li_2CO_3, $(NH_4)_2HPO_4$ and Li_3N, as described in the experimental section (green traces in figure 3.2).
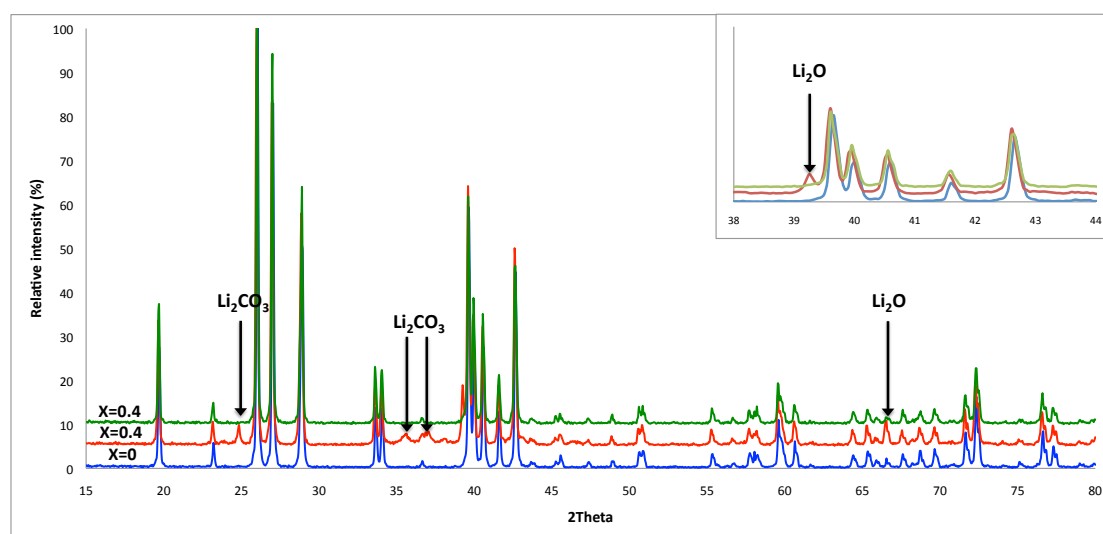
Figure 3.2. XRD profiles of $Li_{(3+X)}PO_{(4-X)}N_X$. Red traces: Samples made from Li_3PO_4 and Li_3N; green traces: samples made from Li_2CO_3, $(NH_4)_2HPO_4$ and Li_3N (Co Kα$_1$ radiation).

Following successful synthesis of $Li_{3.4}PO_{3.6}N_{0.4}$, a range of compositions (from 5%-20% of oxygen substituted by nitrogen) was made. The X-ray diffraction patterns of $Li_{(3+X)}PO_{(4-X)}N_X$: X=0.2, 0.4, 0.6, 0.8 are shown in figure 3.3, and compared with that of Li_3PO_4. XRD patterns of these oxynitrides correspond well to the Li_3PO_4 peaks. At high values of nitrogen (X=0.6, 0.8) however, traces of unreacted Li_2CO_3 were detected but the samples appear predominantly phase-pure. The main peaks in the XRD trace for all compositions match with ICDD card [84-64] and can be indexed as orthorhombic with *Pnma* symmetry (♯62) within good errors. X-ray diffraction data of $Li_{3.2}PO_{3.8}N_{0.2}$ are listed in table 3.2.
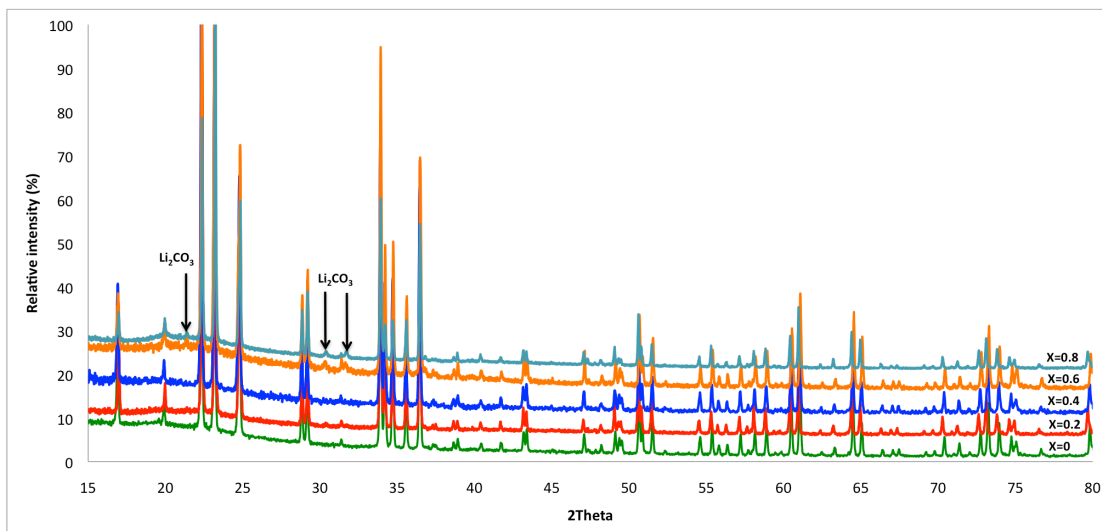
Figure 3.3. XRD profiles of $Li_{(3+X)}PO_{(4-X)}N_X$ (Cu $K\alpha_1$ radiation).

The lattice constants and cell volume of Li_3PO_4 and LiPONs are calculated and listed in Table 3.3 and compared with the literature. There is a good agreement between the cell parameters of synthesised Li_3PO_4 and γ-Li_3PO_4 reported by Yakubovic and Wang et al [75, 141]. The cell volume of the nitrogen-doped samples decreases compared to that of Li_3PO_4. Figure 3.4 illustrates cell parameter variation with X. The contraction of the unit cell volume is considerable with X=0.2 but stays more or less unchanged with X>0.2. This may suggest that the solid solution limit is around X=0.2.

Table 3.2. X-ray diffraction data of Li₃PO₄ and Li₃.₂PO₃.₈N₀.₂ (Cu Kα₁ radiation).

Li₃PO₄

d observed (Å)	d calculated (Å)	Δ2θ° (obs-cal)	Intensity	h k l
5.2403	5.2388	-0.0047	23.2	2 0 0
4.4566	4.4568	0.0009	7.1	1 0 1
3.9786	3.9787	0.0002	100.0	2 1 0
3.8355	3.8356	0.0009	93.8	0 1 1
3.5903	3.5881	-0.0150	62.5	2 0 1
3.0944	3.0948	0.0035	14.1	2 1 1
3.0576	3.0579	0.0030	15.7	0 2 0
2.8505	2.8488	-0.0185	0.6	0 3 1
2.6405	2.6409	0.0056	68.5	2 2 0
2.6190	2.6194	0.0045	30.3	4 0 0
2.5820	2.5824	0.0051	31.9	3 1 1
2.5212	2.5215	0.0042	16.1	1 2 1
2.4617	2.4622	0.0077	56.5	0 0 2
2.4059	2.4079	0.0311	1.1	4 1 0
2.3273	2.3274	0.0020	1.7	2 2 1
2.3122	2.3126	0.0065	2.5	4 0 1
2.2291	2.2284	-0.0129	2.0	2 0 2
2.1629	2.1631	0.0040	2.4	4 1 1
2.0934	2.0937	0.0064	5.2	2 1 2

Li₃.₂PO₃.₈N₀.₂

d observed (Å)	d calculated (Å)	Δ2θ° (obs-cal)	Intensity	h k l
5.2349	5.2362	0.0042	16.7	2 0 0
4.4528	4.4532	0.0018	8.2	1 0 1
3.9756	3.962	0.0035	100.0	2 1 0
3.8325	3.8324	-0.0007	96.6	0 1 1
3.5876	3.5856	-0.0142	53.7	2 0 1
3.0927	3.0926	-0.0006	15.0	2 1 1
3.0562	3.0556	-0.0067	17.8	0 2 0
2.8461	2.8470	0.0102	0.5	0 3 1
2.6390	2.6391	0.0011	81.7	2 2 0
2.6179	2.6181	0.0023	23.6	4 0 0
2.5806	2.5807	0.0021	26.7	3 1 1
2.5195	2.5195	0.0002	16.6	1 2 1
2.4601	2.4601	-0.0007	63.3	0 0 2
2.4061	2.4066	0.0070	0.8	4 1 0
2.3258	2.3257	-0.0020	2.1	2 2 1
2.3108	2.3113	0.0077	2.1	4 0 1
2.2284	2.2298	0.0268	2.1	1 1 2
2.1621	2.1618	-0.0053	2.5	4 1 1
2.0918	2.0921	0.0049	5.9	2 1 2

51

Table 3.3. X-ray diffraction data of synthesised and reported Li₃PO₄ and LiPONs.

	a(Å)	b(Å)	c(Å)	V(Å)	Space group
Li_3PO_4	10.4777 (4)	6.11579(24)	4.92447(17)	315.557(14)	$P\,n\,m\,a$
Li_3PO_4 (γ) [75]	10.4612(2)	6.1113(1)	4.9208(1)	314.60(2)	$P\,n\,m\,a$
Li_3PO_4 (γ) [141]	10.490	6.120	4.9266	316.2818	$P\,n\,m\,a$
$Li_{3.2}PO_{3.8}N_{0.2}$	10.4725(5)	6.1111(3)	4.92020(23)	314.886(18)	$P\,n\,m\,a$
$Li_{3.4}PO_{3.6}N_{0.4}$	10.4703(7)	6.1105(4)	4.9204(3)	314.798(24)	$P\,n\,m\,a$
$Li_{3.6}PO_{3.4}N_{0.6}$	10.4740(8)	6.1125(4)	4.9213(3)	315.07(3)	$P\,n\,m\,a$
$Li_{3.8}PO_{3.2}N_{0.8}$	10.4712(6)	6.1105(3)	4.91978(24)	314.788(19)	$P\,n\,m\,a$
$Li_{2.88}PO_{3.73}N_{0.14}$ [75]	10.469(1)	6.1153(9)	4.9195(8)	314.9(1)	$P\,n\,m\,a$
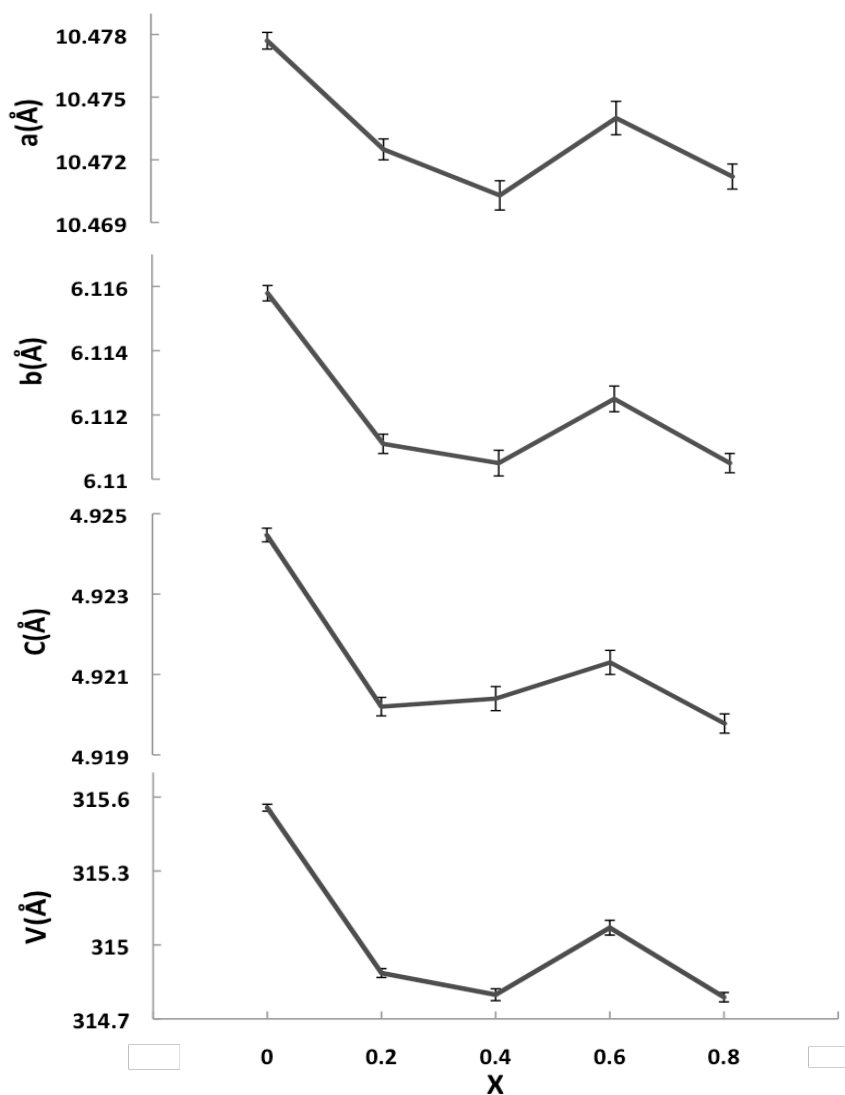
Figure 3.4. Change in unit cell parameters of $Li_{(3+X)}PO_{(4-X)}N_X$ with increasing X.

Impedance Spectroscopy

The conductivity has been measured over a wide frequency range for Li_3PO_4 and its nitrogen-doped analogues. Due to the high resistivity of all samples, measurements required a temperature in excess of 250°C to reduce the resistance to measurable values. The data were analysed using conductivity ($Y^{'}$), capacitance ($C^{'}$), $Z^{''}$ and $M^{''}$ versus frequency ($\log f$) and impedance (Z^*) complex plane plots.

Typical impedance spectroscopy (IS) data sets of Li_3PO_4 and nitrogen-doped Li_3PO_4 are presented in figures 3.5 and 3.6. The Z^* plots show a single, nearly ideal semicircle for all samples. The associated capacitance can be calculated from the relation $\omega RC=1$ at the semicircle maximum (≈ 4 $pFcm^{-1}$ for Li_3PO_4, 0.1 $pFcm^{-1}$ for $Li_{3.2}PO_{3.8}N_{0.2}$ and $Li_{3.4}PO_{3.6}N_{0.4}$, 9.5 $pFcm^{-1}$ for $Li_{3.6}PO_{3.4}N_{0.6}$ and 0.2 $pFcm^{-1}$ for $Li_{3.8}PO_{3.2}N_{0.8}$). This is in good agreement with the C' spectra where the high frequency plateaux in the $\log C'$ vs. $\log f$ plots are in the range of 10^{-12} Fcm^{-1}, suggesting that these data are associated with the bulk response. Although the capacitance data are largely in the range of bulk response, there is considerable variation among them, mainly because the data have not been corrected for different jig and cable contributions that have been used. During impedance measurements, apart from the sample, everything between the two terminals is being measured including the jig and the leads. In this case, the jig is assumed to be the dominant additional source of capacitance in parallel with the sample response. The additional capacitance is in the range of 0.1 and 10 $pFcm^{-1}$ depending on which jig system is being used [151].

Overlapping of peaks in combined Z"/M" spectra and especially the fact that the peak maxima in the Z" and M" plots occur at the same frequency and only one peak is seen in each spectrum, confirms the electrical homogeneity of the samples. The bulk resistance can be obtained directly from the intercept of the impedance complex plane plot with the real axis (Z' axis) [152] and also, in the absence of any significant grain boundary effects, from the frequency independent conductance plateau in the $\log \sigma$ vs. $\log f$ plots [153].

In a typical ion-conducting material, the electrode-sample interface behaves as an electrical double layer with an associated resistance and capacitance. The electrode-sample interface does not permit the passage of current, leading to the blockage of ionic species at the interface and acting as an impedance barrier. The Z^* plane response, in this case, is dominated by the blocking nature of the electrode:
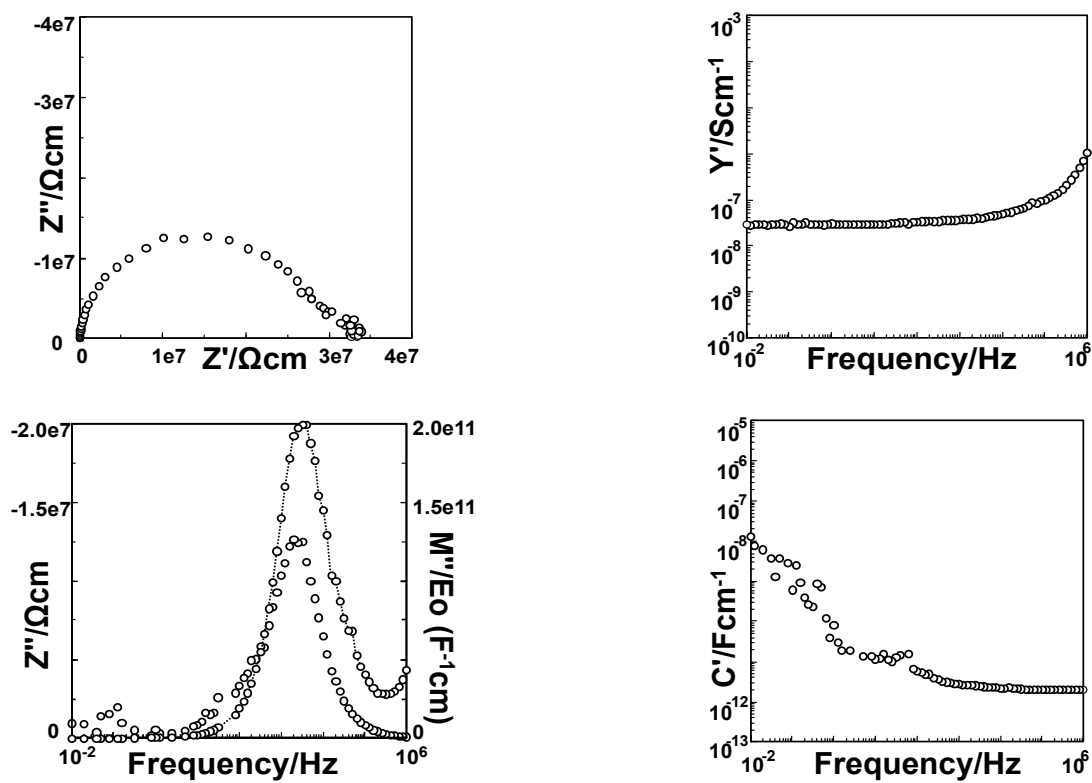
Figure 3.5. Impedance spectroscopy data of Li$_3$PO$_4$ at 351°C.
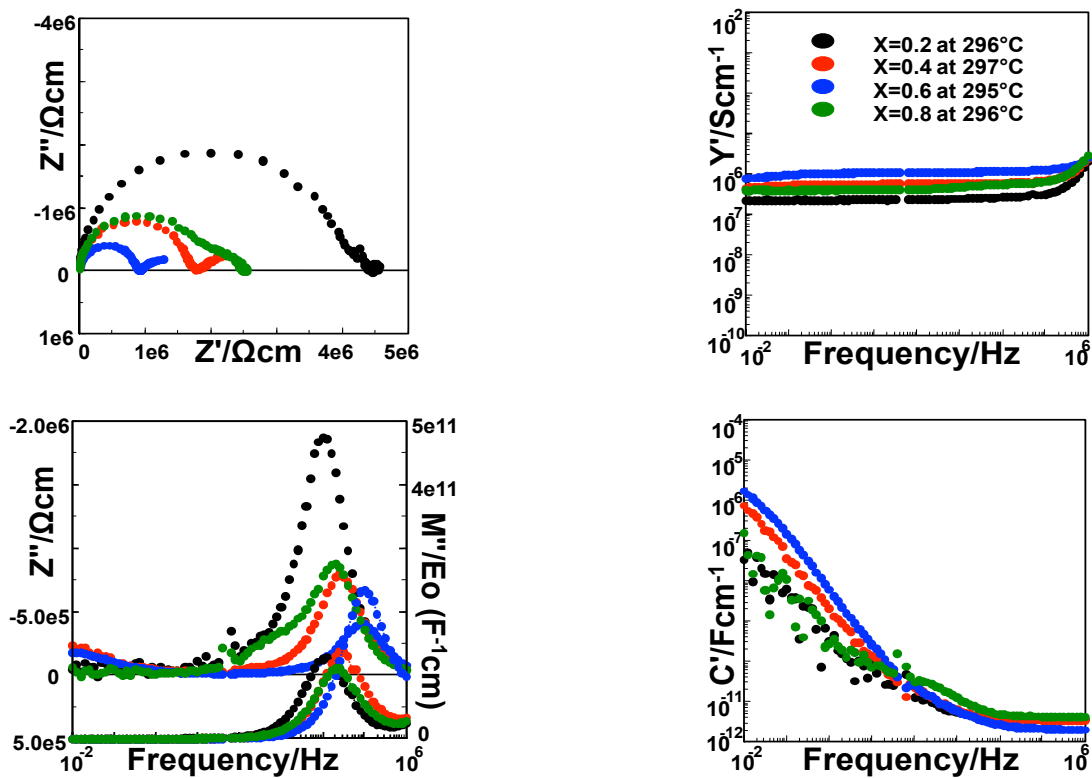
Figure 3.6. Impedance spectroscopy data of Li$_{(3+X)}$PO$_{(4-X)}$N$_X$.

$$-Z'' = \frac{1}{\omega C} \quad [127]$$

This response results in a nearly vertical low frequency spike in Z* plots and a dramatic increase in measured capacitance (around one microfarad) [126].

Figure 3.7 illustrates the Z^* plots of Li_3PO_4 and nitrogen-doped samples at different temperatures and their associated capacitance. In these results, a low frequency dispersion with a capacitance in the range of microfarads, which has the character of an inclined spike attributed to partial blocking of ionic charge carriers at the metal-sample interface, can be evidenced in samples with X=0.2 (above 346°C) , 0.4, 0.6 and X=0.8 (above 398°C). These can be signs of ionic conduction. No sign of ionic conduction was seen at X=0.

Electrical conductivity was determined as a function of temperature and a linear Arrhenius behaviour was observed for X=0 at all temperatures and for X=0.2, 0.4, 0.6 and 0.8 below ≈400°C (figure 3.8). Activation energies and related conductivities of Li_3PO_4 and N-doped Li_3PO_4 are given in table 3.4 and compared with the result reported by Wang et al [75, 141]. Activation energies (Ea) were calculated from the linear part of Arrhenius plots. Conductivity data are in good agreement with those reported in the literature for X=0, 0.2 and 0.4. The results indicate a decrease in activation energy for compositions with X=0.2 and 0.4 compared to Li_3PO_4 below 400°C (from 1.18 to 0.91-0.92 eV), also in agreement with computational studies of these materials [76]. Activation energies for compositions with X=0.6 and 0.8 however, are almost identical to that of Li_3PO_4. In these results conductivity of the N-doped samples is between 1-2 orders of magnitude higher than that of Li_3PO_4 over the same temperature range.
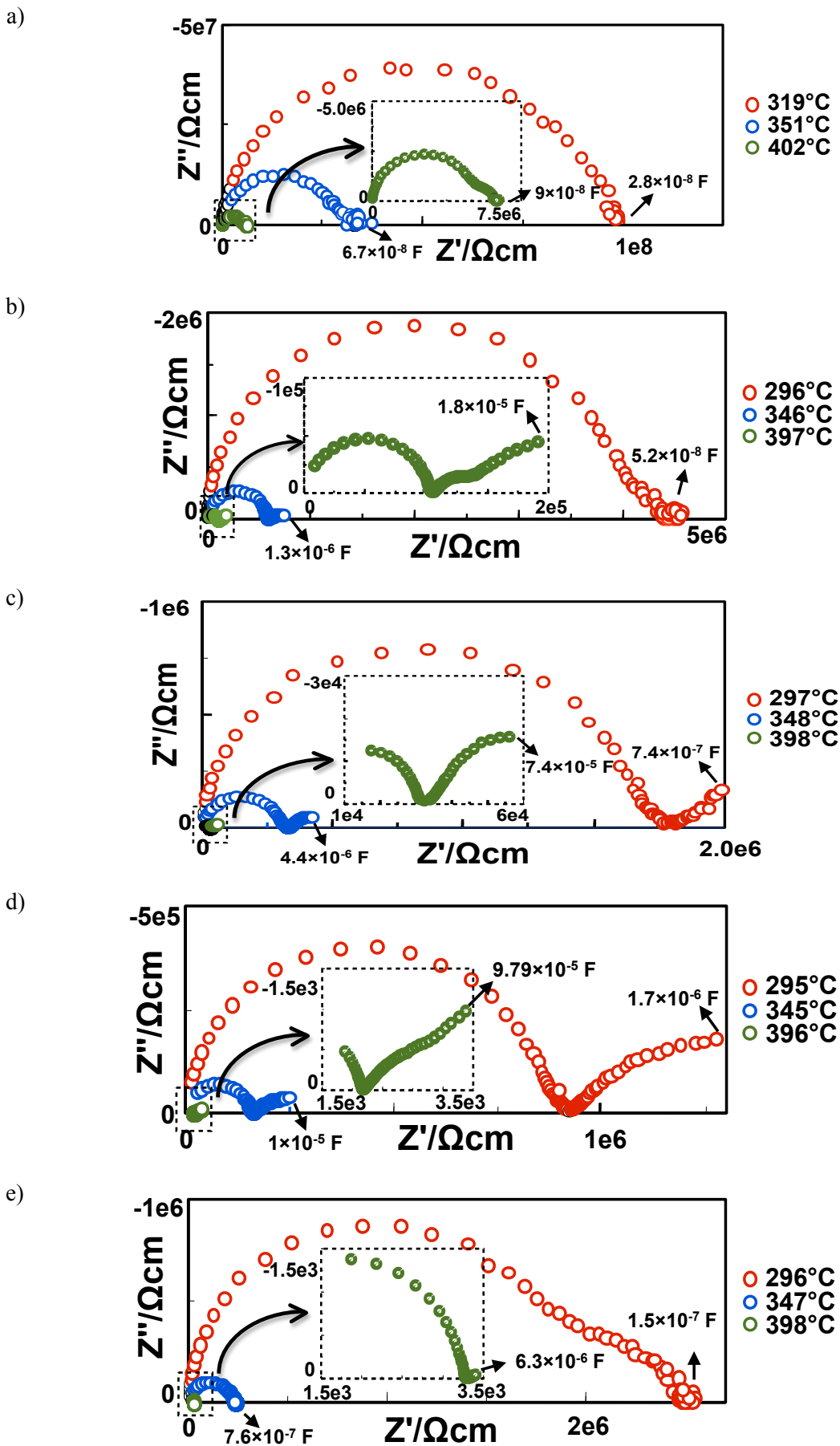
Figure 3.7. Z* plot of Li$_{(3+X)}$ PO$_{(4-X)}$ N$_X$ and the associated capacitance at different temperatures: a) X=0, b) X=0.2, c) X=0.4, d) X=0.6, e) X=0.8.
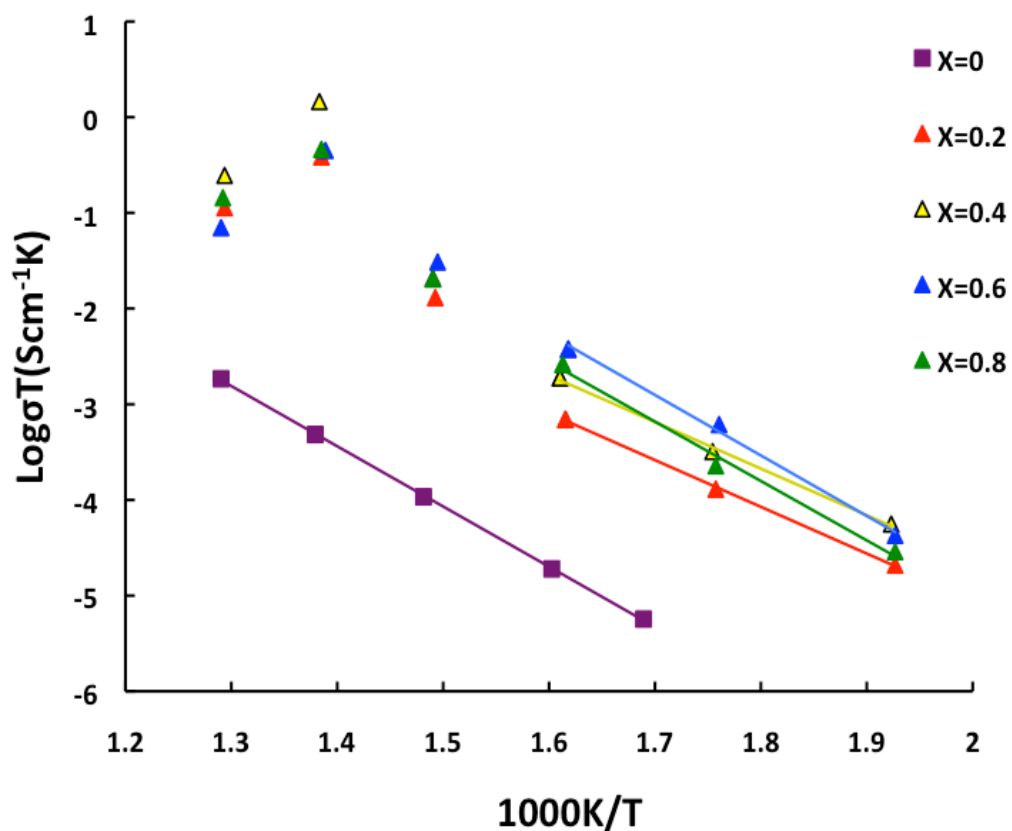
Figure 3.8. Arrhenius plots of conductivity of $Li_{(3+X)} PO_{(4-X)} N_X$ (N-doped samples showed linear Arrhenius behaviour only below ≈400°C).

Table 3.4. Activation energies (below 400°C) and conductivities (extrapolated for comparison).

	Activation Energy (eV)	Conductivity (Scm^{-1}) at $T°C$
Li_3PO_4	1.18	$1 \times 10^{-18}(25)$
$Li_{3.2}P_{3.8}N_{0.2}$	0.92	$9.6 \times 10^{-15}(25)$
$Li_{3.4}P_{3.6}N_{0.4}$	0.91	$2.5 \times 10^{-14}(25)$
$Li_{3.6}P_{3.4}N_{0.6}$	1.20	$2 \times 10^{-16}(25)$
$Li_{3.8}P_{3.2}N_{0.8}$	1.18	$1.6 \times 10^{-16}(25)$
Li_3PO_4 [75, 141]	1.24	$4.2 \times 10^{-18}(25)$
$Li_{2.88}P_{3.73}N_{0.14}$ [75, 141]	0.97	$1.4 \times 10^{-13}(25)$

Data for nitrogen-doped samples show deviation from linear regression above 400°C. Especially at ≈450°C a jump in conductivity can be seen followed by a drop in conductivity at ≈500°C. The Z* plots of these samples show a low frequency spike with an associated capacitance in the range of electrochemical reactions (≈10^{-4} F) at ≈450°C (figure 3.9). The electrical conductivity of three oxynitride samples was studied as a function of temperature on a cooling cycle. The Arrhenius plots obtained on cooling and heating, are compared in figure 3.10 and are reversible at all temperatures except at ≈450°C, suggesting a reversible transformation has occurred in the discussed temperature range, later confirmed by DSC and TGA results.
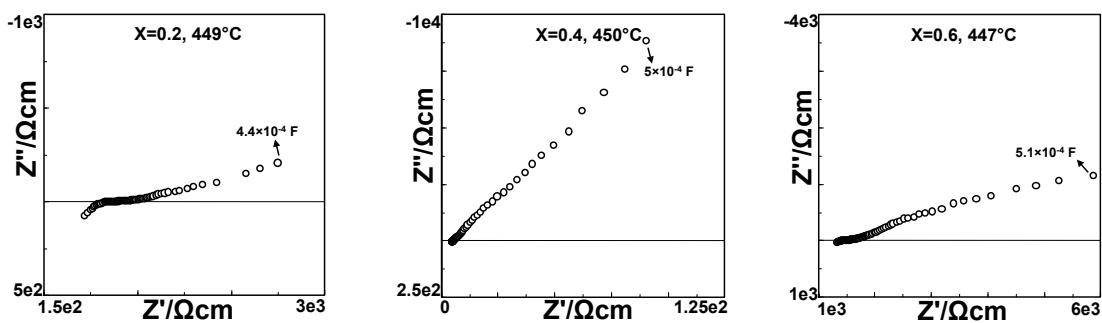
Figure 3.9. Z* plots of Li$_{(3+X)}$ PO$_{(4-X)}$ N$_X$ and their associated capacitances at ≈450°C.
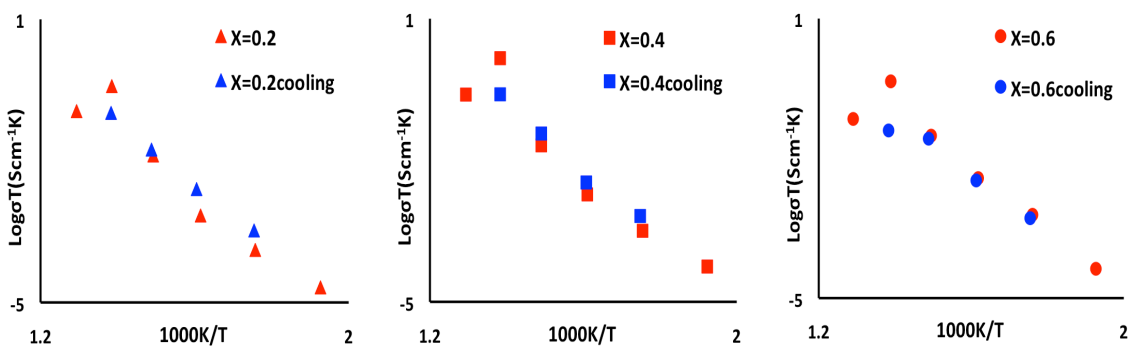
Figure 3.10. Arrhenius plots of conductivity of Li$_{(3+X)}$ PO$_{(4-X)}$ N$_X$ on heating and cooling.

Figure 3.11 illustrates the DSC results of two samples: a nitrogen-doped sample (two cycles) and a sample made of 95% Li$_3$PO$_4$ and 5% Li$_2$CO$_3$, in nitrogen atmosphere. The reason for testing a mechanical mixture of Li$_3$PO$_4$ and Li$_2$CO$_3$ was to make sure that the observed high temperature effect is not due to the presence, in some way, of Li$_2$CO$_3$

secondary phase, previously evidenced in XRD of high nitrogen-doped samples. The result shows an endothermic transition for $Li_{3.4}PO_{3.6}N_{0.4}$ in first and second heating cycles at $\approx425°C$, with no effect evidenced on cooling, nor for the $Li_3PO_4 + Li_2CO_3$ mixture on either heating or cooling.

TGA results of Li_3PO_4 and $Li_{3.4}PO_{3.6}N_{0.4}$ in nitrogen atmosphere are shown in figure 3.12. The results of both samples are affected by buoyancy, however weight changes can be distinguished clearly. There is a prominent weight gain that starts at approximately 300°C and is completed by $\approx425°C$ in the nitrogen-doped sample, followed by a weight loss between $\approx450°C$ and 500°C. On cooling, the $Li_{3.4}PO_{3.6}N_{0.4}$ sample gains weight again between approximately 425°C and 300°C. No weight change was evidenced for Li_3PO_4 on either heating or cooling.

The TGA weight gain on heating must indicate chemical reaction of the nitrogen-doped sample with the atmosphere. The reaction was also evidenced in both DSC and impedance spectroscopy. The weight loss effect however, can not be clearly seen in DSC results. The weight increase on cooling was also missed by the DSC experiment. Several attempts were made to retain the chemically-reacted phase at room temperature using the final product of TGA and DSC or by quenching the reacted sample from 425°C and 600°C; no change in the X-ray pattern could be evidenced.

There are a small number of possibilities for reaction between sample and atmosphere, but the most probable one involves loss of nitrogen at high temperature and reaction with oxygen. As the surrounding gas was not entirely oxygen-free, although all the tests were carried out under nitrogen atmosphere, there is a good chance that oxygen could react with the oxynitride sample. Consequently the original reaction involved in synthesis of lithium phosphorus oxynitride could be reversed in favour of Li_3PO_4 formation:

$$Li_{3+X}PO_{4-X}N_X + (X/2)O_2 \rightarrow Li_3PO_4 + (X/3)Li_3N + (X/3)N_2.$$

At X=0.4, $Li_{3.4}PO_{3.6}N_{0.4}$, Li_3PO_4 and $(0.4/3)Li_3N$ would weigh 117.77, 115.79 and 4.64g respectively. Reaction with oxygen therefore, would increase the sample weight, assuming that O_2 and N_2 molecules would not affect the weight measurement in the above formula. It would also generate an endothermic peak in DSC and dramatically reduce sample conductivity, as there is no interstitial lithium available. On the other hand, perhaps Li_3N decomposes below 500°C, decreasing the weight of the sample.
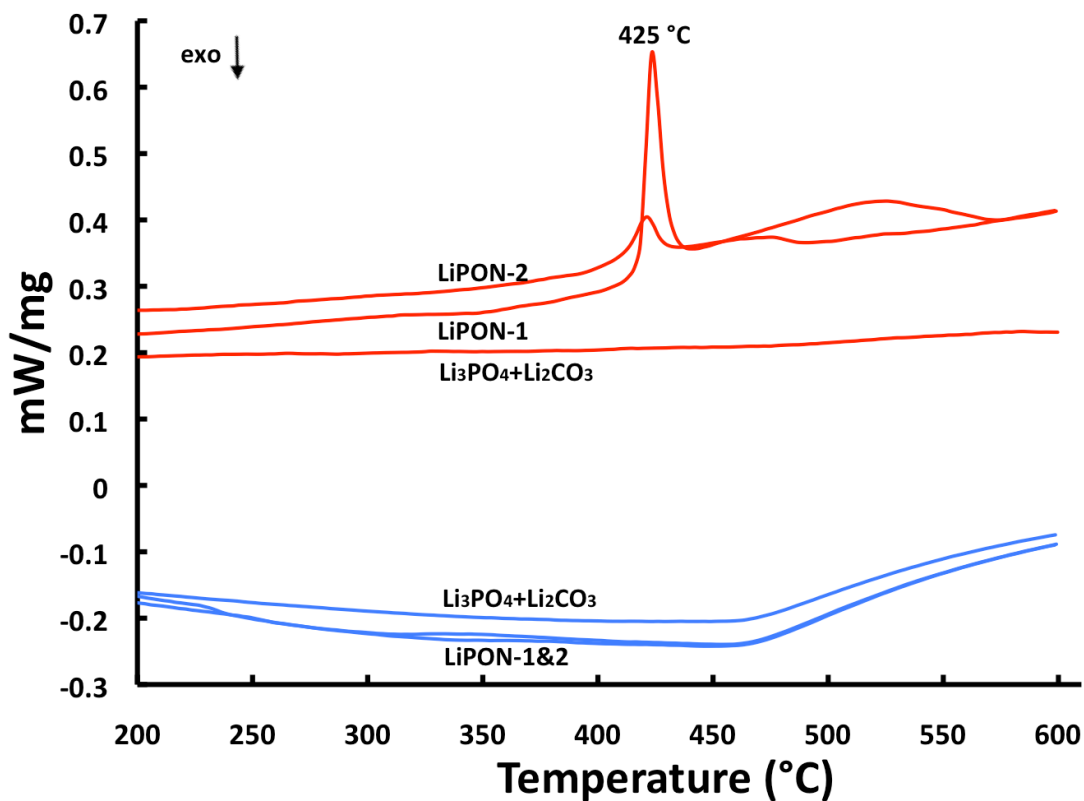
Figure 3.11. DSC results for $Li_{3.4}PO_{3.6}N_{0.4}$ (1st and 2nd cycle) and 95%Li_3PO_4+5% Li_2CO_3 on heating (red) and cooling (blue).
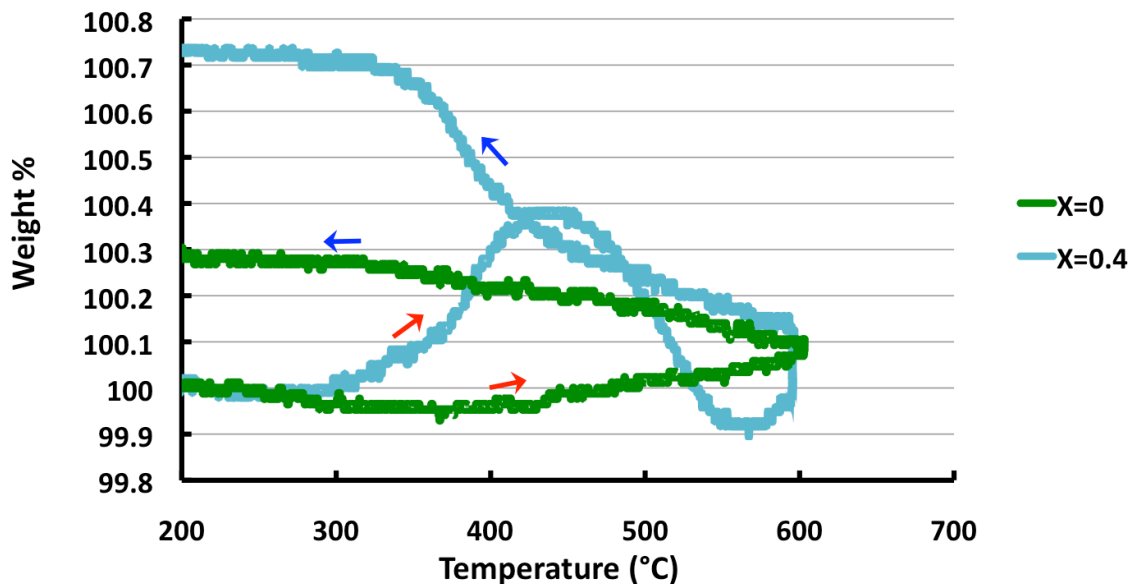
Figure 3.12. TGA results for $Li_{(3+X)}PO_{(4-X)}N_X$ on heating (red arrow) and cooling (blue arrow).

On cooling, in the presence of extra lithium and nitrogen from the atmosphere, reaction is in favour of reformation of the oxynitride compound:

$$Li_3PO_4 + XLi + (X/2)N_2 \rightarrow Li_{3+X}PO_{4-X}N_X + (X/2)O_2.$$

Another possibility for reaction between sample and atmosphere is H_2O. This is despite the fact that the Arrhenius plot data for nitrogen-doped samples show deviation from linear regression even in dry nitrogen. In other words, although measurements were carried out in dry atmosphere, samples could absorb/lose H_2O reversibly on heating and then reabsorb H_2O on cooling. Moreover, nitrogen doping could produce oxide ion vacancies, leading to proton conductivity in the presence of moisture and increased sample conductivity. H_2O reaction with samples at 425°C is either reversible on cooling and could not be detected by DSC or occurs on a small scale and its degraded products are not detectable by XRD/IS.

Combustion analysis

The nitrogen contents were determined using a thermo-conductive detector after fusion in the presence of an inert gas. Tests were performed on a Leco TC-500 instrument at the AMG Analytical Services at Rotherham. Theoretical and experimental values of nitrogen in LiPO(N) samples are shown in table 3.5 and the compositions are corrected accordingly. The results indicate that the nitrogen content in nitrogen-doped samples is significantly lower than expected. In $Li_{3.2}PO_{3.8}N_{0.2}$ and $Li_{3.6}PO_{3.4}N_{0.6}$ for instance, ≈6% and 24% of the targeted nitrogen could be found in the sample, respectively.

Table 3.5. Theoretical and experimental values of nitrogen in LiPO(N) samples determined by combustion analysis and their corrected formula.

	N(g) in 1(g) sample (Exp.)	N(g) in 1(g) sample (Theo .)	mol N (Exp.)	mol N (Theo .)	Corrected formula
Li_3PO_4	<0.0001	0	0.00082	0	Li_3PO_4
$Li_{3.2}PO_{3.8}N_{0.2}$	0.00153	0.0241	0.012	0.2	$Li_{3.012}PO_{3.988}N_{0.012}$
$Li_{3.4}PO_{3.6}N_{0.4}$	0.00526	0.0478	0.043	0.4	$Li_{3.043}PO_{3.957}N_{0.043}$
$Li_{3.6}PO_{3.4}N_{0.6}$	0.0167	0.0711	0.14	0.6	$Li_{3.14}PO_{3.86}N_{0.14}$

Smaller content of nitrogen than calculated, which was also evidenced in previous studies [75], may be related to either the difficulty/impossibility of doping Li_3PO_4 with

nitrogen or loss of nitrogen during synthesis. The loss of nitrogen can be due to the high temperature required for the solid-state reaction. It is also possible that despite all the precautions, nitrogen is lost by exposure of Li_3N to air and moisture, before or during the reaction.

Figure 3.13 illustrates lattice parameter variation against the true nitrogen content that have been obtained from the combustion analysis. According to the XRD and combustion results, the overall nitrogen content can be estimated to be around 0.012
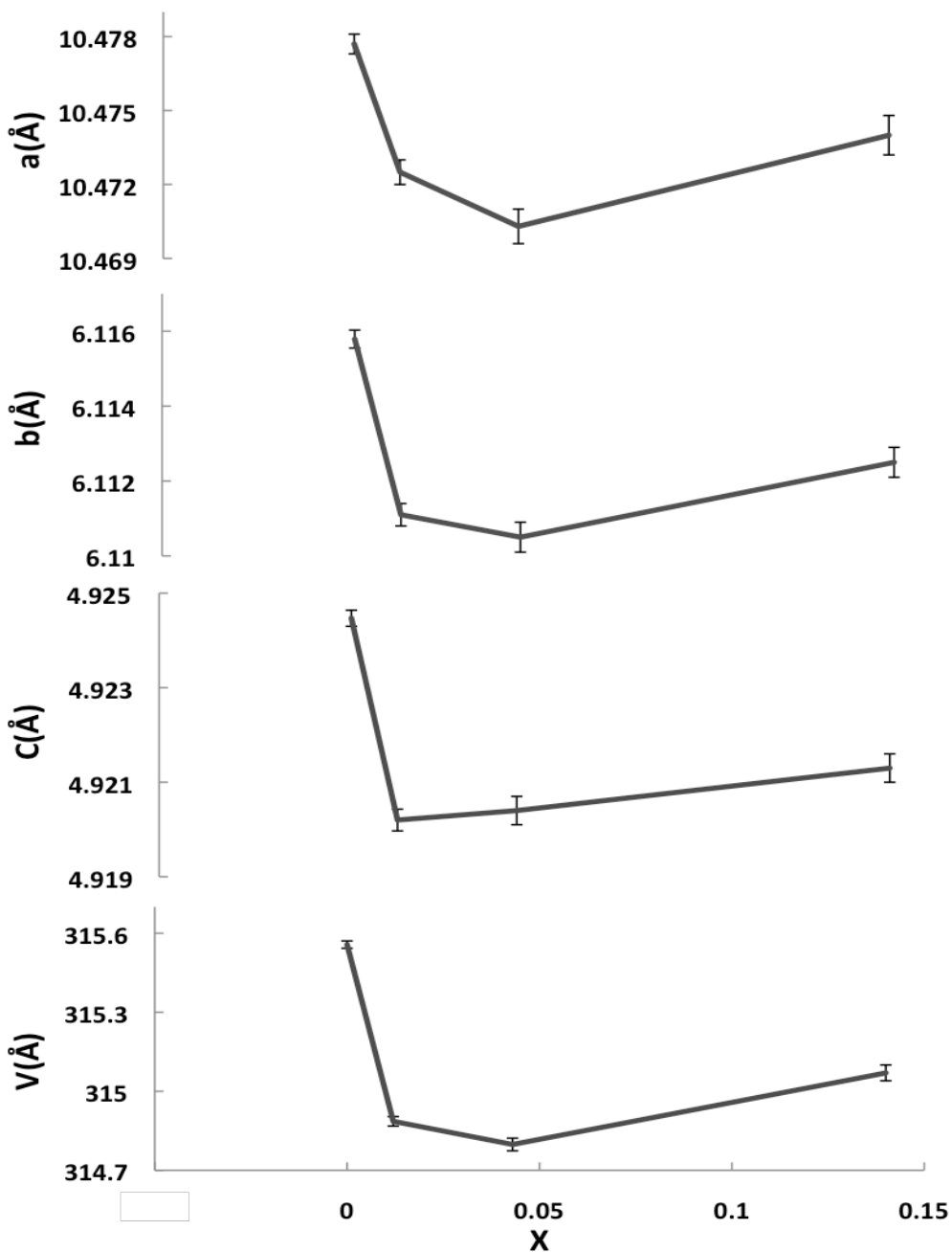
Figure 3.13. Change in unit cell parameters of $Li_{(3+X)}PO_{(4-X)}N_X$ with increasing X (X is corrected according to combustion analysis results).

mol, as the unit cell volume variation is considerable upon this point (X=0.012), but more or less unchanged after it. More nitrogen, however, could be found in X=0.043 and 0.14, suggesting that some other nitrogen-containing products should be present in these samples that perhaps avoided X-ray detection due to their small quantity.

Conclusions

Ceramics with the $Li_{3+X}PO_{4-X}N_X$ (0≤X≤0.8) formula were fabricated via a solid-state route and phase-pure samples were achieved for X≤0.4. The structure was assigned as that of γ-Li_3PO_4 with orthorhombic (*Pnma*) symmetry. XRD results show a decrease in unit cell volume with initial substitution by nitrogen. The unit cell volume change was considerable for X=0.2 but unchanged with adding more nitrogen, suggesting the solid solution limit is around X=0.2.

Electrical properties were studied using impedance spectroscopy over a range of temperature. It was found that doping of lithium phosphate with nitrogen improves the ionic conductivity between 1-2 orders of magnitude compared to that of Li_3PO_4 over the same temperature range. Moreover, activation energy of conduction for N-doped compositions with X=0.2 and X=0.4 decreased dramatically below ≈400°C, in accordance with the literature data. Arrhenius plots of N-doped composition show fully reversible, nonlinear behavior at temperatures above ≈400°C. IS/DSC/TGA results suggest that samples may have reacted with the atmosphere at elevated temperatures. Two possibilities were suggested, indicating reaction with H_2O and/or O_2.

The nitrogen contents were determined for all samples, using combustion analysis and the compositions were corrected accordingly. The result indicates the presence of nitrogen in the nitrogen-doped samples. Data show that the nitrogen content is significantly lower than expected, indicating nitrogen loss before or during the synthesis.

Chapter 4

Preparation and characterisation of crystalline lithium vanadium oxynitride solid solutions

"Live as if you were to die tomorrow. Learn as if you were to live forever."

— Mahatma Gandhi

Introduction

Li$_3$VO$_4$ is a member of a family of tetrahedrally coordinated oxides based on Li$_3$XO$_4$ (X=P, V, As, Cr) [136]. Unlike Li$_3$PO$_4$, Li$_3$VO$_4$ shows complex polymorphism [118, 135, 154]. In addition to the high temperature form (γ) and low temperature form (β), there is also an intermediate phase (T). The low temperature and high temperature polymorphs of Li$_3$VO$_4$ however, are essentially isostructural with low and high forms of Li$_3$PO$_4$ [139, 155, 156]. In both β and γ polymorphs, oxide ions are packed into a distorted hexagonal close packed (hcp) array, with lithium and vanadium occupying half of the available
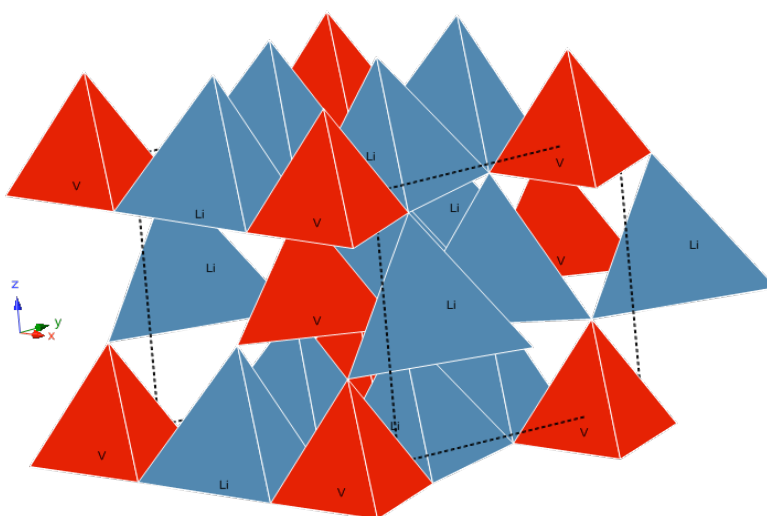
Figure 1. Schematic projection of β-Li$_3$VO$_4$.

tetrahedral sites [140, 156]. Several vacant octahedral sites exist within the oxygen framework, allowing Li^+ ion migration, along with the empty tetrahedral sites [155] (Figure 4.1).

Structure refinement of a single crystal of β_{II}-Li_3VO_4 was performed based on the low form of the Li_3PO_4 structure by Shannon et al [156]. The structure was assigned to be orthorhombic *Pmn2₁*, with *a=6.3259(12), b=5.4460(8), c=4.9469(9) Å*. Lithium ions occupy two different crystallographic sites and V^{5+} the third cationic site similar to Li_3PO_4. In β-Li_3VO_4 only corner-shared tetrahedra exist while in γ-Li_3VO_4, LiO_4 tetrahedra are arranged in groups of edge-sharing sites [155]. In both polymorphs, VO_4 tetrahedra are isolated from each other. The atomic positions of the β_{II} polymorph are given in table 4.1. No detailed structure study of the high temperature polymorph could be found.

Phase transitions in Li_3VO_4 were studied in detail by West and Glasser [135]. The low temperature form (β) phase is stable up to ≈650°C. At this temperature it reversibly transforms to a transitional phase (T phase). β and T phases, both show different variants. The powder patterns of the T phases have close similarities to both γ and β polymorphs, but can not be classified as either of them. The T phase converts reversibly to γ_{II} at ≈750°C. γ_{II} can not be retained at room temperature and transforms to one of the transitional phases even at fast cooling rates. Li_3VO_4 finally melts at ≈1150°C [154]. At temperatures between 1050 and 1150°C, the presence of an unknown phase was evidenced, which is not related to any phase discussed [118].

Table 4.1. Atomic parameters in the refined structure of β_{II}-Li_3VO_4 [156].

Atom	*x*	y	z
Li(1)	0.2470(5)	0.3315(4)	0.9872(22)
Li(2)	0.5	0.8326(6)	0.9848(30)
V	0	0.82961(4)	0
O(1)	0.2239(2)	0.6804(2)	0.8931(2)
O(2)	0	0.1296(3)	0.8952(3)
O(3)	0.5	0.1736(3)	0.8478(3)

Pure Li_3VO_4 is classified as an ionic insulator as all Li-ions are used for building the structure; therefore, there is no partially occupied lithium site. Li_3PO_4-based materials are generally known to have higher conductivity in their high-temperature form [49].

However, Song et al [157] report a relatively high conductivity ($\approx 10^{-9}$ Scm^{-1}) in β-Li$_3$VO$_4$ at room temperature. The surprising high room-temperature conductivity value for insulating β-phase was questioned [158] and recently suggested to be due to the effect of humidity [159]. Several studies have been made on Li-ion conductivity in solid solutions based on γ structures. In most cases, aliovalent doping of cations was employed to create Li$^+$ ion vacancies/interstitials; however, solid solutions that led to Li-ion vacancies appear to be less conductive [114]. One example of aliovalent doping of Li$_3$VO$_4$ is the solid solution between Li$_3$VO$_4$ and Li$_4$MO$_4$ (M=Ge, Si), with Li$_{(3+X)}$V$_{(1-X)}$M$_X$O$_4$ general formula and conductivity in the range of $\approx 10^{-5}$ Scm^{-1} at room temperature [128, 155, 160, 161], which places it amongst the best Li$^+$-ion conductors and has been used as a high-temperature thermal battery solid electrolyte [145].

Lithium vanadium oxides have been investigated as an electrode material for batteries due to their attractive characteristics such as high specific energy, good rate capacity and reasonable cycle stability [119, 120]. Very recently Li$_3$VO$_4$ was studied and reported as a promising insertion anode material for lithium ion batteries with a large reversible specific capacity (≈ 323 mAh/g), a low and safe discharge voltage (≈ 0.75 V Vs. Li/Li$^+$ in average) and an acceptable cycling stability [16].

In the previous chapter, nitrogen doping of Li$_3$PO$_4$ was investigated and improvement in the ionic conductivity by an interstitial defect mechanism was evidenced. In this chapter the possible formation of crystalline lithium vanadium oxynitride, based on an interstitial defect mechanism is studied; structure, composition and electrical properties of solid solutions, based on Li$_{3+X}$VO$_{4-X}$N$_X$ ($0 \leq X \leq 0.6$) formula, is investigated. Electrochemical performances of Li$_3$VO$_4$ and Li$_{3.4}$VO$_{3.6}$N$_{0.4}$ are also compared and discussed in this chapter.

Results and discussion

X-ray diffraction

Li$_3$VO$_4$ was prepared by mixing and grinding appropriate amounts of Li$_2$CO$_3$ and V$_2$O$_5$ and heating the mixture initially at 650°C and then 850°C for 10 hours. The X-ray diffraction pattern of Li$_3$VO$_4$ is shown in figure 4.2. All peaks correspond well to ICDD card [38-1247] and match with β$_{II}$-Li$_3$VO$_4$ reported by Shannon et al [156]. Cell parameters were determined using a high-resolution powder diffractometer. All peaks in

the XRD pattern can be indexed orthorhombic with $Pmn2_1$ (#31) symmetry within errors (table 4.2). A range of nitrogen-doped compositions (5%-15% of oxygen substituted by nitrogen) was made by mixing appropriate amounts of Li_2CO_3, V_2O_5 and Li_3N, as described in the experimental chapter. XRD patterns of $Li_{3.2}VO_{3.8}N_{0.2}$, $Li_{3.4}VO_{3.6}N_{0.4}$ and $Li_{3.6}VO_{3.4}N_{0.6}$ correspond well to the Li_3VO_4 peaks (figure 4.2) and can be indexed as orthorhombic with $Pmn2_1$ (#31) symmetry within good errors. X-ray diffraction data of $Li_{3.4}VO_{3.6}N_{0.4}$ are listed in table 4.2.
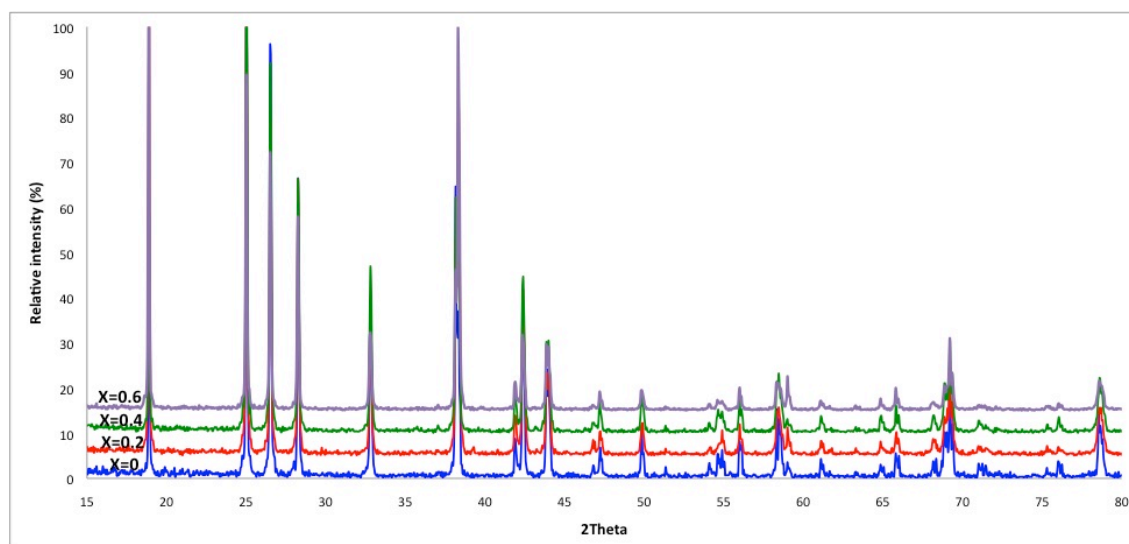
Figure 4.2. XRD profiles of $Li_{(3+X)}VO_{(4-X)}N_X$ (Co Kα$_1$ radiation).

The lattice constants and volume of Li_3VO_4 and LiVONs are calculated and listed in Table 4.3 and compared with the literature. There is a good agreement between the cell parameters of synthesised Li_3VO_4 and $β_{II}$-Li_3VO_4 reported by Shannon et al [156]. The cell volume of the nitrogen-doped samples increases compared to that of Li_3VO_4. Figure 4.3 illustrates cell parameter variation with X. The expansion of the unit cell volume is considerable with X=0.2, but stays more or less unchanged with X>0.2. This may suggest that the solid solution limit is around X=0.2.

Table 4.2. X-ray diffraction data of Li_3VO_4 and $Li_{3.4}VO_{3.6}N_{0.4}$ (Cu $K\alpha_1$ radiation).

Li_3VO_4

d observed (Å)	d calculated (Å)	$\Delta 2\theta°$ (obs-cal)	Intensity	$h\ k\ l$
5.4377	5.4444	0.0212	14.6	0 1 0
4.1225	4.1259	0.0181	66.3	1 1 0
3.8929	3.8948	0.0112	100.0	1 0 1
3.6578	3.6600	0.0145	47.3	0 1 1
3.1630	3.1619	-0.0100	34.2	2 0 0
2.7327	2.7342	0.0192	42.4	2 1 0
2.7214	2.7222	0.0104	14.7	0 2 0
2.5004	2.5004	-0.0002	3.3	1 2 0
2.4719	2.4719	-0.0005	50.4	0 0 2
2.3916	2.3927	0.0170	21.7	2 1 1
2.3840	2.3846	0.0095	6.6	0 2 1
2.2301	2.2312	0.0208	5.3	1 2 1
2.1204	2.1204	0.0006	11.8	1 1 2
1.9653	1.9657	0.0095	3.6	3 1 0
1.9474	1.9474	-0.0013	5.9	2 0 2
1.9388	1.9390	0.0057	6.2	3 0 1
1.9037	1.9039	0.0050	8.6	2 2 1
1.8329	1.8336	0.0215	16.1	2 1 2

$Li_{3.4}VO_{3.6}N_{0.4}$

d observed (Å)	d calculated (Å)	$\Delta 2\theta°$ (obs-cal)	Intensity	$h\ k\ l$
5.4457	5.4476	0.0057	22.6	0 1 0
4.1281	4.1282	0.0005	75.5	1 1 0
3.8978	3.8980	0.0012	100.0	1 0 1
3.6628	3.6630	0.0010	50.6	0 1 1
3.1663	3.1635	-0.0254	36.2	2 0 0
2.7348	2.7357	0.0112	48.4	2 1 0
2.7233	2.7238	0.0062	15.3	0 2 0
2.5020	2.5018	-0.0024	4.8	1 2 0
2.4747	2.4743	-0.0064	53.7	0 0 2
2.3928	2.3942	0.0228	32.2	2 1 1
2.3872	2.3865	-0.0123	12.1	0 2 1
2.2323	2.2327	0.0074	5.1	1 2 1
2.1220	2.1223	0.0056	8.8	1 1 2
1.9667	1.9668	0.0020	4.1	3 1 0
1.9495	1.9490	-0.0134	5.1	2 0 2
1.9407	1.9402	-0.0139	5.5	3 0 1
1.9055	1.9050	-0.0126	8.0	2 2 1
1.8346	1.8351	0.0132	14.2	2 1 2

Table 4.3. X-ray diffraction data of Li₃VO₄ and LiVONs.

	a(Å)	b(Å)	c(Å)	V(Å)	Space group
Li_3VO_4	6.3237(6)	5.4444(6)	4.9437(6)	170.207(23)	*P m n 2₁*
$Li_3VO_4 (\beta_{II})$ [156]	6.3259(12)	5.4460(8)	4.9469(9)	170.42	*P m n 2₁*
$Li_{3.2}VO_{3.8}N_{0.2}$	6.3271(7)	5.4476(8)	4.9487(6)	170.57 (3)	*P m n 2₁*
$Li_{3.4}VO_{3.6}N_{0.4}$	6.3271(5)	5.4484(5)	4.9485(5)	170.590(20)	*P m n 2₁*
$Li_{3.6}PO_{3.4}N_{0.6}$	6.3263(6)	5.4464(6)	4.9480(5)	170.486(25)	*P m n 2₁*
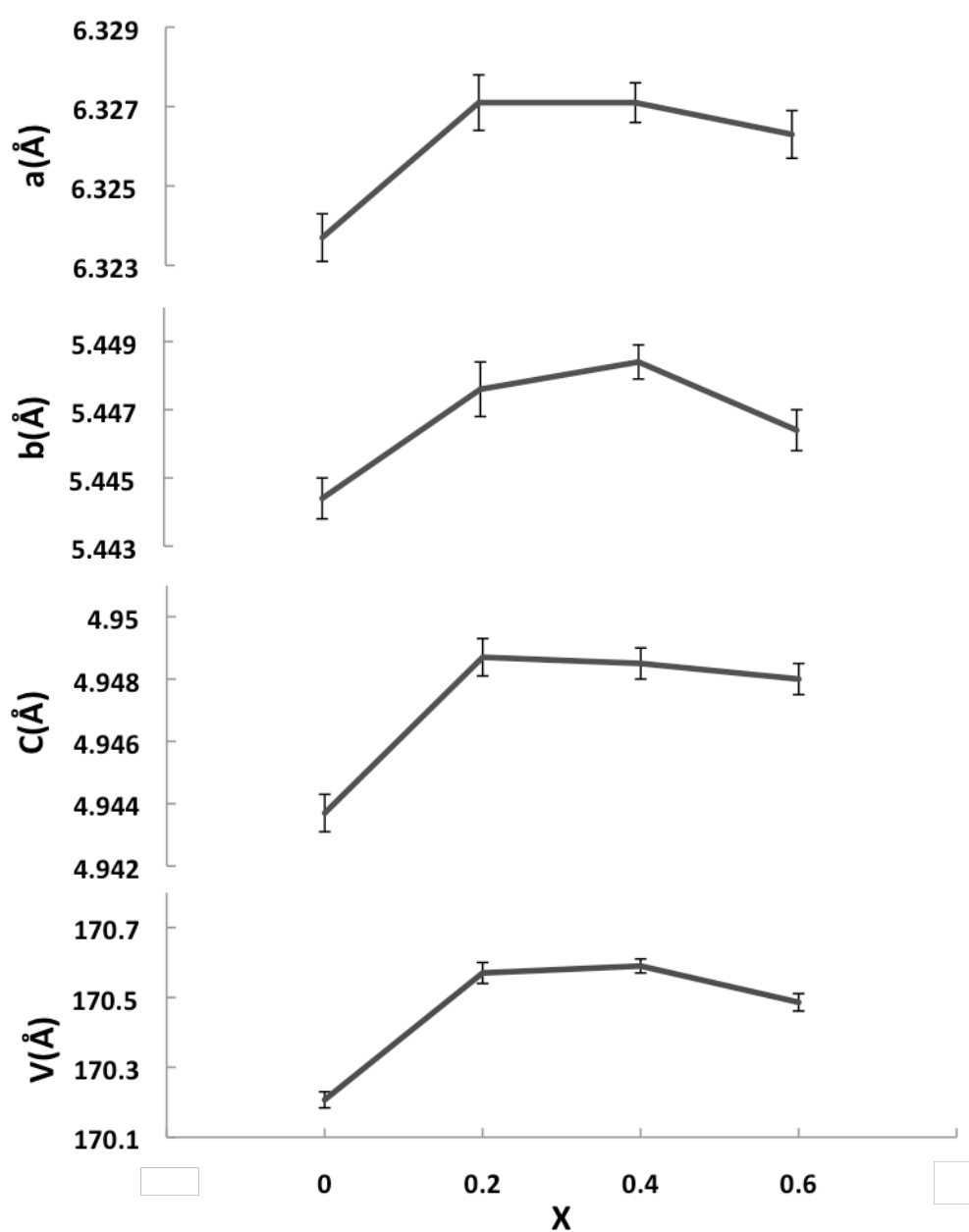
Figure 4.3. Change in unit cell parameters of $Li_{(3+X)}VO_{(4-X)}N_X$ with increasing X.

Impedance Spectroscopy

Conductivity measurements were conducted on Li_3VO_4 and its nitrogen-doped analogues. Ceramics were too resistive to be measured by IS at room temperature and temperatures in excess of 200°C were required to obtain useful data. Figures 4.4 and 4.5 show typical IS data sets of Li_3VO_4 and nitrogen-doped Li_3VO_4. The Z^* plots show a single, nearly ideal semicircle for all samples. The arc has an associated capacitance of ≈ 1.6, 0.2, 0.2 and 0.3 $pFcm^{-1}$ for Li_3VO_4, $Li_{3.2}VO_{3.8}N_{0.2}$, $Li_{3.4}VO_{3.6}N_{0.4}$ and $Li_{3.6}VO_{3.4}N_{0.6}$ respectively in good agreement with the high frequency plateaux in the $\log C'$ vs. $\log f$ plots, suggesting that the measurements are associated with the bulk response. The variation of capacitance data between Li_3VO_4 and its nitrogen-doped analogues is mainly because the data have not been corrected for different jig and cable contributions. Combined Z"/M" spectra show a single, Debye-like peak for both Z" and M" plots, with the peak maximum occurring at the same frequency; which indicates the electrical homogeneity of the samples with only a bulk response being measured. A low frequency dispersion in the Z" plot of N-doped samples may be associated with an electrode effect. The bulk resistance was obtained directly from the intercept of the impedance complex plane plot with the real axis (Z' axis).
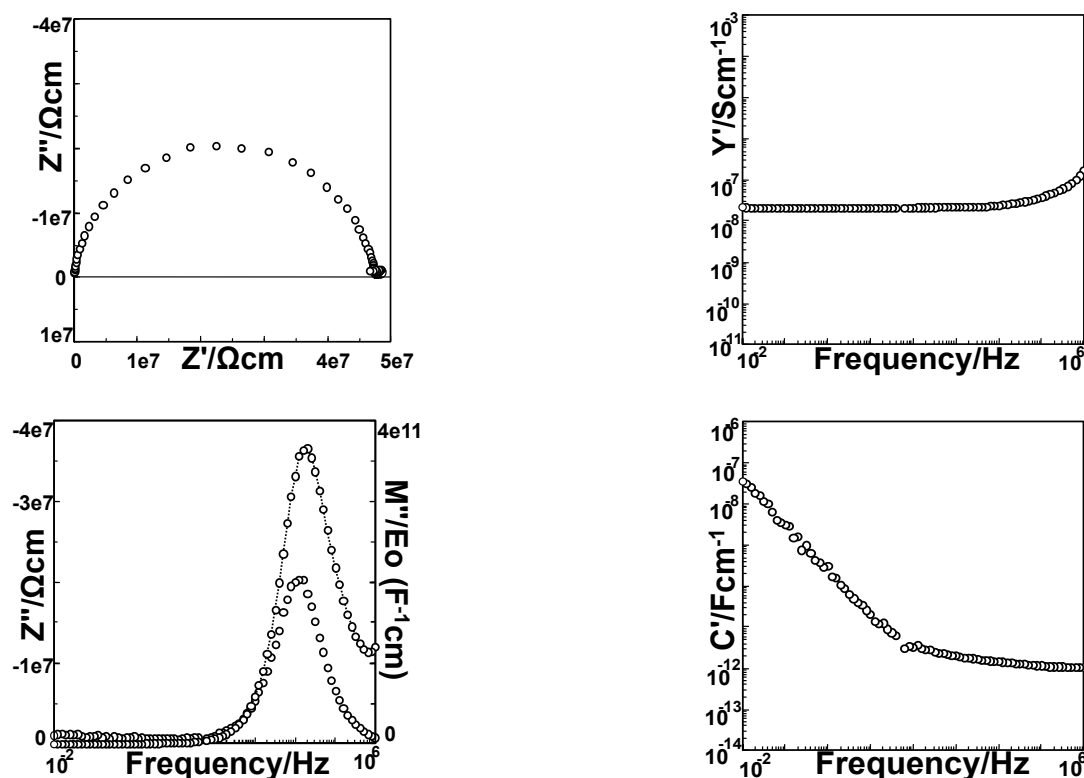
Figure 4.4. Impedance spectroscopy data of Li_3VO_4 at 332°C.
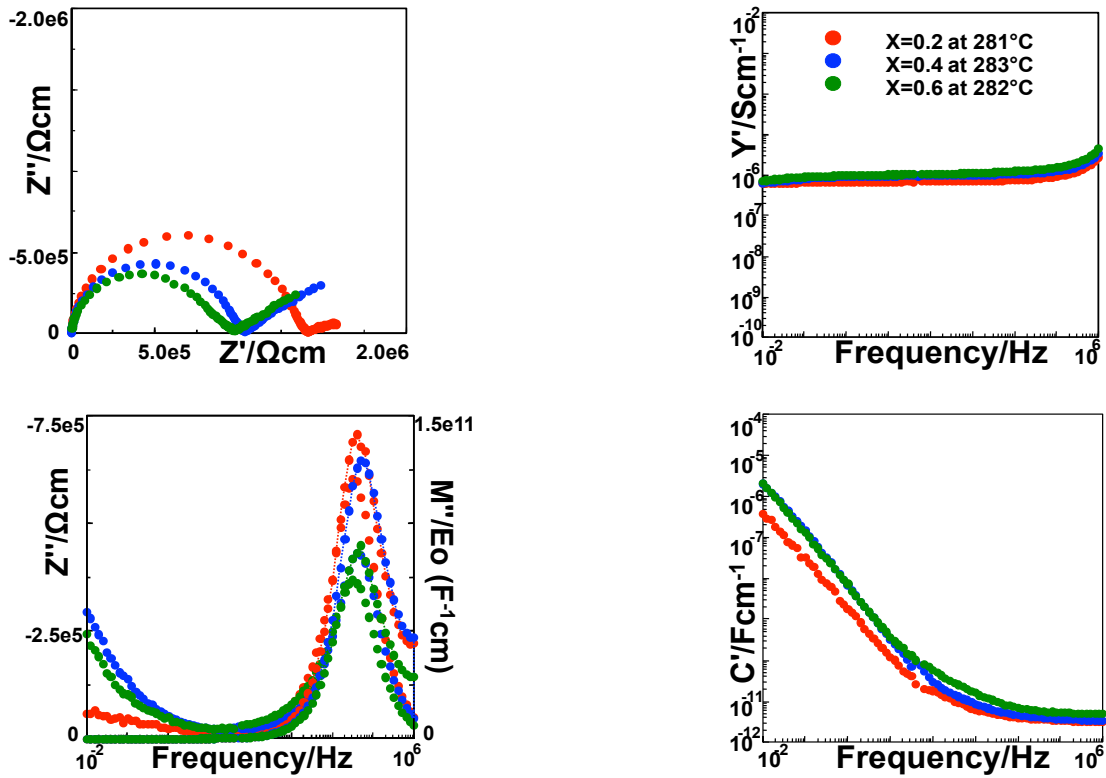
Figure 4.5. Impedance spectroscopy data of Li$_{(3+X)}$VO$_{(4-X)}$N$_X$.

Figure 4.6 illustrates the Z* plots of Li$_3$VO$_4$ and nitrogen-doped samples at different temperatures and their associated capacitance. In these results, a low frequency dispersion with a capacitance in the range of microfarads, which has the character of an inclined spike attributed to partial blocking of ionic charge carriers at the metal-sample interface, can be evidenced in samples with X=0.2 (above 330°C), 0.4 and 0.6. These can be signs of a typical ionic conductor.

Low frequency data in the Z* plots of Li$_3$VO$_4$ show a residual tail which collapses to become a broad, flat semicircle at temperatures above ≈350°C (Figure 4.7). The residual tail in these plots does not have the character of a blocking electrode. Associated capacitance of the residual tail however, shows capacitance values as high as 1 μFcm^{-1}, which could indicate the blocking of ionic charge carriers at the metal-sample interface. On the other hand, in the case of blocking electrodes, with capacitance in the range of μFcm^{-1} and frequency in the range of 0.01 Hz, then the impedance response should have Z" values of more than 1 MΩ (Z"=1/ωC [162]) resulting in a nearly vertical spike in Z* plots. This is not seen in the experimental Z" values and can not suggest that the
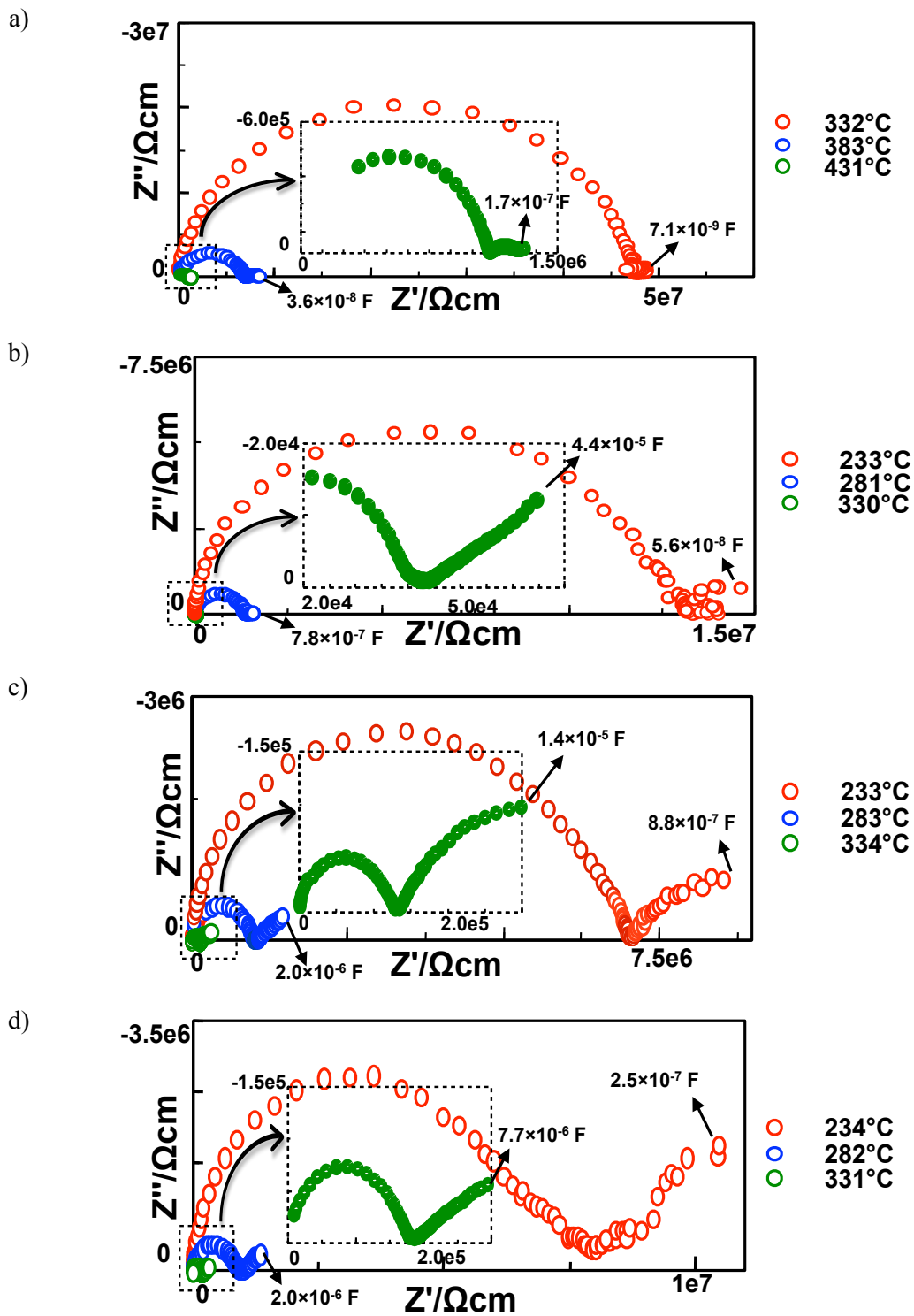
Figure 4.6. Z* plot of Li$_{(3+X)}$ VO$_{(4-X)}$ N$_X$ and the associated capacitance at different temperatures: a) X=0, b) X=0.2, c) X=0.4, d) X=0.6.

blockage of the ionic species has happened in Li_3VO_4. In this case, therefore, the conduction is primarily electronic. The capacitance dispersion could have happened as a result of electrode effects due to the surface roughness or porosity [163], which gave rise to a constant phase element (CPE) at low frequencies.
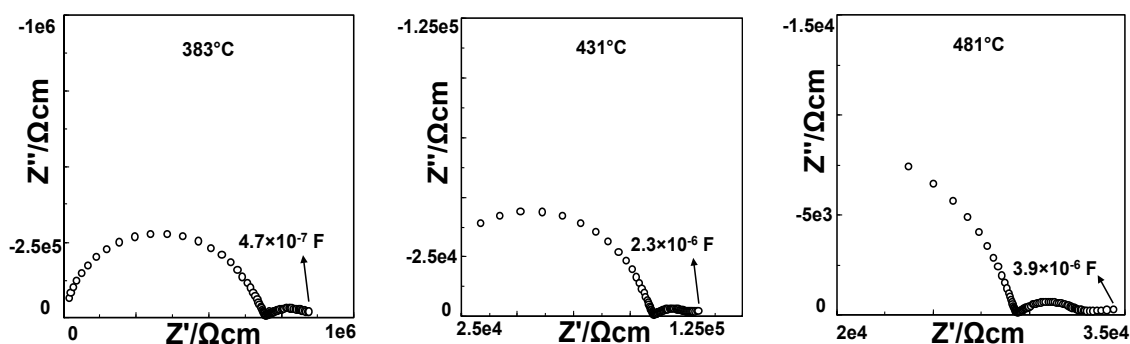
Figure 4.7. Z* plot of Li_3VO_4 at different temperatures.

The pellet conductivities were extracted from the intercept of the impedance complex plane plot with the Z' axis and after correction for the cell constant are plotted in Arrhenius format (figure 4.8). A linear Arrhenius behaviour was observed for X=0 at all temperatures and for X= 0.2, 0.4 and 0.6 below ≈350°C. Activation energies for conductivity of Li_3VO_4 and nitrogen-doped Li_3VO_4 were calculated from the linear part of the Arrhenius plots and compared with literature values (table 4.4). Conductivity data of Li_3VO_4 are slightly lower than the data reported in the literature; however, the activation energy is higher than that of reported by Guar et al [164]. The results indicate a decrease in the activation energy of N-doped samples compared to Li_3VO_4 below ≈350°C (from 1.29 to 1.00-1.02 eV). In these results, the conductivity of N-doped samples is about two orders of magnitude higher than that of Li_3VO_4 over the same temperature range.

Data for nitrogen-doped samples show deviation from linear regression above ≈350°C. Especially in X= 0.2 a sudden jump in conductivity can be seen followed by a drop in conductivity. This effect happens on a smaller scale for X= 0.4 and X= 0.6. The Z* plot of these samples (figure 4.9), illustrates a low frequency spike with an associated
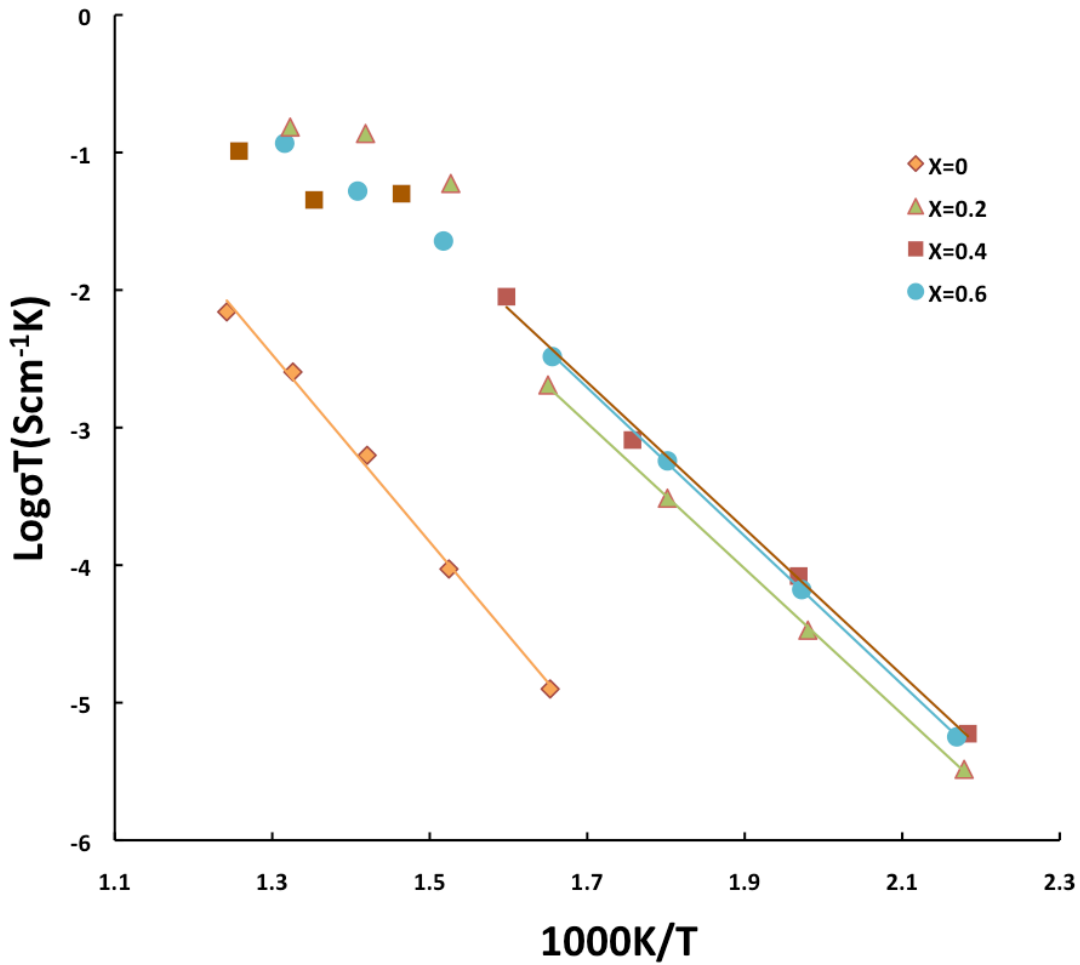
Figure 4.8. Arrhenius plots of conductivity of Li$_{(3+X)}$VO$_{(4-X)}$N$_X$ (N-doped samples showed linear Arrhenius behaviour only below ≈350°C).

Table 4.4. Activation energies (below 350°C) and conductivities.

	Activation Energy (eV)	Conductivity (Scm^{-1}) at T°C
Li$_3$VO$_4$	1.29	1.1×10^{-6}(431)
Li$_{3.2}$V$_{3.8}$N$_{0.2}$	1.00	4×10^{-4}(330)
Li$_{3.4}$V$_{3.6}$N$_{0.4}$	1.01	1.2×10^{-5}(334)
Li$_{3.6}$V$_{3.4}$N$_{0.6}$	1.02	3×10^{-5}(335)
Li$_3$VO$_4$ [157]		1.8×10^{-5}(600)
Li$_3$VO$_4$ [164]	0.98	8×10^{-6}(427)

capacitance in the range of electrochemical reactions ($\approx 10^{-4}$ Fcm^{-1}). The electrical conductivity of three oxynitride samples was studied as a function of temperature on a cooling cycle. The Arrhenius plots obtained on cooling and heating, are compared in figure 4.10 and are reversible at all temperatures except at temperatures that do not follow a linear Arrhenius behaviour, suggesting that either a reversible transformation has occurred or the suspected reaction does not affect the number of interstitial lithium ions and lithium channels.
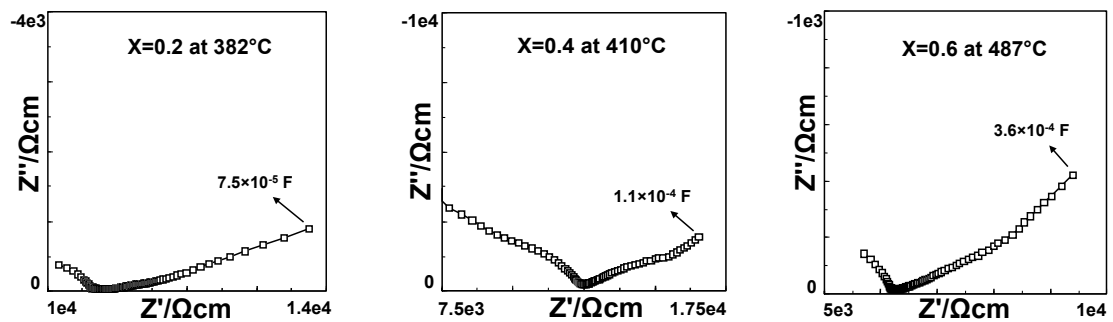
Figure 4.9. Z* plots of Li$_{(3+X)}$VO$_{(4-X)}$N$_X$ and their associated capacitance.
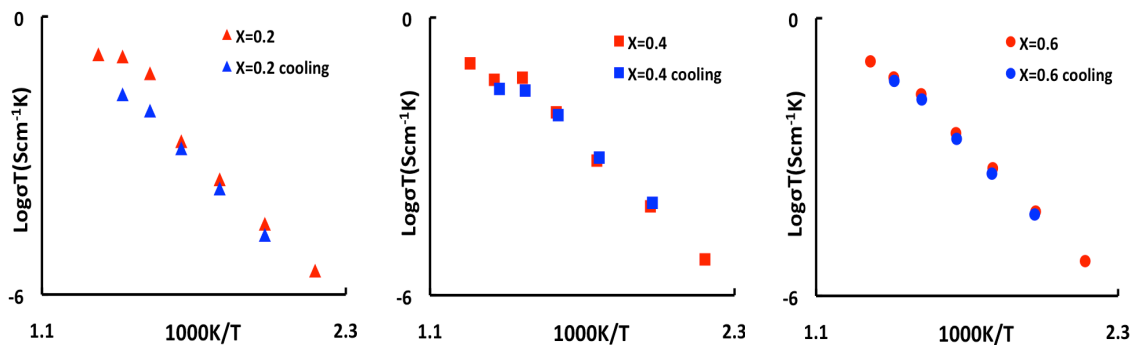
Figure 4.10. Arrhenius plots of conductivity of Li$_{(3+X)}$VO$_{(4-X)}$N$_X$ on heating and cooling.

The appearance of a second semicircle in the Z* plot of Li$_{3.2}$VO$_{3.8}$N$_{0.2}$ on cooling is attributed to the grain boundary response as the capacitance of the second semicircle is in the range of grain boundary response (figure 4.11). This may suggest that degradation of the sample has occurred to some extent. XRD results of Li$_{3.2}$VO$_{3.8}$N$_{0.2}$ after cooling indicates the presence of Li$_2$CO$_3$ as a secondary phase (figure 4.12). The conductivity of

Li_2CO_3 has been reported to be in the range 10^{-5} Scm^{-1} at $\approx300°C$ [165], Therefore it is reasonable to suggest that the grain boundary response belongs to Li_2CO_3. No sign of degradation was evidenced either in IS results as conductivity loss on cooling or in XRD results as the appearance of secondary peaks in both $Li_{3.4}VO_{3.6}N_{0.4}$ and $Li_{3.6}VO_{3.4}N_{0.6}$ samples.
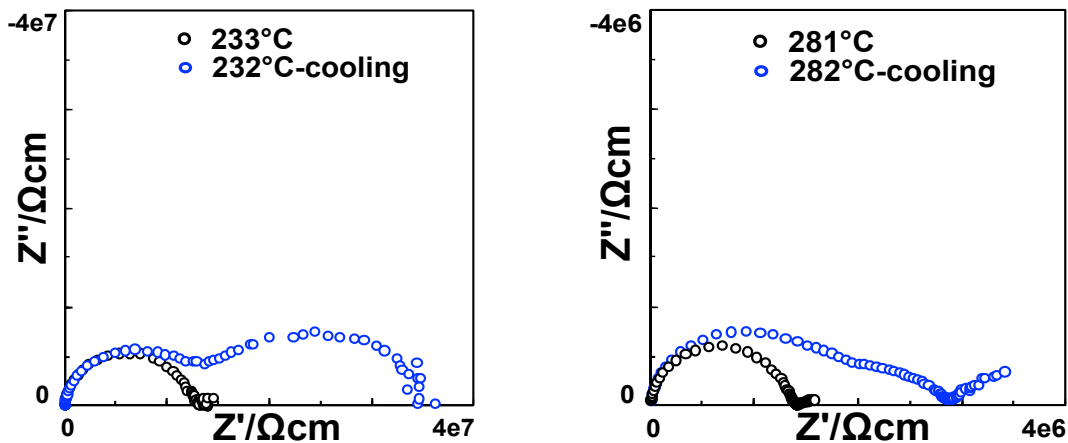
Figure 4.11. Z* plots of $Li_{3.2}VO_{3.8}N_{0.2}$ on heating and cooling.
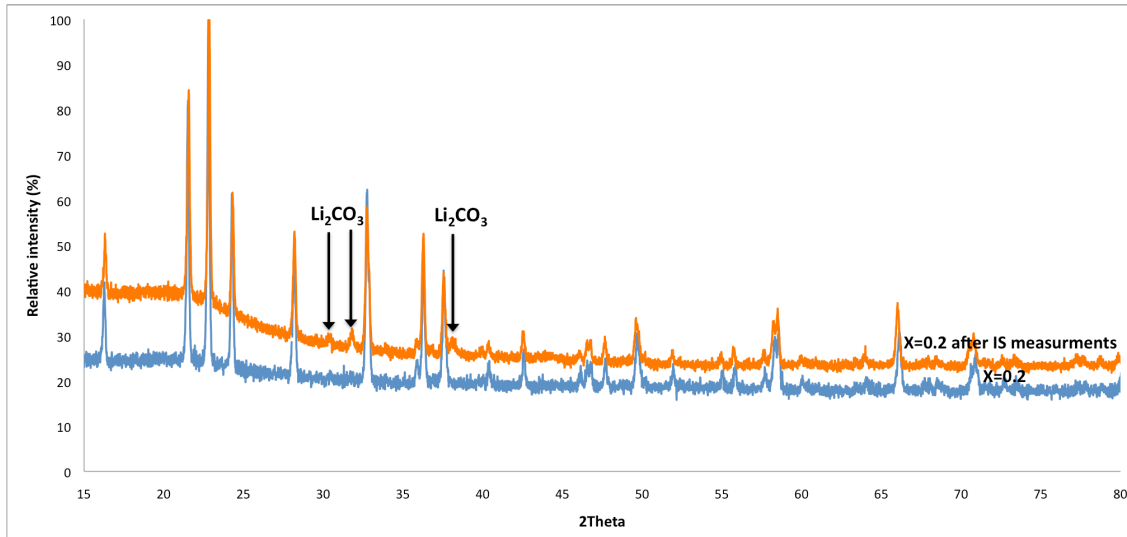
Figure 4.12. XRD profiles of $Li_{3.2}VO_{3.8}N_{0.2}$ before and after IS measurements (Cu $K\alpha_1$ radiation).

Figure 4.13 illustrates the DSC results of Li_3VO_4 and two nitrogen-doped samples in nitrogen atmosphere. The results show a sharp endotherm at $\approx415°C$ and a broader endothermic transition between $\approx420°C$ and $500°C$ for $Li_{3.6}VO_{3.4}N_{0.6}$ on heating. For $Li_{3.2}VO_{3.8}N_{0.2}$ however, only a broad peak can be seen between $\approx360°C$ and $490°C$,

which is probably made up of two separate broad peaks. No effect was seen on cooling of both N-doped samples, nor for Li_3VO_4 on either heating or cooling.
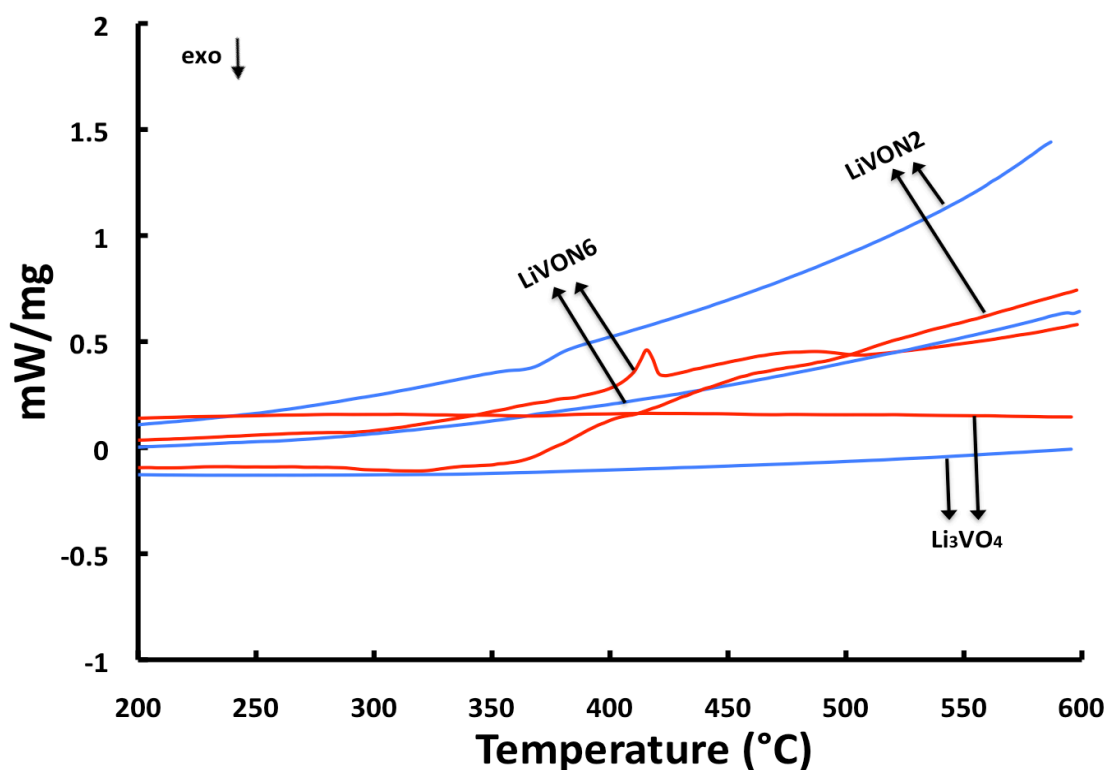
Figure 4.13. DSC results for Li_3VO_4, $Li_{3.2}VO_{3.8}N_{0.2}$ and $Li_{3.4}VO_{3.6}N_{0.4}$ on heating (red) and cooling (blue).

TGA results of Li_3VO_4 and two N-doped samples in nitrogen atmosphere are shown in figure 4.14. The results are affected by buoyancy; however, weight changes can be distinguished clearly. Low temperature weight loss (below ≈200°C) is attributed to the loss of absorbed humidity from the $Li_{3.6}VO_{3.4}N_{0.6}$ sample on heating (blue traces). At approximately 300°C, a prominent weight gain starts and is completed by ≈400°C in $Li_{3.6}VO_{3.4}N_{0.6}$, rapidly followed by a major weight loss between ≈400°C and 550°C. On cooling, $Li_{3.6}VO_{3.4}N_{0.6}$ gains weight again between approximately 400°C and 250°C. For $Li_{3.2}VO_{3.8}N_{0.2}$ (green traces), there is also a prominent weight gain between ≈300°C and 400°C; however, no weight loss occurred after these temperatures and the sample continued to gain weight after 400°C but at a lower rate, unlike $Li_{3.6}VO_{3.4}N_{0.6}$. On cooling, a slight weight gain can be observed between approximately 400°C and 300°C for both N-doped samples (more prominent in $Li_{3.2}VO_{3.8}N_{0.2}$). No major weight change was seen for Li_3VO_4 on either heating or cooling.
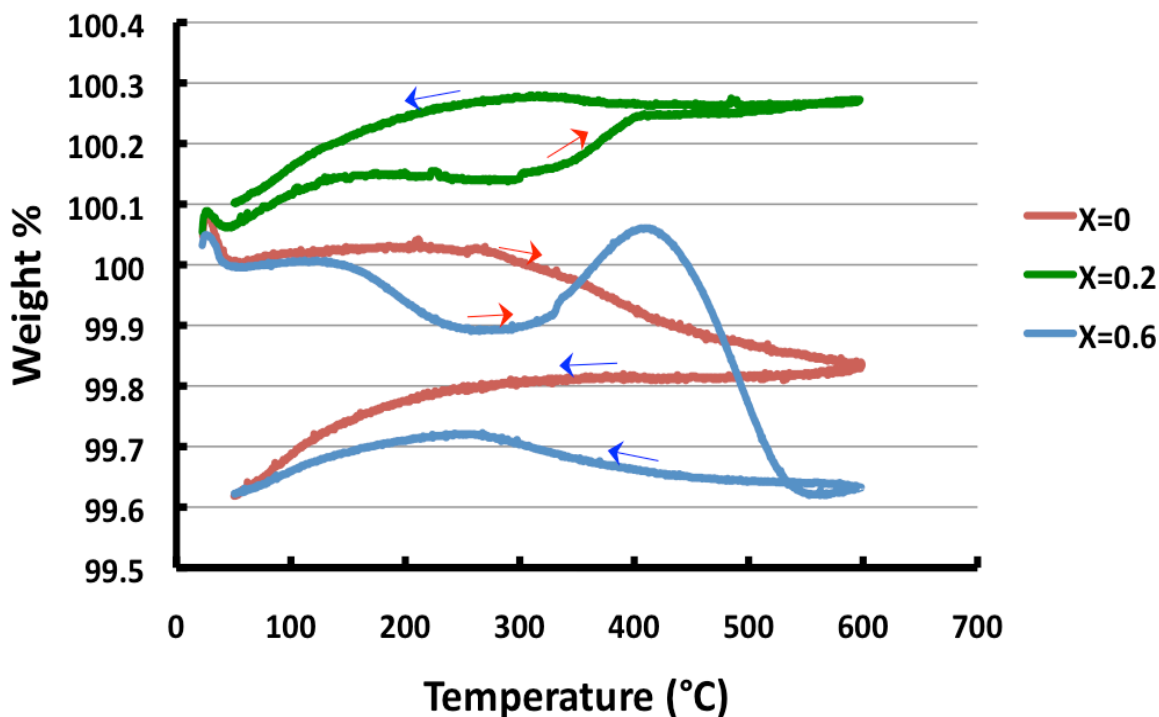
Figure 4.14. TGA results for $Li_{(3+X)}VO_{(4-X)}N_X$ on heating (red arrow) and cooling (blue arrow).

The TGA weight gain on heating must indicate chemical reaction of the nitrogen-doped sample with atmosphere. The reaction was also evidenced in both DSC and impedance data. Some of the effects in the TGA results however, were completely missed or only can be seen as broad peaks in DSC results.

Nitrogen-doped lithium vanadates and nitrogen-doped lithium phosphates seem to act similarly at high temperatures. In both of the cases a reversible reaction occurs (apart from the $Li_{3.2}VO_{3.8}N_{0.2}$ sample) and therefore, similar possible reactions can be proposed. There is first, reaction with oxygen and nitrogen loss on heating and the reverse reaction on cooling and second, H_2O absorption/loss and proton conductivity at high temperature. $Li_{3.2}VO_{3.8}N_{0.2}$ however, seems to react partly with CO_2 at high temperatures to make Li_2CO_3, which appeared in IS and XRD measurements on cooling.

Battery tests

Lithium vanadate and nitrogen-doped lithium vanadate battery performances as possible anode materials were compared using a Bio-Logic VMP device. Cells were

constructed as described in the experimental chapter and were cycled galvanostatically at C/20 in the potential range 0.5-4.5V. The theoretical cell capacities of Li_3VO_4 and $Li_{3.4}VO_{3.6}N_{0.4}$ were calculated as 197.4 mAh/g and 198.2 mAh/g, respectively, based on insertion/extraction of $1Li^+$, upon V^{4+}/V^{5+} redox reaction.

The typical galvanostatic discharge/charge of Li_3VO_4 and $Li_{3.4}VO_{3.6}N_{0.4}$ electrodes are presented in figure 4.15. Li_3VO_4 delivered a discharge/charge capacity of ≈ 35 mAh/g, which is about 18% of theoretical capacity and inserted/extracted $0.26Li^+$. The insertion of Li^+ occurs at approximately 0.8V against Li/Li^+. The extraction of lithium however, occurs in multiple stages with different potential plateaux. Mostly the plateaux end with a dramatic increase followed by a sharp drop in potential and the cell eventually fails afterwards. Electrode failure, in materials that are tested against a reference electrode, can be due to loss of active material (such as oxidation of electrode or surface film formation) or a rise in the impedance of the battery and decrease in the output voltage (such as material degradation or structural changes) [166-168]. In the present case, it seems that an increase in the internal impedance is the main reason for battery failure. This could be due to the poor conductivity (both electronic and ionic) of the active material, irreversible phase transformation during insertion/extraction of lithium ions and/or formation of minor cracks due to volume change caused by the phase transformation [98].

$Li_{3.4}VO_{3.6}N_{0.4}$ inserted $1Li^+$ and extracted $0.6Li^+$ on the first cycle to deliver a discharge capacity of ≈ 140 mAh/g and a charge capacity of 80 mAh/g (about 70% and 40% of theoretical capacity respectively). The difference in capacity on charge and discharge may be due to side reaction between electrode and electrolyte during the first discharge process. The insertion/extraction of Li^+ occurs approximately between 0.8 and 1.2V against Li/Li^+ ($\approx 0.8V$ in discharge and 1.2V in charge) and therefore $Li_{3.4}VO_{3.6}N_{0.4}$ can potentially be used as an anode. The voltage difference on charge and discharge can be a result of difference between electronic and ionic conductivity in Li_3VO_4 and $Li_{3.4}VO_{3.6}N_{0.4}$. Electronic conductivity in both of the compositions is quite low compared to the ionic conductivity, which may generate a polarisation resistance and cause the voltage gap [20].

a)

b)
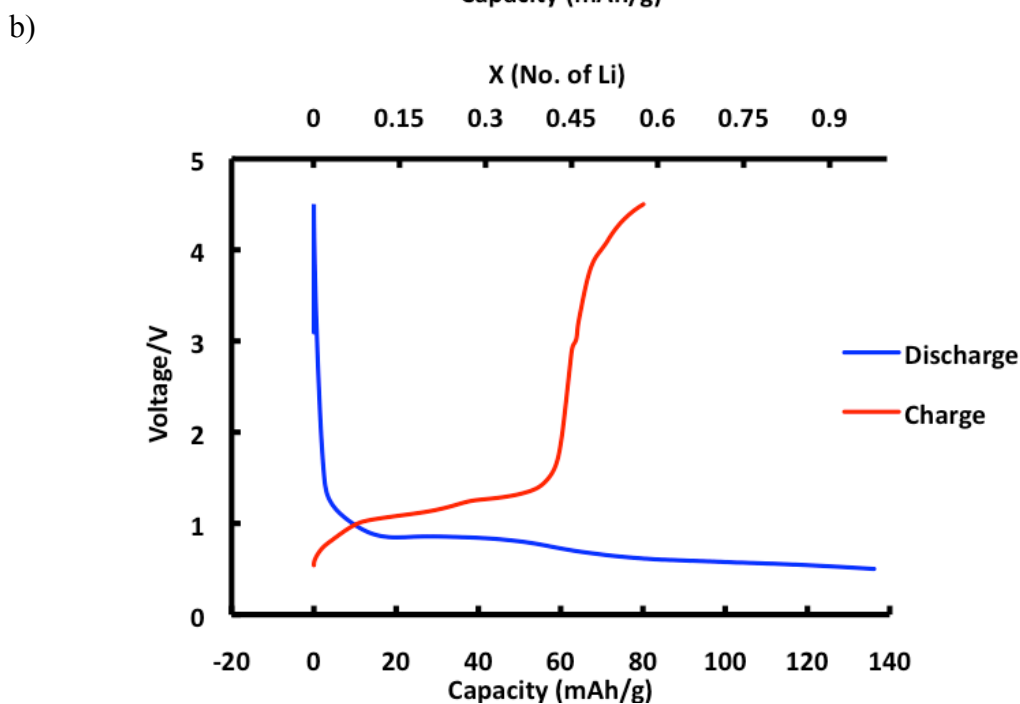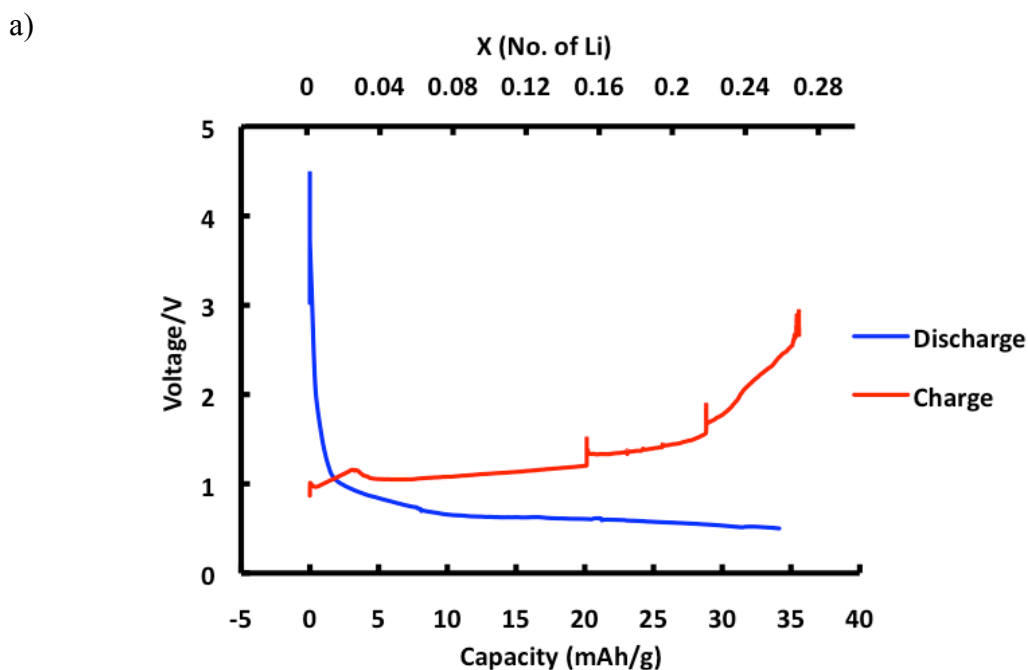
Figure 4.15. The first galvanostatic discharge/charge curve of a) Li$_3$VO$_4$ and b) Li$_{3.4}$VO$_{3.6}$N$_{0.4}$.

Capacity changes on cycling the Li$_{3.4}$VO$_{3.6}$N$_{0.4}$ cell are shown in figure 4.16. The initial capacity is lost during cycling. A reversible capacity of ≈20 mAh/g is obtained on subsequent cycles. The depth of discharge (the amount of capacity withdrawn compared to the total capacity available) and charging regime strongly influence the battery life [169]. Cell performances under a deep discharge/charge regime were the focus of this experiment. Cycling performances can be improved by using a less-deep discharge.
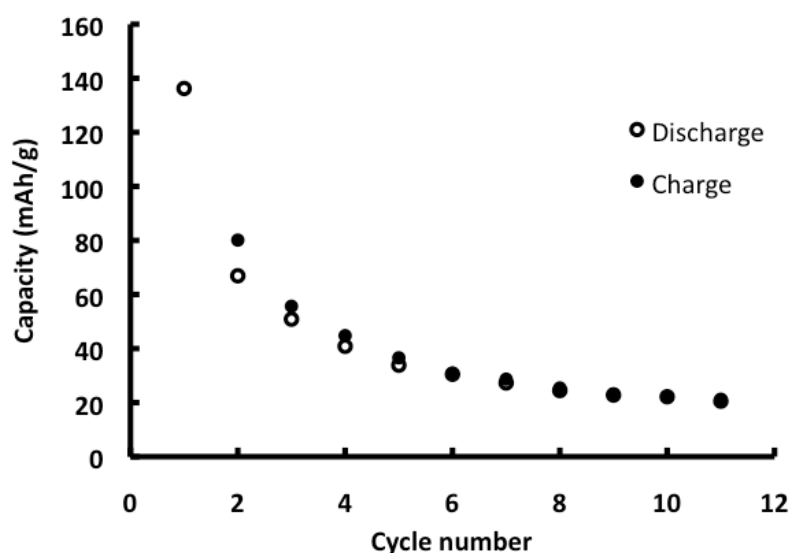
Figure 4.16. Capacity retention on charge and discharge of the $Li_{3.4}VO_{3.6}N_{0.4}$ cell.

Further improvement in battery performance can be expected by controlling discharge depth, reducing the particle size and using a narrower voltage range.

Combustion analysis

Table 4.5 shows combustion analysis results obtained at the AMG Analytical Services at Rotherham, compared with theoretical values of nitrogen in LiVO(N). The results indicate that the nitrogen content in nitrogen-doped samples is significantly lower than expected. In $Li_{3.2}VO_{3.8}N_{0.2}$ and $Li_{3.6}VO_{3.4}N_{0.6}$ for instance, $\approx 0.7\%$ and 2% of the targeted nitrogen could be found in the sample, respectively.

Table 4.5. Theoretical and experimental values of nitrogen in LiVO(N) samples determined by combustion analysis and their corrected formula.

	N(g) in 1(g) sample (Exp.)	N(g) in 1(g) sample (Theo.)	mol N (Exp.)	mol N (Theo.)	Corrected formula
Li_3VO_4	0.00009	0	0.00087	0	Li_3VO_4
$Li_{3.2}VO_{3.8}N_{0.2}$	0.00014	0.0204	0.0013	0.2	$Li_{3.0013}VO_{3.9987}N_{0.0013}$
$Li_{3.4}VO_{3.6}N_{0.4}$	0.00056	0.0406	0.0055	0.4	$Li_{3.0055}VO_{3.9945}N_{0.0055}$
$Li_{3.6}VO_{3.4}N_{0.6}$	0.00120	0.0605	0.011	0.6	$Li_{3.011}VO_{3.989}N_{0.011}$

It is possible that nitrogen-doping of Li_3VO_4 is impractical after all. It is also possible that smaller content of nitrogen than calculated is due to loss of nitrogen during synthesis. This theory looks more feasible when the result of nitrogen-doping of Li_3PO_4 and Li_3VO_4 is compared. In Li_3PO_4, where decomposition of raw materials starts from very low temperatures (diammonium phosphate starts decomposing at $\approx 140°C$), more incorporation of nitrogen into the structure was evidenced. In Li_3VO_4 however, decomposition of either V_2O_5 or Li_2CO_3 does not start till $\approx 600°C$. The loss of nitrogen therefore, can be due to the high temperature required for the solid-state reaction.

Figure 4.17 illustrates lattice parameter variation against the true nitrogen content
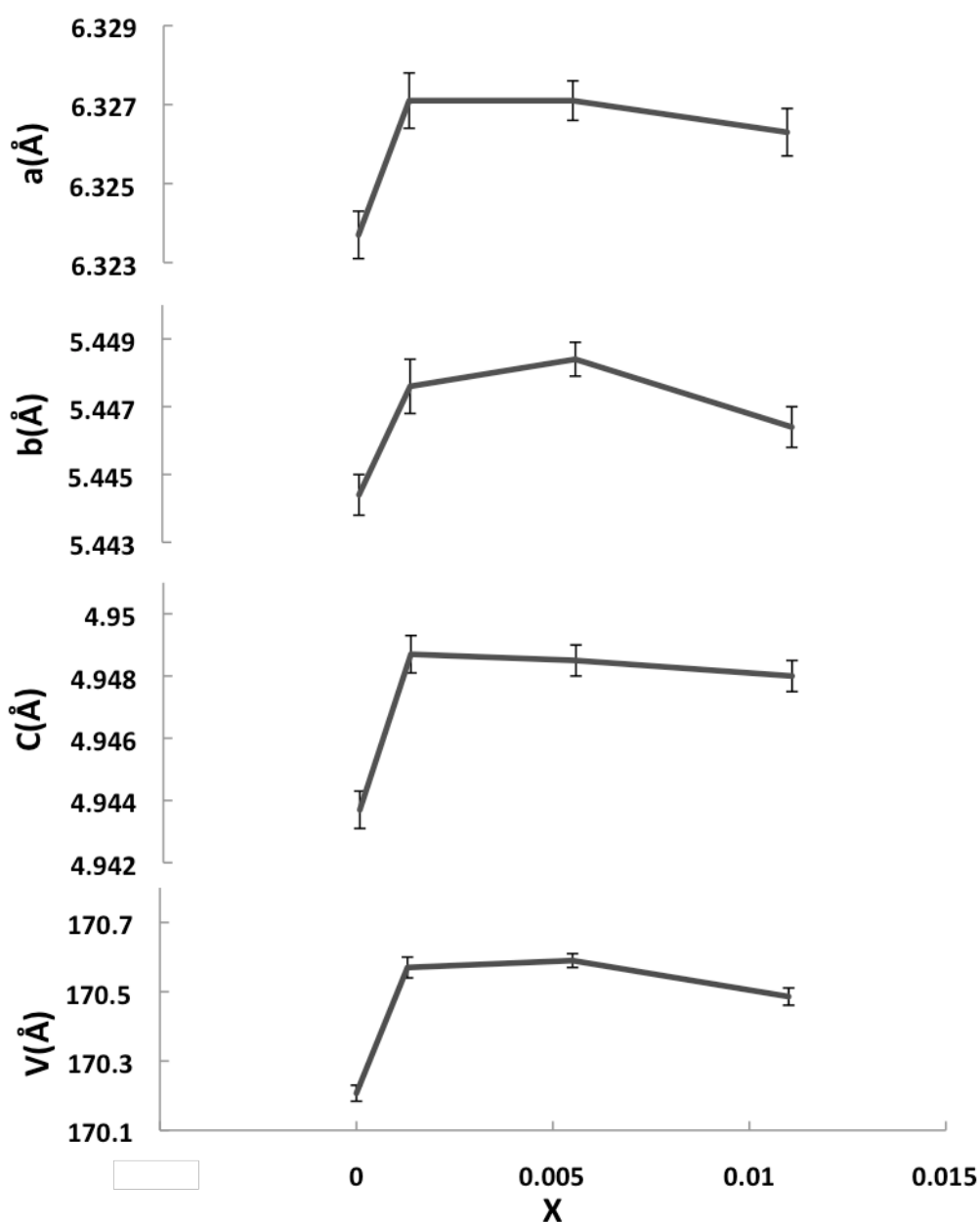
Figure 4.17. Change in unit cell parameters of $Li_{(3+X)}VO_{(4-X)}N_X$ with increasing X (X is corrected according to combustion analysis results).

that have been obtained from the combustion analysis. According to the XRD and combustion results, the overall nitrogen content can be estimated to be around 0.0013 mol, as the unit cell volume variation is considerable upon X=0.0013, but more or less unchanged on adding more nitrogen. More nitrogen that could be found in X=0.0055 and 0.011, is probably due to other nitrogen-containing products that perhaps skipped X-ray detection.

Conclusions

Ceramics with the $Li_{3+X}VO_{4-X}N_X$ (0≤X≤0.6) formula were prepared via a solid-state route and phase-pure samples were achieved in all compositions. X-ray diffraction patterns for all compositions matched with β_{II}-Li_3VO_4 and can be indexed as orthorhombic (*Pmn2₁*) symmetry. XRD results show increasing unit cell volume with increasing nitrogen content. This expansion was considerable for X=0.2 but unchanged with addition of more nitrogen, suggesting the solid solution limit is around X=0.2.

Electrical property studies indicate improvement of the ionic conductivity by about two orders of magnitude in N-doped compositions compared to undoped samples. In addition, the activation energy of conduction for N-doped compositions decreased dramatically below ≈350°C. Above this temperature, Arrhenius plots show fully reversible, nonlinear behaviour. IS/DSC/TGA results suggest that N-doped samples may have reacted with the atmosphere at elevated temperatures. Possible reaction between $Li_{3.2}VO_{3.8}N_{0.2}$ and CO_2 at high temperature was seen in XRD/IS data.

Battery tests were conducted in order to compare the electrochemical activity of lithium vanadate and its nitrogen-doped counterpart. $Li_{3.4}VO_{3.6}N_{0.4}$ inserted a substantial amount of lithium during the first cycle to deliver about 70% and 40% of theoretical capacity for discharge and charge respectively. Li_3VO_4 however, can deliver only about 18% of theoretical capacity on discharge/charge, probably due to high internal impedance of the cell.

The nitrogen contents were determined, using combustion analysis and the compositions were corrected accordingly. The result indicates the presence of nitrogen in the nitrogen-doped samples; however, nitrogen content is significantly lower than expected. Possible nitrogen-loss during the high-temperature synthesis is suggested.

Chapter 5

Preparation and characterisation of crystalline lithium zinc (magnesium) silicon oxynitride solid solutions

"Learn from yesterday, live for today, hope for tomorrow. The important thing is to not stop questioning."

— Albert Einstein

Introduction

Li_2ZnSiO_4

Li_2ZnSiO_4 is polymorphic and its polymorphs divide into two main groups, a low temperature form, β and a high temperature form γ, which are essentially isostructural with the low and high forms of Li_3PO_4. Both polymorphs belong to the family of
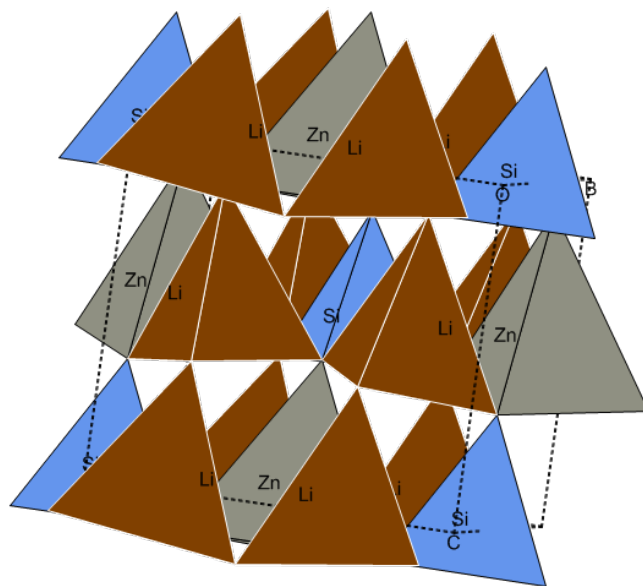
Figure 5.1. Schematic projection of β-Li_2ZnSiO_4.

tetrahedral structures [136], where oxide ions are packed into a distorted hexagonal close packed (hcp) array and cations occupy half of the tetrahedral interstices [170] (figure 5.1). The β and γ polymorphs vary mostly due to the different occupancies of tetrahedral sites and orientation of the resulting tetrahedra [142].

The β-γ transition occurs in both forward and reverse directions in Li_2ZnSiO_4, at $\approx 880°C$ [171]. Unlike Li_3PO_4, the transformation in the $\gamma \rightarrow \beta$ direction is a typical example of a nucleation and growth mechanism, where the rate of transition is slow initially, increases and passes through a maximum as it moves away from the equilibrium transformation temperature and then drops sharply until it is too slow to be observed [143, 171].

Figure 5.2 shows the phase relations in the binary system Li_4SiO_4-Zn_2SiO_4 and the large extent of solid solution that exists between these two orthosilicates. Li_2ZnSiO_4 (1:1 composition) forms a solid solution with Zn_2SiO_4 by replacing Li^+ with Zn^{2+} and creating cation vacancies ($Li_{(2-2X)}Zn_{(1+X)}SiO_4$) and with Li_4SiO_4 by replacing Zn^{2+} with Li^+ together with creation of lithium interstitials ($Li_{(2+2X)}Zn_{(1-X)}SiO_4$) [172]. The solid solution is most extensive for the γ polymorph and less extensive for β.

Figure 5.2. Phase equilibrium diagram for the system Li_4SiO_4-Zn_2SiO_4 [172].

Polymorphism is complex in Li_2ZnSiO_4 and structural variations exist within the low temperature and high temperature forms. Seven polymorphs can occur at the 1:1 composition (γ_{II}, γ_I, γ_0, β_{II}, $\beta_{II'}$, β_I, $\beta_{I'}$); only three exist in equilibrium and the rest are thermodynamically metastable [172, 173] (figure 5.3).
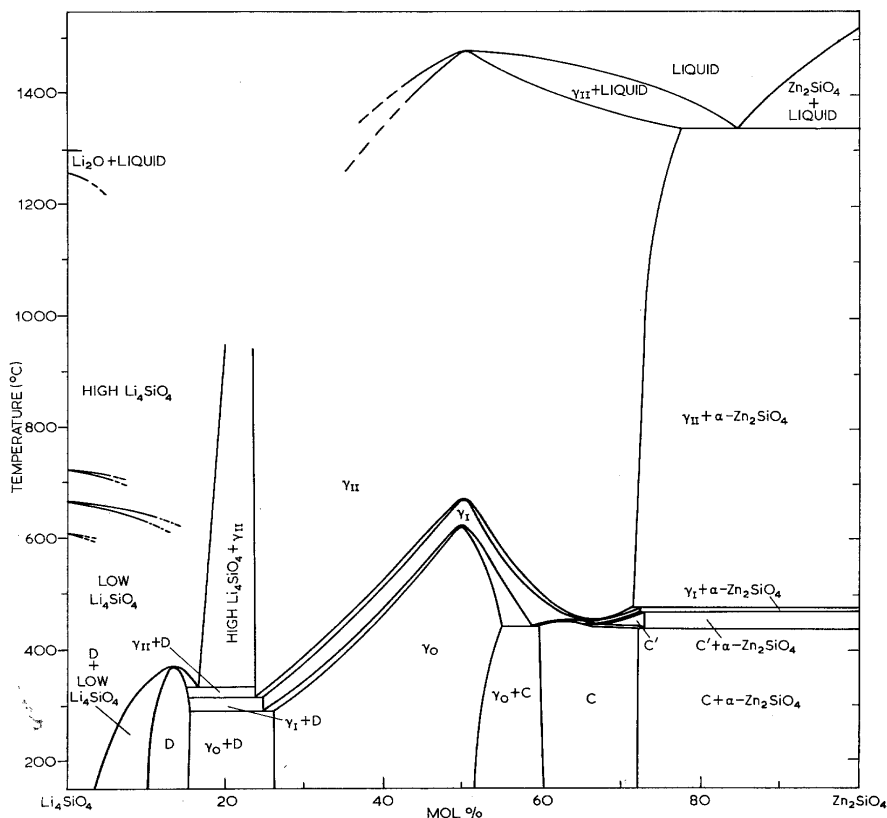
Figure 5.3. Phase non-equilibrium diagram for the system Li_4SiO_4-Zn_2SiO_4 (cooling rates ranging from 2 to 20°C/min) [173].

Both β and γ polymorphs are known to have orthorhombic symmetry; however, it was shown by West and Glasser [172, 173] that on cooling of the γ polymorph, the orthorhombic symmetry may not be retained at ambient temperatures, even with cooling rates faster than 20°C/min. This was shown by the appearance of an extra set of reflections in the powder pattern and a minor structural distortion that was indicated by slight splitting of some of the X-ray lines, which makes the low temperature form (γ_0) more likely to be monoclinic. Despite its polymorphic phase complexity, Li_2ZnSiO_4 is a stable phase. Therefore, upon heating and during the β→γ transformation (at ≈880°C), the composition remains the same until it melts at ≈1475°C [170, 172].

86

The transformation of phases can have a direct effect on the electrical properties of these orthosilicates. This was shown by a drop in conductivity that can reach nearly two orders of magnitude when the γ→β transformation occurs [173]. Conversion of one phase to another within a family however, can have a small impact.

A single crystal study on the lithium zinc silicate structure was performed by Yamaguchi et al [174]. A single crystal of γ-Li_2ZnSiO_4 was assigned to be monoclinic *$P2_1/n$* with *a=6.262(3), b=10.602(4), c=5.021(4) Å, β=90.51(5)°*, at room temperature (corresponding to the γ_0 polymorph). The structure and atomic coordinates are similar to the high temperature framework of Li_3PO_4 [137], with lithium occupying one of the 8-fold and one of the 4-fold tetrahedral sites and silicon and zinc each occupying a 4-fold tetrahedral site. The atomic positions are given in table 5.1 and compared with Zemann's proposed structure.

Table 5.1. Atomic parameters in the refined structure of lithium phosphate and lithium zinc silicate.

Atom	*x*	*y*	*z*	*Site*
Li_3PO_4 [137]				
Li(1)	0.005(21)	0.162	0.196	8d
Li(2)	0.25	0.078	0.804	4c
P	0.25	0.411	0.192	4c
O(1)	0.042	0.342	0.295	8d
O(2)	0.25	0.052	0.205	4c
O(3)	0.25	0.41	-0.125	4c
γ-Li_2ZnSiO_4 [174]				
Li(1)	-0.0088(19)	0.1603(12)	0.3033(12)	
Li(2)	0.2381(21)	0.0765(12)	0.7157(25)	
Zn	0.4986(1)	0.1647(1)	0.3095(1)	
Si	0.2474(3)	0.4124(2)	0.3135(3)	
O(1)	0.2484(8)	0.4092(4)	0.6378(9)	
O(2)	0.2551(7)	0.5564(3)	0.2072(9)	
O(3)	0.0329(7)	0.3414(4)	0.2033(9)	
O(4)	0.4596(7)	0.3387(4)	0.2094(9)	

Li₂MgSiO₄

Li$_2$MgSiO$_4$ is a member of the tetrahedral structure family and γ-Li$_2$MgSiO$_4$ is isostructural with γ-Li$_2$ZnSiO$_4$ (and with γ-Li$_3$PO$_4$) [175]. The Li$_4$SiO$_4$-Mg$_2$SiO$_4$ binary system was studied in detail by West and Glasser [175, 176]. Li$_2$MgSiO$_4$ forms a range of solid solution (γ$_{II}$) with Li$_4$SiO$_4$ (figure 5.4). No β phase has been obtained in this system under any cooling rates or hydrothermal conditions [118]. Instead, γ$_{II}$ transforms quickly to γ$_0$ at temperatures lower than 600°C. The inversion happens over a wide range of temperatures (shaded zone) and unlike the γ transformation in Li$_2$ZnSiO$_4$, there are no intermediate phases. At the lithia-rich part of the phase diagram, Li$_4$SiO$_4$ forms an extensive range of solid solutions, all of which are a superstructure of Li$_4$SiO$_4$. The solubility of Mg in Li$_4$SiO$_4$ is high in equilibrium conditions and can extend to over 25% Mg$_2$SiO$_4$ until reaching a two-phase region. A range of metastable polymorphs can also be produced under non-equilibrium conditions in this region, depending on the composition and cooling rate, all related to the Li$_4$SiO$_4$ structure. The solubility of Li in Mg$_2$SiO$_4$ is very low and therefore a large part of the Mg$_2$SiO$_4$-rich side of the diagram is a mixture of γ$_{II}$+Mg$_2$SiO$_4$ at high and γ$_0$+Mg$_2$SiO$_4$ at low temperatures. No additional metastable phases can be produced at these compositions.
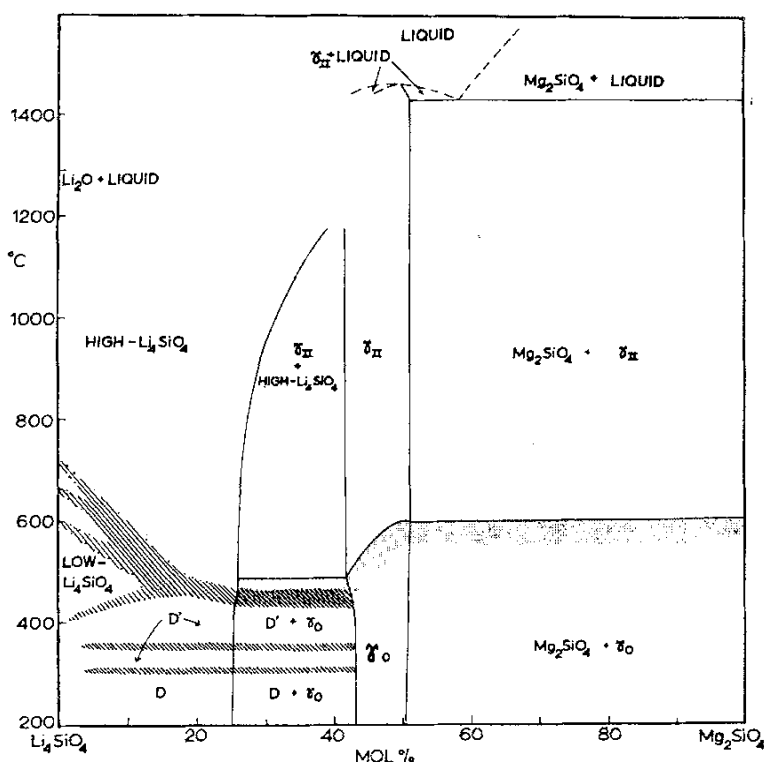
Figure 5.4. Phase equilibrium diagram for the system Li$_4$SiO$_4$-Mg$_2$SiO$_4$ [175].

88

The structure of Li_2MgSiO_4 was refined by neutron diffraction and was assigned to be monoclinic $P2_1/n$ with $a=6.300(0)$, $b=10.692(2)$, $c=4.995(5)$ Å, $\beta=90.47(1)°$, at room temperature and orthorhombic above 600°C [177]. Four independent tetrahedral sites exist at room temperature (table 5.2). One is occupied by Si, one by Mg and two by Li. No detailed information could be found on the structure of the high temperature polymorph.

The electrical properties of Li_2MgSiO_4 and Li_2ZnSiO_4 are comparable and both show very little ionic conductivity ($\approx 10^{-6}$ Scm^{-1} at $\approx 500°C$) [173, 176]. Electrical properties of the solid-solution system $Li_{(16-2X)}M_{(X)}(TO_4)_4$ (M=Zn, Mg and T=Ge, Si) were extensively studied by Hong et al [47] and led to the discovery of the so-called LISICON compound. Their conductivities can range between 0.5-2.2 Scm^{-1} at 400°C, although they show modest conductivities at room temperature. The high conductivity of these compositions is due to high concentration of mobile lithium ions that occupy interstitial sites, the suitable size of bottleneck that these ions must pass and weak Li-O bonds [47, 49, 75, 128]. It was also shown that substituting Mg and Si with Zn and Ge would increase the conductivity by enlarging the size of bottlenecks [47]. In other words, systems with the highest conductivity are generally those with largest unit cell volume [49].

Table 5.2. Atomic parameters in the refined structure of γ_0-Li_2MgSiO_4 [177].

Atom	x	y	z
Li(1)	-0.0050(21)	0.1595(10)	0.3072(21)
Li(2)	0.2370(19)	0.0740(9)	0.7155(21)
Mg	0.4967(7)	0.1645(4)	0.3075(8)
Si	0.2483(9)	0.4131(4)	0.3134(10)
O(1)	0.2459(6)	0.4087(3)	0.6429(6)
O(2)	0.2515(6)	0.5578(3)	0.2113(6)
O(3)	0.0334(5)	0.3411(3)	0.2034(7)
O(4)	0.4599(5)	0.3397(3)	0.2077(7)

In the previous chapters, nitrogen doping of Li_3MO_4 (M=P, V) was investigated, electrical properties were studied and an improvement in conductivity by an interstitial defect mechanism was seen. In this chapter, the possible formation of crystalline $Li_{(2+Y)}MSiO_{(4-Y)}N_Y$ (M=Zn,Mg) based on an interstitial defect mechanism is

investigated. Moreover, the composition, structure and electrical properties of these new phases are studied. In addition, Li-ion conductivity of N-doped Li_2ZnSiO_4 and $Li_{(2+2X)}Zn_{(1-X)}SiO_4$ is compared.

Results and discussion

X-ray diffraction

Li_2ZnSiO_4

The X-ray diffraction pattern of Li_2ZnSiO_4 is shown in figure 5.5. Our first attempt to make pure Li_2ZnSiO_4 by mixing appropriate amounts of ZnO, SiO_2 and Li_2CO_3 followed by reaction at 650°C and 1100°C, led to the presence of Li_2SiO_3 as a secondary phase (green traces). The phase mixture still remained after further grinding and heating at higher temperatures. A pure Li_2ZnSiO_4 was made by reaction between Li_4SiO_4 and Zn_2SiO_4 at 1100°C for 10 hours and cooling to room temperature at 5°C/min rate (blue traces). All peaks correspond well to the ICDD card [24-677] and match with γ_0-Li_2ZnSiO_4.
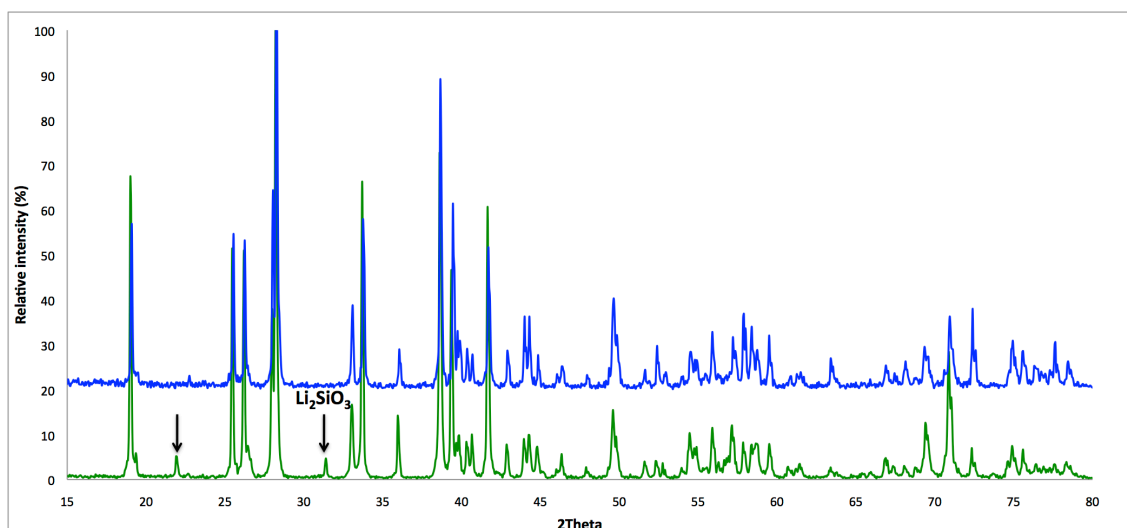
Figure 5.5. XRD profiles of Li_2ZnSiO_4, from ZnO, SiO_2 and Li_2CO_3 (green traces) and from Li_4SiO_4 and Zn_2SiO_4 (blue traces) respectively (Co Kα_1 radiation).

Slow cooling of the same composition with cooling rates < 2°C/min and annealing at 400°C led to the formation of the β polymorph (blue traces in figure 5.6). Despite

having fairly similar X-ray patterns, there are characteristic differences [170]. According to Villafuerte-Castrejon and West, the peaks with the Miller indices (101) and (002) are characteristic of these two phases. Even with several hours of annealing there are still some traces of the γ_0 polymorph detectable in the β X-ray pattern, suggesting the $\gamma \rightarrow \beta$ transformation has not been fully completed.
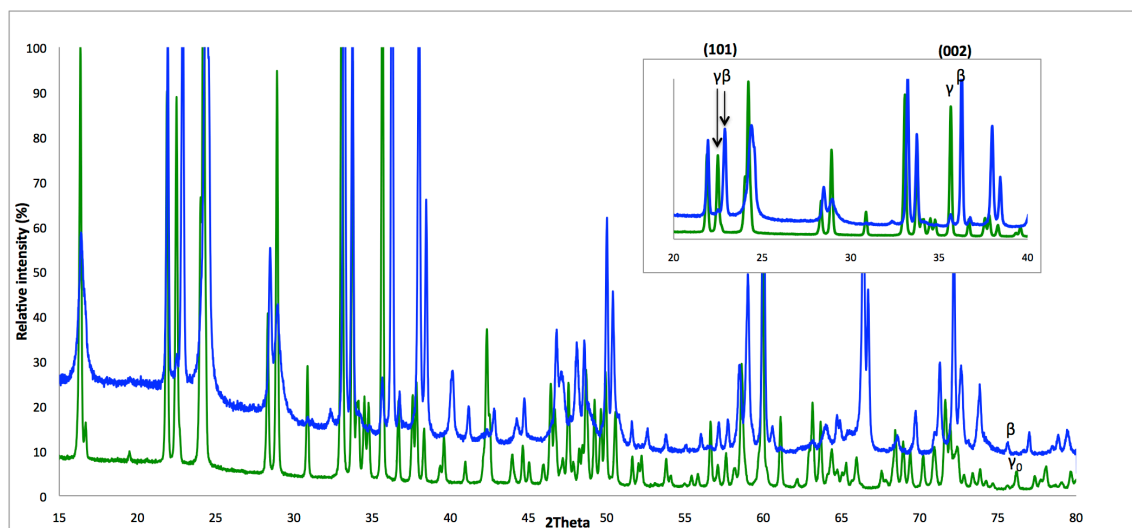
Figure 5.6. XRD profiles of γ_0 and β polymorph (Cu Kα_1 radiation).

The γ_0 and β polymorphs can be indexed as monoclinic $P2_1/n$ (♯14) and orthorhombic $Pmn2_1$ (♯31) respectively. The indexed diffraction data of the γ_0 polymorph are given in table 5.3. Cell parameters were determined for both polymorphs, compared with the previously reported data and are given in table 5.4. Cell parameters of the synthesised β and γ Li$_2$ZnSiO$_4$ are in a good agreement with the previously reported data.

Progressive increase in structural complexity was evidenced with cooling the high temperature form. It was seen that the orthorhombic symmetry of the γ_{II} polymorph can not be preserved at ambient temperatures at the 1:1 composition. This complexity was reported to be more significant in the lithium-rich part of the γ_{II} solid solution. Slow cooling or brief annealing of these compositions at lower temperatures produces more monoclinic distortion than is obtained by fast quenching of the same composition [173]. This was shown by the appearance of the new set of reflections and/or slight splitting of some of the XRD lines (introduced by minor structural distortion) upon cooling [172].

According to the phase diagram (figure 5.2 and 5.3), γ_0 is the resulting phase for compositions containing 25-35% Zn$_2$SiO$_4$ in equilibrium/non-equilibrium conditions.

This was corrected later by the authors [175], suggesting that lithia-γ_0 (distorted γ_0), is the equilibrium condition and the γ_0 phase is metastable at all compositions. Thus in figure 5.2, the γ_0 field, between 25-35% Zn_2SiO_4, should change to lithia-γ_0. It was also suggested that in the non-equilibrium diagram (figure 5.3), the γ_0 area should be divided to include a field of lithia-γ_0 at its lithia-rich end.

X-ray diffraction patterns of the compositions with 30% and 40% Zn_2SiO_4 (on the Li_4SiO_4-Zn_2SiO_4 phase diagram) are shown in figure 5.7 and compared with Li_2ZnSiO_4. $Li_{2.4}Zn_{0.8}SiO_4$ and $Li_{2.8}Zn_{0.6}SiO_4$ were made by reaction between ZnO, SiO_2 and Li_2CO_3 at 1100°C and cooling at 5°C/min rate. The XRD pattern indicates the formation of lithia-γ_0 phase, by appearance of some extra peaks in the area between ≈2.45-2.70 Å (≈39-42°, Co $K\alpha_1$ radiation). This new set of peaks does not correspond to any known secondary phase.
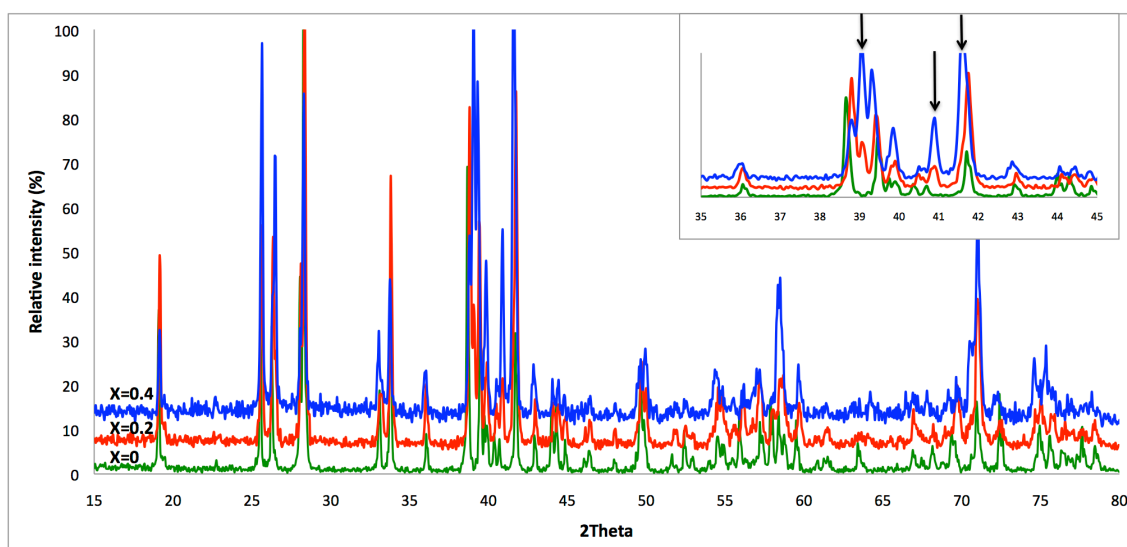
Figure 5.7. XRD profiles of $Li_{2+2X}Zn_{1-X}SiO_4$. Black arrows indicate peak alteration in samples with extra lithium (Co $K\alpha_1$ radiation).

Quenching and slow cooling of $Li_{2.4}Zn_{0.8}SiO_4$ and $Li_{2.8}Zn_{0.6}SiO_4$ however, leads to different results (figure 5.8 and 5.9). Quenching $Li_{2.4}Zn_{0.8}SiO_4$ (from 1100°C) results in the γ_0 polymorph (green traces in figure 5.8) and slow cooling with further annealing at 350°C leads to the γ_0+β polymorphs (blue traces), in agreement with the equilibrium/non-equilibrium phase diagram. In none of the above experiments was lithia-γ_0 obtained. Quenching of $Li_{2.8}Zn_{0.6}SiO_4$ (from 1100°C), leads to a phase whose X-ray pattern mainly corresponds to the γ_0 polymorph (with some slight differences from the γ_0 of the 1:1 composition) (green traces in figure 5.9) and can be indexed with

the same symmetry within good errors (cell parameters are given in table 5.4). In slow cooled samples however, lithia-γ_0 was obtained (blue traces). DSC experiments do not indicate any phase transformation for either composition even at low cooling/heating rates.
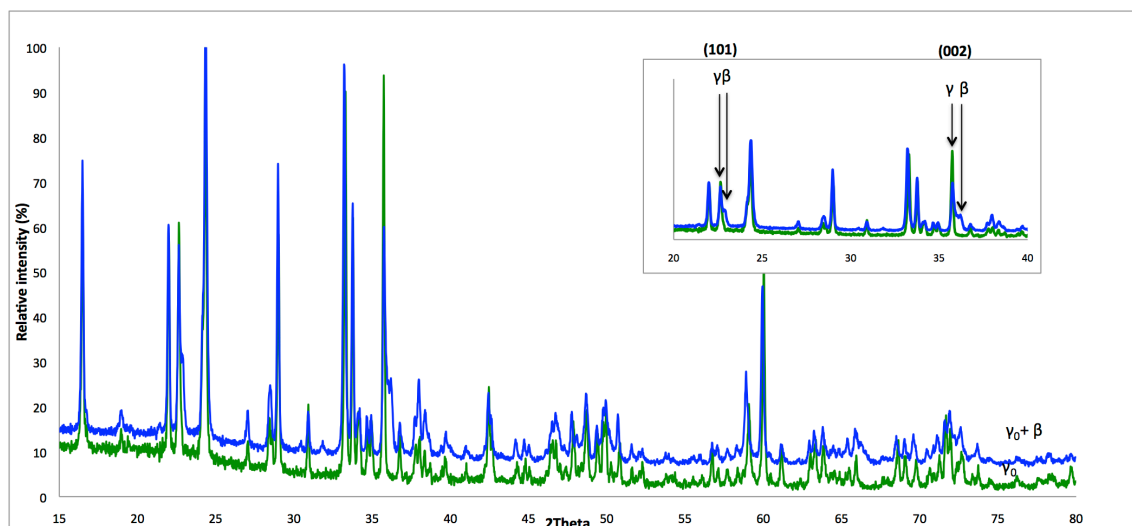
Figure 5.8. XRD profiles of Li$_{2.4}$Zn$_{0.8}$SiO$_4$ for quenched (green traces), and slow cooled and annealed (blue traces) samples (Cu Kα_1 radiation).
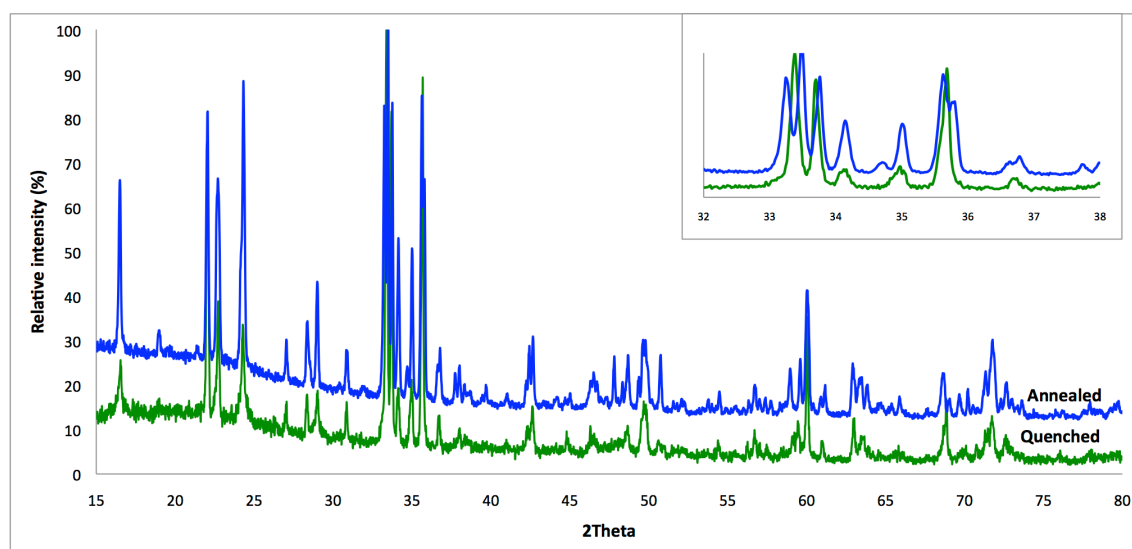
Figure 5.9. XRD profiles of Li$_{2.8}$Zn$_{0.6}$SiO$_4$ for quenched (green traces) and slow cooled and annealed (blue traces) samples (Cu Kα_1 radiation).

A range of nitrogen-doped compositions, with Li$_{2+Y}$ZnSiO$_{4-Y}$N$_Y$ formula, was made by mixing appropriate amounts of ZnO, SiO$_2$, Li$_2$CO$_3$ and Li$_3$N followed by reaction at 1050°C (2.5%-15% of oxygen substituted by nitrogen). The X-ray diffraction patterns

of these oxynitrides are shown in figure 5.10, and compared with the oxide parent. XRD patterns generally correspond well to the Li_2ZnSiO_4 peaks. The XRD pattern of $Li_{2.1}ZnSiO_{3.9}N_{0.1}$ is very similar to that of γ_0-Li_2ZnSiO_4. By adding more nitrogen, although the main peaks remain unchanged, some differences can be evidenced. The relative intensities of some of the X-ray reflections, for instance, altered markedly, which can be due to different cation distribution. In Y≥0.2, in particular, a new set of extra peaks can be seen between ≈2.45-2.70 Å (≈39-42°, Co $K\alpha_1$ radiation), which does not correspond to any known impurity, indicating the formation of lithia-γ_0 phase, similar to $Li_{2.4}Zn_{0.8}SiO_4$ and $Li_{2.8}Zn_{0.6}SiO_4$ samples. Despite attempts to make oxynitrides with more than 15% of nitrogen, phase mixtures were obtained.
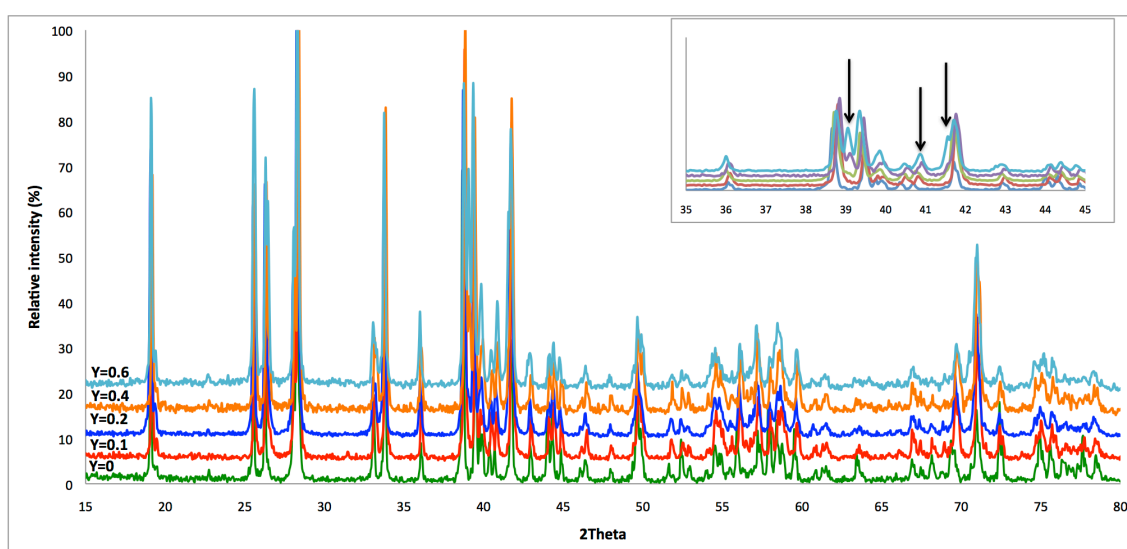
Figure 5.10. XRD profiles of $Li_{2+Y}ZnSiO_{4-Y}N_Y$. Black arrows indicate extra peaks in samples with nitrogen (Co $K\alpha_1$ radiation).

The main peaks in the XRD trace of oxynitride samples were indexed as monoclinic with *P2₁/n* symmetry. Indexed summaries are listed in table 5.3 and compared with Li_2ZnSiO_4. The XRD pattern of $Li_{2.1}ZnSiO_{3.9}N_{0.1}$ is similar to that of γ_0-Li_2ZnSiO_4 and can be indexed within good errors. Nitrogen doping of lithium zinc silicates tends to encourage monoclinicity by distorting γ_0 to lithia-γ_0 phase. In Y≥0.2, some of the XRD lines can not be indexed with the *P2₁/n* symmetry or can only be indexed with large errors. This is more evident in samples with high concentrations of nitrogen (Y=0.6), which causes them to probably have a different symmetry than the γ_0 polymorph. Despite that, the lattice constants of the N-doped compositions have been determined based on the monoclinic *P2₁/n* symmetry, listed in table 5.4 and compared with the result of Li_2ZnSiO_4 and Li-rich, lithium zinc silicates. Cell parameter variations in

$Li_{2+Y}ZnSiO_{4-Y}N_Y$ with increasing Y are presented in figure 5.11. The cell parameter variation is considerable, upon adding nitrogen, compared to the lithium phosphate (vanadate) cases. Cell volume decreases initially by adding nitrogen, while the γ_0 structure is maintained (Y=0.1). This is in accordance with the cell variation in $Li_{2.8}Zn_{0.6}SiO_4$, which has also the γ_0 form (table 5.4). Adding more nitrogen leads to a lithia-γ_0 phase and cell volume remains more or less unchanged (Y≥0.2). Due to the polymorphic transformation it is difficult to indicate the solid solution limit.

Table 5.3. X-ray diffraction data of Li$_2$ZnSiO$_4$ and N-doped Li$_2$ZnSiO$_4$ (Cu Kα_1 radiation).

Li$_2$ZnSiO$_4$ **Li$_{2.1}$ZnSiO$_{3.9}$N$_{0.1}$**

d observed (Å)	d calculated (Å)	$\Delta 2\theta°$ (obs-cal)	Intensity	$h\,k\,l$	d observed (Å)	d calculated (Å)	$\Delta 2\theta°$ (obs-cal)	Intensity	$h\,k\,l$
5.4133	5.4124	-0.0029	47.2	1 1 0	5.3986	5.3985	-0.0002	53.2	1 1 0
5.3043	5.3080	0.0118	3.0	0 2 0	5.3093	5.3142	0.0156	2.2	0 2 0
4.5454	4.5462	0.0033	3.0	0 1 1	4.5471	4.5454	-0.0074	2.9	0 1 1
4.0576	4.0570	-0.0032	40.7	1 2 0	4.0506	4.0531	0.0139	51.5	1 2 0
3.9465	3.9470	0.0028	52.7	-1 0 1	3.9362	3.9399	0.0214	56.2	-1 0 1
3.6981	3.6996	0.0094	33.3	-1 1 1	3.6942	3.6943	0.0004	28.7	-1 1 1
3.6683	3.6703	0.0133	100.0	1 1 1	3.6629	3.6649	0.0139	100.0	1 1 1
3.0841	3.0843	0.0013	49.7	1 3 0	3.0839	3.0840	0.0016	55.2	1 3 0
2.8943	2.8944	0.0006	12.5	0 3 1	2.8958	2.8961	0.0024	11.6	0 3 1
2.7059	2.7062	0.0037	74.5	2 2 0	2.6985	2.6993	0.0096	88.0	2 2 0
2.6539	2.6540	0.0010	42.5	0 4 0	2.6568	2.6570	0.0024	53.5	0 4 0
2.6340	2.6348	0.0111	6.1	-1 3 1	2.6275	2.6240	-0.0478	10.6	1 3 1
2.6245	2.6242	-0.0046	7.5	1 3 1	2.5896	2.5901	0.0063	9.4	-2 1 1
2.5965	2.5970	0.0074	9.3	-2 1 1	2.5692	2.5699	0.000	11.7	2 1 1
2.5769	2.5768	-0.0017	9.0	2 1 1	2.5137	2.5142	0.0070	78.2	0 0 2
2.5156	2.5154	-0.0027	94.0	0 0 2	2.4461	2.4467	0.0092	8.3	0 1 2
2.4477	2.4477	-0.0009	9.5	0 1 2	2.3858	2.3862	0.0073	9.1	-2 2 1
2.3907	2.3912	0.0078	9.8	-2 2 1	2.3702	2.3704	0.0035	12.5	2 2 1

Table 5.3. Continued

Li$_{2.4}$ZnSiO$_{3.6}$N$_{0.4}$

d observed (Å)	d calculated (Å)	Δ2θ° (obs-cal)	Intensity	h k l
5.4027	5.3977	-0.0152	68.0	1 1 0
4.0472	4.0532	0.0331	70.6	1 2 0
3.9404	3.9406	0.015	72.3	-1 0 1
3.6965	3.6982	0.0034	39.0	-1 1 1
3.6660	3.6650	-0.0071	100.0	1 1 1
3.0852	3.0844	-0.0081	60.6	1 3 0
2.8967	2.8973	0.0065	38.2	0 3 1
2.6991	2.6989	-0.0025	70.7	2 2 0
2.6776	--not indexed--		51.6	
2.6581	2.6576	-0.0072	68.9	0 4 0
2.6292	2.6245	0.0636	31.6	1 3 1
2.5903	2.5901	-0.0039	21.9	-2 1 1
2.5669	2.5694	0.0352	28.0	2 1 1
2.5155	2.5150	-0.0078	77.9	0 0 2
2.4474	2.4474	0.0001	28.3	0 1 2
2.3865	2.3863	-0.0040	19.4	-2 2 1
2.3701	2.3701	-0.0003	20.6	2 2 1
2.3495	2.3498	0.0053	18.0	0 4 1

Li$_{2.6}$ZnSiO$_{3.4}$N$_{0.6}$

d observed (Å)	d calculated (Å)	Δ2θ° (obs-cal)	Intensity	h k l
5.4030	5.3987	-0.0131	63.3	1 1 0
4.0520	4.0539	0.0105	55.8	1 2 0
3.9405	3.9406	0.0006	65.5	-1 0 1
3.6918	3.6950	0.0209	49.1	-1 1 1
3.6653	3.6659	0.0038	100.0	1 1 1
3.0850	3.0849	-0.0013	52.6	1 3 0
2.8978	2.8972	-0.0064	19.7	0 3 1
2.6994	2.6994	-0.0007	68.3	2 2 0
2.6817	--not indexed--		41.6	
2.6582	2.6580	-0.0072	46.8	0 4 0
2.6292	--not indexed--		20.5	
2.5907	2.5902	-0.0069	15.9	-2 1 1
2.5693	2.5702	0.0115	18.6	2 1 1
2.5154	2.5152	-0.0029	82.8	0 0 2
2.4475	2.4476	0.0027	15.1	0 1 2
2.3863	2.3864	0.0030	13.5	-2 2 1
2.3711	2.3707	-0.0052	14.8	2 2 1
2.3500	2.3501	0.0019	11.4	0 4 1

Table 5.4. X-ray diffraction data of LiZnSiO(N).

	a(Å)	b(Å)	c(Å)	β(°)	V(Å)	Space group
Li$_2$ZnSiO$_4$ (γ$_0$)	6.2917(6)	10.6160(7)	5.0314(3)	90.530(8)	336.03(4)	*P2$_1$/n*
Li$_2$ZnSiO$_4$ (γ$_0$) [174]	6.262(3)	10.602(4)	5.021(4)	90.51(5)		*P2$_1$/n*
Li$_2$ZnSiO$_4$ (β)	12.511(3)	10.6194(19)	4.9457(10)		657.08(16)	*Pmn2$_1$*
Li$_2$ZnSiO$_4$ (β) [172]	6.32	10.68	4.98			
Li$_{2.1}$ZnSiO$_{3.9}$N$_{0.1}$	6.2675(5)	10.6279(8)	5.0286(4)	90.531(7)	334.95(3)	*P2$_1$/n*
Li$_{2.2}$ZnSiO$_{3.8}$N$_{0.2}$	6.2700(5)	10.6285(8)	5.0287(5)	90.524(9)	335.10(4)	*P2$_1$/n*
Li$_{2.4}$ZnSiO$_{3.6}$N$_{0.4}$	6.2658(8)	10.6304(12)	5.0302(7)	90.543(12)	335.03(5)	*P2$_1$/n*
Li$_{2.6}$ZnSiO$_{3.4}$N$_{0.6}$	6.2670(6)	10.6322(10)	5.0306(6)	90.527(10)	335.18(4)	*P2$_1$/n*
Li$_{2.8}$Zn$_{0.6}$SiO$_4$ (γ$_0$)	6.262(5)	10.638(3)	5.025(3)	90.51(3)	334.78(5)	*P2$_1$/n*
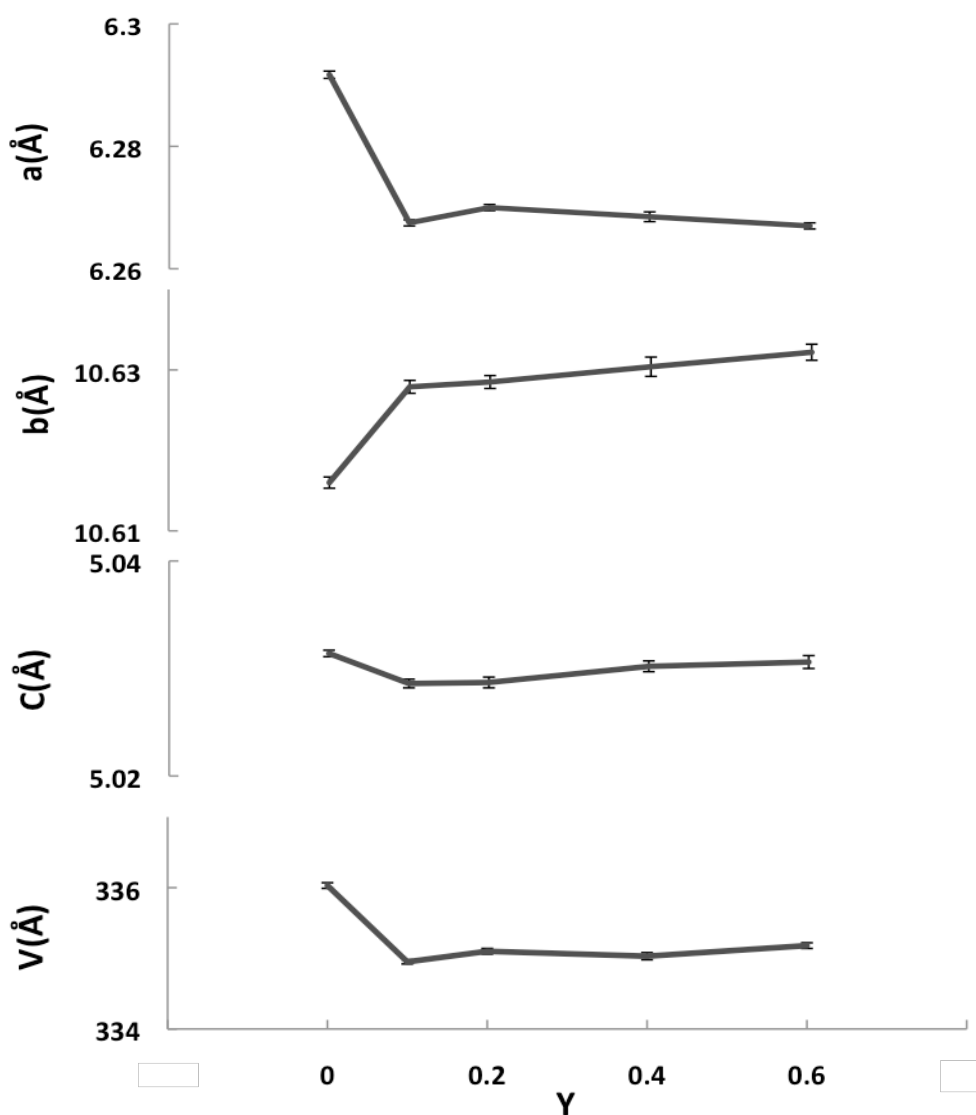
Figure 5.11. Change in unit cell parameters in Li$_{2+Y}$ZnSiO$_{4-Y}$N$_Y$ with increasing Y.

Although no thermal event could be seen in Li-rich, lithium zinc silicates, polymorphic change of the N-doped samples can be followed by DSC. Figure 5.12 illustrates the DSC results of $Li_{2.6}ZnSiO_{3.4}N_{0.6}$ and compares it with $Li_{2.8}Zn_{0.6}SiO_4$ in nitrogen atmosphere. The N-doped sample was heated to 500°C (1st cycle) and 800°C (2nd cycle). After each heating cycle, the sample was cooled to room temperature and X-ray diffraction was performed for phase determination. The results show a sharp endotherm at ≈250°C, followed by a small endotherm at ≈400°C and a broader endotherm between ≈600°C and 700°C for $Li_{2.6}ZnSiO_{3.4}N_{0.6}$ on heating (red traces). Only a small endotherm can be seen at ≈500°C on cooling (blue traces). No effect was evidenced for the $Li_{2.8}Zn_{0.6}SiO_4$ sample on either heating or cooling (black traces).
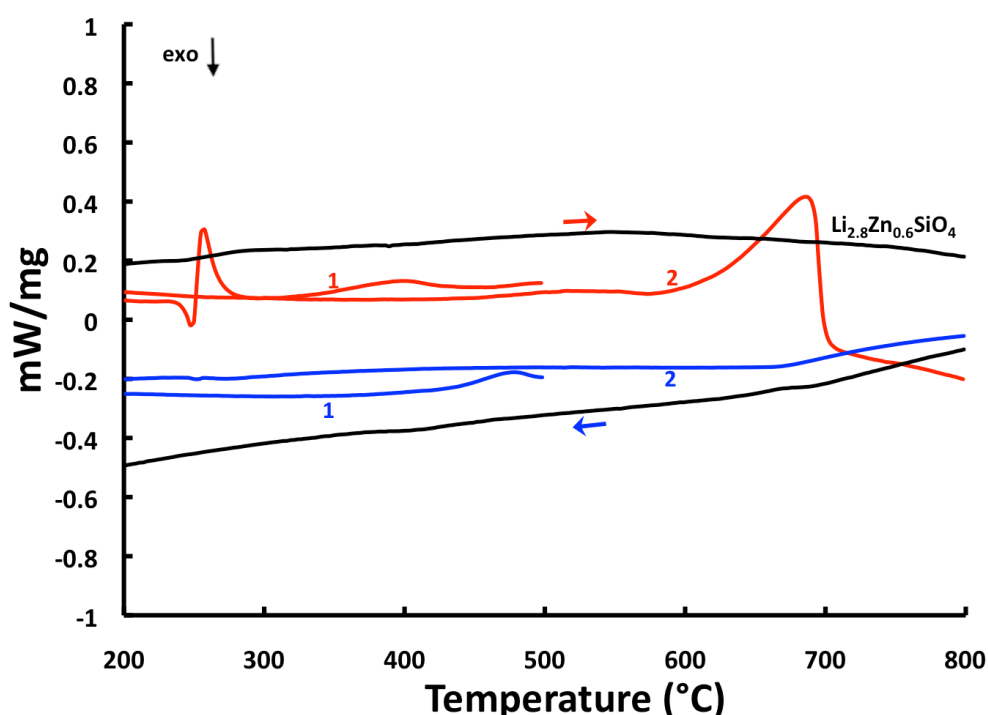
Figure 5.12. DSC results for $Li_{2.6}ZnSiO_{3.4}N_{0.6}$ (1st and 2nd cycle) on heating (red)/cooling (blue) and $Li_{2.8}Zn_{0.6}SiO_4$ (black).

XRD results of $Li_{2.6}ZnSiO_{3.4}N_{0.6}$ after the 2nd cycle (800°C) indicate the occurrence of the lithia-γ_0 phase (blue traces in figure 5.13). The X-ray pattern after the 1st cycle (500°C), is very similar to the γ_0 polymorph (green traces); however, the phase has some differences from the γ_0 phase of 1:1 composition and can not be indexed with the same symmetry within acceptable errors.
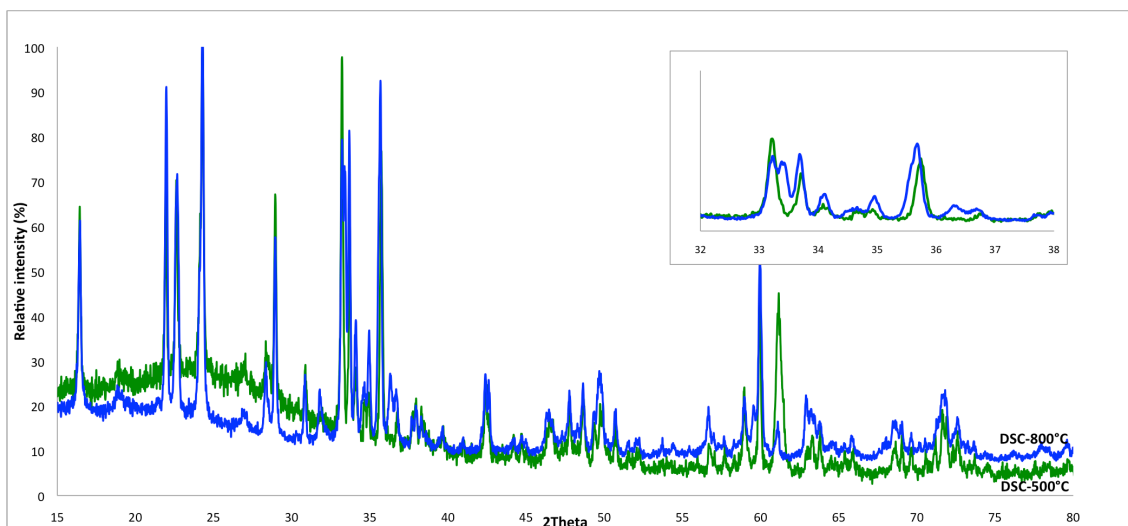
Figure 5.13. XRD profiles of Li$_{2.6}$ZnSiO$_{3.4}$N$_{0.6}$ following DSC at 500°C (green traces) and 800°C (blue traces), (Cu Kα$_1$ radiation).

The broad endotherm between ≈600°C and 700°C was also evidenced in previous reports [173] and must be due to the γ$_0$➔γ$_I$ and γ$_I$➔γ$_{II}$ transition. The sharp endotherm at ≈250°C is probably a lithia-γ$_0$➔γ$_0$ transformation and the small endotherm in between is probably a small distortion of the γ$_0$ phase. With slower cooling rates (longer annealing times) γ$_0$ tends to convert to the β polymorph. That is the reason why that the phase obtained from the 1st cycle of the DSC experiment could not be indexed with the same symmetry as γ$_0$-Li$_2$ZnSiO$_4$.

Li$_2$MgSiO$_4$

The X-ray diffraction pattern of Li$_2$MgSiO$_4$ is shown in figure 5.14. Our first attempt to make pure Li$_2$MgSiO$_4$ by mixing appropriate amounts of MgO, SiO$_2$, Li$_2$CO$_3$ followed by reaction at 650°C and 1050°C, led to the presence of Li$_2$SiO$_3$ as a secondary phase (green traces). The phase mixture still remained after further grinding and heating at 1100°C (red traces). In the second attempt, reaction of an appropriate mixture of Li$_4$SiO$_4$ and Mg$_2$SiO$_4$ at 650°C and 1050°C overnight and cooling at 5°C/min rate led to a phase, which corresponds well with the ICDD card [24-637]; however, there are still some traces of the Li$_2$SiO$_3$ secondary phase present in the X-ray pattern (blue traces). Higher temperature reaction intensifies the secondary phase peaks.

Li$_2$(Mg, Zn)SiO$_4$ had to be prepared from Li$_4$SiO$_4$ and (Mg, Zn)$_2$SiO$_4$ [172, 175]. Moreover, volatility of lithia was reported at elevated temperatures, especially towards the lithium-rich part of the system [175]. It is therefore possible that the high temperature needed for preparation of these compositions leads to appreciable lithia loss, indicated by the formation of secondary phases in the sample.
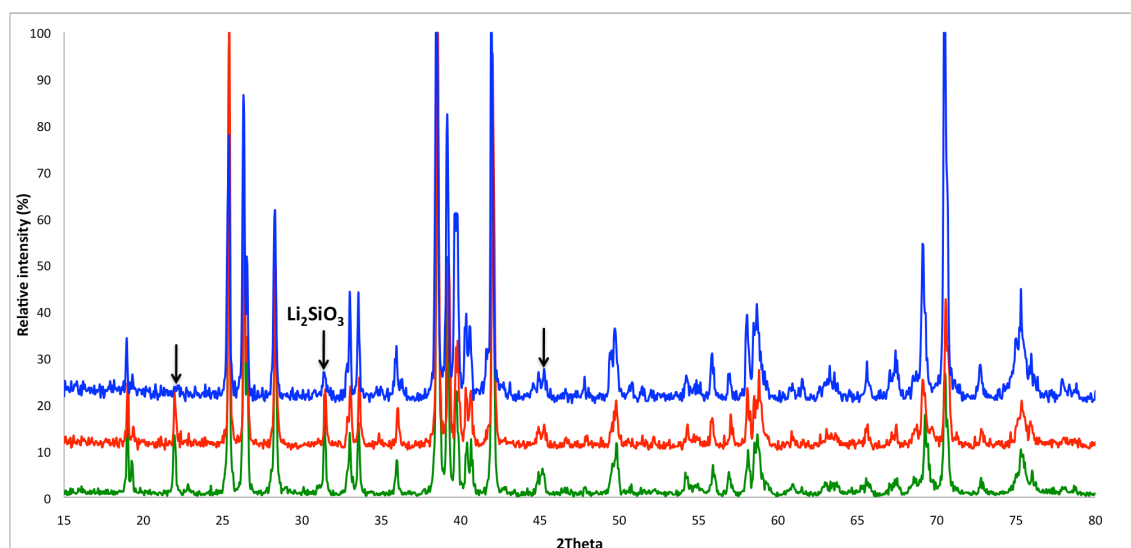
Figure 5.14. XRD profiles of Li$_2$MgSiO$_4$, from MgO, SiO$_2$ and Li$_2$CO$_3$ at 1050°C and 1100°C (green and red traces), and from Li$_4$SiO$_4$ and Mg$_2$SiO$_4$ at 1050°C (blue traces), (Co Kα$_1$ radiation).

The main peaks in the XRD pattern match with γ$_0$-Li$_2$MgSiO$_4$ and can be indexed as monoclinic *P2$_1$/n* symmetry (♯14) within good errors (table 5.5). The lattice constants and cell volumes of γ$_0$-Li$_2$MgSiO$_4$ are calculated and listed in Table 5.6. Cell parameters of the synthesised Li$_2$MgSiO$_4$ are in a good agreement with the previously reported data.

A range of nitrogen-doped compositions, with Li$_{2+Y}$MgSiO$_{4-Y}$N$_Y$ formula, was made by reacting an appropriate mixture of MgO, SiO$_2$, Li$_2$CO$_3$ and Li$_3$N at 1050°C (2.5%-20% of oxygen substituted by nitrogen). The X-ray diffraction patterns of these oxynitrides are shown in figure 5.15, and compared with the oxide parent. The main peaks in the XRD pattern of compositions with low nitrogen (Y≤0.2) correspond well to the γ$_0$-Li$_2$MgSiO$_4$ peaks; however, there is also some Li$_2$SiO$_3$ secondary phase present. The peaks corresponding to Li$_2$SiO$_3$ are less intense in Y=0.2. Attempts to make pure

samples from an appropriate mixture of Li_4SiO_4, Mg_2SiO_4 and Li_3N still resulted in some Li_2SiO_3 secondary phase. It is possible that solid solutions close to the 1:1 composition are subject to lithia loss.

Compositions with Y≥0.4 indicate that the formation of lithia-γ_0 polymorphs similar to N-doped Li_2ZnSiO_4 (peaks between ≈39-42°, Co $K\alpha_1$ radiation, are characteristic of lithia-γ_0 polymorph). The occurrence of a lithia-γ_0 phase was also reported in the study of Li_4SiO_4-Mg_2SiO_4 binary system. It was described as (probably) a metastable phase that forms by distortion of the γ_0 phase at, or very close to, lithia-rich limits of the γ solid solution on cooling [175]. In these compositions, there are also some minor extra peaks present that do not correspond to any known impurity, especially in Y≥0.5. Further heating of the mentioned compositions at 1300°C and cooling at 5°C/min rate, led to phases that mostly resemble the high-D polymorph (figure 5.16). High-D is structurally related to the Li_4SiO_4 phase, occurring between ≈30-35% Mg_2SiO_4 in the Li_4SiO_4-Mg_2SiO_4 binary system and forms by quenching high-Li_4SiO_4 solid solution to ambient temperature, followed by annealing at 400°C [175]. Compositions with Y≥0.5 therefore, probably are in the "γ_{II} + high-Li_4SiO_4" two-phase region at 1050°C, which transforms to "lithia-γ_0 + a Li_4SiO_4-type phase" at room temperature (depending on the cooling rate).
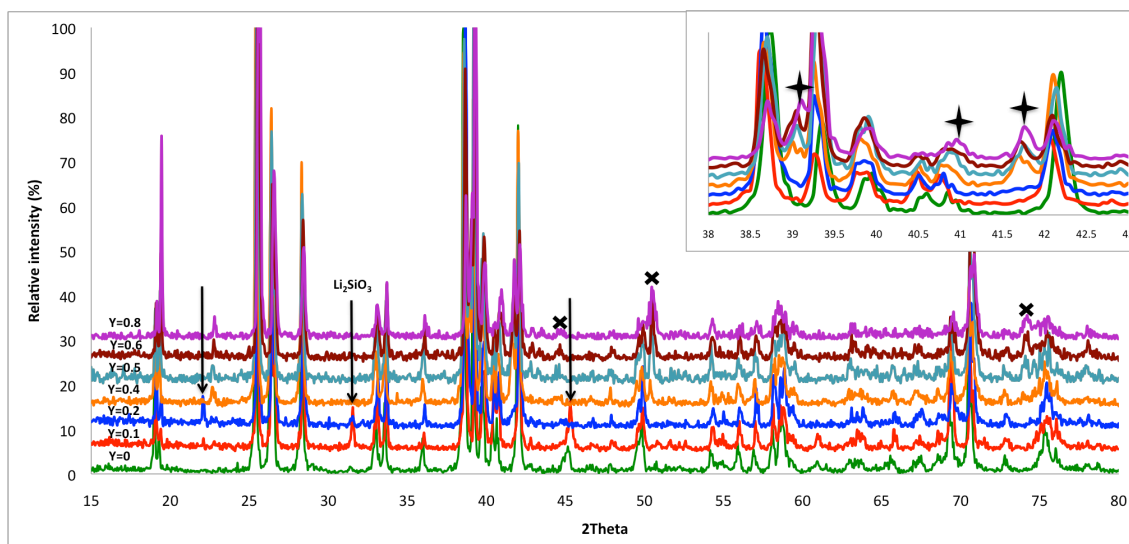
Figure 5.15. XRD profiles of $Li_{2+Y}MgSiO_{4-Y}N_Y$ synthesised at 1050°C. Arrows indicate presence of Li_2SiO_3 secondary phase in Y≤0.2. Stars indicate formation of lithia-γ_0 in Y≥0.4. Crosses indicate presence of Li_4SiO_4-type phase in Y≥0.5. (Co $K\alpha_1$ radiation).
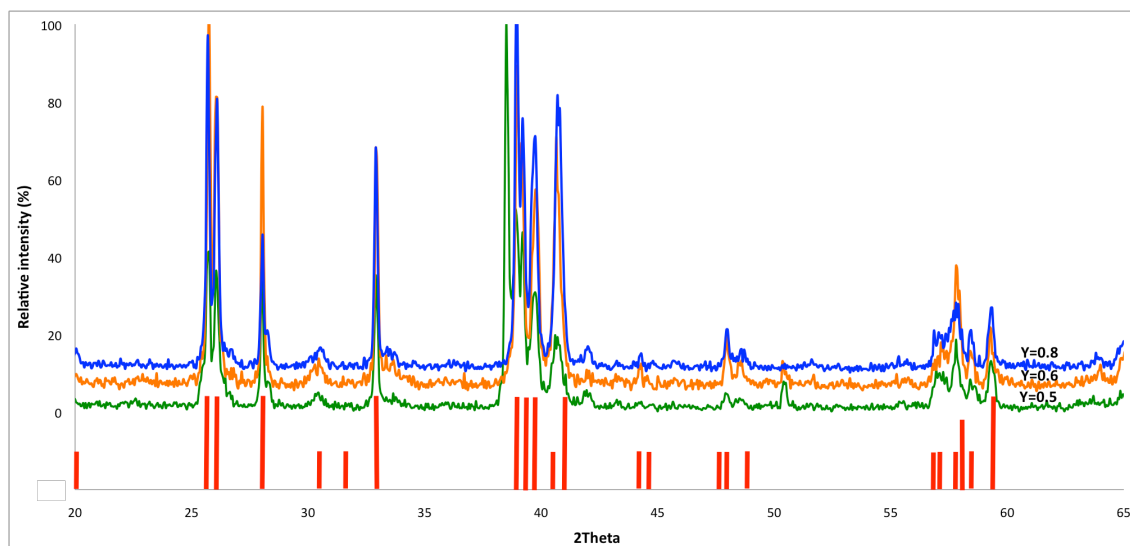
Figure 5.16. XRD profiles of $Li_{2+Y}MgSiO_{4-Y}N_Y$ synthesised at 1300°C. Red bars belong to the X-ray diffraction data of $Li_{2.8}Mg_{0.6}SiO_4$ (high-D phase) [175], (Co Kα_1 radiation).

The main peaks in the XRD traces of oxynitride samples were indexed as monoclinic with *P2₁/n* symmetry. Indexed summaries are listed in table 5.5 and compared with Li_2MgSiO_4. The XRD pattern of all compositions generally can be indexed within good errors; however, in lithia-γ_0 phases (Y≥0.4), some of the XRD lines can be indexed with the *P2₁/n* symmetry only with large errors, suggesting that the proposed unit cell may not be correct. Despite that, the lattice constants of the N-doped compositions have been determined based on the γ_0 structure (table 5.6) and compared with those of Li_2MgSiO_4. Cell parameter variations in $Li_{2+Y}MgSiO_{4-Y}N_Y$ with increasing Y are presented in figure 5.17. The cell volume decreases considerably in Y≤0.2; however, it increases by transforming to lithia-γ_0 phase (Y≥0.4). Due to the polymorphic transformation it is difficult to indicate the solid solution limit.

Table 5.5. X-ray diffraction data of Li$_2$MgSiO$_4$ and N-doped Li$_2$MgSiO$_4$ (Cu Kα$_1$ radiation).

Li$_2$MgSiO$_4$

d observed (Å)	d calculated (Å)	Δ2θ° (obs-cal)	Intensity	$h\ k\ l$
5.4247	5.4233	-0.0040	11.1	1 1 0
5.3393	5.3402	0.0028	3.5	0 2 0
4.0731	4.0724	-0.0040	66.2	1 2 0
3.9282	3.9283	0.0163	52.5	-1 0 1
3.8965	3.8971	0.0034	20.6	1 0 1
3.6599	3.6610	0.0071	43.2	1 1 1
3.1003	3.0989	-0.0125	10.5	1 3 0
2.8999	2.8990	-0.0097	2.8	0 3 1
2.7112	2.7117	0.0056	82.8	2 2 0
2.6705	2.6701	-0.0044	39.6	0 4 0
2.6376	2.6380	0.0045	11.9	-1 3 1
2.6291	2.6285	-0.0090	11.2	1 3 1
2.5923	2.5928	0.0075	8.5	-2 1 1
2.5751	2.5749	-0.0033	7.9	2 1 1
2.4971	2.4971	0.0002	100.0	0 0 2
2.3315	2.3292	-0.0398	7.8	-1 0 2
2.2626	2.2625	-0.0019	1.1	0 2 4
2.2626	2.2622	-0.0075	0.9	1 1 2

Li$_{2.2}$MgSiO$_{3.8}$N$_{0.2}$

d observed (Å)	d calculated (Å)	Δ2θ° (obs-cal)	Intensity	$h\ k\ l$
5.4176	5.4171	-0.0014	27.3	1 1 0
5.3363	5.3368	0.0014	21.9	0 2 0
4.0675	4.0686	0.0061	92.0	1 2 0
3.9230	3.9246	0.0093	74.4	-1 0 1
3.6566	3.6571	0.0032	57.5	1 1 1
3.1453	3.1450	-0.0030	19.8	1 2 1
3.0958	3.0964	0.0055	21.8	1 3 0
2.8967	2.8969	0.0019	13.8	0 3 1
2.7080	2.7086	0.0076	85.3	2 2 0
2.6680	2.6684	0.0054	61.3	0 4 0
2.6339	2.6359	0.0273	27.3	-1 3 1
2.5895	2.5901	0.0076	16.0	-2 1 1
2.5718	2.5717	-0.0021	18.6	2 1 1
2.4950	2.4950	0.0008	100.0	0 0 2
2.3288	2.3265	-0.0405	7.4	-1 0 2
2.2601	2.2602	-0.0025	6.9	1 1 2
2.2061	2.2067	0.0100	6.9	-1 4 1
2.1353	2.1355	0.0025	10.6	-2 3 1

Table 5.5. Continued.

Li$_{2.4}$MgSiO$_{3.6}$N$_{0.4}$

d observed (Å)	d calculated (Å)	Δ2θ° (obs-cal)	Intensity	$h\ k\ l$
5.4144	5.4167	0.0072	37.1	1 1 0
5.3332	5.3369	0.0148	31.9	0 2 0
4.0650	4.0685	0.0191	100.0	1 2 0
3.9199	3.9244	0.0267	80.3	-1 0 1
3.6560	3.6568	0.0054	66.6	1 1 1
3.1471	3.1448	-0.0210	24.5	1 2 1
3.0965	3.0964	-0.0005	25.2	1 3 0
2.8967	2.8969	0.0021	17.7	0 3 1
2.7079	2.7084	0.0053	94.7	2 2 0
2.6680	2.6685	0.0058	74.3	0 4 0
2.6407	2.6409	0.0016	25.3	-1 3 1
2.6355	2.6361	0.0061	26.1	1 3 1
2.5899	2.599	0.0003	20.3	-2 1 1
2.5704	2.5714	0.0139	15.3	2 1 1
2.4947	2.4949	0.028	84.0	0 0 2
2.1355	2.1354	-0.0012	13.8	-2 3 1
2.1226	2.1250	0.0494	18.8	2 3 1
1.9631	1.9627	-0.0111	13.1	0 5 1

Li$_{2.5}$MgSiO$_{3.5}$N$_{0.5}$

d observed (Å)	d calculated (Å)	Δ2θ° (obs-cal)	Intensity	$h\ k\ l$
5.4218	5.4196	-0.0067	13.7	1 1 0
5.3421	5.3417	-0.0013	4.2	0 2 0
4.0709	4.0713	0.0022	82.5	1 2 0
3.9280	3.9279	-0.0008	71.4	-1 0 1
3.8967	3.8968	0.0006	22.3	1 0 1
3.6600	3.6609	0.0059	55.5	1 1 1
3.0996	3.0988	-0.0075	13.1	1 3 0
2.9001	2.9000	-0.0008	5.1	0 3 1
2.7094	2.7098	0.0049	94.8	2 2 0
2.6708	2.6709	0.0005	44.6	0 4 0
2.6341	2.6383	0.0550	26.5	-1 3 1
2.5909	2.5914	0.0068	10.9	-2 1 1
2.5739	2.5714	-0.0052	11.6	2 1 1
2.4985	2.4984	-0.0014	100.0	0 0 2
2.1367	2.1368	0.0032	5.8	-2 3 1
2.1252	2.1268	0.0333	13.1	2 3 1
1.9646	1.9646	0.0009	5.7	0 5 1
1.9084	1.9076	-0.0215	11.0	-3 1 1

105

Table 5.6. X-ray diffraction data of LiMgSiO(N).

	$a(\text{Å})$	$b(\text{Å})$	$c(\text{Å})$	$\beta(°)$	$V(\text{Å})$	Space group
Li_2MgSiO_4	6.2956(10)	10.6805(13)	4.9944(6)	90.469(10)	335.81(5)	$P2_1/n$
Li_2MgSiO_4 [177]	6.300(0)	10.692(2)	4.995(5)	90.47(1)		$P2_1/n$
$Li_{2.2}MgSiO_{3.8}N_{0.2}$	6.2872(5)	10.6736(8)	4.9902(3)	90.480(10)	334.87(3)	$P2_1/n$
$Li_{2.4}MgSiO_{3.6}N_{0.4}$	6.2866(5)	10.6739(10)	4.9900(5)	90.483(8)	334.83(4)	$P2_1/n$
$Li_{2.5}MgSiO_{3.5}N_{0.5}$	6.2891(9)	10.6834(13)	4.9970(7)	90.467(11)	335.73(5)	$P2_1/n$
$Li_{2.6}MgSiO_{3.4}N_{0.6}$	6.3107(7)	10.6730(15)	4.9945(6)	90.481(6)	335.89(9)	$P2_1/n$
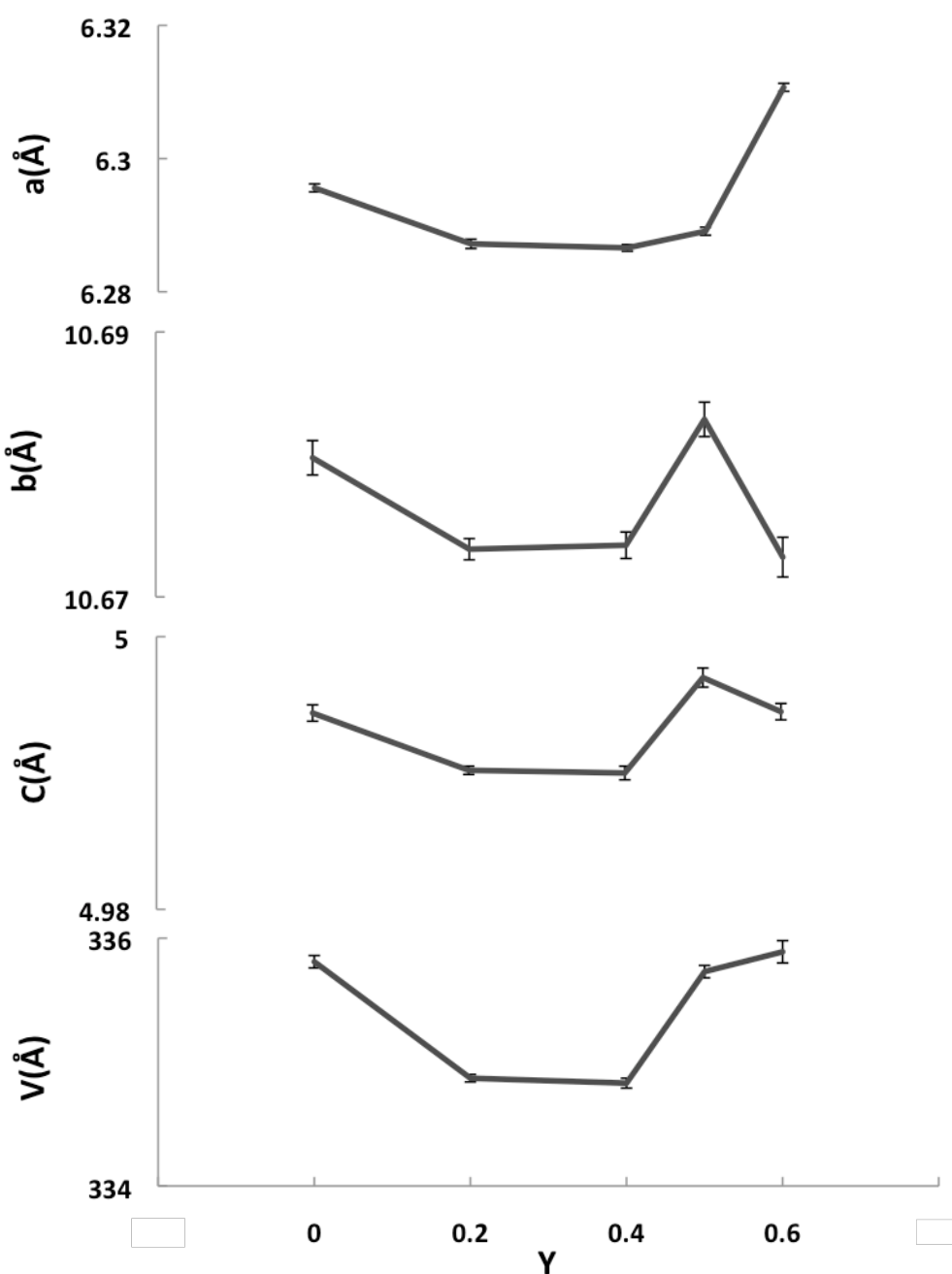
Figure 5.17. Change in unit cell parameters in $Li_{2+Y}MgSiO_{4-Y}N_Y$ with increasing Y.

106

Impedance Spectroscopy

Typical IS data sets of Li_2ZnSiO_4, Li_2MgSiO_4 and their nitrogen-doped analogues are presented in figures 5.18-21. Li_2ZnSiO_4 and Li_2MgSiO_4 show very high resistivity. Experiments required a temperature in excess of 400°C to reduce the resistance to within measurable limits.

The Z^* plots show a nearly ideal semicircle for all samples, except in Y= 0.4 and 0.6 in $Li_{(2+Y)}ZnSiO_{(4-Y)}N_Y$, where two arcs can be seen. From the relation $\omega RC=1$ at the semicircle maximum, the associated capacitance of the arc can be calculated (table 5.7). The associated capacitance of the semicircles are in good agreement with the high frequency plateaux in the logC' vs. log$f$ plots and suggest that the measurements are associated with the bulk response. In Y= 0.4 and 0.6 in $Li_{(2+Y)}ZnSiO_{(4-Y)}N_Y$ (figure 5.20), the associated capacitance of the second arc indicates the existence of a minor secondary component, possibly an intergranular effect.

The combined Z"/M" plots show a single, Debye-like peak with the peak maximum occurring at the same frequency, which confirms the electrical homogeneity of the samples. Four compositions are shown separately in figure 5.22 for clarity. In Y= 0.4 and 0.6 in $Li_{(2+Y)}ZnSiO_{(4-Y)}N_Y$ the peaks do not exactly coincide and a low frequency arc in Y= 0.6 (broad arc in Y= 0.4) in the Z" peak indicates the possible presence of a grain boundary risistance. A low frequency dispersion (or spike) in the Z" plot of N-doped samples may be associated with an electrode effect.

Table 5.7. Associated capacitance of the semicircle(s) in the Z* plot.

Sample	Capacitance	Sample	Capacitance
Li_2ZnSiO_4	3 pFcm^{-1}	Li_2MgSiO_4	6 pFcm^{-1}
$Li_{2.1}ZnSiO_{3.9}N_{0.1}$	5 pFcm^{-1}	$Li_{2.1}MgSiO_{3.9}N_{0.1}$	5 pFcm^{-1}
$Li_{2.2}ZnSiO_{3.8}N_{0.2}$	5 pFcm^{-1}	$Li_{2.2}MgSiO_{3.8}N_{0.2}$	6 pFcm^{-1}
$Li_{2.4}ZnSiO_{3.6}N_{0.4}$	5 pFcm^{-1}, 0.2 nFcm^{-1}	$Li_{2.4}MgSiO_{3.6}N_{0.4}$	5 pFcm^{-1}
$Li_{2.6}ZnSiO_{3.4}N_{0.6}$	7 pFcm^{-1}, 0.5 nFcm^{-1}	$Li_{2.5}MgSiO_{3.5}N_{0.5}$	8 pFcm^{-1}
		$Li_{2.6}MgSiO_{3.4}N_{0.6}$	4 pFcm^{-1}
		$Li_{2.8}MgSiO_{3.2}N_{0.8}$	0.8 pFcm^{-1}
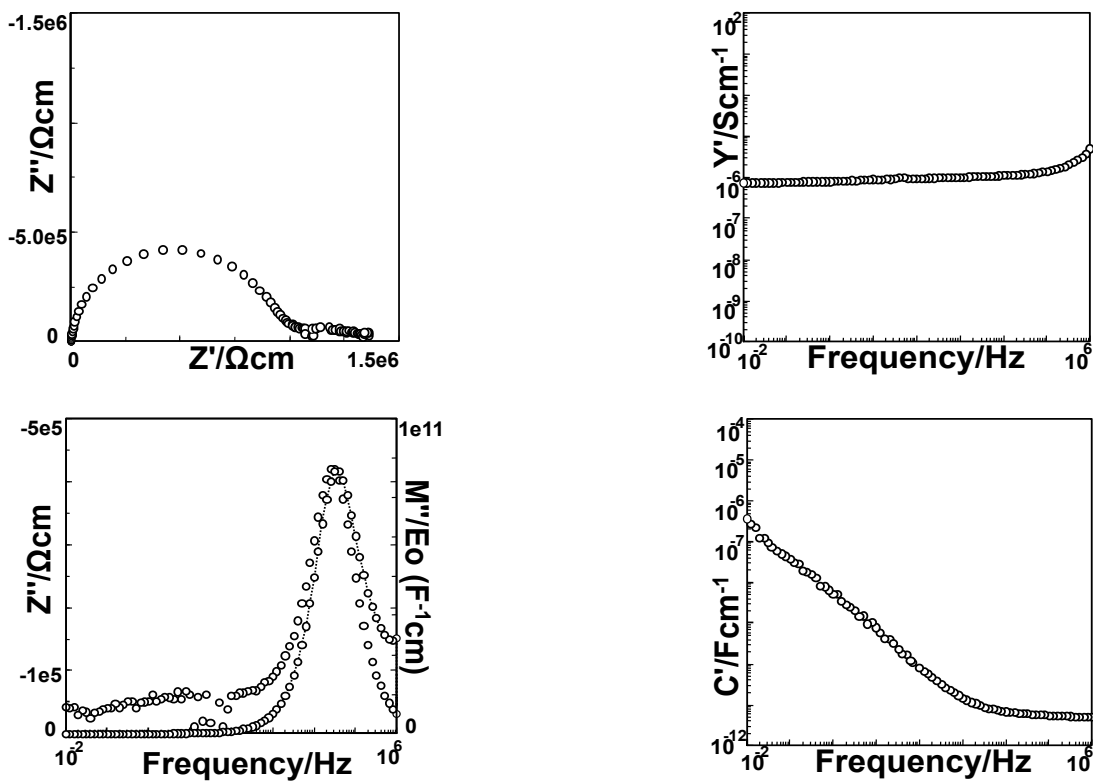
Figure 5.18. Impedance spectroscopy data of Li₂ZnSiO₄ at 490°C.
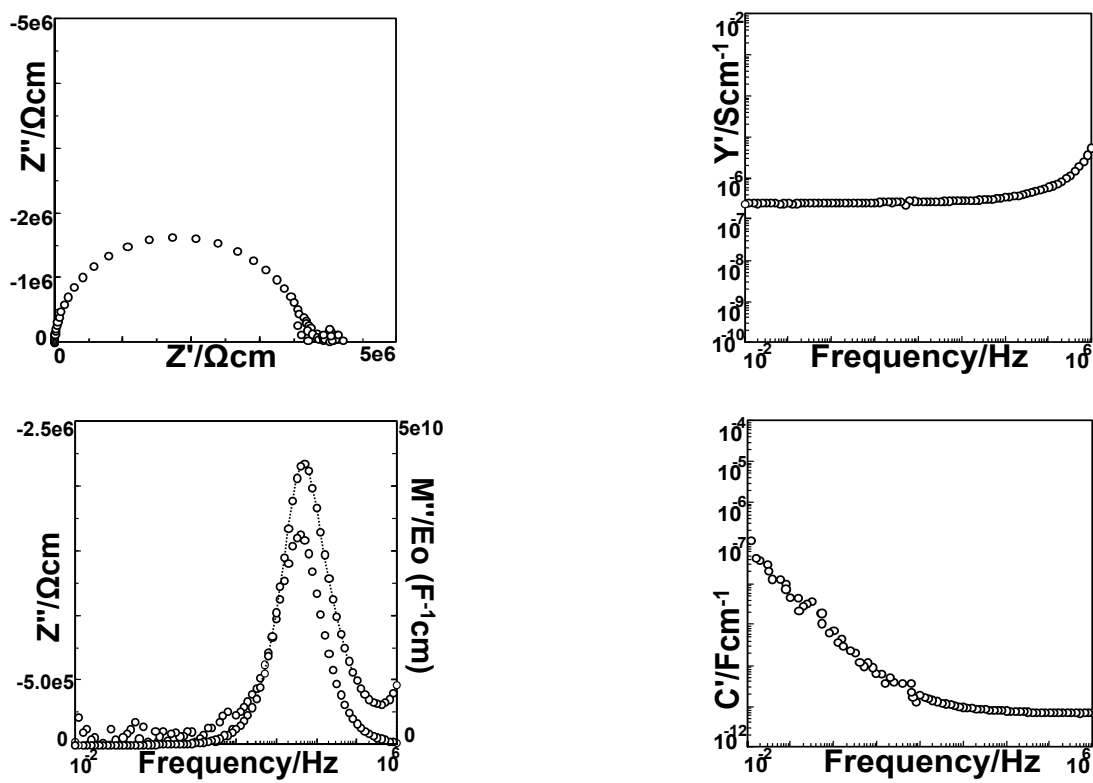
Figure 5.19. Impedance spectroscopy data of Li₂MgSiO₄ at 470°C.
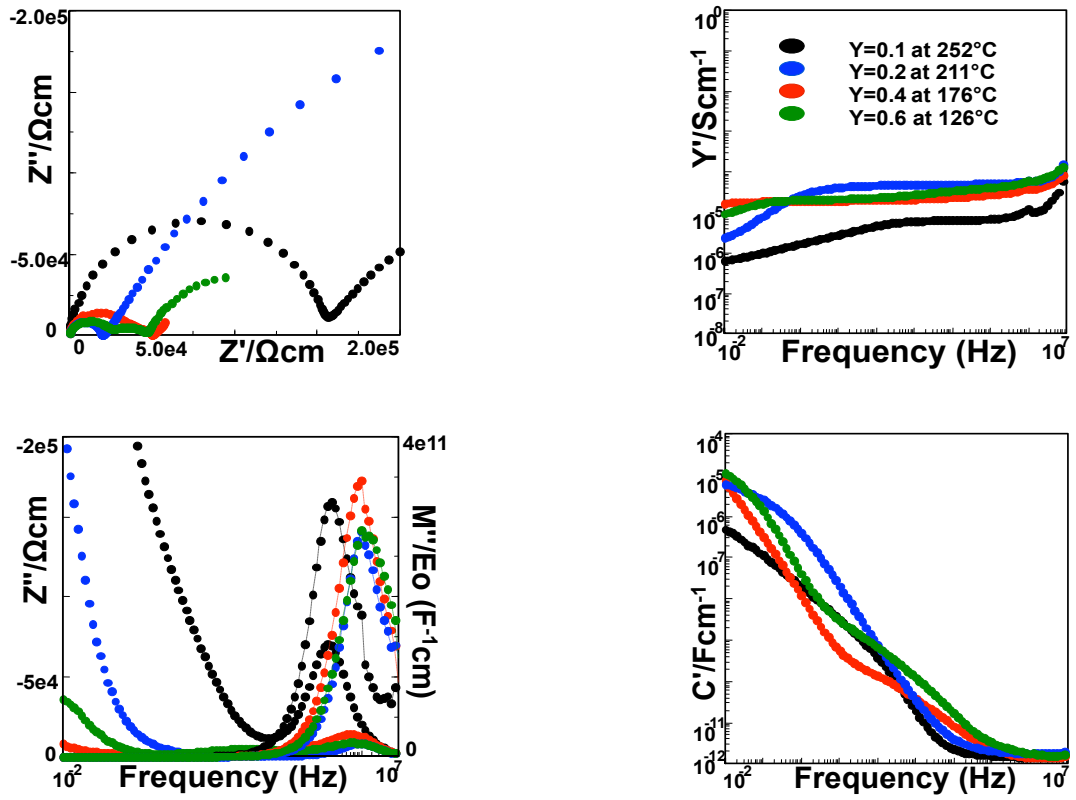
Figure 5.20. Impedance spectroscopy data of Li$_{(2+Y)}$ZnSiO$_{(4-Y)}$N$_Y$.
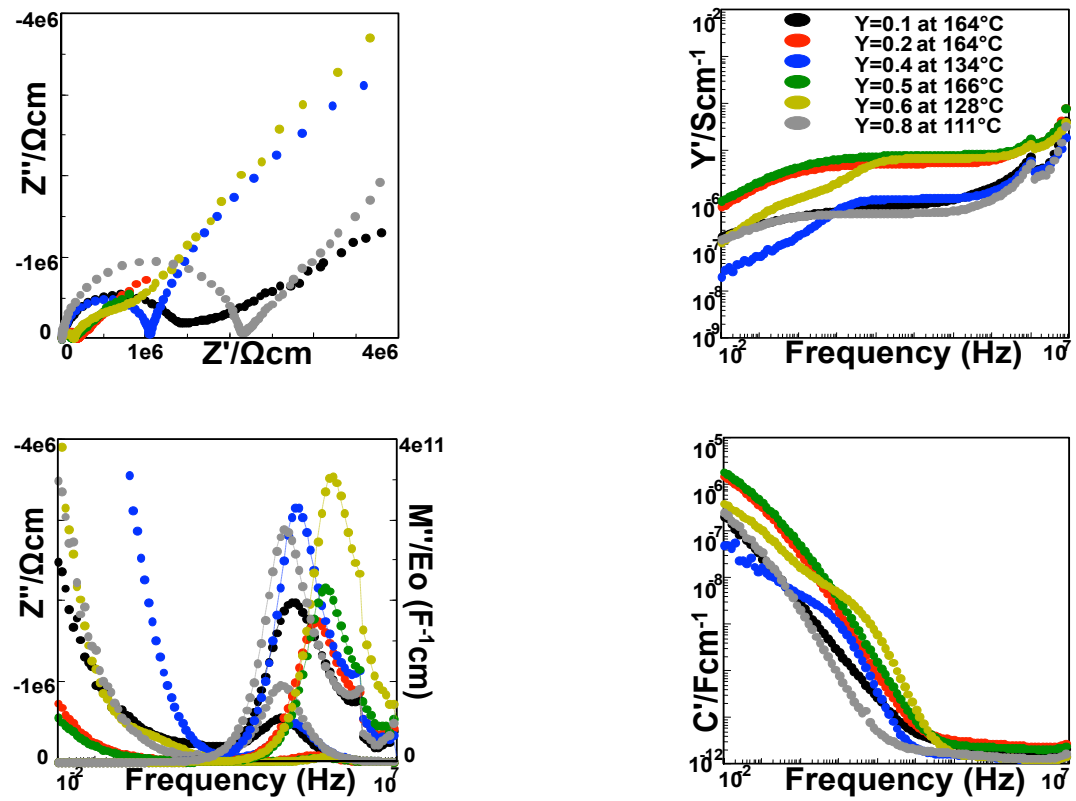
Figure 5.21. Impedance spectroscopy data of Li$_{(2+Y)}$MgSiO$_{(4-Y)}$N$_Y$.
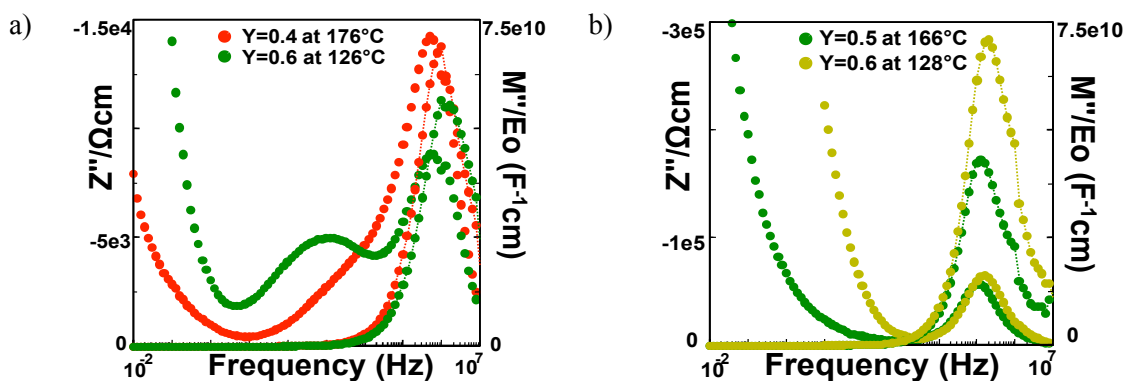
Figure 5.22. Z$^{''}$ and M$^{''}$ plots of a) Li$_{(2+Y)}$ZnSiO$_{(4-Y)}$N$_Y$ and b) Li$_{(2+Y)}$MgSiO$_{(4-Y)}$N$_Y$.

The bulk resistance was obtained directly from the intercept of the impedance complex plane plot with the real axis (Z' axis). In case of absence of any significant grain boundary effects, this can be also obtained from the frequency independent conductance plateau in the logσ vs. log$f$ (Y') plots. The extent of this plateau is limited at high frequencies by a frequency dependent conductivity dispersion, which seems to follow a power law. This effect is also observed in disordered materials, like ionically conducting glasses/polymers and doped crystalline solids and believed to be attributed to a distribution of ionic conductivities and relaxation time [75]. According to the jump relaxation model, at low frequencies an ion can successfully jump to its vacant neighbour site. At higher frequencies the probability for an ion to go back to its initial place increases due to the short time window available. Therefore, random hopping of mobile ions and high probability of short distance forward-backward hopping of ions is responsible for the rise in the conductivity at high frequencies [178, 179].

A low frequency dispersion is also observed in the logσ vs. log$f$ plots of N-doped samples, unlike in more resistive Li$_2$ZnSiO$_4$ and Li$_2$MgSiO$_4$ samples, which is attributed to electrode polarisation. At very low frequencies, and therefore long times, charge pileup at the electrodes encourages a back-field and therefore a noticeable decrease in conductivity [153, 178, 180].

Figures 5.23 and 5.24 illustrates the Z* plots of Li$_2$ZnSiO$_4$, Li$_2$MgSiO$_4$ and their nitrogen-doped analogues at various temperatures and their associated capacitance. In these results, a low frequency dispersion with a capacitance in the range of microfarads, which has the character of an inclined spike attributed to partial blocking of ionic charge carriers at the metal-sample interface, can be evidenced in N-doped samples. These can be signs of a typical ionic conductor.
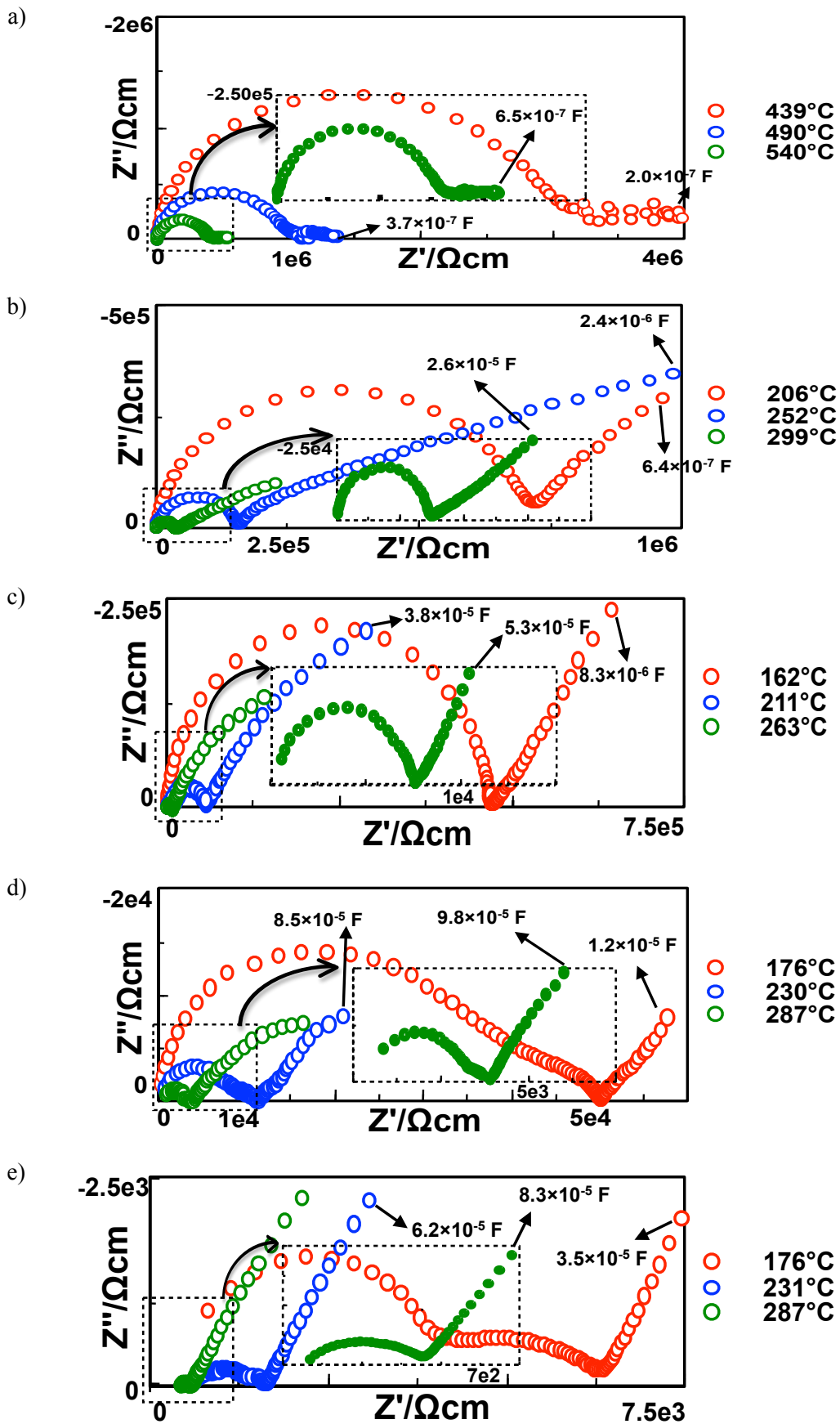
Figure 5.23. Z* plot of $Li_{(2+Y)}ZnSiO_{(4-Y)}N_Y$ and the associated capacitance at different temperatures: a) Y=0, b) Y=0.1, c) Y=0.2, d) Y=0.4 and e) Y=0.6.
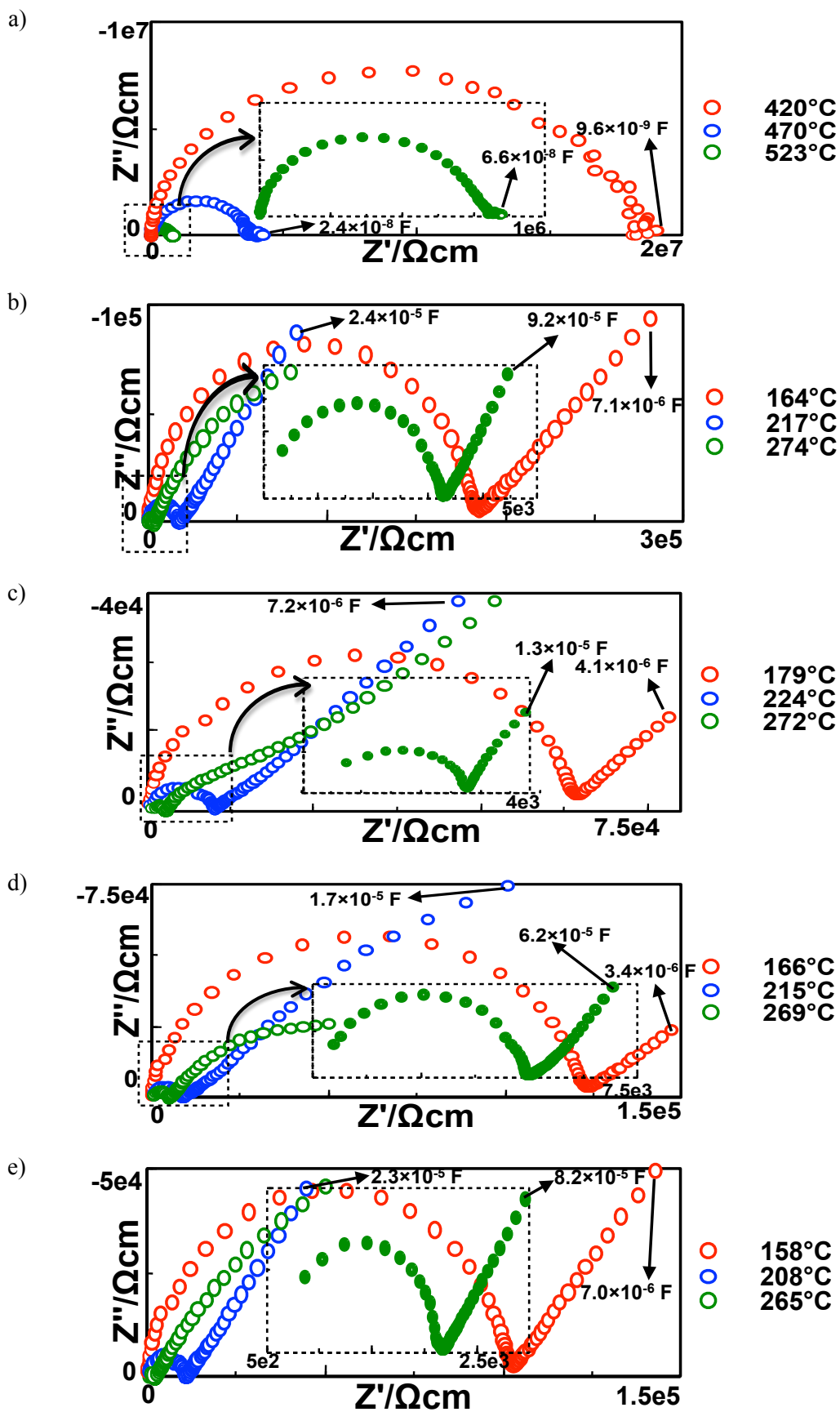
Figure 5.24. Z* plot of $Li_{(2+Y)}MgSiO_{(4-Y)}N_Y$ and the associated capacitance at different temperatures: a) Y=0, b) Y=0.2, c) Y=0.4, d) Y=0.5 and e) Y=0.8.

Low frequency data in the Z^* plots of Li_2ZnSiO_4 show a residual tail which collapses to become a broad, flat semicircle (Figure 5.23-a). Associated capacitance of the residual tail shows capacitance values as high as 0.6 μFcm^{-1}. These capacitance values together with frequencies in the range of 0.01 Hz indicates that the impedance response should have $Z^{''}$ values of more than 100 MΩ ($Z^{''}=1/\omega C$ [162]), which should have resulted in a nearly vertical spike in Z* plot. This is not seen in the experimental $Z^{''}$ values and therefore can not suggest that the blockage of the ionic species has happened in Li_2ZnSiO_4. The capacitance dispersion therefore, is probably a constant phase element (CPE) that happened as a result of electrode effect due to the surface roughness or porosity [163].

Impedance spectroscopy data were also collected for $Li_{2.4}Zn_{0.8}SiO_4$ and $Li_{2.8}Zn_{0.6}SiO_4$ (figure 5.25). Z^* plots of both samples consist of a nearly ideal semicircle at high frequencies attributed to the bulk response (the capacitance data show a high frequency plateau in the $pFcm^{-1}$ range) and a low frequency spike which could be attributed to the sample electrode interface and double layer effect (the capacitance data show a low frequency dispersion in μFcm^{-1} range). The $Z^{''}$ and $M^{''}$ peaks appear over a similar frequency range and a Debye-like peak is observed.
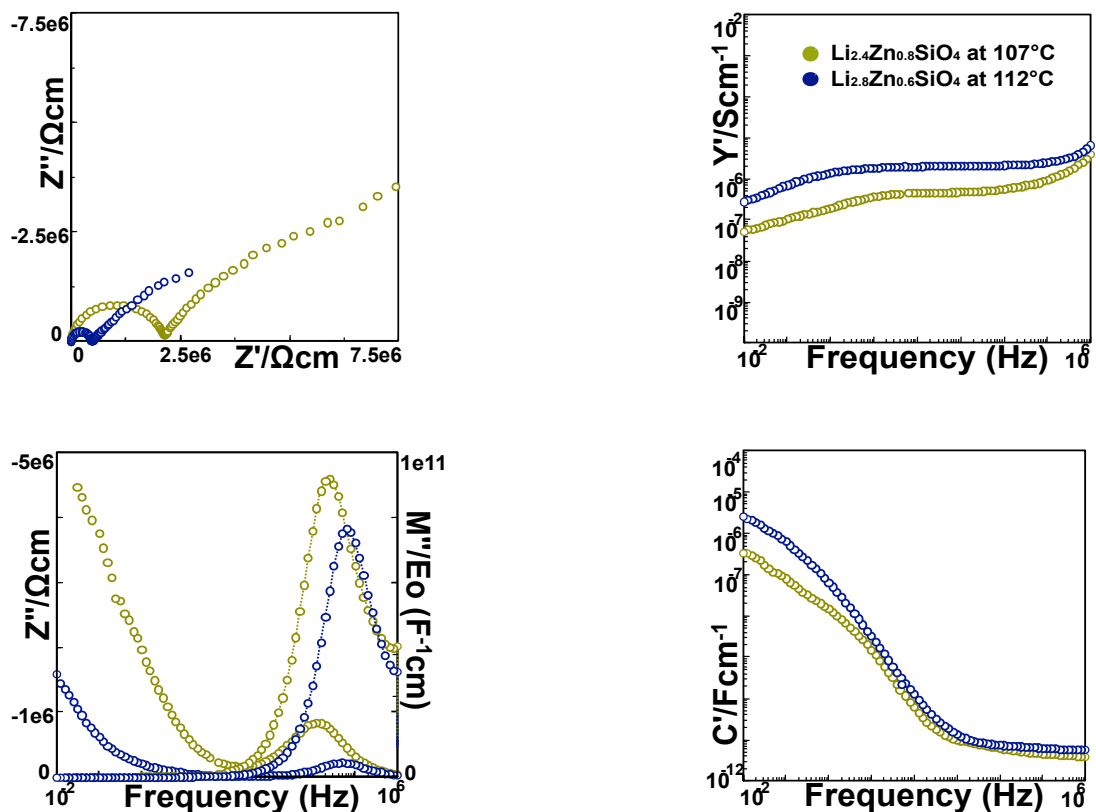
Figure 5.25. Impedance spectroscopy data of $Li_{2.4}Zn_{0.8}SiO_4$ and $Li_{2.8}Zn_{0.6}SiO_4$.

The conductivities of Li_2ZnSiO_4, Li_2MgSiO_4 and their nitrogen-doped analogues are presented as Arrhenius plots in figures 5.26 and 5.27. Activation energies and related conductivities are shown in table 5.8. Conductivities of N-doped samples (below 230°C) are approximately 4-6 orders of magnitude greater than that of Li_2ZnSiO_4 and Li_2MgSiO_4. The results also indicate a decrease in activation energy of nitrogen-doped samples. In N-doped Li_2MgSiO_4, activation energies drop to 0.87-0.77 eV from 1.39 eV. In $Li_{(2+Y)}ZnSiO_{(4-Y)}N_Y$ however, reduction in activation energies of Y=0.4 and 0.6 (from 1.14 to 0.55-0.44 eV) is greater than that in Y=0.1 and Y=0.2 (from 1.14 to 1.09-0.99 eV). Arrhenius plots of $Li_{2.4}Zn_{0.8}SiO_4$ and $Li_{2.8}Zn_{0.6}SiO_4$ are also shown and compared with Li_2ZnSiO_4 and its N-doped counterparts. The results indicate that the increase in conductivity of these two samples is very similar to N-doped compositions. Activation energies are similar to compositions with Y=0.1 and Y=0.2.
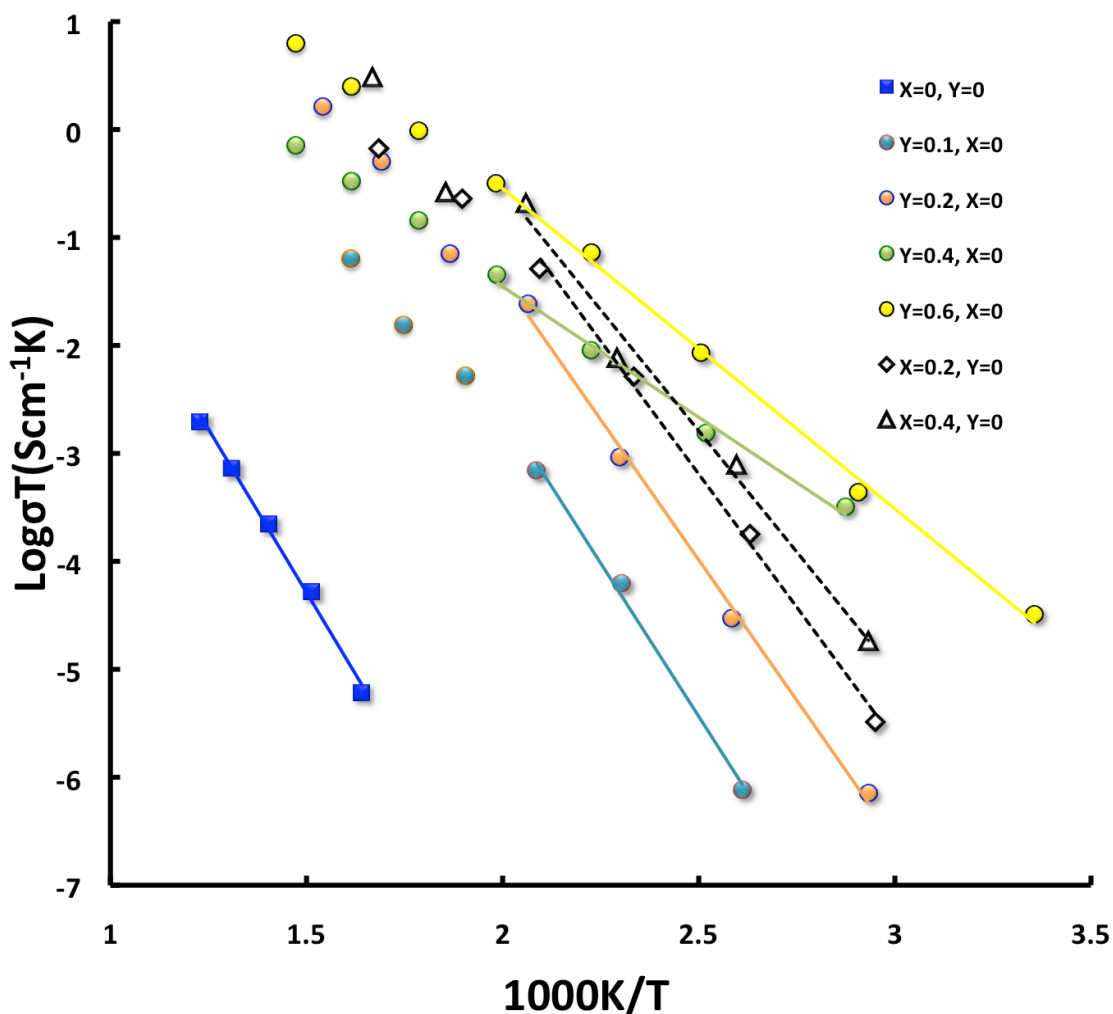
Figure 5.26. Arrhenius plots of conductivity of $Li_{(2+2X+Y)}Zn_{(1-X)}SiO_{(4-Y)}N_Y$.
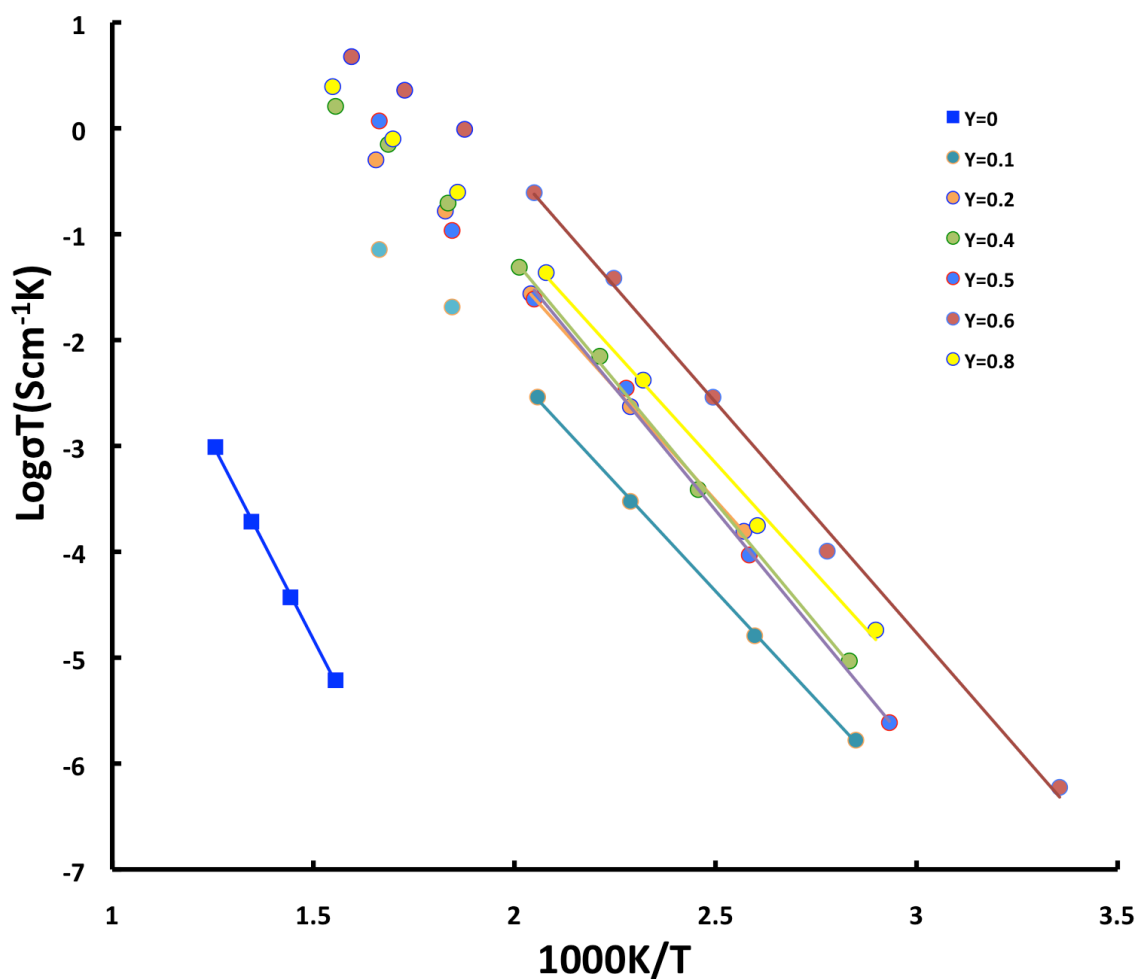
Figure 5.27. Arrhenius plots of conductivity of $Li_{(2+Y)}MgSiO_{(4-Y)}N_Y$.

Table 5.8. Activation energies (for N-doped samples below 230°C) and related conductivities.

	Activation Energy (eV)	Conductivity (Scm^{-1}) at T$^\circ$C		Activation Energy (eV)	Conductivity (Scm^{-1}) at T$^\circ$C
Li_2ZnSiO_4	1.14	8×10^{-8}(388)	Li_2MgSiO_4	1.39	4×10^{-8}(420)
$Li_{2.1}ZnSiO_{3.9}N_{0.1}$	1.09	1×10^{-7}(161)	$Li_{2.1}MgSiO_{3.9}N_{0.1}$	0.77	5×10^{-8}(112)
$Li_{2.2}ZnSiO_{3.8}N_{0.2}$	0.99	8×10^{-8}(114)	$Li_{2.2}MgSiO_{3.8}N_{0.2}$	0.80	4×10^{-7}(116)
$Li_{2.4}ZnSiO_{3.6}N_{0.4}$	0.44	4×10^{-6}(124)	$Li_{2.4}MgSiO_{3.6}N_{0.4}$	0.87	1×10^{-6}(134)
$Li_{2.6}ZnSiO_{3.4}N_{0.6}$	0.55	2×10^{-6}(71)	$Li_{2.5}MgSiO_{3.5}N_{0.5}$	0.87	2×10^{-7}(114)
$Li_{2.4}Zn_{0.8}SiO_4$	0.95	5×10^{-7}(107)	$Li_{2.6}MgSiO_{3.4}N_{0.6}$	0.83	7×10^{-6}(128)
$Li_{2.8}Zn_{0.6}SiO_4$	0.85	2×10^{-6}(112)	$Li_{2.8}MgSiO_{3.2}N_{0.8}$	0.79	5×10^{-7}(111)

Arrhenius plots of the N-doped composition show nonlinear behavior at high temperatures. This is more evident in N-doped Li_2MgSiO_4, where the data show a change in slope around ≈200°C. similar to N-doped $Li_3P(V)O_4$, the Z* plot of these samples illustrates a low frequency spike with an associated capacitance in the range of electrochemical reactions (≈10^{-4} Fcm^{-1}) above ≈200°C. Electrical conductivity of oxynitride samples was studied as a function of temperature on a cooling cycle. The Arrhenius plots of four of them are compared with their heating cycles (figure 5.28) and are reversible at all temperatures.
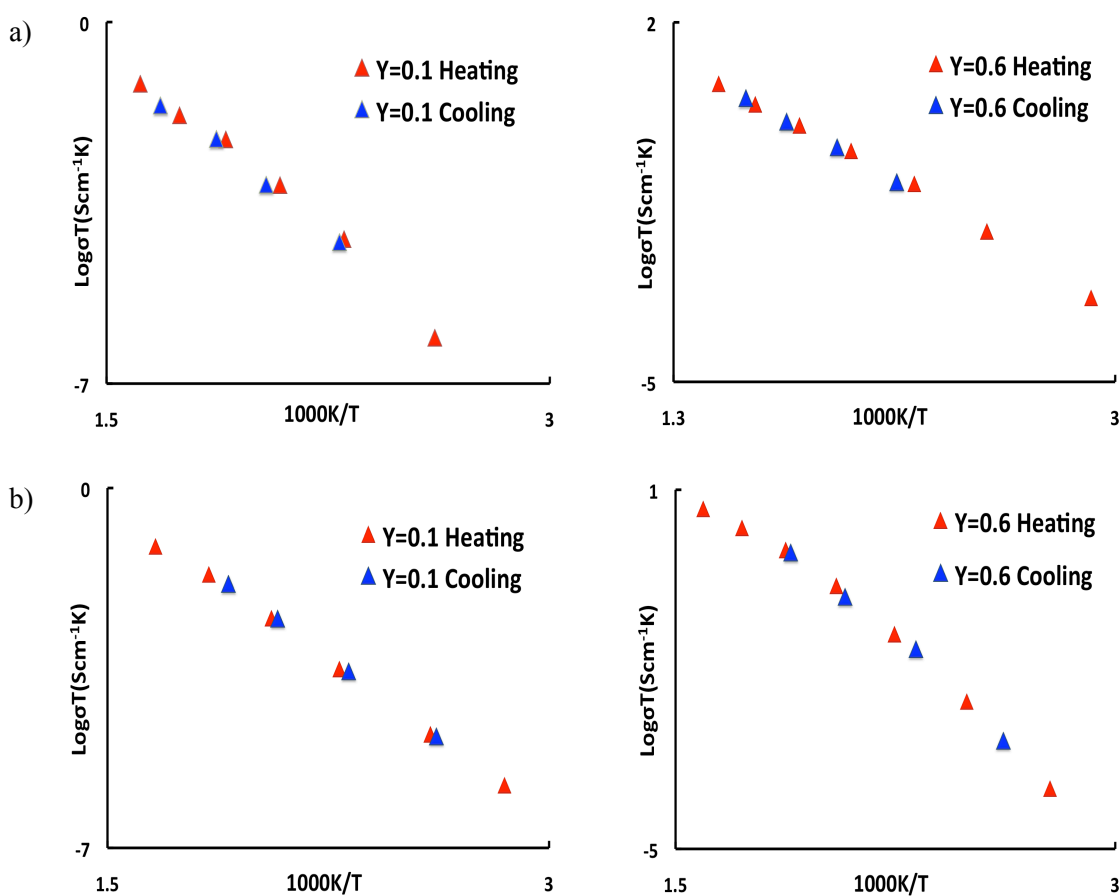
Figure 5.28. Arrhenius plots of conductivity of a) $Li_{(2+Y)}ZnSiO_{(4-Y)}N_Y$ and b) $Li_{(2+Y)}MgSiO_{(4-Y)}N_Y$, on heating and cooling.

DSC results of $Li_{2.6}ZnSiO_{3.4}N_{0.6}$ (figure 5.11) suggests that probably a lithia-$\gamma_0 \rightarrow \gamma_0$ transformation occurs at ≈250°C. The transition temperature is very close to the temperature that the Arrhenius plots of N-doped compositions illustrate a curvature. It

is, therefore, possible that the low temperature form (lithia-γ_0) is more resistive than the high temperature form (γ_0) and consequently, the Arrhenius plot is nonlinear.

N-doped samples also show reduction in conductivity with time at room temperature (ageing effect). Figure 5.29 illustrates Arrhenius plots of freshly prepared N-doped pellets and similar pellets stored under inert conditions for a month. The conductivity of the aged samples is approximately 1-2 orders of magnitude lower than that of freshly prepared pellets. No change in the XRD pattern of the aged samples could be seen. Moreover, sintering of the aged samples for two hours at 800°C would recover the conductivity to its original values.
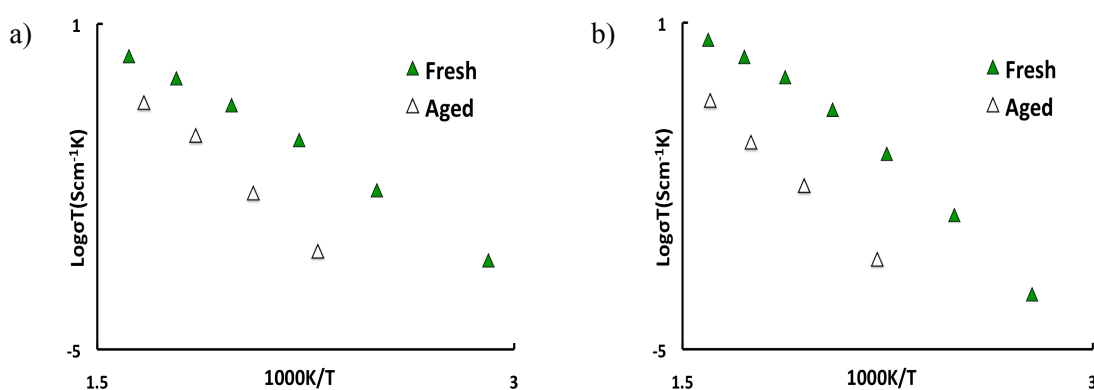
Figure 5.29. Z* plots of fresh and aged a) $Li_{2.6}ZnSiO_{3.4}N_{0.6}$ and b) $Li_{2.6}MgSiO_{3.4}N_{0.6}$.

Reversible nonlinear Arrhenius behaviour at high temperatures and an ageing effects are previously seen in many γ-structure materials [145, 181, 182]. In LISICON solid-solutions, the trapping of mobile lithium ions by the immobile sublattice at low temperatures was suggested as an explanation for lower conductivities and ageing effects [111]. Neutron diffraction of these materials found different type of defect clusters at high and low temperatures (that are essential for lithium ion conduction) [50, 51]. It suggests that the high energy required to generate the high-temperature clusters is mainly responsible for increase in the gradient of the Arrhenius plot at low temperatures. Recently it was discovered that several features of these γ solid-solutions have many characteristics of a glass transition, even though the materials are crystalline. In $Li_{(4-3X)}Al_XGeO_4$ and $Li_{(4-2X)}Ge_{(1-X)}S_XO_4$, the curvature in conductivity plots leads to zero activation energies above ≈700°C, indicating a liquid-like disorder of mobile lithium ions [52, 183]. In $Li_{(4-3X)}Al_XGeO_4$, there is also evidence of a second-order, glass-

like transition from DSC experiments in the region of the start and maximum of the curvature (230 and 480°C) [184].

There are many similarities in the unusual Arrhenius plot behaviour of N-doped Li_2ZnSiO_4-Li_2MgSiO_4 and other γ-structure materials that suggests being associated with a change in conduction mechanism; however, the possibility of phase transitions, proton conduction and nitrogen loss should not be ignored.

Combustion analysis

Table 5.9 shows combustion analysis results obtained at the AMG Analytical Services, compared with expected values of nitrogen in LiZnSiO(N). The nitrogen content of the undoped sample is slightly higher than that of $Li_3(P,V)O_4$. The reason for that is not clearly known. The nitrogen content of the $Li_{2.2}ZnSiO_{3.8}N_{0.2}$ sample is very close to the result of Li_2ZnSiO_4, indicating that significant nitrogen loss has happened. The nitrogen content in $Li_{2.4}ZnSiO_{3.6}N_{0.4}$ and $Li_{2.6}ZnSiO_{3.4}N_{0.6}$ however, is considerably higher than $Li_{2.2}ZnSiO_{3.8}N_{0.2}$. In both cases ≈7.5% of the targeted nitrogen could be found in the sample. The lattice parameter variation against the true nitrogen content is illustrated in figure 5.30.

Table 5.9. Theoretical and experimental values of nitrogen in LiZnSiO(N) samples determined by combustion analysis and their corrected formula.

	N(g) in 1(g) sample (Exp.)	N(g) in 1(g) sample (Theo.)	mol N (Exp.)	mol N (Theo.)	Corrected formula
Li_2ZnSiO_4	0.00088	0	0.010	0	
$Li_{2.2}ZnSiO_{3.8}N_{0.2}$	0.00094	0.0162	0.011	0.2	$Li_{2.011}ZnSiO_{3.989}N_{0.011}$
$Li_{2.4}ZnSiO_{3.6}N_{0.4}$	0.00244	0.0323	0.030	0.4	$Li_{2.030}ZnSiO_{3.970}N_{0.030}$
$Li_{2.6}ZnSiO_{3.4}N_{0.6}$	0.00374	0.0482	0.046	0.6	$Li_{2.046}ZnSiO_{3.954}N_{0.046}$

Nitrogen loss was also seen in the data for N-doped Li_3PO_4 and Li_3VO_4. It is possible that nitrogen-doping of these materials is impractical after all. It is also possible that a
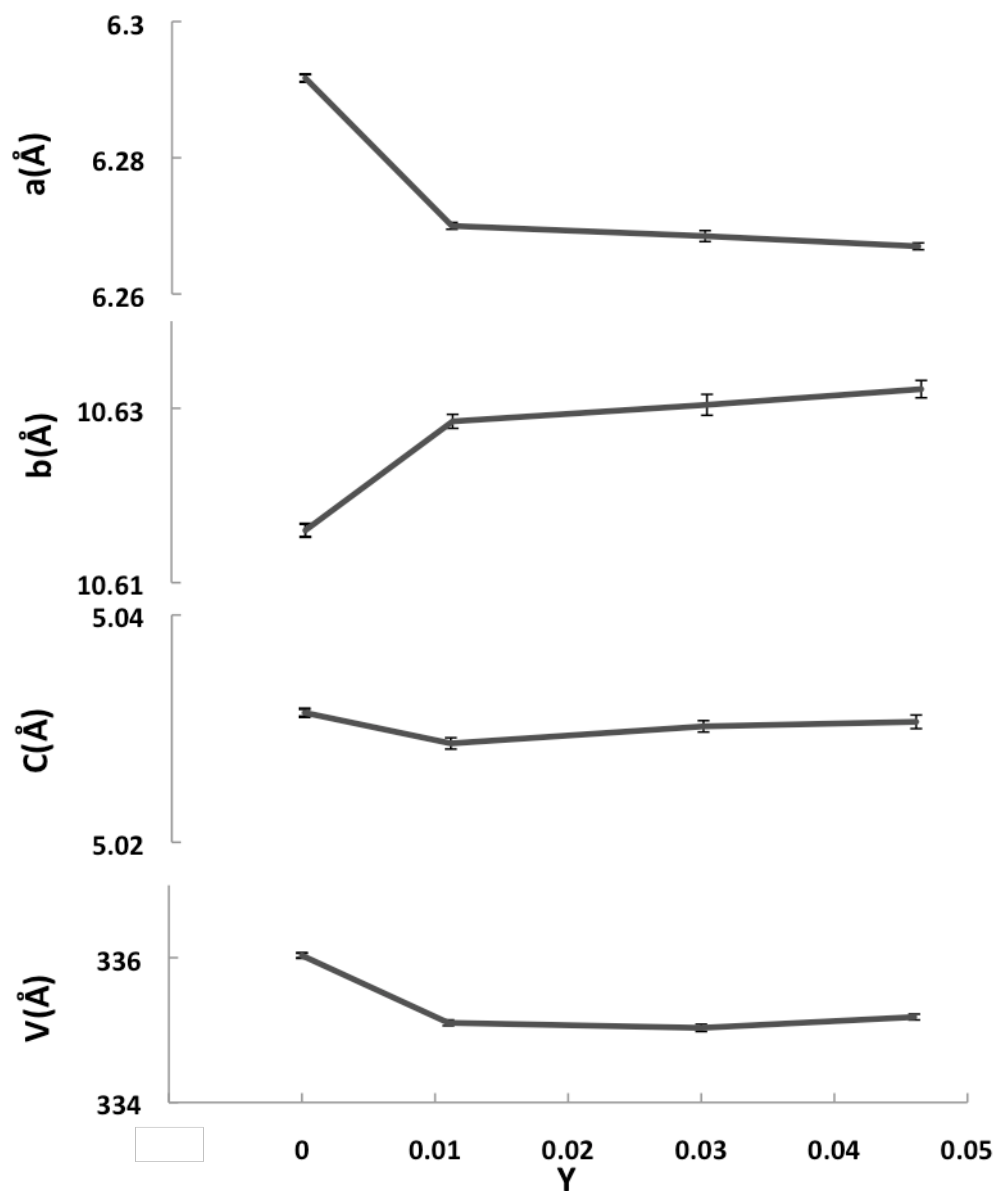
Figure 5.30. Change in unit cell parameters in Li$_{2+Y}$ZnSiO$_{4-Y}$N$_Y$ with increasing Y (Y is corrected according to combustion analysis results).

smaller content of nitrogen than calculated is due to loss of nitrogen before and/or during the synthesis.

Conclusions

Ceramics with the Li$_{2+Y}$ZnSiO$_{4-Y}$N$_Y$ ($0 \leq Y \leq 0.6$) and Li$_{2+Y}$MgSiO$_{4-Y}$N$_Y$ ($0 \leq Y \leq 0.8$) formula have been synthesised via solid-state reaction. In Li$_{2+Y}$ZnSiO$_{4-Y}$N$_Y$, phase-pure products were achieved in all compositions. The X-ray diffraction patterns of compositions with $Y \leq 0.1$ matched that of γ_0-Li$_2$ZnSiO$_4$ and are indexed as monoclinic ($P2_1/n$) within errors. Compositions with $Y \geq 0.2$ matched data for the lithia-γ_0

polymorph, similar to Li-rich lithium zinc silicates ($Li_{2+2X}Zn_{1-X}SiO_4$). These compositions can be indexed with the $P2_1/n$ symmetry only with large errors (especially in Y=0.6), suggesting that the proposed unit cell may not be correct. Cell parameter variations indicated that the N-doped sample with the γ_0 structure has a smaller unit cell volume (similar to Li-rich lithium zinc silicates with the γ_0 structure). The γ_0 phase transforms to lithia-γ_0 upon adding more nitrogen and cell volume remains more or less unchanged (Y$\geq$0.2).

In $Li_{2+Y}MgSiO_{4-Y}N_Y$, compositions with Y$\leq$0.2 have the γ_0 structure and can be indexed as monoclinic ($P2_1/n$) within errors. In these compositions there is also some Li_2SiO_3 secondary phase present. It was suggested that solid solutions close to the 1:1 composition are subject to lithia loss. In Y=0.4 lithia-γ_0 and in compositions with Y$\geq$0.5 mixtures of lithia-γ_0 and a Li_4SiO_4-type phase were obtained. These compositions can be indexed only with the $P2_1/n$ symmetry with large errors suggesting that they might have a different unit cell. Cell parameter variations indicated that cell volume decreases considerably in Y$\leq$0.2 while have γ_0 phase, but increases by adding more nitrogen and transforming to lithia-γ_0 phase (Y$\geq$0.4). In this situation it is difficult to separate the effect of nitrogen doping and polymorphic transformation on the unit cell parameters of N-doped $Li_2(Zn,Mg)SiO_4$.

Electrical property studies indicate improvement of the ionic conductivity by 4-6 orders of magnitude in N-doped samples, similar to Li-rich lithium zinc silicates ($Li_{2.4}Zn_{0.8}SiO_4$ and $Li_{2.8}Zn_{0.6}SiO_4$). Furthermore, the activation energy of conduction for N-doped samples decreased dramatically. Arrhenius plots of both N-doped and Li-rich compositions show fully reversible, nonlinear behavior at temperatures above $\approx$200°C. Results also indicate a reversible ageing effect, which was also seen in some other γ-structure materials. Several possibilities were suggested including phase transition, nitrogen loss and change in conduction mechanism.

The nitrogen contents were determined for all samples using combustion analysis. The results indicate the presence of some nitrogen in the nitrogen-doped samples but the nitrogen content is significantly lower than expected, indicating nitrogen loss before or during the synthesis.

Chapter 6

Overall discussion, conclusions and future work

"A conclusion is the place where you get tired of thinking."

— Arthur Bloch

Discussion

Improvement in ionic conductivity of solid solutions based on γ structures by cation doping has been extensively examined previously [145]. This study is one of the very first to investigate anion doping of crystalline, Li_3PO_4-based materials, prepared by high temperature solid-state reaction. Amorphous lithium phosphorus oxynitrides, both in thin film and bulk glass form, have been extensively studied and excellent ionic conductivity and chemical stability was seen in thin film LiPON [57]. Despite its desirable characteristics, the detailed structure and the effect of nitrogen on its properties are not known. There are two studies on synthesis and characterisation of crystalline lithium phosphorus oxynitrides; first, based on formation of lithium vacancies in the structure of Li_3PO_4 following substitution of oxygen by nitrogen [75] and second, Li_2PO_2N that is derived from the structure of $LiPO_3$, by modification of the phosphate chains following introduction of nitrogen [78]. Computational studies on Li-ion conduction of Li_3PO_4 predict that an interstitial defect mechanism would provide the most efficient Li-ion transport [80]. The aim of this project was to investigate the possible formation of crystalline, Li_3PO_4-type materials, based on an interstitial defect mechanism using conventional solid-state reaction and characterise their properties.

Samples were prepared by solid-state reaction between Li_3N (as nitrogen-containing reactant) and several other precursors in a N_2 atmosphere. Li_3N is very reactive, therefore enormous care has to be taken in order to minimise its contact with atmosphere. Synthesis procedures were designed in a way to reduce any possible

nitrogen loss before and/or during the synthesis. A new modified synthesis technique was employed in order to prepare several new solid solutions. The technique was based on using Li_3N as a nitrogen-containing reactant and N_2 as protective gas. Consequently, N-doped samples were prepared inside an argon-filled glove box, placed on a Mo foil inside a sealable silica tube ampoule and fired in a horizontal tube furnace under N_2. The technique was first used to synthesise N-doped Li_3PO_4 and then continued with the synthesis of $Li_{(3+X)}VO_{4-X}N_X$ and $Li_{2+Y}(Zn,Mg)SiO_{4-Y}N_Y$ solid solutions.

These N-doped compositions are mainly phase pure by X-ray diffraction. Appearance of secondary phases was seen only in nitrogen-rich, N-doped compositions of Li_3PO_4 and $Li_2(Zn,Mg)SiO_4$ and also in N-doped Li_2MgSiO_4 close to the 1:1 composition, where lithia loss had been reported previously [175]. Combustion analysis of these N-doped materials revealed that a great deal of nitrogen loss had occurred. The best results were found in N-doped Li_3PO_4, where in $Li_{3.4}PO_{3.6}N_{0.4}$ for instance, about 10% of the targeted nitrogen was found in the sample ($Li_{3.043}PO_{3.957}N_{0.043}$). In N-doped Li_3VO_4, the majority of nitrogen was lost (more than 98% in $Li_{3.6}VO_{3.4}N_{0.6}$); yet no evidence of secondary phases could be found in the XRD pattern of both compositions. Li_3N is unstable at elevated temperatures and if it has not participated in the formation of $Li_{3.6}VO_{3.4}N_{0.6}$, it must have decomposed and most likely reacted with the oxygen (carbon dioxide) from the raw materials and/or atmosphere to make more stable Li_2O (Li_2CO_3). Assuming all the $(0.6)Li_3N$ that participated in the formation of $Li_{3.6}VO_{3.4}N_{0.6}$ has decomposed:

$$(0.6)Li_3N + (0.45)O_2 \rightarrow (0.9)Li_2O + (0.3)N_2 \text{ or}$$

$$(0.6)Li_3N + (0.9)CO_2 + (0.45)O_2 \rightarrow (0.9)Li_2CO_3 + (0.3)N_2.$$
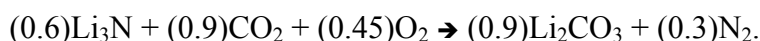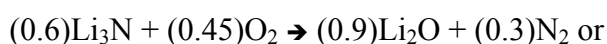
The limit of detection of secondary phases in powder X-ray diffraction method is typically a few percent. $0.9\ Li_2O(Li_2CO_3)$ could take account for about 20(weight)% of the whole sample and consequently, extra phase(s) should have appeared in the XRD pattern as secondary phase(s). The fact that, from the conductivity data, the extra lithium seems to be in the structure may suggest that some nonstoichiometry of lithium has arisen as a result of extra Li^+ ($Li_{(3+X+\square)}VO_{4-X}N_X$).

The extra Li^+ ($\square$) in the structure of N-doped Li_3PO_4-type materials can be compensated by several mechanisms:

1. The oxidation state of P^{5+}/V^{5+}, for instance, can partially change to lower oxidation states.

2. Nonstoichiometry of other cations in the structure, for example: $Li_{(2+Y+\square)}Zn_{(1+X)}Si_{(1-X)}O_{4-Y}N_Y$ or $Li_{(3+X+\square)}V_{(1-Y)}O_{4-X}N_X$

3. Possible reaction with Mo foil or silica tube: $Li_{(3+Y+\square)}V_{(1-X)}Mo_{(1+X)}O_{4-Y}N_Y$ or $Li_{(3+Y+\square)}P_{(1-X)}Si_{(1+X)}O_{4-Y}N_Y$

The second and third mechanisms would have lead to secondary phase formation and the first mechanism would have enhanced the electronic conductivity, neither of which was seen in our experiments.

Nitrogen loss was also apparent in two previous studies on crystalline LIPON. Wang et al [75] estimated the nitrogen content of their expected end product (2/3Li$_3$N+ LiPO$_3$→Li$_3$PO$_3$N$_{2/3}$) to be $Li_{2.88}PO_{3.73}N_{0.14}$ (≈75% loss), from the total weight gain during TGA measurements in oxygen atmosphere. In a more recent study by Holzwarth et al [78], it was found that a slight excess of P$_3$N$_5$ precursor was needed in order to achieve a single phase product, although non-air-sensitive P$_3$N$_5$ was used instead of Li$_3$N. In none of the above studies was the actual content of nitrogen directly measured. The smaller than expected content of nitrogen can be related to either the difficulty of doping with nitrogen and/or loss of nitrogen before/during/after synthesis. The loss of nitrogen could be due to the high temperature required for the solid-state reaction, as it was seen in higher nitrogen detection of N-doped Li$_3$PO$_4$ compare to N-doped Li$_3$VO$_4$, perhaps due to the lower decomposition temperature of diammonium phosphate compared to vanadium oxide. Moreover, it is possible that despite all the precautions, nitrogen is lost by the early decomposition of Li$_3$N before or during the reaction due to its severe reactivity. It is also possible that N-doped products have been decomposed prior to nitrogen analysis.

Nitrogen doping of all compositions yielded a γ-type phase or solid solutions, except in Li$_3$VO$_4$ that resulted in a β phase. XRD patterns of $Li_{3+X}(P,V)O_{4-X}N_X$ are similar to the undoped polymorphs (γ-Li$_3$PO$_4$ and β$_{II}$-Li$_3$VO$_4$), suggesting that they have comparable structures with similar unit cells and space groups (orthorhombic with *Pnma* symmetry for Li$_3$PO$_4$ and orthorhombic with *Pmn2$_1$* symmetry for Li$_3$VO$_4$). The unit cell parameters vary only slightly by adding nitrogen, especially for Li$_3$VO$_4$. X=0.2 was suggested as the solid solution limit, as the variation is more considerable up to this

composition in both systems. The unit cell parameter variation is more significant in $Li_{2+Y}(Zn,Mg)SiO_{4-Y}N_Y$. Compositions with low concentration of nitrogen have the γ_0 structure (monoclinic with $P2_1/n$ symmetry), similar to undoped polymorphs. Compositions with higher concentrations of nitrogen match with Li-rich, lithium zinc (magnesium) silicates: lithia-γ_0 for N-doped Li_2ZnSiO_4 and a mixture of lithia-γ_0 and Li_4SiO_4-type phase in N-doped Li_2MgSiO_4. Nitrogen doping seems to encourage monoclinicity, similar to Li-rich compositions, by distorting the γ_0 phase to lithia-γ_0. Lithia-γ_0 can not be straightforwardly indexed with the same symmetry as the γ_0 phase, suggesting that samples with higher concentration of nitrogen probably have a different symmetry or unit cell to those of the γ_0 polymorph.

The unit cell volume decreases in N-doped Li_3PO_4 and increases in N-doped Li_3VO_4; however, the change is less significant in the latter case. This might be due to the fact that the content of nitrogen in N-doped Li_3VO_4 was measured to be considerably lower than that in N-doped Li_3PO_4. In $Li_{2+Y}(Zn,Mg)SiO_{4-Y}N_Y$, samples with the γ_0 structure have smaller unit cell volumes compared to $Li_2(Zn,Mg)SiO_4$. By adding more nitrogen samples transform from γ_0 to lithia-γ_0 polymorphs, consequently the unit cell volume remains unchanged in N-doped Li_2ZnSiO_4 but increases in N-doped Li_2MgSiO_4. In this situation it is difficult to separate the effect of nitrogen doping and polymorphic transformation on the unit cell parameters. Decreasing of the unit cell volume in $Li_{2.1}ZnSiO_{3.9}N_{0.1}$, with the γ_0 structure, is in accordance with the cell volume extraction in $Li_{2.8}Zn_{0.6}SiO_4$, also in the γ_0 form.

Nitrogen is expected to replace an oxygen in the $P(V, Si)O_4$ group to create a $P(V, Si)O_3N$ tetrahedron and an interstitial lithium. The ionic radii of oxygen and nitrogen in tetrahedral coordination are quite similar (1.24 and 1.32 Å respectively) and therefore not a great deal of unit cell volume expansion is expected on substituting oxygen by nitrogen. Especially, in N-doped $Li_3(P,V)O_4$ hardly any change in the intensity distribution of XRD patterns and peak positions occurred, which could indicate the existence of an almost ideal solid solution. In two previous studies on crystalline LIPON, Wang et al [75] reported a slight increase in the unit cell volume of their N-doped material, which has 4% Li and 3.25% anion vacancy per formula unit ($Li_{3-X}PO_{4-2X}N_X$), based on the γ-Li_3PO_4 structure. In the second work by Holzwarth et al [78], no judgment on cell parameter variation can be made as the parent material $LiPO_3$ and the N-doped component Li_2PO_2N (based on the Li_2SiO_3 structure), have different structures.

It is useful to compare the unit cell variation data, from the XRD results, to combustion analysis data in order to estimate the overall nitrogen content. In $Li_{3+X}(P,V)O_{4-X}N_X$, where X=0.2 was indicated as the solid solution limit, the nitrogen content was suggested to be around 0.012 mol in LiPON and 0.0013 mol in LiVON respectively. In compositions with X>0.2, which are beyond the solid solution limit, more nitrogen could be found in the sample, suggesting that other nitrogen-containing components might be present in the sample. Li_3N decomposes at elevated temperature and therefore is unlikely to be present in the sample following synthesis. Earlier it was suggested that some nonstoichiometry of P/V/Si or possible reaction of sample with Mo foil is essential to compensate for the extra lithium that is believed to be in the sample (mechanism 2 and 3). It can be suggested that extra P/V/Si from these reactions perhaps reacted with nitrogen and therefore were detected by N-analysis. None of the discussed secondary phases (Li_3N, V_3N_5, P_3N_5 and Si_3N_4) could be detected by XRD.

Electrical properties were studied using impedance spectroscopy over a range of temperature. High-density pellets were prepared by a one-step, reaction-sintering synthesis. Net pellet conductivity values were obtained from impedance complex plane plots. In the majority of cases a single, somewhat broadened, semicircle was seen in the impedance plane plots (Z^*), with an associated capacitance in the range of 10^{-12} Fcm^{-1}, indicative of a bulk response. In some cases, a second component was present. From the X-ray diffraction results no consistent relationship between the occurrence of a second component and presence of the additional phases could be seen. Hence, the second component and the grains should have the same composition and the second component is probably due to poorly resolved grain boundary resistances.

It was found that nitrogen doping significantly improved the ionic conductivity by about two orders of magnitude in N-doped $Li_3(P,V)O_4$ and by 4-6 orders of magnitude in N-doped $Li_2(Zn,Mg)SiO_4$. The impedance data also showed clear evidence of a blocking electrode response in the Z^* plane plots for N-doped samples, evidenced by a low frequency inclined spike with associated capacitance values in the range of 10^{-6} Fcm^{-1}. The high capacitance values indicate that the level of electronic conductivity in these N-doped compositions is small or negligible [128]. This is consistent with the view that the principal current carriers are lithium ions [49, 183].

Electrical conductivity was determined as a function of temperature and linear Arrhenius behaviour was observed for $Li_3P(V)O_4$ and $Li_2(Zn,Mg)SiO_4$ at all

temperatures, for N-doped $Li_3(P,V)O_4$ below ≈350°C and for N-doped $Li_2(Zn,Mg)SiO_4$ below ≈200°C. From the linear part of the plots, the activation energy (Ea) was calculated, which indicates a decrease by about 0.3 eV in N-doped $Li_3(P,V)O_4$, between 0.05-0.15 in N-doped Li_2ZnSiO_4 with low concentration of nitrogen and between 0.6-0.7 in N-doped Li_2ZnSiO_4 with high concentrations of nitrogen and N-doped Li_2MgSiO_4. Higher ionic conductivity and lower activation energy in N-doped samples was attributed to the high number of interstitial lithium ions created as the result of the substitution of nitrogen for oxygen. Ionic conductivity data of N-doped Li_3PO_4 (2.5×10^{-14} Scm^{-1} at 25°C and activation energy of 0.91 eV) is comparable to those of reported by Wang et al [75] and to computational studies that predicted the migration energy of N-doped Li_3PO_4 with a PO_3N defect and lithium interstitial to be 0.9 eV [76]. N-doped Li_2ZnSiO_4 also showed similar conductivities to Li-rich compositions ($Li_{2+2X}Zn_{1-X}SiO_4$).

Above ≈350°C for N-doped $Li_3(P,V)O_4$ and ≈200°C for N-doped $Li_2(Zn,Mg)SiO_4$ a fully reversible, nonlinear behaviour was evidenced, where the curvature in Arrhenius plots leads to near zero activation energies (apart from $Li_{3.2}VO_{3.8}N_{0.2}$, which will be discussed later). Such behaviour was also seen in $Li_{2+2X}Zn_{1-X}SiO_4$ in which no N-doping occurred. N-doped $Li_2(Zn,Mg)SiO_4$ also showed signs of ageing, which can be recovered by reheating to high temperature. Such behaviour has been seen in many fast ionic conductors, either glassy [185] or crystalline [186], oxide ion conductors [187], perovskite lanthanum lithium titanate [40] and many γ-structure materials [145, 181, 182]. The conduction mechanism of systems with low concentrations of charge carriers can be explained by point defect models, unlike systems with large carrier concentration that can not be simply described by such models. The origin of non-linear behavior of fast ionic conductors is not clear. A number of theories and possibilities are given by different authors including: trapping of mobile ions by the immobile sublattice at lower temperatures [111], different types of defect clusters and conduction mechanisms at high and low temperatures [50, 51], a liquid-like disorder of mobile ions after a glass-type phase transition [52, 183] and opening up of new conduction paths at high temperatures [187].

DSC results show an endothermic transition for N-doped compositions and TGA results indicate weight gain in N-doped $Li_3(P,V)O_4$ on heating. As a result, several other possibilities for nonlinear Arrhenius behavior of these materials were suggested including: phase transition, nitrogen loss and proton conduction. Polymorphism is quite common among these materials and the effect of it on conductivity was reported

previously [173]. The polymorphic transformation of $Li_{2.6}ZnSiO_{3.4}N_{0.6}$, in particular, was discussed in chapter 5 and suggested as one of the possible explanations of Arrhenius nonlinear behaviour. DSC/TGA results can indicate the possibility of sample reaction with atmosphere. First, sample reaction with O_2/CO_2 can lead to partial nitrogen loss and decomposition of the sample (as was seen in $Li_{3.2}VO_{3.8}N_{0.2}$) and second, sample reaction with H_2O, which, in the presence of oxide ion vacancies, can lead to proton conduction [188]. In all TGA experiments (apart from $Li_{3.2}VO_{3.8}N_{0.2}$), the weight gain was followed by weight loss at higher temperatures and weight gain on cooling. Furthermore, no sign of sample degradation could be seen either by X-ray diffraction or by impedance measurements. $Li_{3.2}VO_{3.8}N_{0.2}$ showed no sign of weight loss. Degradation of $Li_{3.2}VO_{3.8}N_{0.2}$ at high temperatures was shown by XRD and IS measurements, suggesting that a partial, irreversible, reaction between the sample and CO_2 occurred. Comparing the TGA results of $Li_{3.2}VO_{3.8}N_{0.2}$ with other samples, it is reasonable to suggest that in N-doped $Li_3(P,V)O_4$ either the reaction between the sample and atmosphere happens on a small scale and can not be detected by XRD/IS or a reverse reaction occurs on cooling.

Electrochemical testing was performed on $Li_{3.4}VO_{3.6}N_{0.4}$ and compared with Li_3VO_4. Both materials demonstrate an average working voltage between 0.8-1.2V. The Li_3VO_4 did not show the good electrochemical properties reported by Li et al [16] and failed after the first cycle, perhaps due to an increase in the internal impedance as a result of poor electronic/ionic conductivity and/or irreversible phase transformation. Unsuccessful intercalation of lithium into Li_3VO_4 was also reported previously [83] and believed to be due to its low electronic conductivity. Using conductive additives and reducing particle size may overcome this drawback. The $Li_{3.4}VO_{3.6}N_{0.4}$ cell showed improved electrochemical performance on the first cycle, attributed to its enhanced ionic conductivity. A modified charging regime and a reduced particle size was suggested to improve its cycle performance. The average working voltage of $Li_{3.4}VO_{3.6}N_{0.4}$ is low and it shows a promising ionic conductivity. Moreover, its theoretical capacity can exceed 400 mAh/g [16] (based on insertion/extraction of two Li^+), therefore by improving its electronic conductivity, it might be a potential anode material.

Conclusions

- A new modified solid-state synthesis technique was employed, using Li_3N as nitrogen-containing reactant and N_2 as protective gas. Due to severe reactivity of Li_3N with the atmosphere, an argon-filled glove box, sealable silica tube ampoule and horizontal tube furnace were employed to reduce any possible nitrogen loss before and/or during the synthesis. Several new crystalline, Li_3PO_4-based, materials, based on creation of interstitial lithium ions were synthesised, in order to enhance Li-ion conductivity.

- $Li_{(3+X)}(P,V)O_{4-X}N_X$ and $Li_{2+Y}(Zn,Mg)SiO_{4-Y}N_Y$ solid solutions have been identified single phase by X-ray diffraction. Secondary phases were seen only in nitrogen-rich, N-doped compositions of Li_3PO_4 and $Li_2(Zn,Mg)SiO_4$ and also in N-doped Li_2MgSiO_4 close to the 1:1 composition, where lithia loss had been reported previously.

- XRD patterns of N-doped $Li_3(P,V)O_4$ are similar to the undoped polymorphs suggesting that they have comparable structures with similar unit cells and space groups. N-doping decreases the unit cell volume in Li_3PO_4 and increases it in Li_3VO_4 and the solid solution limit is X=0.2 in both systems. However, the unit cell variation is small upon adding nitrogen. The variation is more significant in $Li_{2+Y}(Zn,Mg)SiO_{4-Y}N_Y$. XRD patterns of compositions with low concentrations of nitrogen are similar to undoped polymorphs (γ_0). Nitrogen doping encourages the monoclinicity by distorting the γ_0 phase to lithia-γ_0. Compositions with higher concentrations of nitrogen match with Li-rich compositions in $Li_{2+2X}(Zn,Mg)_{1-X}SiO_4$. N-doped samples with γ_0 structure have smaller cell volume compared to undoped samples. By adding more nitrogen, γ_0 structure transform to lithia-γ_0, consequently the unit cell volume remains unchanged in N-doped Li_2ZnSiO_4 and increases in N-doped Li_2MgSiO_4.

- N-doping significantly improved the conductivity by about two orders of magnitude in N-doped $Li_3(P,V)O_4$ and by 4-6 orders of magnitude in N-doped $Li_2(Zn,Mg)SiO_4$ from the impedance spectroscopy experiments. The data indicated that the level of electronic conductivity in N-doped compositions is small or negligible and the principal current carriers are lithium ions. Arrhenius behaviour was observed for $Li_3(P,V)O_4$ and $Li_2(Zn,Mg)SiO_4$ at all temperatures and for N-doped $Li_3(P,V)O_4$ and

$Li_2(Zn,Mg)SiO_4$ below $\approx 350°$ and $200°C$, respectively. Activation energies significantly decreased in N-doped samples. Improvement in the ionic conductivity of N-doped Li_3PO_4 is comparable to experimental and computational studies reported in the literature. Higher ionic conductivity and lower activation energy in N-doped samples was attributed to the high number of interstitial lithium ions created as the result of the substitution of nitrogen for oxygen. Interstitial lithium formation in Li_2ZnSiO_4 by cation and anion doping showed similar enhanced electrical effects.

- Above the mentioned temperatures a fully reversible, nonlinear behavior was evidenced, where the curvature in Arrhenius plots leads to near zero activation energies similar to many fast ionic conductors and $Li_{2+2X}Zn_{1-X}SiO_4$. TGA/DSC results indicated that N-doped samples might have reacted with atmosphere at high temperatures.

- Combustion analysis confirmed nitrogen incorporation into the N-doped samples. It was revealed that a great deal of nitrogen loss had occurred that was also reported in previous studies of crystalline LiPON. Nitrogen loss was suggested to be due to the high temperature required for the solid-state reaction, early decomposition of Li_3N and/or by decomposition of N-doped products before N-analysis.

- Electrochemical testing was performed on $Li_{3.4}VO_{3.6}N_{0.4}$ and compared with Li_3VO_4. $Li_{3.4}VO_{3.6}N_{0.4}$ showed improved electrochemical properties such as higher (dis)charge capacity and improved cycle life due to its enhanced ionic conductivity. Due to its low working voltage (0.8-1.2V), high capacity and reasonable cycling performance it was suggested as a potential candidate for anode material.

Future work

While this thesis has demonstrated the effect of nitrogen doping on properties of some of the crystalline, Li_3PO_4-type materials, many aspects for studying the effectiveness of nitrogen doping still remain and therefore further work in these areas is needed:

- Optimization of synthesis procedures to reduce likely nitrogen loss and look into possible alternative synthesis methods such as sol-gel and ammonolysis.

129

- Structural studies by TEM to confirm nitrogen incorporation into the structure and also ascertain the space group for the N-doped $Li_2(Zn,Mg)SiO_4$ phases.
- Neutron diffraction studies on new N-doped phases to determine the structure and also to detect any possible secondary phases.
- Extensive and improved electrochemical analysis of the N-doped samples, in particular look into assembly of an all-solid-state battery with the new N-doped samples as solid electrolytes.
- High temperature XRD studies on the possible phase transformation of N-doped compositions evidenced in DSC experiments.

It would be also interesting to investigate:

- N-doping of other γ-type structure materials (like Li_3AsO_4, Li_4SiO_4 and Li_2ZnGeO_4) in order to improve their ionic conductivity
- N-doping in order to improve the ionic and/or electronic conductivity in materials with mixed oxidation cations as was shown by a considerable improvement in the electronic conductivity of $Li_2FeP_2O_{6.95}N_{0.05}$ [189].

References

1. A. Manthiram, in *Lithium Batteries: Science and Technology*, ed. G-A. Nazri, G. Pisoia, Kluwer Publishing Company, 2004, p. 3.

2. Y. Nishi, in *Lithium Ion Batteries: Fundamentals and Performance*, ed. M. Wakihara, O. Yamamoto, Kodansha, 1998, p. 181.

3. Y. Lu, Z. Tu, L.A. Archer, *Nature Materials*, 2014, **13**, 961-969.

4. K. Mizushima, P.C. Jones, P.J. Wiseman, J.B. Goodenough, *Mater. Res. Bull.*, 1980, **15**, 783-789.

5. T. Nagaura, K. Tozawa, *Prog. Batteries Solar Cells*, 1990, **9**, 209.

6. J.-M. Tarascon, M. Armand, *Nature*, 2001, **414**, 359.

7. J. Alper, *Science*, 2002, **296**, 1224.

8. M.S. Whittingham, *Chem. Rev.*, 2004, **104**, 4271.

9. J. Kim, B.H. Kim, Y.H. Baik, P.K. Chang, H.S. Park, K. Amine, *J. Power Sources*, 2006, **158**, 641.

10. T. Ohzuku, Y. Makimura, *Chem. Lett.* , 2001, 744.

11. M.S. Whittingham, *Science* 1976, **192**, 1126.

12. M.S. Whittingham, *J. Electrochem. Soc.*, 1976, **123**, 315.

13. M.M. Thackeray, *Prog. Solid State Chem.*, 1997, **25**, 1-71.

14. A.K. Padhi, K.S. Nanjundaswamy, J.B. Goodenough, *J. Electrochem. Soc.*, 1997, **144**, 1188.

15. WJ. Zhang, *J. Power Sources*, 2011, **196**, 13-24.

16. H. Li, X. Liu, T. Zhai, D. Li, H. Zhou, *Adv. Energy Mater.*, 2013, **3**, 428.

17. R. Benedek, M.M. Thackeray, *J. Power Sources*, 2002, **110**, 406.

18. P.G. Bruce, B. Scrosati, J.M. Tarascon, *Angew. Chem. Int. Ed.*, 2008, **47**, 2930.

19. T. Ohzuku, A. Ueda, N. Yamamoto, *J. Electrochem. Soc.*, 1995, **142**, 1431.

20. R.M. Dell, D.A.J. Rand, *Understanding Batteries*, RSC paperbacks, 2001.

21. M. Contestabile, M. Morselli, R. Paraventi, R.J. Neat, , *J. Power Sources*, 2003, **119/121**, 943.

22. P.V. Wright, *Br. Polym. J.*, 1975, **7**, 319.

23. J.Y. Song, Y.Y. Wang, C.C. Wan, *J. Power Sources* 1999, **77**, 183.

24. K. Xu, *Chem. Rev.*, 2004, **104**, 4303.

25. T. Minami, M. Tatsumisago, M. Wakihara, C. Iwakura, S. Kohjiya, I. Tanaka, *Solid State Ionics for Batteries*, Springer-Verlag, 2005.

26. N.J. Dudney, in *Lithium Batteries: Science and Technology*, ed. G-A. Nazri, G. Pisoia, Kluwer Publishing Company, 2004, pp. 623-642.

27. S. Kondo, in *Lithium Ion Batteries: Fundamentals and Performance*, ed. M. Wakihara, O. Yamamoto, Kodansha, 1998, p. 199.

28. J.F.M. Oudenhoven, L. Baggetto, P.H.L. Notten, *Adv. Energy Mater.*, 2011, **1**, 10-33.

29. A. Patil, V. Patil, D. Shin, J-W. Choi, D-S. Paik, S-J.Yoon, *Mat. Res. Bull.*, 2008, **43**, 1913.

30. N. Kamaya, K. Homma, Y. Yamakawa, M. Hirayama, R. Kanno, M. Yonemura, T. Kamiyama, and S. H. Y. Kato, K. Kawamoto, A. Mitsui, *Nature Materials*, 2011, **10**, 682.

31. C.R. Schlaikjer, C.C. Liang, *J. Electrochem. Soc.*, 1971, **118**, 1447.

32. R.F. Bartholomew, D.M. Young, A.J.G. Ellison, *J. Non-Cryst. Sol.*, 1999, **257**, 242.

33. J.H. Kennedy, Y. Yang, *J. Solid State Chem.*, 1987, **69**, 252.

34. Y. Yang, Y. Jia, Z. Yao, *Solid State Ionics*, 1997, **96**, 215.

35. Y. Tomita, H. Ohki, K. Okuda, *Z Naturfosch. A*, 2000, **55**, 117.

36. R. Rabenau, *Solid State Ionics*, 1981, **6**, 267.

37. T. Lapp, S. Skaarup, A. Hooper, *Solid State Ionics*, 1983, **11**, 97.

38. Y. Inaguma, C. Liquan, M. Itoh, T. Makamura, T. Uchida, H. and M. W. Ikuta, *Solid State Comm.*, 1993, **86**, 689.

39. O. Bohnke, *Solid State Ionics*, 2008, **179**, 9.

40. O. Bohnke, C. Bohnke, J.L. Fourquet, *Solid State Ionics*, 1996, **91**, 21-31.

41. S. Stramare, V. Thangadurai, W. Weppner,, *Chem. Mater.*, 2003, **15**, 3974.

42. J.B. Goodenough, H.Y.-P. Hong, J.A. Kafalas, *Mat. Res. Bull.*, 1976, **11**, 203.

43. L.O. Hagman, P. Kierkegard,, *Acta Chem. Scand.*, 1968, **22**, 1822.

44. H. Aono, E. Sugimoto, Y. Sadaoka, G. Adachi, *J. Electrochem. Soc.*, 1989, **136**, 590.

45. B.V.R. Chowdari, K. Radhakrishnan, K.A. Thomas, G.V. Subba Rao, *Mat. Res. Bull.*, 1989, **24**, 221.

46. P.G. Bruce, A.R. West, *Mat. Res. Bull.*, 1980, **15**, 117.

47. H.Y-P. Hong, *Mater. Res. Bull.*, 1978, **13**, 117.

48. K. Fujimura, A. Seko, Y. Koyama, A Kuwabara, I. Kishida, K. Shitara, C.A.J. Fisher, H. Moriwake, I. Tanaka, *Adv. Energy Mater.*, 2013, **3**, 980.

49. A.R. Rodger, J. Kuwano, A.R. West, *Solid State Ionics*, 1985, **15**, 185.

50. P.G. Bruce, I. Abrahams, A.R. West, *Solid State Ionics*, 1990, **40-41**, 293.

51. P.G. Bruce, I. Abrahams, *J. Solid State Chem.*, 1991, **95**, 74-82.

52. C.K. Lee, A.R. West, *J. Mat. Chem.*, 1991, **1**, 91.

53. R. Kanno, T. Hata, Y. Kawamoto, M. Irie, *Solid State Ionics*, 2000, **130**, 97.

54. S. Kondo, K. Takada, Y. Yamaura, *Solid State Ionics* 1992, **53-56**, 1183.

55. M. Murayama, R. Kanno, M. Irie, S. Ito, T. Hata, N. Sonoyama, Y. Kawamoto,, *J. Solid State Chem.*, 2002, **168(1)**, 140.

56. R. Kanno, M. Murayama, *J. Electrochem. Soc.* , 2001, **148**, A742.

57. J.B. Bates, N.J. Dudney, G.R. Gruzalski, R.A. Zuhr, A. Choudhury, C.F. Luck, J.D. Robetson, *J. Power Sources*, 1993, **43-44**, 103.

58. K. Kanehori, K. Matsumoto, K. Miyauchi, T. Kudo, *Solid State Ionics*, 1983, **9-10**, 1445.

59. J.B. Bates, N.J. Dudney, G.R. Gruzalski, R.A. Zuhr, A. Choudhury, C.F. Luck, J.D. Robetson, *Solid State Ionics*, 1992, **53-56**, 647-654.

60. X. Yu, J.B. Bates, G.E. Jellison Jr., F.X. Hart, *J. Electrochem. Soc.*, 1997, **44**, 524.

61. H. Ohtsuka, S. Okada, J. Yamaki, *Solid State Ionics* 1990, **40**, 964.

62. R. Creus, J. Sarradin, R. Astier, A. Pradel, A.M. Ribes, *Mater. Sci. Eng.* , 1989, **B3**, 109.

63. S.D. Jones, J.R. Akridge, *Solid State Ionics* 1992, **53-6**, 628.

64. K. Takada, N. Aotani, K. Iwamoto, S. Kondo, *Solid State Ionics*, 1995, **79**, 284.

65. B. Wang, J.B. Bates, F.X. Hart, B.C. Sales, R.A. Zuhr, J.D. Robertson, *J. Electrochem. Soc.*, 1996, **143**, 3203.

66. M. Baba, N. Kumagai, N. Fujita, K. Ohta, K. Nishidate, S. Komaba, H. Groult, D. Devilliers, B. Kaplan, *J. Power Sources*, 2001, **97-98**, 798.

67. F. Muñoz, L. Pascual, A. Durán, L. Montagne, R. Berjoan, G. Palavit, R. Marchand, *J. Non-Cryst. Solids*, 2003, **324**, 142.

68. L. Boukbir, R. Marchand, *Rev. Chim. Miner.*, 1986, **23**, 343.

69. R. Marchand, *J. Non-Cryst. Solids* 1983, **56**, 173.

70. B. Wang, B.S. Kwak, B.C. Sales, J.B. Bates, *J. Non-Cryst. Solids*, 1995, **183**, 297-306.

71. F. Muñoz, L. Pascual, A. Durán, J. Rocherullé, R. Marchand, *C. R. Chimie*, 2002, **5**, 731.

72. R. Marchand, D. Agliz, L. Boukbir, A. Quémerais, *J. Non-Cryst. Solids*, 1988, **103**, 35.

73. F. Muñoz, A. Durán, L. Pascual, L. Montagne, B. Revel, A.C.M. Rodrigues, *Solid State Ionics*, 2008, **179**, 574.

74. F. Muñoz, *J. Power Sources*, 2012, **198**, 432.

75. B. Wang, B.C. Chakoumakos, B.C. Sales, B.S. Kwak, J.B. Bates, *J. Solid State Chem.*, 1995, **115**, 313-323.

76. Y.A. Du, N.A.W. Holzwarth, *Phys. Rev.*, 2008, **B78**, 174301.

77. H. Rabaa, R. Hoffmann, *J. Solid State Chem.*, 1999, **145**, 619-628.

78. K. Senevirathne, C.S. Day, M.D. Gross, A. Lachgar, N.A.W. Holzwarth, *Solid State Ionics*, 2013, **233**, 95-101.

79. Y.A. Du, N.A.W. Holzwarth, *Phys. Rev.*, 2010, **B81**, 184106.

80. Y.A. Du, N.A.W. Holzwarth, *Phys. Rev.*, 2007, **B76**, 174302.

81. Y.A. Du, N.A. W. Holzwarth, *J. Electrochem. Soc.*, 2007, **154**, A999.

82. Y.-W. Hu, I.D. Raistrick, R.A. Huggins, *J. Electrochem. Soc.*, 1977, **124**, 1240.

83. S. Garcia-Martin, A.D. Robertson, M.A.K.L. Dissanayake, A.R. West, *Solid State Ionics,*, 1995, **76**, 309-314.

84. A. Khorassani, A.R. West, *Solid State Ionics*, 1982, **7**, 1-8.

85. A. Fuertes, *J. Mater. Chem.*, 2012, **22**, 3293.

86. A. Fuertes, *Dalton Trans.*, 2010, **39**, 5942.

87. P. Ettmayer, W. Lengauer, in *Ullmann's Encyclopedia of Industrial Chemistry*, Wiley-VCH, 2000.

88. S.H. Elder, F.J. Di Salvo, L. Topor, A. Navrotsky, *Chem. Mater.*, 1993, **5**, 1545.

89. D. Mckay, J.S.J. Hargreaves, J.L. Rico, J.L. Rivera, X.L. Sun, *J. Solid State Chem.*, 2008, **181**, 325.

90. J.C. Fitzmaurice, A. Hector, I.P. Parkin, *J. Chem. Soc., Dalton Trans.*, 1993, **16**, 2435.

91. H. Zhao, M. Lei, X. Yang, J. Jian, X. Chen, *J. Am. Chem. Soc.*, 2005, **127(45)**, 15722.

92. M. Yang, J.A. Rodgers, L.C. Middler, J. Oro-Sole, A.B. Jorge, A. Fuertes, J.P. Attfield, *Inorg. Chem.*, 2009, **48**, 11498.

93. G. Demazeau, G. Goglio, A. Denis, A. Largeteau, *J. Phys.: Condens. Matter*, 2002, **14**, 11085.

94. R Marchand, Y Laurent, J Guyader, P L'Haridon, P Verdier, *J. Eur. Ceram. Soc.*, 1991, **8**, 197.

95. J.C. Fitzmaurice, A. Hector, I.P. Parkin, *Polyhedron*, 1993, **12(11)**, 1295.

96. B. Song, J.K. Jian, G. Wang, M. Lei, Y.P. Xu, X.L. Chen, *Chem. Mater.*, 2007, **19**, 1497.

97. B. Song, J.K. Jian, H.Q. Bao, M. Lei, H. Li, G. Wang, Y.P. Xu, X.L. Chen, *Appl. Phys. Lett.*, 2008, **92**, 192511.

98. D. Linden, T.B. Reddy, *Handbook of batteries*, McGraw-Hill, 2001.

99. S. Zhao, Z. Fu, Q. Qin, *Thin Solid Films*, 2002, **415**, 108.

100. F. Vereda, R.B. Goldner, T.E. Hass, P Zerigian, *Electrochem. Solid State Lett.*, 2002, **5**, A239.

101. Z-W. Fu, W-Y. Liu, C-L. Li, Q-Z. Qin, Y. Yao, F. Lu, , *Appl. Phys. Lett.*, 2003, **83**, 5008.

102. Y.G. Kim, H.N.G. Wadley, *J. Power Sources*, 2009, **187**, 591.

103. N.J. Dudney, *ECS Interface*, 2008, **17(3)**, 44.

104. R.B. Bradstreet, *Anal. Chem.*, 1954, **26**, 185.

105. A. Rachel, S.G. Ebbinghaus, M. Güngerich *Thermochimica Acta*, 2005, **438**, 134.

106. J. Perrière, *Vacuum*, 1987, **37**, 429.

107. F.R. Bryan, S. Bonfiglio, *J. Gas Chromatogr.*, 1964, **2**, 97.

108. A.R. West, in *Chemistry of solid state materials*, ed. P. G. Bruce, Cambridge University Press, 1995.

109. J. Maier, *Physical Chemistry of Ionic Materials - Ions and Electrons in Solids*, John Wiley & Sons Ltd, 2004.

110. A.R. West, *Basic Solid State Chemistry*, John Wiley & Sons, 2003.

111. P.G. Bruce, A.R. West, *J. Solid State Chem.*, 1984, **53**, 430-434.

112. A.R. West, *Solid State Chemistry and its Applications*, John Wiley & Sons, 2014.

113. J.B. Goodenough, ed. P. G. Bruce, Cambridge University Press, 1995.

114. P.G. Bruce, A.R. West, *J. Solid State Chem.*, 1982, **44**, 354.

115. A.R. West, *Solid State Chemistry and its Applications*, John Wiley & Sons, 1987.

116. E. Parthe, *Crystal Chemistry of Tetrahedral Structures*, Gordon & Breach, 1964.

117. A.R. West, *Z. Kristallogr.*, 1975, **141**, 422.

118. A.R. West, F.P. Glasser, *NBS Spec. Publ. 364, 'Solid State Chemistry'*, 1972, 457-469.

119. V.R. Channu, R. Holze, E.H. Walker Jr, S.A. Wicker Sr, R.R. Kalluru, Q.L. Williams, W. Walters, *Int. J. Electrochem. Sci.*, 2010, **5**, 1355.

120. J. Kohler, H. Makihara , H. Uegaito, H. Inoue, M. Toki, *Electrochim. Acta.*, 2000, **46**, 59.

121. R.E. Dinnebier, S.J.L. Billinge, *Powder Diffraction: Theory and Practice*, RSC Publishing, 2008.

122. B.D. Cullity, S.R. Stock, , *Elements of X-ray Diffraction*, Prentice-Hall, 2001.

123. E. Barsoukov, J.R. Macdonald, *Impedance Spectroscopy: Theory, Experiment, and Applications*, John Wiley & Sons, 2005.

124. D.C. Sinclair, F.D. Morrison, A.R. West, *Internat. Ceram.*, 2000, **2**, 33-37.

125. V.F. Lvovich, *Impedance Spectroscopy: Application to Electrochemical and Dielectric Phenomena*, John Wiley & Sons, 2012.

126. J.T.S. Irvine, D.C. Sinclair, A.R. West, *Adv. Mater.*, 1990, **2(3)**, 132.

127. D.C. Sinclair, *Boletín de la Sociedad Española de Cerámica y Vidrio*, 1994, **34(2)**, 55-65.

128. J. Kuwano, A.R. West, *Mat. Res. Bull.*, 1980, **15**, 1661.

129. C.M.A. Brett, A.M.O. Brett, *Electrochemistry: Principles, Methods and Applications*, Oxford University Press, 1996.

130. K. Mizushima, P.C. Jones, P.J. Wiseman, J.B. Goodenough, *Solid State Ionics*, 1981, **3-4**, 171-174.

131. J.N. Reimers, J.R. Dahn, *J. Electrochem. Soc.*, 1992, **139(8)**, 2091-2097.

132. H. T. M. Yoshio, K. Tominga, H. Noguchi, *J. Power Sources*, 1992, **40**, 347-353.

133. K. Mizushima, P. C. Jones, P. J. Wiscman, and J. B. Goodenough, *Mater. Res. Bull.*, 1980, **15**, 783-789.

134. *Test and conditions for Leco*, AMG Analytical Services, Internal notes.

135. A.R. West, F.P. Glasser, *J. Solid State Chem.*, 1972, **4**, 20-28.

136. I. Abrahams, P.G. Bruce, W.I.F. David, A.R. West, *J. Solid State Chem.*, 1994, **110**, 243-249.

137. S. Zemann, *Acta Cryst.*, 1960, **13**, 863-867.

138. F. Zambonini, F. Laves, *Z. Krist.*, 1932, **83**, 26.

139. P. Tarte, *J. Inorg. Nucl. Chem.*, 1967, **29**, 915-923.

140. C. Keffer, A. Mighell, F. Mauer, H. Swanson, S. Block, *Inorg. Chem.*, 1967, **6**, 119.

141. O.V. Yakubovic, V.S. Urusov, *Crystallogr. Rep.*, 1997, **42**, 261.

142. C. Frayret, C. Masquelier, A. Villesuzanne, M. Morcrette, J-M. Tarascon, *Chem. Mater.*, 2009, **21**, 1861–1874.

143. C. Ramirez, M.E. Castrejon, A.R.West, *J. Mater. Sci.*, 1985, **20**, 812-816.

144. L. Popovic, B. Manoun, D. de Waal, M.K. Nieuwoudt and J.D. Comins, *J. Raman Spectrosc.*, 2003, **34**, 77-83.

145. A.D. Robertson, A.R. West, A.G. Ritchie, *Solid State Ionics*, 1997, **104**, 1-11.

146. N.S. Roh, S.D. Lee, H.S. Kwon, *Scripta materialia*, 1999, **42(1)**, 43.

147. Z. Hu, D. Li, K. Xie, *Bull. Mater. Sci.*, 2008, **31**, 681.

148. T Minami, *J. Non-cryst. Solids*, 1985, **73**, 273.

149. H. Rabaa, R. Hoffmann, N.C. Hernandez, J.F. Sanz, *J. Solid State Chem.*, 2001, **161**, 73.

150. A.K. Ivanov-Shitz, V.V. Kireev, O.K. Mel'nikov, L.N. Demainets, *Crystallogr. Rep.*, 2001, **46**, 864.

151. E. Abrams, *Guidelines for the correction of impedance spectroscopy data for the jig and cable contributions*, Internal notes, 2003.

152. I.M. Hodge, M.D. Ingram, A.R. West, *J. Electroanal. Chem.*, 1976, **74**, 125-143.

153. I.M. Hodge, M.D. Ingram, A.R. West, *J. Am. Ceram. Soc.*, 1976, **59**, 360-366.

154. A. Reisman, J. Mineo, *J. Phys. Chem.*, 1962, **66**, 1181.

155. I. Abrahams, P.G. Bruce, *Acta Cryst.*, 1991, **B47**, 696-701.

156. R.D. Shannon, C. Calvo, *J. Solid State Chem.*, 1973, **6**, 538-549.

157. X. Song, M. Jia, R. Chen, *J. Mater. Process. Technol.*, 2002, **120**, 21.

158. V. Massarotti, D. Capsoni, M. Bini, P. Mustarelli, G. Chiodelli, C.B. Azzoni, P. Galinetto, M.C. Mozzati, *J. Phys. Chem.*, 2005, **B109**, 14845.

159. A. Kazakopoulos, O. Kalogirou, *J. Mater. Sci.*, 2009, 4987.

160. J. Yamaki, H. Ohtsuka, T. Shodai, *Solid State Ionics*, 1996, **86-88**, 1279.

161. A. Khorassani, A.R. West, *J. Solid State Chem.*, 1984, **53**, 369-375.

162. D.C. Sinclair, A.R. West, *Phys. Rev. B*, 1989, **39**, 13486.

163. T. Pajkossy, *J. Electroanal. Chem.*, 1994, **364**, 111-125.

164. K. Gaur, A.J. Pathak, H.B. Lal, *J. Mater. Sci.*, 1988, **23**, 4257.

165. J. Mizusaki, H. Tagawa, K. Saito, K. Uchida, M. Tezuka, *Solid State Ionics*, 1992, **53-56**, 791.

166. J. Vetter, *Journal of Power Sources*, 2005, **147**, 269.

167. D. Belov, M. Yang, *Journal of Solid State Electrochemistry*, 2008, **12**, 885.

168. M. Broussely, P. Biensan, F. Bonhomme, *Journal of Power Sources*, 2009, **146**, 90.

169. L.H. Thaller, *J. Electrochem. Soc.*, 1983, **130(5)**, 986.

170. M.E. Villafuerte-Castrejon, A.R. West, *J.C.S. Faraday I*, 1979, **75**, 374-384.

171. M.E. Villafuerte-Castrejon, A.R. West, *J.C.S. Faraday I*, 1981, **77**, 2297-2307.

172. A.R. West, F.P. Glasser, *J. Mater. Sci.*, 1970, **5**, 557-565.

173. A.R. West, F.P. Glasser, *J. Mater. Sci.*, 1970, **5**, 676-688.

174. H. Yamaguchi, K. Akatsuka, M. Setoguchi, *Acta Cryst.*, 1979, **B35**, 2678-2680.

175. A.R. West, F.P. Glasser, *J. Mater. Sci.*, 1971, **6**, 1100-1110.

176. A.R. West, F.P. Glasser, *J. Mater. Sci.*, 1972, **7**, 895-908.

177. C. Jousseaume, A. Kahn-Harari, D. Vivien, J. Derouet, F. Ribot, F. Villain, *J. Mater. Chem.*, 2002, **12**, 1525-1529.

178. D. K. Pradhan, R.N.P. Choudhary, B.K. Samantaray, *Materials Chemistry and physics*, 2009, **115**, 557-561.

179. K. Funke, D. Wilmer, T. Lauxtermanna, R. Holzgreve, S.M. Benningtonb, *Solid State Ionics*, 1996, **86-88**, 141-146.

180. D.L. Kinser, L.L. Hench, *J. Am. Ceram. Soc.*, 1969, **52(12)**, 638.

181. A.D. Robertson, A.R. West, *Solid State Ionics*, 1992, **58**, 351.

182. A.D. Robertson, A.R. West, *J. Mat. Chem.*, 1994, **4**, 457.

183. M.A.K.L. Dissanayake, R.P. Gunawardane, A.R. West, and P. W. S. K. B. G.K.R. Senadeera, M.A. Careem, *Solid State Ionics*, 1993, **62**, 217-223.

184. C.K. Lee, A.R. West, *J. Mat. Chem.*, 1993, **3**, 191.

185. N. Kuwataa, T. Saito, M. Tatsumisago, T. Minami, J. Kawamura, *Solid State Ionics*, 2004, **175**, 679.

186. M. Ribes, G. Taillades, A. Pradel, *Solid State Ionics*, 1998, **105**, 159.

187. G. Corbel, E. Suard, P. Lacorre, *Chemistry of Materials*, 2011, **23(5)**, 1288.

188. K.D. Kreuer, *Annu. Rev. Mater. Res.*, 2003, **33**, 333.

189. K-C. Hsiao, University of Sheffield, 2014.